ISBN 978-82-326-2452-2 (printed ver.)
ISBN 978-82-326-2453-9 (electronic ver.)
ISSN 1503-8181

Sofie Snipstad

Doctoral thesis

Doctoral theses at NTNU, 2017:190

Sofie Snipstad

Ultrasound-mediated delivery of nanomedicine across biological barriers - for improved treatment of cancer and diseases in the brain

Doctoral theses at NTNU, 2017:190

NTNU

NTNU
Norwegian University of Science and Technology
Thesis for the Degree of
Philosophiae Doctor
Faculty of Natural Sciences
Department of Physics

NTNU
Norwegian University of
Science and Technology

NTNU
Norwegian University of
Science and Technology

Sofie Snipstad

Ultrasound-mediated delivery of nanomedicine across biological barriers - for improved treatment of cancer and diseases in the brain

Thesis for the Degree of Philosophiae Doctor

Trondheim, June 2017

Norwegian University of Science and Technology
Faculty of Natural Sciences
Department of Physics

NTNU
Norwegian University of
Science and Technology

NTNU
Norwegian University of Science and Technology

Thesis for the Degree of Philosophiae Doctor

Faculty of Natural Sciences
Department of Physics

ISBN 978-82-326-2452-2 (printed ver.)
ISBN 978-82-326-2453-9 (electronic ver.)
ISSN 1503-8181

Doctoral theses at NTNU, 2017:190

Printed by NTNU Grafisk senter

Abstract

Despite major progress in the field of cancer research during the last decades, cancer remains a leading cause of death worldwide. Treatment with conventional chemotherapy is limited by inadequate delivery to the tumor and severe side-effects due to accumulation in healthy tissues. Encapsulation of drugs in nanoparticles can enable a more targeted delivery, for improved efficacy and reduced toxicity. However, delivery of nanoparticles is often insufficient and heterogeneous, due to various biological barriers in the tumor microenvironment. Ultrasound in combination with microbubbles has emerged as a promising method to enhance delivery of nanomedicines to tumor tissue. It can also facilitate non-invasive and localized opening of the blood-brain barrier for drug delivery to the brain.

A unique microbubble-platform was investigated, which demonstrated great potential for controlled drug delivery. It consisted of a shell of polymeric nanoparticles, encapsulating drugs and contrast agents. Various payloads demonstrated different degree of stability in the nanoparticles, and also affected nanoparticle-cell interactions. Depending on the payload, the nanoparticles could effectively deliver hydrophobic dyes and drugs to cells by either contact-mediated delivery directly to cytosol, or uptake by endocytosis followed by intracellular release. Cellular uptake and toxicity of the nanoparticles, as well as in vivo circulation and biodistribution were determined. Ultrasound treatment caused cavitation and collapse of the microbubbles, resulting in significantly improved accumulation and distribution of nanoparticles in solid tumors. Too low pressures, or short pulses did not enhance uptake, whereas too high pressures combined with long pulses resulted in tissue damage. In a proof-of-principle therapy study, the enhanced delivery resulted in complete and stable remission in all animals. Furthermore, it was shown that this platform could be used in combination with ultrasound to open the blood-brain barrier and successfully deliver and distribute nanoparticles in the brain.

Another highly interesting microbubble-platform was also explored, based on clusters of microdroplets and microbubbles, which upon activation by ultrasound form

large bubbles that deposit in the microvasculature. They were previously shown to enhance therapeutic efficacy of co-injected drugs to tumors in mice. Herein, we demonstrated that the same platform could be used to transiently and safely open the blood-brain barrier for delivery of macromolecules to the brain. These results provide an important fundament for future studies, and indicate that ultrasound-mediated delivery of nanomedicines across biological barriers can significantly improve treatment of cancer and diseases in the brain.

Acknowledgements

I feel privileged to have worked in such a fascinating and cross-disciplinary area of research, combining new technology with medicine. This is an exciting time for the field, and I am looking forward to seeing what the future holds. The work presented herein would not have been possible without valuable contributions from many people, who I would like to acknowledge.

First, I would like to thank my supervisor, Catharina, for giving me the opportunity to do this, and for guiding me through these years with your contagious enthusiasm and optimism. Thank you for sharing your knowledge with me, and for useful advice and constructive feedback.

My co-supervisor Ýrr, you are a dedicated and inspiring researcher, and have also been essential in this project. Thank you for many valuable discussions. In addition to Ýrr, I would also like to thank Einar, Anne, and the rest of the nanomedicine- and bubble-team at SINTEF, for synthesizing, optimizing and characterizing nanoparticles and microbubbles.

My co-supervisor Rune, thank you for contributing with your expertise in ultrasound, and for valuable input to our discussions about parameters and bubbles.

Kristin and Astrid, thank you for keeping the labs running smoothly, for solving practical problems and always being happy to help. Your competence and assistance have been very valuable in my work.

Andreas, thank you for your helpfulness, creativity, and for always being eager to discuss ideas, challenges and solutions with me. Sigrid, thank you for your contribution to discussions on bubbles and ultrasound treatments, and for our collaboration in the lab. To other previous and present group members, co-authors and master students, thank you Sjoerd, Annemieke, Einar, Sara, Siv, Mercy, Sylvie, Habib, Ingeborg, Astri and Eva for all your contributions to this work. I would also like to mention Inger, Linda, Mia, Sigurd, Stein Martin, Petros and Marieke. It has been

a pleasure to work with you all, thank you for creating a nice atmosphere in the group.

To my other co-authors; thanks to Sverre at St. Olavs Hospital for analysis of histological sections, to Phoenix Solutions, Andrew, Svein and Per, for microbubbles and microdroplets, and to Marcus, Peter, Andrey, and Frits for your contributions.

To Armend, Sindre, Nina, Kai, Jonas, Liv, Jakob, David, Andreas, Alicja, Alexandros and the rest of my colleagues at the Biophysics, thank you for making it a wonderful place to work.

Department of Physics, Department of Circulation and Medical Imaging, Department of Comparative Medicine, Cellular and Molecular Imaging Core Facility, NTNU Nanolab, and the MR-core facility are acknowledged for technical assistance, access to equipment and care of animals in various experiments. The Norwegian Research School in Medical Imaging and the Central Norway Regional Health Authority are acknowledged for financial support.

The work presented herein has also been presented at various conferences and popular scientific arenas. I am grateful to the Researchers' Grand Prix-crew, for a great experience and for teaching me how to better communicate science.

To my fellow students from Nanotechnology, who I shared five outstanding years with, I am so happy that many of you stayed in Trondheim, I have greatly enjoyed both lunches and fun evenings with you over the last years. Torstein, Jonas and Sindre, thank you for technical latex support.

To all my family and friends, thank you for always supporting me in what I set out to do, but more importantly, for so many memorable experiences outside of work during these years. Lunches, coffee breaks, dinners, late nights with good conversations, various gatherings, travels to remote places around the world, camping and cabin trips, hiking, ski-trips, climbing, surfing or kayaking. I am so lucky to have you all in my life.

And last but not least, I would especially like to thank my dear aunt Mai Bente, who passed away much too early, but continues to be a source of motivation and inspiration. Katrine, thank you for reminding me of the most important things in life. And Knut, thank you for everything. You are the best.

List of papers

The following publications are included in this thesis:

I **Contact-mediated intracellular delivery of hydrophobic drugs from polymeric nanoparticles.**
Snipstad S, Westrøm S, Mørch Ý, Afadzi M, Åslund AKO and Davies C de L.
Cancer Nanotechnology 5:8, 2014.

All authors were involved in designing and planning experiments. SS carried out cellular uptake studies. MA carried out toxicity studies, SW participated in experiments on cellular uptake and toxicity, ÝM synthesized the nanoparticles, and AÅ did NMR measurements. SS wrote the manuscript together with ÝM, AÅ and CD. All authors have read and approved the final manuscript.

II **Labeling nanoparticles: dye leakage and altered cellular uptake.**
Snipstad S, Hak S, Baghirov H, Sulheim E, Mørch Ý, Lélu S, von Haartman E, Bäck M, Nilsson KPR, Klymchenko AS, Davies C de L, Åslund AKO.
Cytometry, 2016. DOI: 10.1002/cyto.a.22853

SS, SH, YM, CD and AÅ designed the study. SH, ES and ÝM synthesized nanoparticles. MB, PN and AK synthesized fluorescent dyes. SS and HB performed cellular uptake experiments, with contributions from AÅ, SL and EvH. SS wrote the paper. All authors contributed in the revision and discussion of the paper.

III **Ultrasound improves the delivery and therapeutic effect of nanoparticle-stabilized microbubbles in breast cancer xenografts.**
Snipstad S, Berg S, Mørch Ý, Bjørkøy A, Sulheim E, Hansen R, Grimstad IH, van Wamel A, Maaland AF, Torp SH, Davies C de L.
Submitted to Ultrasound in Medicine and Biology.

SS and CD designed the study together with SB, RH and ÝM. SS and SB performed in vivo experiments. AvW contributed to ultrasound imaging. SS

performed ex vivo imaging and image analysis, with contribution from AB. ÝM and ES synthesized nanoparticles and microbubbles. IG and AM performed in vitro toxicity and uptake experiments, respectively. ST performed histological evaluation of sections. SS wrote the paper. All authors contributed in the revision and discussion of the paper.

IV **Ultrasound-mediated delivery and distribution of polymeric nanoparticles in the normal brain parenchyma and melanoma metastases.**
Baghirov H, Snipstad S, Sulheim E, Berg S, Hansen R, Thorsen F, Mørch Ý, Davies C de L, Åslund AKO.
Submitted to Scientific Reports.

HB, CD and AÅ designed the study with the assistance of RH, ÝM and FT. AÅ, HB, SS, SB and ES performed in vivo experiments. ÝM and ES synthesized nanoparticles and microbubbles. HB, AÅ and SB analysed data and HB performed ex vivo imaging and image analysis. HB wrote the manuscript. All authors contributed in writing and have approved the manuscript.

V **Efficient enhancement of blood–brain barrier permeability using Acoustic Cluster Therapy (ACT).**
Åslund AKO, Snipstad S, Healey A, Kvåle S, Torp SH, Sontum PC, Davies C de L, van Wamel A.
Theranostics 7, 23-30, 2017.

AÅ and AvW designed the study together with CD, AH and PS. AÅ, AvW and SS performed in vivo experiments. SK synthesized microbubbles and microdroplets. ST contributed to histological analysis. AÅ performed image analysis and wrote the paper. All authors contributed in the revision and discussion of the paper.

Related publications not included in this thesis:

- **Nanoparticle-stabilized microbubbles for multimodal imaging and drug delivery.**
  Mørch Ý, Hansen R, Berg S, Åslund AKO, Glomm WR, Eggen S, Schmid R, Johnsen H, Kubowicz S, Snipstad S, Sulheim E, Hak S, Singh G, McDonagh BH, Blom H, Davies C de L, Stenstad PM.
  Contrast Media & Molecular Imaging 10, 356-366, 2015.

- **Quantification and qualitative effects of different PEGylations on poly(butyl cyanoacrylate) nanoparticles.**
  Åslund AKO, Sulheim E, Snipstad S, von Haartman E, Baghirov H, Starr NJ, Løvmo MK, Lélu S, Scurr DJ, Davies C de L, Schmid RB, Mørch Ý.
  Molecular Pharmaceutics 2017.

- **Multi-modal characterization of vasculature and nanoparticle accumulation in five tumor xenograft models.**
  Sulheim E, Kim J, van Wamel A, Kim E, Snipstad S, Vidic I, Grimstad IH, Widerøe M, Waxman DJ, Torp SH, Lundgren S, Davies C de L.
  Manuscript in preparation.

List of abbreviations

ACT	Acoustic cluster therapy
ARF	Acoustic radiation force
BBB	Blood-brain-barrier
CLSM	Confocal laser scanning microscopy
EPR	Enhanced permeability and retention
FCM	Flow cytometry
FUS	Focused ultrasound
MI	Mechanical index
MRI	Magnetic resonance imaging
NPMB	Nanoparticle-stabilized microbubble
P-gp	P-glycoprotein
PACA	Poly(alkyl cyanoacrylate)
PBCA	Poly(butyl cyanoacrylate)
PEBCA	Poly(2-ethyl-butyl cyanoacrylate)
PEG	Poly(ethylene glycol)
POCA	Poly(octyl cyanoacrylate)
PRF	Pulse repetition frequency

Contents

1 Introduction

1.1 Cancer

During the last decades, our understanding of cancer, its causes and possible cures, has increased dramatically. Still, there are many unknowns, and cancer continues to be one of the leading causes of death worldwide. The term cancer refers to more than 100 different forms of the disease, and these malignancies can reside in almost every tissue in the body [1].

The 30 trillion cells of the healthy human body live in a complex environment, regulating one another's proliferation [1]. Normal cells reproduce only when instructed to by their surrounding cells, ensuring that each tissue maintains its size and appropriate architecture. This is possible because every cell carries a copy of the human genome, instructions which encode proteins that execute most of the functions of life [2]. Cancer cells are however characterized by uncontrolled and abnormal cell proliferation. This transformation of the cell from normal to malignant occurs due to the accumulation of mutations in specific genes within it. Such damage to the DNA can be inherited, or acquired by random changes or exposure to environmental factors such as specific chemicals or radiation. Healthy cells will repair this damage during the cell cycle, or halt progression of the cell cycle or undergo programmed cell death [3], but these repair mechanisms do not always function as intended. Even though each tumor can have its own unique traits, some common important features for these malignant cells exist. These hallmarks are acquired during the multistep development of cancer. They include sustaining proliferative signaling, evading growth suppressors, resisting cell death, enabling replicative immortality, inducing angiogenesis, activating invasion and metastasis, reprogramming energy metabolism and evading immune destruction [4].

The main methods for treating cancer have been surgery, radiotherapy and chemotherapy. With the majority of cancer related deaths being caused by metastasis

[5], cancer often requires systemic therapy. Chemotherapy however suffers from a non-specific mode of action, harming normal cells as well as cancer cells [6]. Chemotherapeutics are usually administered intravenously, and act as DNA damaging agents, which aim to prevent mitosis and cause cell death. They have a low molecular weight which causes them to be rapidly cleared from systemic circulation by renal filtration [7]. Due to their small size and generally high hydrophobicity, these drugs often have a large volume of distribution and tend to accumulate and cause toxicity towards many different healthy tissues [8]. New classes of anti-tumor molecularly targeted therapeutics have been developed, to more selectively interfere with certain hallmarks of cancer, but these second-generation agents often share the same limitations as the classical chemotherapeutics [7]. Because of these limitations, only a small fraction of the injected dose reaches the tumor, typically 0.01 to 0.001% [9, 10], and the side-effects of the treatment will limit the therapeutic dose that can be used. A wide range of different substances exist, with various mechanisms of action and thus different dose limiting toxicities, such as cardiotoxicity or neurotoxicity [11, 12]. In many cases, cancer treatment thus becomes a balance between destroying the cancer cells and minimizing damage to the normal cells. As such, and one of the greatest challenges in development and use of anti-cancer drugs is delivering them to the target tissue, without poisoning the rest of the body.

1.2 Nanomedicine

Nanotechnology has opened opportunities to manipulate and engineer matter at the nanoscale, with specific properties different from those at the bulk or molecular level, and is already being used in a vast amount of applications. One of these is within medicine, for improved diagnosis and treatment of various diseases, especially cancer [13–16]. Nanomedicines have been researched for several decades, as a way of achieving more specific delivery of cytostatic drugs, to reduce side effects and increase efficacy. The idea of 'magic bullets' which localize and affect only the target tissue and remain harmless to healthy tissue was postulated already a century ago [17]. A range of different nanomedicine platforms have been explored, including polymeric, lipid-based, protein-based, and metallic nanocarriers, dendrimers, nanotubes and viral particles [6, 15, 18, 19]. Nanoparticles are highly versatile; they have a high surface to volume ratio and thus a high reactivity. They can be tailored to different compositions, sizes, shapes and surface properties, depending on their application. Drugs, fluorescent dyes, contrast agents or targeting ligands can be encapsulated or bound to their surface [20], as illustrated in figure 1.

Nanocarriers as drug delivery vehicles offer many potential advantages compared to administration of a free drug [7, 19, 21]. They can provide increased stability of a drug in circulation and protect it from degradation. They can decrease toxicity, and increase the solubility of hydrophobic drugs. Furthermore, they may prolong circulation time in blood, and offer the possibility of targeted delivery in various ways [22], as described below. Incorporation of multiple drugs in the same particle allows for combination therapy with possible synergistic effects to overcome resistance [22–24]. In addition, multifunctional nanoparticles can be developed, enabling diagnostics and image guided drug delivery by incorporation of contrast agents for various imaging modalities [25, 26]. Once they have reached the target tissue, they can potentially enhance cellular uptake, and allow for controlled and sustained release of the drug [22]. This way, the release kinetics can be tuned to match the mechanism of action of the drug [27]. After completing their mission, they should ideally be cleared from the body without causing toxic effects.

To reach its target, a nanocarrier has to circulate for a prolonged period of time. For low molecular weight drugs, renal clearance by the kidney is efficient [28, 29]. Increasing the size by encapsulation in nanoparticles is thus a possible strategy to prolong circulation [28, 30]. A foreign material, bacteria, nanoparticles and other, will however normally be rapidly cleared from circulation by the immune system, by the mononuclear phagocyte system (MPS) [28, 31, 32]. This is facilitated by the adsorption of plasma proteins, opsonins, onto the particle surface, which interact with receptors on the surface of macrophages and other phagocytic cells, resulting in accumulation in the liver and spleen [28, 29, 31, 33]. To make nanoparticles hydrophilic, and stable against agglomeration (to avoid capillary occlusion) and non-specific uptake, surface modification is needed. Nanoparticles are therefore often coated with poly(ethylene glycol) (PEG), resulting in stealth behavior [28, 30, 32–34]. PEG creates a hydrated corona on the particle surface, which prevents protein adsorption and thus extends their time in circulation by decreasing uptake in macrophages [33, 35]. By decreasing the accumulation in liver and spleen, the bioavailability of nanoparticles for imaging and therapy increases [30]. Even though PEGylation is the most common strategy to achieve this, it has also been suggested that binding of specific proteins is necessary for prolonged circulation, and that PEGylation can also induce immune reactions and reduce cellular uptake at the target, and various other strategies have therefore been investigated [28, 30–32, 36].

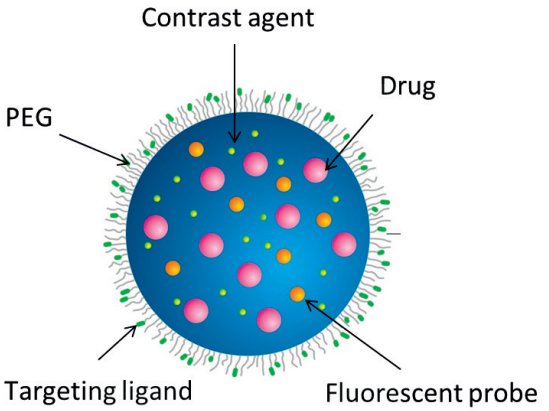

Figure 1: Illustration of a multifunctional nanoparticle, with drug, fluorescent dye, contrast agents, and a surface with PEG and targeting ligands. The figure is adapted from reference [20], with permission from John Wiley and Sons.

1.2.1 Passive targeting

The most common strategy for targeted delivery to tumors is by passive targeting. Passive targeting of nanomedicines to tumor tissue is possible due to the microenvironment in tumors and what is referred to as the enhanced permeability and retention (EPR) effect [37–39]. Leaky vasculature combined with non-functional lymphatics allow nanocarriers to passively extravasate and accumulate with time in tumors, as illustrated in figure 2. In normal tissue, the formation of new blood vessels from existing vasculature, angiogenesis, is normally observed during inflammation, tissue regeneration and wound healing [18]. Similarly, to sustain their rapid growth, cancer cells recruit neovasculature to supply them with oxygen and nutrition [40, 41]. Unlike microvasculature of normal tissue, which has an organized and regular branching structure [40], the blood vessels produced within tumors by an unbalanced mix of proangiogenic signals are often abnormal [4, 40]. Tumor neovasculature is tortuous and highly disorganized, characterized by capillary sprouting and excessive vessel branching, dilated vessels, and structural abnormalities such as large gaps in the vessel wall, causing leakiness. In contrast, most healthy tissues, except liver and spleen, have lower permeability, and thus less extravasation of nanocarriers [42]. In addition, tumors often have non-functional lymphatics and thus reduced clearance compared to normal tissue, where the lymphatic system effectively recovers macromolecules and lipid particles from the interstitial space [39].

1.2.2 Active targeting

Another strategy for improving selectivity is to couple the therapeutic or its carrier to antibodies or other ligands that recognize tumor-associated receptors, which are either uniquely expressed or overexpressed in the target cells, relative to normal tissues [15, 43, 44]. An illustration is shown in figure 2. Active targeting to cancer cells has resulted in improved target cell recognition and cellular uptake, but has not yet improved overall tumor accumulation [7, 21, 45]. These formulations still rely on the EPR-effect to travel from vasculature to the cancer cells which express their target receptors. In addition, their successful binding to a target receptor can lead to a 'binding-site barrier' which limits further tissue penetration and prevents them from reaching cells that are distant from the vessels [6, 46]. Another approach is to target the carriers to receptors expressed at the neoangiogenic endothelium [8, 47], such as specific integrins [48]. Destruction of the endothelium can result in death of tumor cells to due lack of oxygen and nutrients [7].

1.2.3 Triggered targeting

A third strategy for increased specificity, is by the use of triggered drug delivery with stimuli-responsive nanocarriers [49], as illustrated in figure 2. Stimuli-responsive systems recognize their local environment and react to it, to allow delivery and release with spatial and temporal control. Specific microenvironmental changes associated with the target disease, such as specific enzymes, redox potential, or changes in pH can be used as triggers. Other examples are local external triggers such as light, temperature, magnetic fields or ultrasound [21, 49, 50]. Thermo-responsive systems and photo-sensitive carriers can trigger release based on stimulation by heat or light, respectively, at the target. Magnetic nanomedicines are guided to the target by an external magnetic field to improve accumulation, and ultrasound can be used to enhance delivery or trigger a release. The diversity in responsive materials that can be assembled into different structures allows great flexibility, although increased complexity of their design could limit scaling up their synthesis and translation to the clinic.

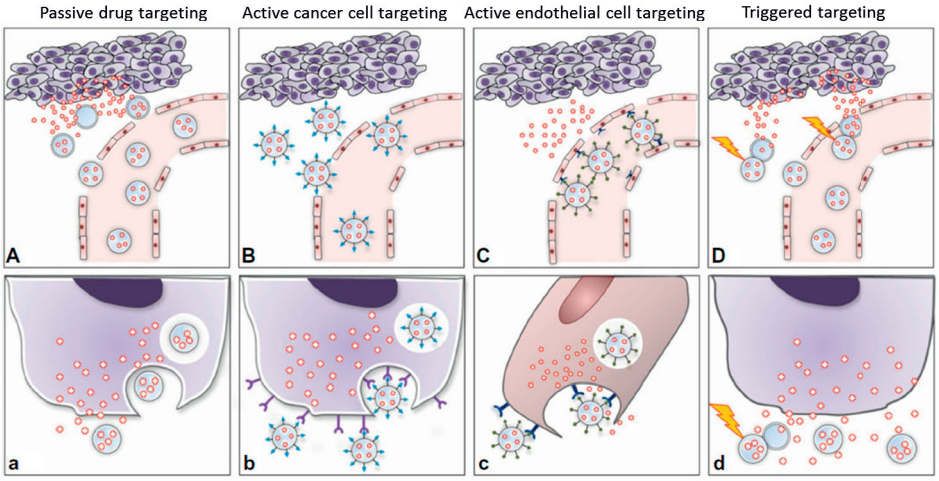

Figure 2: Illustration of various targeting strategies of nanomedicines. (A) Passive extravasation and accumulation of nanocarriers, which then deliver the drug to the cancer cells (a). (B) Active targeting to receptors which are overexpressed at cancer cells (b). (C) Active targeting to endothelial cells (c). (D) Triggered drug delivery by stimuli-responsive nanocarriers, to increase accumulation at the target or induce a release (d). The figure is adapted from references [8, 15], with permission from Elsevier and Dove Medical Press.

1.3 Barriers for drug delivery to tumors

Cancer nanomedicines that have been approved by the Food and Drug Administration (FDA) so far (examples are Myocet, Caelyx, DaunoXome, Abraxane [7, 15, 21, 50]) have shown reduced toxicity compared to conventional chemotherapeutics, although they hardly improve efficacy [7, 21], owing to several physiological barriers that restrict their delivery [8, 45, 47, 51]. These barriers lead to a heterogeneous distribution of the drug, and limit the drug from reaching all the cells. Even a small fraction of remaining cancer cells can result in tumor regrowth [52]. A recent review of nanomedicine literature from the past 10 years, found that a median of only 0.7% of the injected dose was delivered to the tumor [53]. To reach its target, a nanomedicine has to travel through circulation to reach the tumor, penetrate across the capillary wall and through the extracellular matrix, and enter the tumor cells [54] as illustrated in figure 3. On this journey, there are at least four important barriers which they encounter;

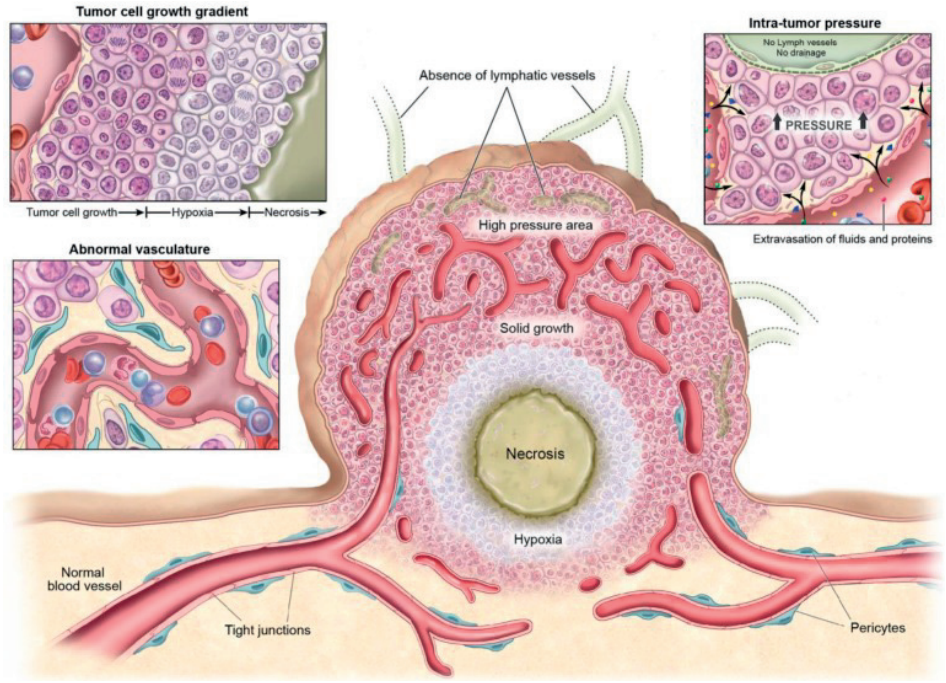

Figure 3: Illustration of the tumor microenvironment, showing some of the barriers to drug delivery. A nanomedicine has to travel through circulation to reach the tumor, penetrate across the blood vessel wall and through extracellular matrix, to reach the cancer cells. The figure is adapted from reference [40], with permission from Ivyspring International Publisher.

1.3.1 Vascular transport

The first barrier is the heterogeneous vasculature and blood flow in tumors [52]. The tumor vessels have an irregular architecture and abnormal branching pattern, different from that seen in normal vasculature [48, 55, 56]. The consequence of this is large heterogeneity in tumor blood flow, and tumor perfusion rates are often low [41]. Parts of a tumor can be highly angiogenic and densely vascularized, whereas proliferating cancer and stromal cells can cause compression and collapse of intra-tumor blood and lymphatic vessels, leaving other parts of a tumor poorly or even unperfused [41, 45, 57].

1.3.2 Extravasation

The second barrier is extravasation across the vessel wall, which can occur by convection due to pressure gradients, or diffusion by concentration gradients. Water and small lipophilic molecules can freely diffuse through endothelial cells and their membranes, whereas larger macromolecules need inter- or intra-cellular pores or active transport through the cells [55]. Compared to normal endothelial cells which form a continuous and uniform monolayer, some tumor vessels have a cellular lining of disorganized, loosely connected, branched, overlapping and sprouting endothelial cells [48]. They can also have discontinuous basement membranes and fewer supporting pericytes [40]. This leakiness of tumor vasculature combined with non-functional lymphatics causes a high interstitial fluid pressure [58]. Unlike normal tissues where interstitial fluid pressure is around 0 mmHg, the intravascular and extravascular pressures in tumors can become almost equal, and vary from 10 to 30 mmHg in different tumors [41, 58]. This will limit convective extravasation, leaving diffusion as the most important mechanism. Furthermore, tumor vessel permeability is highly spatially and temporally heterogeneous. It varies between and within tumors, and with time as the tumor develops, and depends highly on the local microenvironment [41, 52, 55]. The cut-off pore size may also vary substantially [45, 48].

1.3.3 Interstitial transport

The third barrier is the interstitial compartment [52]. The high interstitial fluid pressure will limit transport to diffusion. The extracellular matrix, comprised by collagen, proteoglycans, glycosaminoglycans and other molecules will prevent penetration of therapeutic agents [55, 59]. Small therapeutic agents, such as chemotherapeutics, diffuse fairly rapidly in the interstitium [55]. Nanoparticles, however, are hindered from reaching all the cells due to a dense tumor stroma, high tumor cell density and the varying amount of extracellular matrix components. By decreasing the size of the carriers, diffusion rate is increased, but at a cost of less payload per nanocarrier.

1.3.4 Cellular uptake

The forth barrier is the cell membrane and cytoplasm, since most drugs exert their effects intracellularly [51, 52]. Cellular uptake will depend on properties of the drug, and on interactions between the drug and the cells. Small, nonpolar molecules

can diffuse freely through membranes and into cells, whereas other small solutes make use of specific membrane proteins for transport [60]. For larger nanoparticles, an active uptake is often required to enter the cells. Active uptake into cells will depend highly on the cell line and on particle characteristics such as size, composition, charge and surface properties, and can happen by a number of different endocytic pathways [51, 61–63]. Cells normally use endocytosis for uptake of nutrients, in immune response, signal transduction, intercellular communication and more [61, 62]. Specialized cells such as macrophages can phagocytose large particles, and almost all cells can internalize nanoparticles by pinocytosis; by either macropinocytosis, clathrin-mediated endocytosis, caveolin-mediated endocytosis, or clathrin- and caveolin-independent endocytosis [62, 64]. After internalization, trafficking to various destinations inside the cell may take place [60, 65]. Intracellular trafficking is typically done in endosomal vesicles, and when the entire carrier is taken up, intracellular drug release and endosomal or lysosomal escape are necessary for the drug to be effective. A schematic illustration is shown in figure 4. To increase intracellular delivery, various ways of actively targeting nanocarriers have been attempted [51, 66]. Although active uptake is often required to enter the cells, other mechanisms for delivery are possible as well; nanocarriers can degrade extracellularly, followed by cellular uptake of the drug itself, or deliver drugs by contact-mediated delivery or membrane fusion whereby the drug directly enters the cytosol [67–70]. A variety of cells are however equipped with drug-efflux pumps, such as P-glycoprotein (P-gp), which will limit the fraction of the dose that can actually exert its cytotoxic effects intracellularly [51]. P-gp and other transporter proteins are therefore often associated with multidrug-resistance in cancer [71].

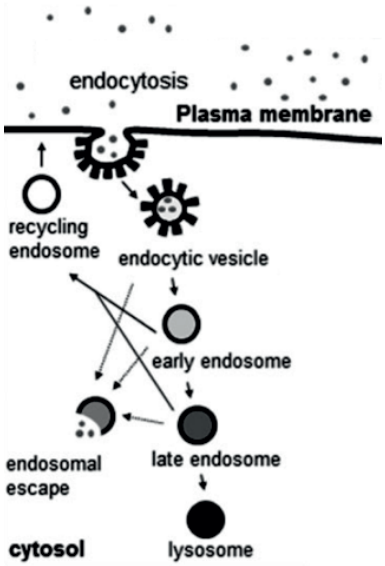

Figure 4: A schematic illustration of a possible internalization route of nanomedicines. The figure is adapted from reference [65], with permission from John Wiley and Sons.

1.3.5 Additional barriers

Altogether, the low tumor perfusion, uneven distribution of blood flow, heterogeneous vessel permeability, and a dense microenvironment, will limit the supply, penetration and distribution of nanomedicines in tumors [45]. In addition, in each compartment, the nanomedicine could be metabolized or degraded, eliminated by excretion, or bind to proteins or other components which could also limit its efficacy [54]. Areas of hypoxia due to limited blood supply can also result in resistance to various forms of treatment [55]. As such, various strategies have been employed to modify and normalize the tumor microenvironment in order to improve delivery of drugs [21, 45, 55].

1.4 Drug delivery to the brain

Another barrier for drug delivery is the blood-brain barrier (BBB). The brain is comprised of a dense and complex vascular network [72]. Unlike the vasculature

in many tumors, however, the vasculature of the brain is highly selective in which substances that are allowed to penetrate. The brain is protected from blood borne potentially harmful constituents by the BBB, which is formed by endothelial cells lining the brain capillaries and their tight junctions [73, 74], as illustrated in figure 5. These cells are supported by a basement membrane, astrocytes and pericytes which contribute to maintaining the barrier [74–76]. This physical barrier limits intercellular passage between the endothelial cells (paracellular transport), and forces most molecular traffic to take transcellular routes across the BBB, by crossing through the cytoplasm of the cells [74, 77]. Transcellular traffic is however strongly regulated by transport systems, which provide a selective transport barrier and excludes or effluxes potentially harmful compounds [74, 78]. The brain capillaries are equipped with drug efflux pumps which efflux various drugs, such as P-gp, whose expression is also associated with multidrug-resistance cancer cells [79]. In addition, there are metabolic barriers, enzymes that metabolize and inactivate molecules in transit [73, 74]. This complex dynamic system regulates influx and efflux of nutrients and waste products, and provides a stable environment for neural function, with a precise regulation of the microenvironment in the brain [74]. A few small lipid-soluble molecules, as well as O_2 and CO_2, can passively diffuse into the brain, whereas other molecules, required nutrients and proteins, use specific transport systems, which permit selective passage of only specific substances [74]. On one side, this barrier is highly useful for maintaining homeostasis and protecting the brain from neurotoxins and infectious agents, but it also effectively prevents delivery of a vast amount of drugs to the brain [80, 81]. The BBB is therefore the most important factor limiting treatment of cancer in the brain, but it also limits the future development and use of already existing therapeutics for neurodegenerative diseases such as Parkinson's, Alzheimer's, Huntington's, Creutzfeldt-Jakob disease and more [72, 82].

Various ways of delivering drugs to the brain have been explored, each with their own benefits and limitations [72, 77, 80, 83, 84]. One option is to bypass the BBB by delivering the therapeutic directly into the brain by a variety of routes. These include delivery to the cerebrospinal fluid by intrathecal or intraventricular routes, interstitial delivery via depot implants or catheters, or intranasal delivery [77]. The diffusion of drugs from cerebrospinal fluid into the brain parenchyma is however limited. Interstitial implants are also limited by poor diffusion from the depot site, and trans-cranial delivery is typically invasive. Intranasal delivery may damage the mucosa. Another option is modification of the transported agent to allow passage on its own, passively or by active transporters, incorporating it into some selected nanoparticles which can cross, or into immune/stem cells which may migrate across the BBB [77]. These methods are however not localized. A third option is various

ways of disrupting the BBB. Examples are substances that osmotically or chemically disrupt the BBB by affecting the endothelial cells and their membranes [77]. These methods are also non-specific, and can lead to edema and other complications such as toxicity and damage to the brain. Another strategy to open the BBB in a non-invasive, localized and reversible manner is by ultrasound in combination with microbubbles [77, 85].

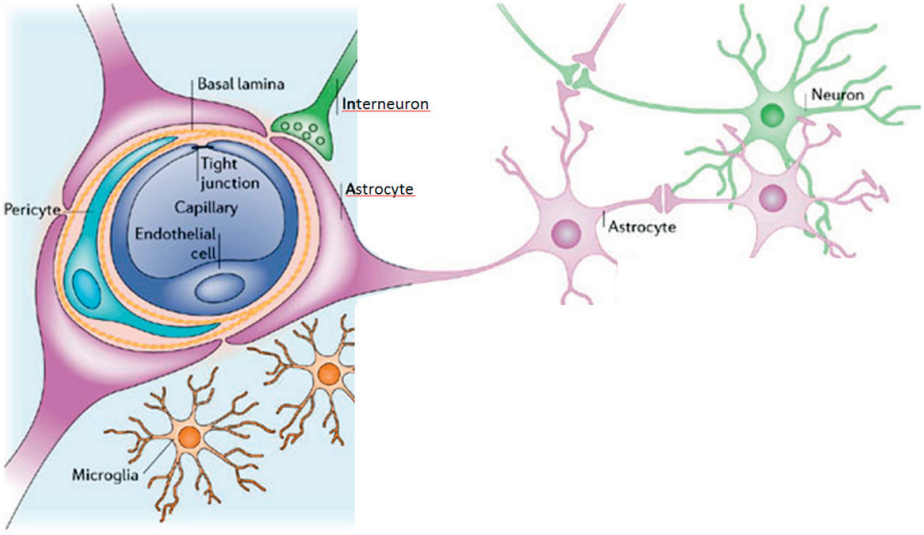

Figure 5: Illustration of the BBB, formed by capillary endothelial cells, surrounded by basal lamina, pericytes, and astrocytes which provide a cellular link to neurons. The figure is adapted from reference [74], with permission from Nature Publishing group.

1.5 Ultrasound and microbubbles

Ultrasound is extensively used for medical diagnostics, but has during the last decades also been applied for therapeutic purposes such as drug delivery across biological barriers [86–88]. One application is to, in combination with gas filled microbubbles, improve accumulation and distribution of drugs in tumors and across the BBB [89–93].

Ultrasound is pressure waves at frequencies above 20 kHz [87, 94], which can be described by their velocity, wavelength, amplitude, and frequency [95]. In therapeutic applications, ultrasound is often pulsed, and described by its burst duration

(with a certain number of pulses per burst), burst repetition frequency, and the duty cycle, the fraction of time the ultrasound is on during the total treatment time [96]. An illustration is shown in figure 6. Molecules in the transmitting medium will undergo slight oscillatory displacement due to compression and expansion caused by the pressure waves. As ultrasound propagates through tissue, it is attenuated due to scattering where parts of the wave change direction, or absorption, where parts of the wave is converted to heat [96]. Water has low attenuation, whereas soft tissues have moderate attenuation, and tissues such as lungs and bone have high attenuation [87]. In diagnostic ultrasound, energy deposition is meant to be minimal, whereas therapeutic ultrasound is based on deposition of energy to create specific effects [97]. Depending on the desired application, ultrasound parameters can be tuned for imaging purposes, or to create effects such as heating, acoustic radiation forces or acoustic cavitation in order to increase delivery of drugs across various biological barriers [87, 97].

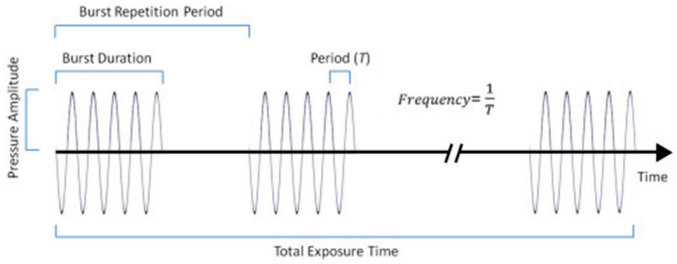

Figure 6: Illustration of pulsed ultrasound, depicted as a sinusoidal wave. The burst duration, burst repetition period, period, frequency, pressure amplitude, and total exposure time are displayed. The figure is adapted from reference [83], with permission from Elsevier.

1.5.1 Heating

The absorption of acoustic energy by tissue causes thermal heating [94, 97], and high intensities have been used to create hyperthermia for applications in physical therapy [98] and tissue ablation [99, 100]. However, local heating can also be used to increase local drug release from carriers, increase blood flow, vascular permeability, diffusion of drugs, and possibly uptake in cells [87, 94, 97, 101, 102], thereby enhancing delivery of therapeutic molecules.

1.5.2 Radiation force

A momentum transfer from the ultrasound wave to the transmitting medium at high frequencies and intensities causes a radiation force in the direction of wave propagation [97]. This force can produce a steady flow in fluids, known as acoustic streaming. The acoustic radiation force (ARF) can thus potentially increase convective transport [87], and can cause local tissue displacements, increase extravasation and disrupt extracellular matrix for increased interstitial penetration [97]. Radiation forces have also been reported to modulate the position and velocity of flow of ultrasound contrast agents [97], to push circulating microbubbles toward the endothelial wall [102].

1.5.3 Cavitation

The strongest forces associated with ultrasound are generated by gas-liquid interfaces [87]. Cavitation refers to the creation and oscillation of gas bubbles upon exposure to an acoustic field, in response to the oscillating pressure [87, 94]. The bubbles can occur naturally or be introduced artificially by microbubbles in the blood stream. The microbubbles which are typically used for this application are ultrasound contrast agents with sizes of 1-10 μm, thus restricting them to the vascular compartment [103]. Various types are available commercially, with shells of polymers, proteins, or lipids. They contain hydrophobic gas instead of air for increased stability, which is excreted by exhalation, whereas the shell is excreted by the reticuloendothelial system in liver and spleen (RES) [103]. They can be used with a co-administration of a drug, or the drug may be loaded onto the bubbles in various ways [102, 104–106]. They may also be targeted to molecular markers expressed on endothelium of specific diseases [88, 102]. As pressure waves pass through the medium, the bubbles will expand at low pressures and contract at high pressures [94], as illustrated in figure 7. The largest oscillation response of microbubbles is obtained at their resonance frequency, which decreases with increasing size [105], and the oscillation behavior can be different for soft shelled bubbles compared to those with more rigid shells [105].

Stable cavitation occurs at relatively low amplitudes, and is characterized by sustained bubble radius oscillation about its equilibrium for a relatively large number of cycles [97]. The oscillation generates a circulating fluid flow around the bubble, known as microstreaming, which has velocities and shear rates proportional to the amplitude of oscillation [87, 107, 108]. If the microbubbles are close to the

endothelium they can also push and pull on the cell membrane [105]. As they oscillate, dissolved gas in the surrounding liquid diffuses and accumulates in the bubbles causing them to grow in size [87].

Inertial cavitation occurs when larger amplitude oscillations result from an increased acoustic pressure or increased bubble size [87]. The amplitude of oscillation increases until the inrushing fluid has sufficient inertia that it cannot reverse its direction [94]. As the inertia of the inward moving fluid overcomes the internal pressure of the bubble, the bubble will collapse [87]. The extreme compression of the gas by the liquid creates high pressures and temperatures [87]. This fragmentation results in smaller bubbles which can again cavitate, grow and collapse [87]. Following the collapse of a bubble, shock waves are created and liquid jets can occur if the bubble collapses near a surface [87, 97, 109]. Mechanical index (MI), defined as the peak negative pressure amplitude divided by the square root of the center frequency of the ultrasound wave, is often used to classify bubble behavior, and the probability of inertial cavitation occurring increases with increasing MI [87, 105].

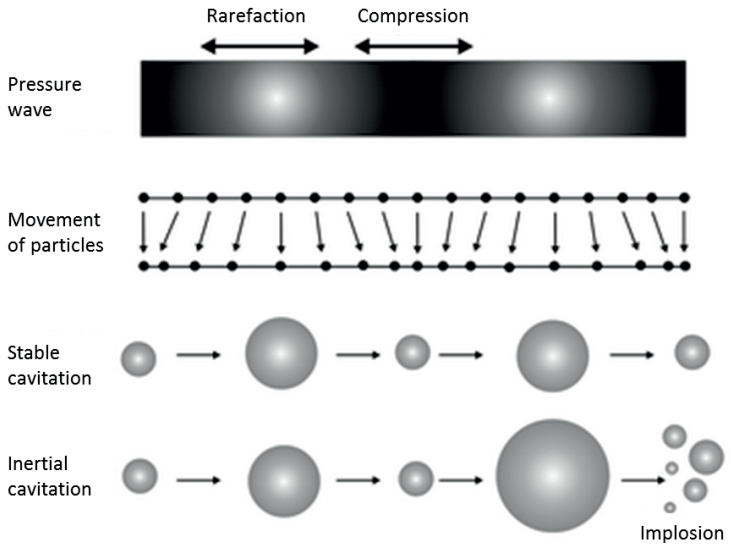

Figure 7: Schematic representation of an acoustic pressure wave and the resulting displacement of particles in the transmitting medium. Stable and inertial cavitation of microbubbles is illustrated. The figure is adapted from reference [110], with permission from The Royal Society of Chemistry.

Various methods have been reported in the literature to study the mechanisms and effects of bubble-cell interactions [111, 112]. Some examples of how oscillating microbubbles can interact with cells are illustrated in figure 8. The resulting streaming and shear forces, and push and pull on the vessel wall from stable cavitation can cause formation of small pores for increased vascular permeability, and enhance endocytosis [102, 105, 109, 113, 114]. Following the collapse of a bubble, the resulting shock waves and liquid jets can create both temporary and permanent pores in the capillary wall and in cell membranes [87, 97, 109]. By the described mechanisms, focused ultrasound has been used to deliver molecules to individual cells in vitro by sonoporation [109, 115, 116], which has also been demonstrated in vivo in endothelial cells [117]. These effects can be employed to increase the extravasation across the capillary wall and potentially improve penetration through the interstitium, thereby improving the accumulation and distribution of nanoparticles and drugs in solid tumors [89–92, 97, 118–121].

Several similar mechanisms have also been suggested to be involved in the BBB disruption for drug delivery to the brain [77, 83, 122]. Oscillations will exert mechanical stresses on the tight junctions, generating a possible paracellular transport route by reduction of tight junction proteins [122, 123]. It has also been suggested that transcytosis can be induced by ultrasound [114, 122, 124, 125], and that transient formation of fenestrations in the endothelial cell membrane can contribute to transcellular transport [114, 122]. Additionally, ultrasound combined with microbubbles has been also been reported down-regulate P-gp expression in brain blood vessels [126, 127].

The response of a microbubble to ultrasound depends highly on the frequency, pressure level, pulse duration, and repetition rate [102, 105], as well as properties of the microbubble such as size, shell thickness and stiffness [105, 109]. A range of different ultrasound parameters have been used for delivery purposes, both in tumors and in the brain [83, 85, 102, 128–131]. One treatment may not be sufficient to deliver a drug, whereas another treatment may damage tissues and cells [87], illustrating the importance of finding parameters that cause the desired effects without damage. In general, increasing the pressure, sonication time, burst length or pulse repetition frequency increase the magnitude of BBB opening [132].

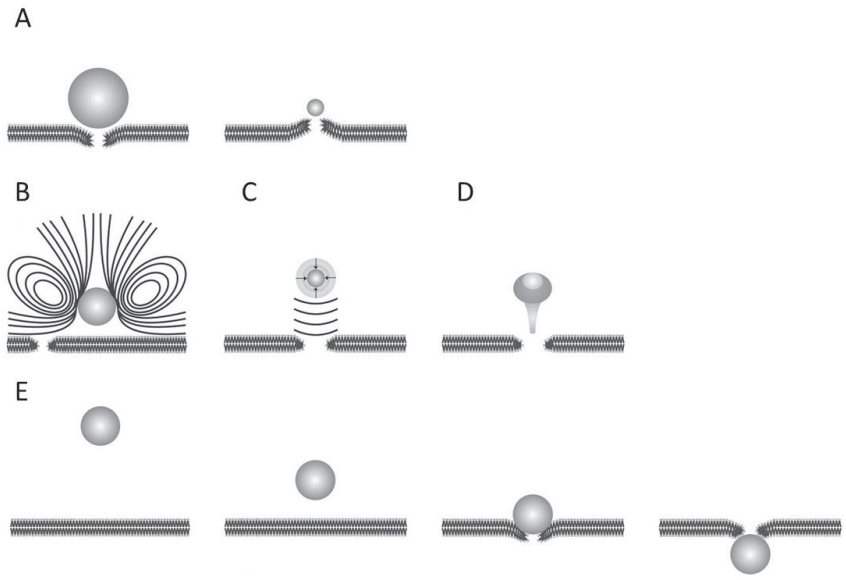

Figure 8: Schematic representation of biophysical effects from oscillating microbubbles on cells which may disrupt membrane integrity. (A) During expansion and contraction, microbubbles may push and pull on the membrane. (B) Fluid streaming around a microbubble causes shear stress to the membrane. (C) Microbubble collapse can produce shock waves that generate high stress on the membrane. (D) Collapsing bubbles near a surface may also produce jets towards the membrane. (E) Radiation forces can cause microbubble displacement towards the membrane. The figure is adapted from references [109, 112], with permission from Elsevier.

1.5.4 Preclinical and clinical relevance

The potential of ultrasound-mediated drug delivery of free or encapsulated chemotherapeutics to cancer has been demonstrated in several preclinical studies [89, 90, 92, 102, 104, 119]. A recent clinical trial evaluated the safety and potential toxicity of combining gemcitabine with microbubbles under sonication in ten inoperable pancreatic cancer patients [91]. They report that the combination of clinically available ultrasound equipment with commercial microbubbles and chemotherapy resulted in no additional toxicities. Further, the combined treatment may improve the clinical efficacy of gemcitabine, prolong the quality of life, and extend survival in patients with pancreatic adenocarcinoma.

Low intensity focused ultrasound in combination with microbubbles has also been shown to non-invasively, transiently, selectively and safely open the blood brain barrier in small animals [83, 85, 133, 134] and non-human primates [135, 136]. Such treatment has been used to deliver free and encapsulated chemotherapeutic drugs [93, 137, 138], antibodies [139–145], interleukins [146], genes [147–149] and cells [150–152] to the brain. Currently, there are also two ongoing clinical trials in glioblastoma patients [153–155], illustrating the promise of this approach for improved drug delivery.

2 Objectives

Nanoparticles are promising for drug delivery, but limited by heterogeneous accumulation at the target. The overall aim of this project was to employ a highly interesting nanoparticle-stabilized microbubble (NPMB) platform in combination with ultrasound, to enhance delivery of nanomedicine across biological barriers, for improved treatment of cancer and diseases in the brain. In addition, another novel concept was explored, based on clusters of microdroplets and microbubbles, which upon activation by ultrasound form large bubbles that deposit in the vasculature. Specific aims were;

- To obtain an understanding of possible mechanisms for drug delivery from polymeric nanoparticles to cancer cells.
- To assess stability of different fluorescent payloads encapsulated in nanoparticles and how they affect nanoparticle properties.
- To characterize the NPMB platform with respect to in vitro cellular uptake and toxicity, and in vivo circulation and biodistribution.
- To employ the NPMBs with various ultrasound treatments for delivery of nanoparticles to tumors, to understand more of the involved mechanisms and the impact of stable versus inertial cavitation.
- To determine if an enhanced delivery of nanoparticles has a therapeutic benefit in tumors, in a proof-of-principle therapy study.
- To apply the NPMBs for opening the BBB, to study delivery and the distribution of nanoparticles in the brain.
- To exploit acoustic cluster therapy (ACT), which has previously shown promising results for enhanced delivery to solid tumors, for its potential to open the BBB.

3 Research platforms and methods

3.1 Nanoparticle- and microbubble-platforms

Polymeric nanocarriers have been studied for several decades [16], and are promising drug delivery vehicles due to their high drug loading capacity and controlled release properties [19, 156]. Poly(alkyl cyanoacrylates) (PACA) are biodegradable polymers with low toxicity [78, 157, 158], of which a variety of subtypes exist [156, 159]. They can easily be synthesized by mini-emulsion polymerization [160] and can encapsulate a range of drugs [158, 161]. Since these polymers are hydrophobic, PACA nanoparticles are especially suitable for encapsulating hydrophobic drugs. Their surface can be functionalized [158], allowing for improved pharmacokinetics, or conjugation of ligands for targeted delivery. The major degradation path in vivo is by surface erosion after hydrolysis of the ester bond of the alkyl side chain of the polymer, resulting in degradation products of alkylalcohol and poly(cyanoacrylic acid), which are water soluble and can be excreted by the kidneys [78]. This process can be catalyzed by esterases from serum, lysosomes and pancreatic juice [78]. Degradation appears to be the main method for release of highly hydrophobic drugs, and the degradation rate depends on the length of the alkyl side chain of the polymer [162, 163]. One type of PACA nanoparticles has already reached phase III clinical trials for treatment of liver cancer (Livatag, Onxeo) [164, 165].

A unique multifunctional drug delivery system consisting of microbubbles stabilized by PACA nanoparticles to be used in ultrasound-mediated drug delivery has recently been developed [20], as illustrated in figure 9. Combining nanoparticles with microbubbles has received interest recently, and many have chemically linked nanoparticles to microbubbles for drug delivery purposes [90, 166–170]. The PEGylated nanoparticles used in this work can be prepared in a one-step synthesis, can encapsulate drugs or contrast agents [20]. Microbubbles are subsequently formed by vigorous stirring and addition of surface active substances (proteins or surfactants).

The nanoparticles possess the sufficient balance of hydrophobicity and hydrophilicity which is to required stabilize the gas-water interface, and self-assemble into a spherical shell containing gas, forming the surface of resulting microbubbles [20]. In addition to those on the bubbles, there is also a large surplus of nanoparticles in the solution. The method is simple, cheap, and is feasible to scale up.

Previous studies have reported drug delivery with this platform to prostate xenograft tumors in mice [171] and across the BBB in healthy rats [133]. Here, stability of various encapsulated dyes was evaluated, along with mechanisms for drug delivery to cells, cellular uptake and toxicity, in vivo circulation time, biodistribution, and ultrasound-mediated nanoparticle delivery to solid tumors and the brain in mice (**paper I-IV**). A systematic study was performed to evaluate the effect of various pressures and pulse lengths on the tumor uptake of PACA nanoparticles, and the first preliminary therapeutic study is described. For delivery to the brain, the relation between extent of BBB opening and nanoparticle delivery was investigated, as well as the effect of ARF on nanoparticle displacement, and expression of P-gp after treatment. In parallel with this, the nanoparticles have been characterized with respect to intracellular degradation [162], and the amount and effects of surface PEGylation [172, 173]. Acoustic and mechanical properties of the microbubbles have also been characterized [174, 175].

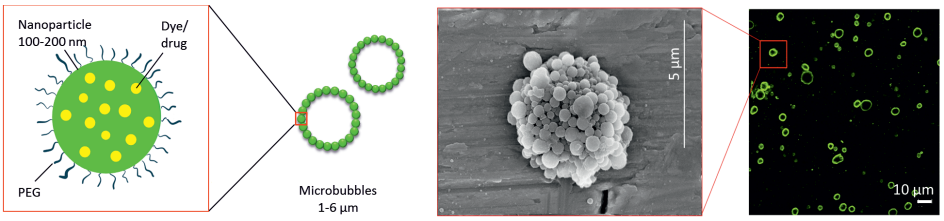

Figure 9: Graphical illustration of the NPMB platform (left), together with a scanning electron micrograph (middle, photo from SINTEF) and confocal microscopy image of the microbubbles (right). The figure is adapted from reference [20], with permission from John Wiley and Sons.

For encapsulation and delivery of hydrophobic drugs, lipid-based nanoemulsions and liposomes are other commonly used platforms, and multiple liposomes have already been clinically approved for cancer treatment [15, 21, 176, 177]. Liposomes have a lipid bilayer enclosing an aqueous core, while nanoemulsions consist of oil droplets stabilized by amphiphilic lipid monolayers, often coated with PEG [178, 179]. An illustration of a liposome is shown in figure 10. In addition to drugs, such platforms

have also been used to encapsulate fluorescent dyes and contrast agents for imaging, and have shown promise also for diagnostic purposes [180, 181]. These two platforms were used together with the polymeric nanoparticles to study drug-carrier stability and how various payloads affect nanoparticle properties (**paper II**).

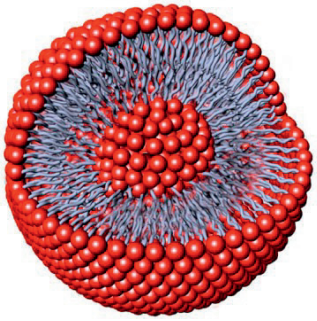

Figure 10: Illustration of a liposome, a vesicle with a bilayer membrane structure containing amphiphilic molecules, with hydrophobic and hydrophilic groups that self-assemble in water. The figure is adapted from reference [15], with permission from Dove Medical Press.

Another promising microbubble-platform for drug delivery, ACT, is based on clusters of negatively charged microbubbles and positively charged microdroplets [182]. These "next-generation" microbubbles are designed to improve sonoporation efficacy by addressing some limitations of commercially available ultrasound contrast agents. After intravenous administration, focused ultrasound (FUS) is applied to the targeted pathology whereby the microbubbles transfer energy to the microdroplets, which undergo a liquid-to-gas phase shift [183], as illustrated in figure 11. Growing in size, these large bubbles transiently lodge and block blood flow at the capillary level. Further exposure to focused ultrasound causes the large bubbles to oscillate and induce biomechanical effects, thereby enhancing extravasation of co-administered molecular or encapsulated drugs to the diseased area [182, 184]. Safety has previously been assessed in rats and dogs [185], and the concept has shown promising preclinical results; it improves the therapeutic efficacy of paclitaxel in subcutaneous pancreatic xenografts [186] and of paclitaxel and abraxane in prostate xenografts in mice [89]. Here, we demonstrate that it can also safely enable localized delivery of macromolecules across the BBB (**paper V**).

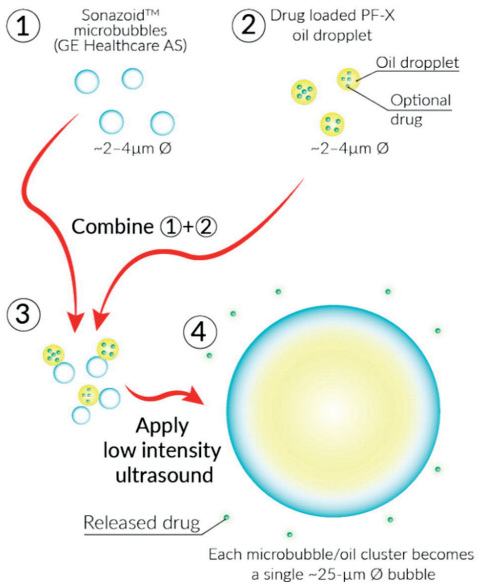

Figure 11: Graphical illustration of the ACT principle. Sonazoid microbubbles are combined with oil droplets, forming clusters. Upon low intensity ultrasound application, the oil droplet vaporizes and forms a large microbubble. The figure is adapted from reference [186], with permission from Elsevier.

3.2 Methods

A brief overview of the different methods used in the thesis are given here, details are supplied in the respective papers.

- Dynamic and electrophoretic light scattering (DLS and ELS) [187, 188] were used to estimate size of the nanoparticles and to measure zeta potential at the hydrodynamic surface, respectively.
- Light microscopy was used to characterize size and concentration of microbubbles, and to evaluate histological tumor and brain sections.
- Flow cytometry (FCM) [189] was used to measure fluorescence from single cells, to obtain quantitative data from large numbers of cells about cellular uptake and association of fluorescent dyes and nanoparticles.

- Confocal laser scanning microscopy (CLSM) [190, 191] is less quantitative, but provided complementary information about intracellular distribution of dyes or nanoparticles with high spatial resolution. CLSM was also used to image distribution and uptake of nanoparticles in xenograft tumor and brain sections from mice.
- Fluorescence spectrophotometry [192] was used to measure fluorescence from nanoparticles, to study dye release, to measure fluorescence in a cell viability assay to study nanoparticle toxicity, and to measure fluorescence in blood samples.
- Contrast enhanced ultrasound imaging (CEUS) [103, 193] was used to characterize destruction of NPMBs and to image in vivo circulation.
- Magnetic resonance imaging (MRI) was used to confirm opening of the BBB, based on extravasation of the contrast agent Omniscan (a gadolinium chelate) [83].
- A small animal imaging system [194] allowed rapid imaging of near infrared fluorescence from organs, tumor and brains, to study biodistribution and delivery of nanoparticles or fluorescent macromolecules.
- Calipers were used to measure tumor growth.

4 Summary of papers

An interesting and novel drug delivery platform was characterized, consisting of microbubbles stabilized by a shell of nanoparticles encapsulating fluorescent model drugs for imaging purposes or cytostatic drugs for treatment (**paper I-III**). This platform was then employed in preclinical studies for ultrasound-mediated drug delivery to solid tumors (**paper III**) and the brain (**paper IV**). Since delivery across the BBB is especially challenging, another promising drug delivery platform, consisting of clusters of microbubbles and microdroplets, was also explored for delivery of co-injected macromolecules to the brain (**paper V**).

Paper I

The aim of this paper was to investigate mechanisms for cellular uptake of a fluorescent hydrophobic model drug from polymeric nanoparticles. To tune nanoparticle properties to obtain efficient delivery and release of drugs at the target in vivo, the mechanisms of interaction between nanoparticles and cells, and the mechanisms for delivery of the encapsulated drug, are crucial to understand. To asses this, prostate adenocarcinoma cells were incubated with Nile Red-loaded nanoparticles or free Nile Red. The kinetics of cellular uptake and intracellular distribution were evaluated by FCM and CLSM. Because the excitation and emission spectra of Nile Red depend on the hydrophobicity of its environment, this could be used to distinguish Nile Red in nanoparticles from Nile Red associated with more or less hydrophobic structures inside the cells. The amount of dye in the nanoparticles and the release of Nile Red into cell culture medium were determined. A rapid diffuse staining of the cytosol was observed, which was not associated with endosomes, and was not inhibited when endocytosis was inhibited. Furthermore, washing of the cells led to efflux of the dye. Cellular uptake of free Nile Red was low and slow. The nanoparticles mediated a higher intracellular level and more rapid uptake of encapsulated Nile Red compared to model drug administered alone. The intracellular distribution

and emission spectra of the dye in various locations were however similar in both cases, and did not correspond to that of Nile Red in nanoparticles. We concluded that the main mechanism of delivery was not via endocytosis of nanoparticles, but rather via nanoparticle-cell contact-mediated transfer directly to the cytosol and, likely to a smaller extent, release of payload from particles to the medium, followed by diffusion into cells. A dual labelled nanoparticle did however indicate different uptake mechanisms for the two different payloads.

Paper II

Various payloads, both contrast agents and drugs, are commonly encapsulated in nanoparticles for diagnostic and therapeutic purposes. Both in vitro and in vivo, nanoparticles are often traced by fluorescent dyes. However, if the dye leaks, that may lead to misinterpretation of results, and wrong conclusions about biodistribution, cellular uptake and intracellular distribution. In this paper, the stability of various fluorescent payloads in nanoparticles was evaluated, and the effect of incorporation of dyes on nanoparticle properties such as cellular uptake. We applied a simple and fast screening method to assess both labeling stability and nanoparticle–cell interactions. Rat brain endothelial cells and prostate cancer cells were used. The cells were incubated with nanoparticles at 4°C or 37°C, and uptake was evaluated by FCM. Energy-dependent uptake is likely the main mechanism of internalization of nanoparticles, and energy depletion at low temperatures was used to inhibit endocytosis to determine if uptake was active or passive. Cell–nanoparticle interaction was confirmed by cellular fluorescence after 37°C incubation. Cellular fluorescence at 4°C was attributed to leakage of incorporated dye, and nanoparticle-dye retention was confirmed when no cellular fluorescence was detected at 4°C, provided that the free dye itself would cross the cell membrane passively and stain cells. Three different commonly used nanoparticle-platforms (polymeric nanoparticles, liposomes and nanoemulsions) labeled with six different hydrophobic dyes were screened. In general, dyes were more stable in polymeric nanoparticles than the lipid-based nanoparticles, and a great variability in dye retention was observed. Surprisingly, incorporation of certain dyes was found to reduce or even inhibit nanoparticle uptake. This work highlights the importance of choosing fluorescent dyes which are compatible with the nanoparticle-platform into which it is incorporated, and of carefully evaluating properties of any dye–nanoparticle combination to obtain correct interpretation of results.

Paper III

The multifunctional drug delivery platform consisting of NPMBs, enabling ultrasound-mediated drug delivery, was characterized. Circulation of microbubbles was found to be in the order of a few minutes in mice, while the circulation half-life of the nanoparticles was 136 minutes. Their biodistribution was determined, without any ultrasound treatment, approximately 1% of the injected dose was located in the subcutaneous breast cancer xenografts. The majority of the injected dose was located in liver and spleen. To study if ultrasound could enhance delivery to the tumors, NPMBs were injected intravenously before the subcutaneous tumors were exposed to FUS. To investigate the mechanisms of ultrasound-mediated delivery, various pressures and pulse lengths were employed, to systematically study the effect of stable versus inertial cavitation on tumor uptake. Tumor sections were imaged, and nanoparticle accumulation was quantified. No effects of low pressures were observed even though the bubbles are acoustically active and oscillate at these pressure levels. Complete bubble destruction at higher pressures and long pulses significantly improved the tumor uptake 2.3 times, without damaging the tissue. Increasing the pressure even further seemingly increased delivery, but also resulted in tissue damage. However, short pulses with the same high pressure did not increase the uptake or damage the tissue. After the nanoparticles have extravasated, they must deliver their cargo to the cells. This cell line showed an effective nanoparticle uptake in vitro, and both free and encapsulated cabazitaxel were potent. To determine if the increased nanoparticle delivery had a therapeutic benefit, and as a first in vivo proof-of-principle, a therapeutic study was performed with nanoparticles encapsulating the anti-cancer drug cabazitaxel. Untreated animals showed a continuous tumor growth. The group treated with NPMBs encapsulating cabazitaxel showed reduced tumor growth, and all animals responded to treatment. They showed large variations in tumor volume between the animals and the tumors started regrowing, indicating that the EPR-effect for the nanoparticles was not sufficient on its own. All animals treated with FUS in addition to NPMBs with cabazitaxel showed regression into complete remission, indicating that this nanoparticle-microbubble platform is promising for controlled drug delivery.

Paper IV

The NPMBs were used in combination with FUS for delivery to the brain in a mouse model with melanoma metastasis. MRI was used to guide the dual-frequency ultrasound treatment. Low frequency was used to open the BBB after an intravenous

injection of NPMBs, to enable nanoparticle extravasation. High frequency ultrasound was used to generate ARF to investigate if nanoparticles could be further displaced away from the vasculature. Opening of the BBB was verified by contrast enhancement in MRI after extravasation of gadolinium, and microscopy was used to image distribution of nanoparticles in the brain tissue. Even though the same pressure was applied for all treatments, the extent of opening varied substantially between the animals. The delivery and distribution of nanoparticles was found to increase with increasing opening. There were indications in some animals that ARF could further displace the nanoparticles, however, this was not observed in all animals, and the results were not conclusive. Nanoparticles were delivered to melanoma metastases, but less than in healthy brain tissue. The expression of P-gp was evaluated by antibody staining, and treated and non-treated areas were similar, indicating that the treatment did not induce any direct damage to P-gp. Still, with increasing opening, histological evaluation showed increased hemorrhage and red blood cell extravasation. In summary, the NPMBs in combination with ultrasound can achieve accumulation and displacement of nanoparticles in the brain parenchyma, and delivery to metastatic tumors. It will however require more optimization to achieve safe and reproducible opening with consistent delivery.

Paper V

The microbubble platform ACT was investigated for its ability to permeabilize the BBB in rats. After intravenous injection of microbubble/microdroplet clusters, ultrasound activation caused a liquid-to-gas phase shift, resulting in large bubbles which transiently lodge in the vasculature for up to 10 minutes. Further sonication induced cavitation and shear forces for increased permeability of the endothelial barrier. The same frequency and sonication sequence was used for both steps, but with a lower pressure and longer time for the last enhancement step. Delivery of gadolinium was assessed by MRI, and intensity of treated tissue was used to determine extent of opening. The delivery of gadolinium was significantly higher after ACT with activation and enhancement, as compared to Sonazoid with the same ultrasound treatment, ACT with either activation or enhancement only, or saline with both activation and enhancement. In addition to gadolinium, ACT also successfully delivered a larger macromolecule, as assessed by fluorescence imaging of the brain. The treatment with ACT was safe and reversible, and the blood-brain barrier was close to or fully recovered within 3 days. In summary, ACT successfully enhanced extravasation, uptake and distribution of small and larger model drugs to the brain,

in a more effective manner than smaller contrast microbubbles, with lower pressures than what is often used for commercial microbubbles.

Overall, the results of this thesis demonstrate that the NPMBs could be used safely in combination with ultrasound to enhance delivery to tumors for increased therapeutic efficacy, they could be used to deliver nanoparticles to the brain and to melanoma metastases, and could effectively deliver hydrophobic dyes and drugs to cancer cells (**paper I-IV**). The ACT could also open the BBB, and appears to be an effective way of transiently and safely enhancing drug delivery to the brain (**paper V**).

5 Discussion and future outlook

The NPMBs seems to be a promising platform for controlled drug delivery. They were found to enhance nanoparticle delivery to tumors and to the brain, and could deliver various hydrophobic payloads to cells (**paper I, III and IV**).

Direct delivery of a hydrophobic model drug into the cytosol mediated by collisions between the nanoparticle and plasma membrane appeared to be an efficient way to deliver drugs which are normally less available for uptake on their own (**paper I**). Because uptake was observed already after minutes, we hypothesized that degradation of nanoparticles was not necessary for this to happen, and that surface associated or encapsulated dye could diffuse/partition rapidly from the nanoparticles. Such a mechanism for delivery into the cytosol could enable delivery of anti-cancer drugs directly to the intracellular molecular targets. The payload avoids entering the endocytic pathway, evading lysosomal degradation and instead gains direct intracellular access [195]. A similar mechanism has also been reported by others for different types of nanoparticles [67–69]. Based on this, nanoparticles are promising tools for efficient intracellular delivery of hydrophobic anticancer drugs, but only if they can be tailored to avoid premature release of their payload in circulation. This could be done by the use of a trigger, so that release is not allowed until a certain stimulus is present. One example is lipid-based nanoparticles targeted to integrins, which deliver lipophilic substances to the plasma membrane and cytoplasm by contact-mediated methods [196]. Delivery only occurred after binding and close apposition to the target cell surface, and was not observed for non-targeted nanoparticles. Such a contact-facilitated delivery was found to be effective for chemotherapeutic agents in vitro [197], but also in vivo, for targeted anti-angiogenic nanoparticles, with a minimal drug dosage [198]. Various other strategies for intracellular delivery have also been reported [195]. Other options for delivery, once a nanoparticle has reached its target tissue, is release in extracellular matrix followed by cellular uptake of the drug itself, or cellular uptake of the nanoparticle followed by intracellular release. For another, more hydrophobic dye, delivery from the same polymeric nanoparticles

was found to depend on cellular uptake by endocytosis, followed by intracellular degradation and release (**paper II** and [162]). The idea behind nanocarriers and perhaps their most important property is to deliver a payload. Understanding how the payload is released, and how it internalizes in cells is therefore crucial. The mechanism of delivery to cells appears to depend highly on properties of the payload, and the intracellular distribution of the payload can change considerably with the different mechanisms. These studies illustrate the importance of finding compatible drug-nanocarrier combinations, and finding suitable assays to study mechanisms for delivery also of non-fluorescent drugs.

To understand how nanoparticles interact with and distribute in cells, it is necessary to detect and localize them, which is in many cases done by fluorescence and optical microscopy. Since the various fluorescent payloads behaved differently, as a continuation of **paper I**, **paper II** reports a more systematic study of various nanoparticles with different dyes. This study did not focus on evaluating detailed mechanisms, but rather on determining which dyes were stable in the different nanoparticles, and how the payload influenced behavior of the nanoparticles. A large variability in dye retention was observed, likely due to varying strength of hydrophobic interactions between the respective dyes and nanoparticles. One alternative to encapsulation could be chemical conjugation of the dye to the nanoparticles, however, degradation could still cause premature release. Furthermore, incorporation of certain dyes was found to limit cellular uptake of the nanoparticles. The underlying mechanisms are not clear, but were probably not linked to a change in nanoparticle size or zeta potential, as these did not change considerably between the different polymeric particles that exhibited different uptake behavior. To elucidate how interactions with the cell changes after a change of dyes would require a more thorough study of both nanoparticle chemistry and the processes involved in endocytosis. The advantage of using flow cytometry in this work, was that it allowed a rapid and quantitative screening of a large number of samples. The limitation is that it does not separate fluorescence from internalized and surface-bound dyes or nanoparticles. Microscopy is useful for imaging nanoparticle uptake, distribution and trafficking, but because free hydrophobic dyes will bind to intracellular hydrophobic molecules, resulting in both diffuse and spotted staining patterns (**paper I**), released dye can be hard to separate from encapsulated dye. This was previously done by imaging differences in spectral properties (**paper I**), fluorescence lifetime imaging microscopy (FLIM) and förster resonance energy transfer (FRET) [162], techniques which are more time consuming. Such techniques have also been used to study how drug-carrier compatibility affects drug release in vivo, where the hydrophobicity of the drug and miscibility with the nanoparticles were found to be important for accumulation in the tumor [176]. This

study emphasizes the importance of carefully evaluating nanoparticle properties after any changes, and the importance of distinguishing between encapsulated dye and released dye. Since nanoparticles with various fluorescent dyes showed different release profiles, mechanisms for delivery and interaction with cells, we hypothesize that this is also the case for various drugs. Thus, for the future, reliable methods to study properties of nanoparticles loaded with drugs will be required. In vivo, premature release of drugs or dissociation of the nanoparticle will lead to decreased therapeutic efficacy and increased side effects, as well as incorrect interpretation of images when contrast agents/dyes are encapsulated in diagnostic/imaging applications (which was done in **paper III** and **IV**).

In addition to encapsulation of dyes, several other important characteristics of nanoparticles will also affect their properties. Cellular uptake of these polymeric nanoparticles was found in another study to be cell line dependent, but also depended on the type of alkyl monomer side chain [162]. The type of alkyl chain also determined their degradation rate; poly(butyl cyanoacrylate) (PBCA) nanoparticles were found to degrade significantly within 24 hours within cells, whereas poly(octyl cyanoacrylate) (POCA) nanoparticles had a very slow degradation. Too fast degradation rates would result in premature release in circulation or in extracellular matrix, whereas too slow degradation might limit the effect of a drug and inhibit a therapeutic response. For the following work, an intermediate was chosen, and poly(2-ethyl-butyl cyanoacrylate) (PEBCA) nanoparticles were used. Surface properties are also of utmost importance, and the type of PEGylation was also found to affect their cellular uptake, in addition to protein adsorption, circulation in blood and diffusion in gels mimicking extracellular matrix [172, 173]. Having characterized compatibility with different dyes of the polymeric nanoparticles (**paper I** and **paper II**), and the effect of monomer and PEGylation, a suitable combination was used for subsequent in vivo drug delivery studies (**paper III** and **paper IV**). The fluorescent dye NR668 was chosen due to its stability (**paper II**), to make sure that nanoparticles could be traced, and PEGylation of Kolliphor and Brij was chosen to obtain sufficient circulation time.

In **paper III**, the NPMB platform showed promising results for enhanced nanoparticle delivery to solid tumors. Biodistribution studies of the nanoparticles confirmed some of the general limitations in nanomedicine; much accumulation in the liver and spleen, which could result in toxicity depending on how fast the particles are eliminated, and only a percentage of the dose accumulating in the tumor. Various ultrasound treatments were therefore investigated for their ability to increase tumor

uptake of nanoparticles. The increased delivery which was observed for some treatments was likely due to increased vascular permeability through increased number of fenestrations, increased endocytosis/exocytosis of nanoparticles in endothelial cells, and/or increased fluid convection in the vasculature and interstitium. The lower pressures that were used did not seem to cause large enough effects for increased delivery, but the higher pressures and thus larger oscillations and collapse probably induced larger pores and more streaming. This is in line with suggestions by others; that ultrasound intensities may be adapted to create pore sizes which correlate with drug size [109], and that delivery of larger agents such as nanoparticles may require higher pressures compared to delivery of low molecular weight drugs [120]. The fact that short pulses did not seem to increase delivery indicates that even though the microbubble is likely destroyed, the remaining gas induces sustained oscillations with longer pulses facilitating sustained bioeffects, in proximity to a high local concentration of nanoparticles. The long pulse could potentially also push the microbubble closer to the vessel wall. We hypothesize that the long pulses with the highest pressure resulted in inertial cavitation of the microbubbles, giving rise to the observed tissue damage. The importance of pulse length has also been observed for other microbubbles [83, 131]. Other pressures could be investigated further, to determine the maximum pressure that can be used before onset of tissue damage. In these experiments, a co-injection of NPMBs and free flowing nanoparticles is used. Others have shown that integrating nanoparticles onto microbubbles was more efficient in ultrasound-enhanced tumor uptake as compared to a co-injection of nanoparticles with microbubbles [90], which should also be confirmed for our platform in future work. It would also be interesting to systematically investigate the effect of nanoparticle size on extravasation after ultrasound treatment, which has been done by another group for co-injected nanoparticles with commercial microbubbles [121].

The relatively large variations in tumor uptake (**paper III**) was probably caused by variable vascularization of the different tumors, with uneven perfusion and vascular permeability as well as areas of necrosis. Some variation was expected, and more animals per group were planned, but the tumor take was lower than expected. Tumor sections were imaged to quantify nanoparticle uptake and study microdistribution of nanoparticles in the tumor tissue. Due to tumor heterogeneity, the selected sections might not be representative for the whole tumors. Imaging more sections from each tumor would be one solution, even though imaging whole tumor sections with high resolution is rather time consuming. As an attempt to normalize tumor uptake to the amount of vasculature in the different sections, and to determine penetration distance from vasculature, fluorescently labeled vasculature was imaged. However, one important aspect was noted in the process of optimizing imaging

protocol; commonly used mounting media disturbed the distribution of fluorescence from the nanoparticles. The sections were therefore imaged dry, without mounting. The vascular stain needed mounting to give good images, and it was challenging to quantify the amount of vasculature in the dry sections. In accordance with **paper I** and **paper II**, this illustrates that not only is dye-nanoparticle compatibility important, but avoiding artefacts in sample preparation is equally important to obtain valid results. As another approach to investigate the tumor heterogeneity, it would be interesting to inject nanoparticles with one dye which accumulate only due to the EPR-effect, then later inject nanoparticles with a different dye to evaluate increased delivery after ultrasound. This would enable a direct comparison of before and after ultrasound treatment in the same tumor. However, due to the dynamic nature of tumor vessels, which may transiently open and close [199], a comparison may not be straight forward.

The increased accumulation and distribution of nanoparticles after ultrasound treatment was further confirmed with a promising proof-of-principle therapeutic study (**paper III**). The drug dose was chosen based on the literature, but slightly on the conservative side to evaluate if ultrasound enhanced the therapeutic effect. Although the number of animals was kept rather low, the results are encouraging and show that ultrasound significantly improved the therapeutic response, likely by overcoming some of the tumor heterogeneity. No weight loss was observed for the animals that were treated two times, which indicates that they tolerated the treatment well. However, two animals died after a third treatment, suggesting that a possible accumulative maximum tolerated dose was reached. The reason for this is not known yet, but since most substances will be toxic if the dose is too high, other doses could be investigated as well. There are several other follow-up studies which would also be of interest. One is to supply more control groups, for instance injection of the free drug only. In another study using similar nanoparticles, encapsulated cabazitaxel resulted in higher efficacy compared to the free drug alone, at a similar dose and in a similar tumor model to that used here (unpublished results, personal communication). Other control groups such as ultrasound alone, ultrasound and microbubbles without drug, and a co-injection of the free drug with empty microbubbles and ultrasound could also be tested. A remaining questions is whether targeting of the microbubbles [103], for instance with ligands to specific integrins on the tumor vasculature before destruction of the microbubbles, would result in even more effective nanoparticle delivery. This would be something to follow up, and such bubbles could also be interesting for diagnostic purposes.

Another follow up should be tumors of various sizes and other characteristics than

the model used here, to evaluate when this system is beneficial. Understanding the impact of a complex tumor biology can allow us to further personalize medicine. To know if a tumor will be responsive to such treatment, pre-screening animals or patients by imaging could be done to identify and select the tumors that are likely to respond [8], and visual methods for measuring and predicting response should be established [8]. This has been done by other groups to determine which tumors are amenable to passive targeting. One example is from a study of spontaneous tumors in dogs, where most carcinomas displayed EPR-effect and a high uptake of liposomes, but few sarcomas displayed signs of liposome retention [200]. In another study, therapeutic outcome was predicted based on imaging tumor accumulation in a mouse breast cancer model, to demonstrate identification of amenable subjects and exclusion of subjects that would not benefit from nanoparticle therapy [201]. The effect of ultrasound treatment will likely also depend on tumor characteristics, as the barriers for delivery of nanomedicine can vary greatly between tumor types. From other studies in our group (unpublished results [202]), there are indications that the perfusion of this tumor model is rather low, and the effect of ultrasound on treatment of tumors with other vascular characteristics is being followed up. Parameters such as collagen content and cellularity may also affect the delivery. Subcutaneous tumor xenografts were used in this study, they are easy to access with ultrasound, and with calipers to measure tumor size. Other tumor models, patient derived, orthotopic and spontaneous tumors in mice would be a natural next step, before going to larger animals. An advantage of the athymic mice is that humane cell lines can be xenografted due to their immunodeficiency, but treatment response should also be studied in immunocompetent mice [47]. Rodent models are highly useful for understanding more, and an absolute requirement before taking something into clinical trials. Still, murine tumors may differ drastically from human cancer making it difficult to extrapolate from mice to men, and considerable differences may be observed when going to human tumors.

A limitation of the described work (**paper III**) is that release profile of the drug is not fully known (it is under investigation). Neither is the behavior of the near infrared dye that was used in biodistribution studies. The dye that was used to study cellular uptake, circulation time, and optimization of ultrasound treatments was in the visible range, and suitable lasers in FCM and CLSM were used to confirm dye retention in the nanoparticles. Previously, encapsulation of another near infrared dye was found to modify properties of the microbubbles, leading to rapid accumulation in the lungs, and severely limited circulation (unpublished results). This is also in accordance with **paper II**, where nanoparticle properties changed due to encapsulation of certain dyes. For this reason, all microbubbles (with visible or near infrared

dyes, or the anti-cancer drug) were imaged in vivo to confirm circulation. Furthermore, we do not suspect that there was significant release of the near infrared dye during circulation, since that would likely have led to increased fluorescence from the kidneys. For future experiments of nanoparticle delivery, homogenization of whole tumors would be interesting, to directly quantify the amount of drug delivered for instance with mass spectrometry. Complementary information about distribution within tissue could then be to obtained for instance by imaging sections with matrix-assisted laser desorption ionization (MALDI) imaging mass spectrometry, to obtain heat maps of the drug and various metabolic pathways to study tumor heterogeneity.

In addition to delivery to tumor tissue, ultrasound has been reported to be promising for opening the BBB for enhanced delivery to the brain. In this work, we applied two different microbubble-concepts for this purpose, the NPMBs and the ACT (**paper IV** and **V**).

In **paper IV**, the NPMBs were applied for opening the BBB. Substantial accumulation and distribution of nanoparticles in the brain was achieved, depending on the extent of BBB opening. BBB opening was previously demonstrated using gadolinium in healthy rats with these microbubbles, at various MIs [133]. Opening was occasionally achieved at an in situ MI of 0.15, and consistently at 0.25, without any signs of damage. The opening closed within 24 hours after treatment. Nanoparticle delivery was demonstrated, but was not quantified systematically. In **paper IV**, the extent of opening, visualized by gadolinium, was therefore correlated to the amount of nanoparticles delivered to sections of the brain. Without opening the delivery was very limited, showing that ultrasound treatment of the microbubbles is necessary to allow the nanoparticles to extravasate into brain parenchyma. Nanoparticles could be delivered to melanoma metastasis, but delivery into tumors was restricted compared to the surrounding healthy brain tissue, presumably due to a lower vascular fraction. The source of the large heterogeneity in opening and delivery should be identified in further work, to obtain more consistent and reliable results and safe treatment. In addition to varying angle and distance of the skull relative to the transducer, there were possibly small batch-to-batch variations in the NPMBs. Furthermore, reflections from the skull might generate standing waves inside the skull, which could result in different in situ MI than predicted, and could lead to variable opening [203]. The opening and level of delivery will depend highly on the properties and concentration of microbubbles, on the ultrasound exposure parameters [83], and on properties of the nanoparticles. Others have also observed increased delivery with increasing amount of opening [143], and it has been commented that there is room for further experimentation in this area, to precisely optimize the amount of

opening with respect to the drug that is being delivered [204]. Other ultrasound sequences might be more beneficial and other injection regimes, for instance multiple boluses or an infusion for prolonged treatment time. The immediate proximity of nanoparticles and microbubbles during sonication is expected to be an advantage [90]. However, the size of these nanoparticles might be in the upper range of what is useful, smaller nanoparticles could be one way to achieve a more even distribution. Other studies have also shown that size can be a critical factor [205], and these nanoparticles are among the largest in studies of ultrasound-mediated delivery across the BBB [206]. It has been shown that the largest openings in the BBB are only present for short time periods, whereas smaller openings are present for longer times [207]. Although smaller particles will also carry less drug, they require smaller pores to extravasate, which can probably be achieved at lower pressures, or shorter pulses. Generation of large pores may also allow for some extravasation of red blood cells. Even though small extravasations and mild inflammatory reactions have been observed in the sonicated area by others, FUS in conjunction with microbubbles was not reported to result in damage to neurons, either directly or through ischemia or apoptosis, or by delayed effects up to one month after sonication [208]. Although a small amount of damage might be acceptable when treating terminal diseases such as brain cancer, where other currently available methods are either invasive or non-localized [208], the treatment should be optimized to be as safe, reproducible, and reliable as possible for translation to the clinic. Even though promising therapeutic results were seen for this platform in subcutaneous tumors (**paper III**), gently opening the BBB might require different parameters compared to drug delivery to leaky tumors. An important question that remains is if the amount of extravasation of nanoparticles observed in the brain is sufficient to achieve a therapeutic effect, which will be investigated in the future by following tumor growth with time.

The effect of ARF was limited in **paper IV**, on top of the displacement caused by opening, but a slightly increased penetration distance was observed for some animals. An inherent limitation of the method used to assess the effect, is that it is not possible to know which blood vessel the nanoparticles originates from. If a nanoparticle was displaced more than half between two vessels, it would be registered as originating from the other vessel. Another uncertainty is that the small focal spot of the high frequency transducer can be difficult to localize after excision and sectioning of the brain. To better evaluate the effect of ARF in the future, one possibility could be to only open the small area that will be treated with radiation force, to make the imaging and quantification easier. Other ultrasound parameters should also be investigated. Another study of ARF is underway in our group, and shows a slightly increased penetration of nanoparticles in tumors tissue after exposure to 10 MHz,

likely due to bulk streaming mechanisms, not direct pushing on individual particles. Spaces in tumors with less dense vasculature might be more suitable to observe an effect of ARF as compared to the brain, where the vascular network is dense. Displacement of tissue with nanoparticles might be feasible, but due to the small focal spot at high frequencies and high intensities, doing this over a large area could be challenging.

P-gp restricts cellular uptake from drugs in circulation into the brain, and is involved in clearing exogenous substances from the brain parenchyma [126]. By inhibiting P-gp expression, one could achieve increased uptake of the drug and enhance retention time in the parenchyma [126, 127]. Ultrasound combined with microbubbles has been reported elsewhere to temporarily down-regulate P-gp expression in brain blood vessels from 1 hour to days post treatment [126, 127]. The fact that no effect was seen here directly after treatment indicates that reduced expression is not due to direct damage, but rather signaling mechanisms that require a certain period of time. More studies are needed to investigate the change in P-gp expression with time.

In **paper V**, ACT bubbles which have recently shown promising results for treatment of solid tumors [89], also successfully and safely opened the BBB. Relatively low pressures were used for efficient delivery of gadolinium and a macromolecule, compared to the pressures that have been used elsewhere for commercial microbubbles, and compared to the NPMBs (**paper IV** and [133]). Compared to regular contrast agents such as Sonazoid, these large microbubbles are in close contact with vessel wall over a larger area. They allow prolonged treatment time compared to commercial agents which circulate typically for a few minutes. The larger volume probably results in larger effects and larger openings even at low pressures. In addition, an increased microvascular pressure on the arterial side likely causes an increased transcapillary pressure gradient, which further enhances extravasation. The decreased pressure needed for volume oscillations could imply a safer treatment. Another difference compared to the treatment in **paper IV**, is that shorter pulses were used here, with a higher pulse repetition frequency (PRF). Others have shown that short pulses emitted at high PRF can reduce the non-uniform effects produced by long pulses with lower PRF [209, 210]. Rapid short-pulse sequences extended microbubble lifetime and enhanced their mobility, thus spreading the acoustic activity in space and time, generating more uniform distributions of delivery with less damage [209, 210]. For future experiments, it would be interesting to also employ this microbubble to deliver the polymeric nanoparticles that were used in **paper I-VI** to the brain or to solid tumors. Preclinical therapeutic results in mice have been

demonstrated for some tumor models, and more tumor models are planned for. Another interesting approach which is being investigated, is to employ clinical scanners for the ultrasound treatment, with other ultrasound parameters, which will ease the transition into the clinic considerably. The ACT concept is likely to enter clinical trials for treatment of non-resectable pancreatic cancer in 2018. Several other types of cancers would also be possible applications, due to ease of co-administration with already used treatment regimens, and no need for encapsulation of the drugs.

Both microbubble platforms described here seem interesting for improved drug delivery purposes. In addition to more therapeutic studies, it is also important to understand more of the mechanisms behind the observed effects. This work provides some mechanistic insights into how we can tune ultrasound parameters to obtain safe and efficient treatments for these microbubble platforms, although further optimization should be done in follow up studies. These microbubbles are currently also being investigated for sonoporation in vitro, and in vivo real time studies with multiphoton intravital microscopy, in tumors and the brain [211, 212], during ultrasound treatment are ongoing. High speed imaging would also provide useful insights [105]. Together with what we know today, such mechanistic studies will enable us to make these platforms even more effective. We should also establish systems for cavitation detection [83, 135, 213] while treating, to learn more about the behavior of the bubbles in vivo. By applying a feedback controller mechanism which has been used by others to detect acoustic emission, the ultrasound pressure can be standardized to the microbubble response in each animal and possibly eliminate in situ pressure fluctuations due to variations in skull thickness or differences in vasculature between animals [214, 215]. In addition, there are also several other aspects which would be interesting to investigate further; ultrasound and microbubbles have been shown to cause a vasoconstriction or vascular shut down, and reduced perfusion in tumors, brain and other tissues [211, 213, 216, 217]. Locally increased perfusion has also been reported [218]. We do not yet know if this happens for the bubbles that were used in this work. Other questions that remain are how these treatments affect interstitial and intravascular pressure, structure of the interstitium, and cellular stress or signaling, cell detachment and metastasis, apoptosis or proliferation, angiogenesis [219], or the immune system.

For applications towards cancer, FUS treatment with microbubbles and nanomedicine could possibly be used as a curative treatment on its own, as neoadjuvant chemotherapy for solid tumors followed by surgical resection, or in combination with/after surgery or radiation to remove residual cells. It could also be combined with immunotherapy, which has gained considerable attention lately. The great potential

of ultrasound-mediated delivery to cancer has been demonstrated in several promising preclinical studies [102, 104, 220]. The first clinical trial combining ultrasound with microbubbles for enhanced delivery of chemotherapy to pancreatic cancer has already been reported [91], and more trials are soon to be started.

Ultrasound and microbubbles have shown promising results for delivery of chemotherapeutics in preclinical therapy of brain tumors [83, 204, 221], but also for delivery of viral vectors and genes, and antibodies and cells for immunotherapy [83, 204, 222]. Two clinical trials are currently underway for patients with brain tumors [153–155]. In addition, ultrasound and microbubbles have shown promising results in preclinical Alzheimer's models, [142, 214], a Huntington's disease model [223], and for neuroprotection and neurorestoration in a Parkinson mouse model by delivery of neurotrophic factors [224]. Together, these results illustrate the diversity of serious diseases which the technology can be applied for in the future.

6 Conclusions

Ultrasound in combination with microbubbles appears to be a highly promising way of enhancing accumulation and distribution of nanomedicines across biological barriers. Commercial microbubbles combined with approved drugs have already shown encouraging results in the first clinical trials. Understanding more of the underlying mechanisms will enable us to further optimize the treatment. Developing new and potentially more effective microbubbles will be an important part of the future, to overcome some of the limitations of the commercial microbubbles and to continue advancing the technology. Thorough evaluation of new microbubble-systems, from fundamental research of properties and interactions with tissues and cells, to preclinical in vivo delivery and efficacy studies, as well as optimization of ultrasound parameters, will be essential to maximize efficacy and safety of novel platforms.

In this thesis, two interesting microbubble-platforms were explored, which are both promising for controlled drug delivery applications. The first microbubble-platform was stabilized by polymeric nanoparticles encapsulating drugs or contrast agents. Various payloads showed different degree of stability in the nanoparticles, and incorporation of model drugs was found to affect their interactions with cells. The nanoparticles demonstrated effective delivery of hydrophobic dyes and drugs to cells. Different mechanisms were responsible, either contact-mediated delivery directly to cytosol, or uptake by endocytosis followed by intracellular release, depending on properties of the payload. Ultrasound treatment after a systemic injection of NPMBs was found to improve the accumulation and distribution of nanoparticles in solid tumors, at a safe pressure level. Too low pressures, or short pulses did not enhance uptake, whereas too high pressures combined with long pulses resulted in tissue damage. An enhanced therapeutic effect was demonstrated in a promising proof-of-concept preclinical study, where all animals showed complete and stable remission. Furthermore, it was demonstrated that the same platform could be used

in combination with ultrasound to open the BBB and successfully deliver and distribute nanoparticles in the brain. The second microbubble-platform was based on a different mechanism of action, where large bubbles transiently lodge in the microvasculature. ACT has already shown highly promising preclinical results for improved delivery and therapeutic efficacy of co-injected drugs to solid tumors in mice. Here, we demonstrate that it can also be employed to effectively, safely and transiently open the BBB with relatively low pressures, enabling successful delivery of macromolecules to the brain. This work has increased our understanding of how ultrasound can be employed in combination with these microbubbles to enhance delivery of nanomedicines. Some opportunities and challenges have been highlighted. Although we have gained new knowledge and answered some important questions, there is yet much to learn in future follow-up studies.

Altogether, ultrasound-enhanced delivery of nanomedicines is an encouraging technique, both in oncology and neurology, of which clinical translation and approval is probably both feasible and near. It has great potential for improved treatment outcomes and could possibly improve therapy of serious neurodegenerative diseases and aggressive cancers with poor prognosis, which will certainly impact and benefit people's lives.

References

[1] R. A. Weinberg. How cancer arises. *Sci Am*, 275(3):62–70, 1996.

[2] J. R. Heath, M. E. Davis, and L. Hood. Nanomedicine targets cancer. *Sci Am*, 300(2):44–51, 2009.

[3] M. B. Kastan and J. Bartek. Cell-cycle checkpoints and cancer. *Nature*, 432(7015):316–23, 2004.

[4] D. Hanahan and R. A. Weinberg. Hallmarks of cancer: the next generation. *Cell*, 144(5):646–74, 2011.

[5] Robert A Weinberg. *The biology of cancer*. Garland Science, 2014.

[6] D. Peer, J. M. Karp, S. Hong, O. C. Farokhzad, R. Margalit, and R. Langer. Nanocarriers as an emerging platform for cancer therapy. *Nat Nanotechnol*, 2(12):751–760, 2007.

[7] T. Lammers, W. E. Hennink, and G. Storm. Tumour-targeted nanomedicines: principles and practice. *Br J Cancer*, 99(3):392–7, 2008.

[8] T. Lammers, F. Kiessling, W. E. Hennink, and G. Storm. Drug targeting to tumors: principles, pitfalls and (pre-) clinical progress. *J Control Release*, 161(2):175–87, 2012.

[9] H. P. Gerber, P. D. Senter, and I. S. Grewal. Antibody drug-conjugates targeting the tumor vasculature current and future developments. *Mabs*, 1(3):247–253, 2009.

[10] K. A. Kurdziel, J. D. Kalen, J. I. Hirsch, J. D. Wilson, H. D. Bear, J. Logan, J. McCumisky, K. Moorman-Sykes, S. Adler, and P. L. Choyke. Human dosimetry and preliminary tumor distribution of F-18-fluoropaclitaxel in healthy volunteers and newly diagnosed breast cancer patients using PET/CT. *J Nucl Med*, 52(9):1339–1345, 2011.

[11] V. Malhotra and M. C. Perry. Classical chemotherapy: mechanisms, toxicities and the therapeutic window. *Cancer Biol Ther*, 2(4 Suppl 1):S2–4, 2003.

[12] K. Cheung-Ong, G. Giaever, and C. Nislow. DNA-damaging agents in cancer chemotherapy: serendipity and chemical biology. *Chem Biol*, 20(5):648–59, 2013.

[13] M. L. Etheridge, S. A. Campbell, A. G. Erdman, C. L. Haynes, S. M. Wolf, and J. McCullough. The big picture on nanomedicine: the state of investigational and approved nanomedicine products. *Nanomedicine*, 9(1):1–14, 2013.

[14] O. C. Farokhzad and R. Langer. Impact of nanotechnology on drug delivery. *ACS Nano*, 3(1):16–20, 2009.

[15] V. Sanna, N. Pala, and M. Sechi. Targeted therapy using nanotechnology: focus on cancer. *Int J Nanomedicine*, 9:467–83, 2014.

[16] J. Kreuter. Nanoparticles–a historical perspective. *Int J Pharm*, 331(1):1–10, 2007.

[17] K. Strebhardt and A. Ullrich. Paul Ehrlich's magic bullet concept: 100 years of progress. *Nat Rev Cancer*, 8(6):473–80, 2008.

[18] K. H. Bae, H. J. Chung, and T. G. Park. Nanomaterials for cancer therapy and imaging. *Mol Cells*, 31(4):295–302, 2011.

[19] N. Kamaly, Z. Xiao, P. M. Valencia, A. F. Radovic-Moreno, and O. C. Farokhzad. Targeted polymeric therapeutic nanoparticles: design, development and clinical translation. *Chem Soc Rev*, 41(7):2971–3010, 2012.

[20] Ý. Mørch, R. Hansen, S. Berg, A. K. O. Åslund, W. R. Glomm, S. Eggen, R. B. Schmid, H. Johnsen, S. Kubowicz, S. Snipstad, E. Sulheim, S. Hak, G. Singh, B. H. McDonagh, H. Blom, C. de L. Davies, and P. M. Stenstad. Nanoparticle-stabilized microbubbles for multimodal imaging and drug delivery. *Contrast Media Mol Imaging*, 10(5):356–366, 2015.

[21] F. Danhier. To exploit the tumor microenvironment: Since the EPR effect fails in the clinic, what is the future of nanomedicine? *J Control Release*, 244(Pt A):108–121, 2016.

[22] C. M. Hu and L. Zhang. Nanoparticle-based combination therapy toward overcoming drug resistance in cancer. *Biochem Pharmacol*, 83(8):1104–11, 2012.

[23] C. He, C. Chan, R. R. Weichselbaum, G. F. Fleming, S. D. Yamada, and W. Lin. Nanomedicine for combination therapy of cancer. *EBioMedicine*, 2(5):366–7, 2015.

[24] L. Ma, M. Kohli, and A. Smith. Nanoparticles for combination drug therapy. *ACS Nano*, 7(11):9518–25, 2013.

[25] T. Lammers, F. Kiessling, W. E. Hennink, and G. Storm. Nanotheranostics and image-guided drug delivery: current concepts and future directions. *Mol Pharm*, 7(6):1899–912, 2010.

[26] S. C. Baetke, T. Lammers, and F. Kiessling. Applications of nanoparticles for diagnosis and therapy of cancer. *Br J Radiol*, 88(1054):20150207, 2015.

[27] M. E. Davis, Z. G. Chen, and D. M. Shin. Nanoparticle therapeutics: an emerging treatment modality for cancer. *Nat Rev Drug Discov*, 7(9):771–82, 2008.

[28] J. J. Verhoef and T. J. Anchordoquy. Questioning the use of PEGylation for drug delivery. *Drug Deliv Transl Res*, 3(6):499–503, 2013.

[29] F. Alexis, E. Pridgen, L. K. Molnar, and O. C. Farokhzad. Factors affecting the clearance and biodistribution of polymeric nanoparticles. *Mol Pharm*, 5(4):505–15, 2008.

[30] K. Knop, R. Hoogenboom, D. Fischer, and U. S. Schubert. Poly(ethylene glycol) in drug delivery: pros and cons as well as potential alternatives. *Angew Chem Int Ed Engl*, 49(36):6288–308, 2010.

[31] H. H. Gustafson, D. Holt-Casper, D. W. Grainger, and H. Ghandehari. Nanoparticle uptake: The phagocyte problem. *Nano Today*, 10(4):487–510, 2015.

[32] Z. Amoozgar and Y. Yeo. Recent advances in stealth coating of nanoparticle drug delivery systems. *Wiley Interdiscip Rev Nanomed Nanobiotechnol*, 4(2):219–33, 2012.

[33] J. V. Jokerst, T. Lobovkina, R. N. Zare, and S. S. Gambhir. Nanoparticle PEGylation for imaging and therapy. *Nanomedicine*, 6(4):715–728, 2011.

[34] D. Papahadjopoulos, T. M. Allen, A. Gabizon, E. Mayhew, K. Matthay, S. K. Huang, K. D. Lee, M. C. Woodle, D. D. Lasic, and C. Redemann. Sterically stabilized liposomes: improvements in pharmacokinetics and antitumor therapeutic efficacy. *Proc Natl Acad Sci USA*, 88(24):11460–4, 1991.

[35] G. Storm, S. O. Belliot, T. Daemen, and D. D. Lasic. Surface modification of nanoparticles to oppose uptake by the mononuclear phagocyte system. *Adv Drug Deliv Rev*, 17(1):31–48, 1995.

[36] B. Romberg, W. E. Hennink, and G. Storm. Sheddable coatings for long-circulating nanoparticles. *Pharm Res*, 25(1):55–71, 2008.

[37] Y. Matsumura and H. Maeda. A new concept for macromolecular therapeutics in cancer chemotherapy: mechanism of tumoritropic accumulation of proteins and the antitumor agent smancs. *Cancer Res*, 46(12 Pt 1):6387–92, 1986.

[38] H. Maeda, J. Wu, T. Sawa, Y. Matsumura, and K. Hori. Tumor vascular permeability and the EPR effect in macromolecular therapeutics: a review. *J Control Release*, 65(1-2):271–284, 2000.

[39] J. Fang, H. Nakamura, and H. Maeda. The EPR effect: Unique features of tumor blood vessels for drug delivery, factors involved, and limitations and augmentation of the effect. *Adv Drug Deliv Rev*, 63(3):136–51, 2011.

[40] H. Kobayashi, R. Watanabe, and P. L. Choyke. Improving conventional enhanced permeability and retention (EPR) effects; what is the appropriate target? *Theranostics*, 4(1):81–9, 2013.

[41] D. Fukumura and R. K. Jain. Tumor microenvironment abnormalities: causes, consequences, and strategies to normalize. *J Cell Biochem*, 101(4):937–49, 2007.

[42] H. Sarin. Physiologic upper limits of pore size of different blood capillary types and another perspective on the dual pore theory of microvascular permeability. *J Angiogenes Res*, 2:14, 2010.

[43] T. M. Allen. Ligand-targeted therapeutics in anticancer therapy. *Nat Rev Cancer*, 2(10):750–63, 2002.

[44] F. Marcucci and F. Lefoulon. Active targeting with particulate drug carriers in tumor therapy: fundamentals and recent progress. *Drug Discov Today*, 9(5):219–28, 2004.

[45] V. P. Chauhan and R. K. Jain. Strategies for advancing cancer nanomedicine. *Nat Mater*, 12(11):958–62, 2013.

[46] J. N. Weinstein and W. van Osdol. Early intervention in cancer using monoclonal antibodies and other biological ligands: micropharmacology and the "binding site barrier". *Cancer Res*, 52(9 Suppl):2747s–2751s, 1992.

[47] T. J. Anchordoquy, Y. Barenholz, D. Boraschi, M. Chorny, P. Decuzzi, M. A. Dobrovolskaia, Z. S. Farhangrazi, D. Farrell, A. Gabizon, H. Ghandehari, B. Godin, N. M. La-Beck, J. Ljubimova, S. M. Moghimi, L. Pagliaro, J. H. Park, D. Peer, E. Ruoslahti, N. J. Serkova, and D. Simberg. Mechanisms and barriers in cancer nanomedicine: Addressing challenges, looking for solutions. *ACS Nano*, 11(1):12–18, 2017.

[48] H. Hashizume, P. Baluk, S. Morikawa, J. W. McLean, G. Thurston, S. Roberge, R. K. Jain, and D. M. McDonald. Openings between defective endothelial cells explain tumor vessel leakiness. *Am J Pathol*, 156(4):1363–80, 2000.

[49] S. Mura, J. Nicolas, and P. Couvreur. Stimuli-responsive nanocarriers for drug delivery. *Nat Mater*, 12(11):991–1003, 2013.

[50] Y. H. Bae and K. Park. Targeted drug delivery to tumors: myths, reality and possibility. *J Control Release*, 153(3):198–205, 2011.

[51] S. K. Sriraman, B. Aryasomayajula, and V. P. Torchilin. Barriers to drug delivery in solid tumors. *Tissue Barriers*, 2:e29528, 2014.

[52] R. K. Jain. Understanding barriers to drug delivery: high resolution in vivo imaging is key. *Clin Cancer Res*, 5(7):1605–6, 1999.

[53] S. Wilhelm, A. J. Tavares, Q. Dai, O. Seiichi, J. Audet, H. F. Dvorak, and W. C. W. Chan. Analysis of nanoparticle delivery to tumours. *Nat Rev Mater*, 1:1–12, 2016.

[54] R. K. Jain. Transport of molecules across tumor vasculature. *Cancer Metastasis Rev*, 6(4):559–93, 1987.

[55] R. K. Jain and T. Stylianopoulos. Delivering nanomedicine to solid tumors. *Nat Rev Clin Oncol*, 7(11):653–64, 2010.

[56] N. K. Reitan, M. Thuen, P. E. Goa, and C. de L. Davies. Characterization of tumor microvascular structure and permeability: comparison between magnetic resonance imaging and intravital confocal imaging. *J Biomed Opt*, 15(3):036004, 2010.

[57] T. P. Padera, B. R. Stoll, J. B. Tooredman, D. Capen, E. di Tomaso, and R. K. Jain. Pathology: cancer cells compress intratumour vessels. *Nature*, 427(6976):695, 2004.

[58] S. Goel, D. G. Duda, L. Xu, L. L. Munn, Y. Boucher, D. Fukumura, and R. K. Jain. Normalization of the vasculature for treatment of cancer and other diseases. *Physiol Rev*, 91(3):1071–121, 2011.

[59] P. A. Netti, D. A. Berk, M. A. Swartz, A. J. Grodzinsky, and R. K. Jain. Role of extracellular matrix assembly in interstitial transport in solid tumors. *Cancer Res*, 60(9):2497–503, 2000.

[60] W. M. Becker, L. J. Kleinsmith, J. Hardin, and G. P. Bertoni. The world of the cell. *Pearson Benjamin Cummings*, 2009.

[61] T. G. Iversen, T. Skotland, and K. Sandvig. Endocytosis and intracellular transport of nanoparticles: Present knowledge and need for future studies. *Nano Today*, 6(2):176–185, 2011.

[62] S. D. Conner and S. L. Schmid. Regulated portals of entry into the cell. *Nature*, 422(6927):37–44, 2003.

[63] G. Sahay, D. Y. Alakhova, and A. V. Kabanov. Endocytosis of nanomedicines. *J Control Release*, 145(3):182–95, 2010.

[64] L. Treuel, X. Jiang, and G. U. Nienhaus. New views on cellular uptake and trafficking of manufactured nanoparticles. *J R Soc Interface*, 10(82):20120939, 2013.

[65] S. A. Ferreira, A. Correia, P. Madureira, M. Vilanova, and F. M. Gama. Unraveling the uptake mechanisms of mannan nanogel in bone-marrow-derived macrophages. *Macromol Biosci*, 12(9):1172–80, 2012.

[66] B. Yameen, W. I. Choi, C. Vilos, A. Swami, J. Shi, and O. C. Farokhzad. Insight into nanoparticle cellular uptake and intracellular targeting. *J Control Release*, 190:485–99, 2014.

[67] P. Xu, E. Gullotti, L. Tong, C. B. Highley, D. R. Errabelli, T. Hasan, J. X. Cheng, D. S. Kohane, and Y. Yeo. Intracellular drug delivery by poly(lactic-co-glycolic acid) nanoparticles, revisited. *Mol Pharm*, 6(1):190–201, 2009.

[68] L. C. Haynes and M. J. Cho. Mechanism of nile red transfer from o/w emulsions as carriers for passive-drug targeting to peritoneal-macrophages invitro. *Int J Pharm*, 45(1-2):169–177, 1988.

[69] A. C. de Verdiere, C. Dubernet, F. Nemati, M. F. Poupon, F. Puisieux, and P. Couvreur. Uptake of doxorubicin from loaded nanoparticles in multidrug-resistant leukemic murine cells. *Cancer Chemother Pharmacol*, 33(6):504–508, 1994.

[70] J. Yang, A. Bahreman, G. Daudey, J. Bussmann, R. C. Olsthoorn, and A. Kros. Drug delivery via cell membrane fusion using lipopeptide modified liposomes. *ACS Cent Sci*, 2(9):621–630, 2016.

[71] G. Szakacs, J. K. Paterson, J. A. Ludwig, C. Booth-Genthe, and M. M. Gottesman. Targeting multidrug resistance in cancer. *Nat Rev Drug Discov*, 5(3):219–34, 2006.

[72] W. M. Pardridge. The blood-brain barrier: bottleneck in brain drug development. *NeuroRx*, 2(1):3–14, 2005.

[73] N. J. Abbott, A. A. Patabendige, D. E. Dolman, S. R. Yusof, and D. J. Begley. Structure and function of the blood-brain barrier. *Neurobiol Dis*, 37(1):13–25, 2010.

[74] N. J. Abbott, L. Ronnback, and E. Hansson. Astrocyte-endothelial interactions at the blood-brain barrier. *Nat Rev Neurosci*, 7(1):41–53, 2006.

[75] B. W. Chow and C. Gu. The molecular constituents of the blood-brain barrier. *Trends Neurosci*, 38(10):598–608, 2015.

[76] A. Al Ahmad, C. B. Taboada, M. Gassmann, and O. O. Ogunshola. Astrocytes and pericytes differentially modulate blood-brain barrier characteristics during development and hypoxic insult. *J Cereb Blood Flow Metab*, 31(2):693–705, 2011.

[77] D. S. Hersh, A. S. Wadajkar, N. B. Roberts, J. G. Perez, N. P. Connolly, V. Frenkel, J. A. Winkles, G. F. Woodworth, and A. J. Kim. Evolving drug delivery strategies to overcome the blood brain barrier. *Curr Pharm Des*, 22(9):1177–93, 2016.

[78] C. Vauthier, C. Dubernet, E. Fattal, H. Pinto-Alphandary, and P. Couvreur. Poly(alkylcyanoacrylates) as biodegradable materials for biomedical applications. *Adv Drug Deliv Rev*, 55(4):519–548, 2003.

[79] M. Demeule, A. Regina, J. Jodoin, A. Laplante, C. Dagenais, F. Berthelet, A. Moghrabi, and R. Beliveau. Drug transport to the brain: key roles for the efflux pump P-glycoprotein in the blood-brain barrier. *Vascul Pharmacol*, 38(6):339–48, 2002.

[80] N. J. Abbott. Blood-brain barrier structure and function and the challenges for CNS drug delivery. *J Inherit Metab Dis*, 36(3):437–49, 2013.

[81] W. M. Pardridge. Drug transport across the blood-brain barrier. *J Cereb Blood Flow Metab*, 32(11):1959–72, 2012.

[82] C. Weissmann and A. Aguzzi. Approaches to therapy of prion diseases. *Annu Rev Med*, 56:321–44, 2005.

[83] C. Poon, D. McMahon, and K. Hynynen. Noninvasive and targeted delivery of therapeutics to the brain using focused ultrasound. *Neuropharmacology*, 2016.

[84] W. M. Pardridge. Blood-brain barrier delivery. *Drug Discov Today*, 12(1-2):54–61, 2007.

[85] K. Hynynen, N. McDannold, N. Vykhodtseva, and F. A. Jolesz. Noninvasive MR imaging-guided focal opening of the blood-brain barrier in rabbits. *Radiology*, 220(3):640–6, 2001.

[86] P. A. Dijkmans, L. J. Juffermans, R. J. Musters, A. van Wamel, F. J. ten Cate, W. van Gilst, C. A. Visser, N. de Jong, and O. Kamp. Microbubbles and ultrasound: from diagnosis to therapy. *Eur J Echocardiogr*, 5(4):245–56, 2004.

[87] G. A. Husseini, W. G. Pitt, and A. M. Martins. Ultrasonically triggered drug delivery: breaking the barrier. *Colloids Surf B Biointerfaces*, 123:364–86, 2014.

[88] F. Kiessling, S. Fokong, P. Koczera, W. Lederle, and T. Lammers. Ultrasound microbubbles for molecular diagnosis, therapy, and theranostics. *J Nucl Med*, 53(3):345–8, 2012.

[89] A. van Wamel, P. C. Sontum, A. Healey, S. Kvåle, N. Bush, J. Bamber, and C. de L. Davies. Acoustic cluster therapy (ACT) enhances the therapeutic efficacy of paclitaxel and abraxane for treatment of human prostate adenocarcinoma in mice. *J Control Release*, 236:15–21, 2016.

[90] C. W. Burke, E. th Alexander, K. Timbie, A. L. Kilbanov, and R. J. Price. Ultrasound-activated agents comprised of 5FU-bearing nanoparticles bonded to microbubbles inhibit solid tumor growth and improve survival. *Mol Ther*, 22(2):321–8, 2014.

[91] G. Dimcevski, S. Kotopoulis, T. Bjånes, D. Hoem, J. Schjøtt, B. T. Gjertsen, M. Biermann, A. Molven, H. Sorbye, E. McCormack, M. Postema, and O. H. Gilja. A human clinical trial using ultrasound and microbubbles to enhance gemcitabine treatment of inoperable pancreatic cancer. *J Control Release*, 2016.

[92] S. Kotopoulis, A. Delalande, M. Popa, V. Mamaeva, G. Dimcevski, O. H. Gilja, M. Postema, B. T. Gjertsen, and E. McCormack. Sonoporation-enhanced chemotherapy significantly reduces primary tumour burden in an orthotopic pancreatic cancer xenograft. *Mol Imaging Biol*, 16(1):53–62, 2014.

[93] L. H. Treat, N. McDannold, Y. Zhang, N. Vykhodtseva, and K. Hynynen. Improved anti-tumor effect of liposomal doxorubicin after targeted blood-brain barrier disruption by mri-guided focused ultrasound in rat glioma. *Ultrasound Med Biol*, 38(10):1716–25, 2012.

[94] W. G. Pitt, G. A. Husseini, and B. J. Staples. Ultrasonic drug delivery–a general review. *Expert Opin Drug Deliv*, 1(1):37–56, 2004.

[95] A. Schroeder, J. Kost, and Y. Barenholz. Ultrasound, liposomes, and drug delivery: principles for using ultrasound to control the release of drugs from liposomes. *Chem Phys Lipids*, 162(1-2):1–16, 2009.

[96] Jr. O'Brien, W. D. Ultrasound-biophysics mechanisms. *Prog Biophys Mol Biol*, 93(1-3):212–55, 2007.

[97] V. Frenkel. Ultrasound mediated delivery of drugs and genes to solid tumors. *Adv Drug Deliv Rev*, 60(10):1193–208, 2008.

[98] D. O. Draper, J. C. Castel, and D. Castel. Rate of temperature increase in human muscle during 1 MHz and 3 MHz continuous ultrasound. *J Orthop Sports Phys Ther*, 22(4):142–50, 1995.

[99] J. E. Kennedy, G. R. Ter Haar, and D. Cranston. High intensity focused ultrasound: surgery of the future? *Br J Radiol*, 76(909):590–9, 2003.

[100] P. E. Huber, J. W. Jenne, R. Rastert, I. Simiantonakis, H. P. Sinn, H. J. Strittmatter, D. von Fournier, M. F. Wannenmacher, and J. Debus. A new noninvasive approach in breast cancer therapy using magnetic resonance imaging-guided focused ultrasound surgery. *Cancer Res*, 61(23):8441–7, 2001.

[101] O. Couture, J. Foley, N. F. Kassell, B. Larrat, and J.-F. Aubry. Review of ultrasound mediated drug delivery for cancer treatment: updates from pre-clinical studies. *Transl Cancer Res*, 3(5):494–511, 2014.

[102] B. H. Lammertink, C. Bos, R. Deckers, G. Storm, C. T. Moonen, and J. M. Escoffre. Sonochemotherapy: from bench to bedside. *Front Pharmacol*, 6:138, 2015.

[103] V. Paefgen, D. Doleschel, and F. Kiessling. Evolution of contrast agents for ultrasound imaging and ultrasound-mediated drug delivery. *Front Pharmacol*, 6:197, 2015.

[104] T. Boissenot, A. Bordat, E. Fattal, and N. Tsapis. Ultrasound-triggered drug delivery for cancer treatment using drug delivery systems: From theoretical considerations to practical applications. *J Control Release*, 241:144–163, 2016.

[105] K. Kooiman, H. J. Vos, M. Versluis, and N. de Jong. Acoustic behavior of microbubbles and implications for drug delivery. *Adv Drug Deliv Rev*, 72:28–48, 2014.

[106] R. Suzuki and A. L. Klibanov. Co-administration of microbubbles and drugs in ultrasound-assisted drug delivery: Comparison with drug- carrying particles. *Adv Exp Med Biol*, 880:205–220, 2016.

[107] J. Collis, R. Manasseh, P. Liovic, P. Tho, A. Ooi, K. Petkovic-Duran, and Y. Zhu. Cavitation microstreaming and stress fields created by microbubbles. *Ultrasonics*, 50(2):273–9, 2010.

[108] S. A. Elder. Cavitation microstreaming. *J Acoust Soc Am*, 31(1):54–64, 1959.

[109] I. Lentacker, I. De Cock, R. Deckers, S. C. De Smedt, and C. T. Moonen. Understanding ultrasound induced sonoporation: definitions and underlying mechanisms. *Adv Drug Deliv Rev*, 72:49–64, 2014.

[110] I. Lentacker, S. C. De Smedt, and N. N. Sanders. Drug loaded microbubble design for ultrasound triggered delivery. *Soft Matter*, 5:2161–2170, 2009.

[111] G. Lajoinie, I. De Cock, C. C. Coussios, I. Lentacker, S. Le Gac, E. Stride, and M. Versluis. In vitro methods to study bubble-cell interactions: Fundamentals and therapeutic applications. *Biomicrofluidics*, 10(1):011501, 2016.

[112] A. Delalande, S. Kotopoulis, M. Postema, P. Midoux, and C. Pichon. Sonoporation: mechanistic insights and ongoing challenges for gene transfer. *Gene*, 525(2):191–9, 2013.

[113] M. Afadzi, S. P. Strand, E. A. Nilssen, S. E. Måsøy, T. F. Johansen, R. Hansen, B. A. Angelsen, and C. de L. Davies. Mechanisms of the ultrasound-mediated intracellular delivery of liposomes and dextrans. *IEEE Trans Ultrason Ferroelectr Freq Control*, 60(1):21–33, 2013.

[114] B. D. Meijering, L. J. Juffermans, A. van Wamel, R. H. Henning, I. S. Zuhorn, M. Emmer, A. M. Versteilen, W. J. Paulus, W. H. van Gilst, K. Kooiman, N. de Jong, R. J. Musters, L. E. Deelman, and O. Kamp. Ultrasound and microbubble-targeted delivery of macromolecules is regulated by induction of endocytosis and pore formation. *Circ Res*, 104(5):679–87, 2009.

[115] A. van Wamel, K. Kooiman, M. Harteveld, M. Emmer, F. J. ten Cate, M. Versluis, and N. de Jong. Vibrating microbubbles poking individual cells: drug transfer into cells via sonoporation. *J Control Release*, 112(2):149–55, 2006.

[116] Y. Hu, J. M. Wan, and A. C. Yu. Membrane perforation and recovery dynamics in microbubble-mediated sonoporation. *Ultrasound Med Biol*, 39(12):2393–405, 2013.

[117] I. Skachkov, Y. Luan, A. F. van der Steen, N. de Jong, and K. Kooiman. Targeted microbubble mediated sonoporation of endothelial cells in vivo. *IEEE Trans Ultrason Ferroelectr Freq Control*, 61(10):1661–7, 2014.

[118] C. Y. Lin, Y. L. Huang, J. R. Li, F. H. Chang, and W. L. Lin. Effects of focused ultrasound and microbubbles on the vascular permeability of nanoparticles delivered into mouse tumors. *Ultrasound Med Biol*, 36(9):1460–9, 2010.

[119] C. Y. Lin, J. R. Li, H. C. Tseng, M. F. Wu, and W. L. Lin. Enhancement of focused ultrasound with microbubbles on the treatments of anticancer nanodrug in mouse tumors. *Nanomedicine*, 8(6):900–7, 2012.

[120] T. Y. Wang, J. W. Choe, K. Y. Pu, R. Devulapally, S. Bachawal, S. Machtaler, S. M. Chowdhury, R. Luong, L. Tian, B. Khuri-Yakub, J. H. Rao, R. Paulmurugan, and J. K. Willmann. Ultrasound-guided delivery of microRNA loaded nanoparticles into cancer. *J Control Release*, 203:99–108, 2015.

[121] C. Y. Lin, T. M. Liu, C. Y. Chen, Y. L. Huang, W. K. Huang, C. K. Sun, F. H. Chang, and W. L. Lin. Quantitative and qualitative investigation into the impact of focused ultrasound with microbubbles on the triggered release of nanoparticles from vasculature in mouse tumors. *J Control Release*, 146(3):291–8, 2010.

[122] N. Sheikov, N. McDannold, N. Vykhodtseva, F. Jolesz, and K. Hynynen. Cellular mechanisms of the blood-brain barrier opening induced by ultrasound in presence of microbubbles. *Ultrasound Med Biol*, 30(7):979–89, 2004.

[123] N. Sheikov, N. McDannold, S. Sharma, and K. Hynynen. Effect of focused ultrasound applied with an ultrasound contrast agent on the tight junctional integrity of the brain microvascular endothelium. *Ultrasound Med Biol*, 34(7):1093–104, 2008.

[124] N. Sheikov, N. McDannold, F. Jolesz, Y. Z. Zhang, K. Tam, and K. Hynynen. Brain arterioles show more active vesicular transport of blood-borne tracer molecules than capillaries and venules after focused ultrasound-evoked opening of the blood-brain barrier. *Ultrasound Med Biol*, 32(9):1399–409, 2006.

[125] J. Deng, Q. Huang, F. Wang, Y. Liu, Z. Wang, Z. Wang, Q. Zhang, B. Lei, and Y. Cheng. The role of caveolin-1 in blood-brain barrier disruption induced by focused ultrasound combined with microbubbles. *J Mol Neurosci*, 46(3):677–87, 2012.

[126] M. Aryal, K. Fischer, C. Gentile, S. Gitto, Y. Z. Zhang, and N. McDannold. Effects on P-glycoprotein expression after blood-brain barrier disruption using focused ultrasound and microbubbles. *PLoS One*, 12(1):e0166061, 2017.

[127] H. Cho, H. Y. Lee, M. Han, J. R. Choi, S. Ahn, T. Lee, Y. Chang, and J. Park. Localized down-regulation of P-glycoprotein by focused ultrasound and microbubbles induced blood-brain barrier disruption in rat brain. *Sci Rep*, 6:31201, 2016.

[128] K. Hynynen, N. McDannold, N. A. Sheikov, F. A. Jolesz, and N. Vykhodtseva. Local and reversible blood-brain barrier disruption by noninvasive focused ultrasound at frequencies suitable for trans-skull sonications. *Neuroimage*, 24(1):12–20, 2005.

[129] N. McDannold, N. Vykhodtseva, and K. Hynynen. Blood-brain barrier disruption induced by focused ultrasound and circulating preformed microbubbles appears to be characterized by the mechanical index. *Ultrasound Med Biol*, 34(5):834–40, 2008.

[130] N. McDannold, N. Vykhodtseva, and K. Hynynen. Effects of acoustic parameters and ultrasound contrast agent dose on focused-ultrasound induced blood-brain barrier disruption. *Ultrasound Med Biol*, 34(6):930–7, 2008.

[131] G. Samiotaki and E. E. Konofagou. Dependence of the reversibility of focused-ultrasound-induced blood-brain barrier opening on pressure and pulse length in vivo. *IEEE Trans Ultrason Ferroelectr Freq Control*, 60(11):2257–65, 2013.

[132] A. Dasgupta, M. Liu, T. Ojha, G. Storm, F. Kiessling, and T. Lammers. Ultrasound-mediated drug delivery to the brain: principles, progress and prospects. *Drug Discov Today Technol*, 20:41–48, 2016.

[133] A. K. O. Åslund, S. Berg, S. Hak, Ý. Mørch, S. H. Torp, A. Sandvig, M. Widerøe, R. Hansen, and C. de L. Davies. Nanoparticle delivery to the brain–by focused ultrasound and self-assembled nanoparticle-stabilized microbubbles. *J Control Release*, 220(Pt A):287–94, 2015.

[134] A. K. O. Åslund, S. Snipstad, A. Healey, S. Kvale, S. H. Torp, P. C. Sontum, C. L. Davies, and A. van Wamel. Efficient enhancement of blood-brain barrier permeability using acoustic cluster therapy (ACT). *Theranostics*, 7(1):23–30, 2017.

[135] F. Marquet, Y. S. Tung, T. Teichert, V. P. Ferrera, and E. E. Konofagou. Noninvasive, transient and selective blood-brain barrier opening in non-human primates in vivo. *PLoS One*, 6(7):e22598, 2011.

[136] M. E. Downs, A. Buch, M. E. Karakatsani, E. E. Konofagou, and V. P. Ferrera. Blood-brain barrier opening in behaving non-human primates via focused ultrasound with systemically administered microbubbles. *Sci Rep*, 5:15076, 2015.

[137] L. H. Treat, N. McDannold, N. Vykhodtseva, Y. Zhang, K. Tam, and K. Hynynen. Targeted delivery of doxorubicin to the rat brain at therapeutic levels using MRI-guided focused ultrasound. *Int J Cancer*, 121(4):901–7, 2007.

[138] M. Aryal, N. Vykhodtseva, Y. Z. Zhang, J. Park, and N. McDannold. Multiple treatments with liposomal doxorubicin and ultrasound-induced disruption of blood-tumor and blood-brain barriers improve outcomes in a rat glioma model. *J Control Release*, 169(1-2):103–11, 2013.

[139] M. Kinoshita, N. McDannold, F. A. Jolesz, and K. Hynynen. Targeted delivery of antibodies through the blood-brain barrier by MRI-guided focused ultrasound. *Biochem Biophys Res Commun*, 340(4):1085–90, 2006.

[140] M. Kinoshita, N. McDannold, F. A. Jolesz, and K. Hynynen. Noninvasive localized delivery of herceptin to the mouse brain by MRI-guided focused ultrasound-induced blood-brain barrier disruption. *Proc Natl Acad Sci U S A*, 103(31):11719–23, 2006.

[141] E. J. Park, Y. Z. Zhang, N. Vykhodtseva, and N. McDannold. Ultrasound-mediated blood-brain/blood-tumor barrier disruption improves outcomes with trastuzumab in a breast cancer brain metastasis model. *J Control Release*, 163(3):277–84, 2012.

[142] J. F. Jordao, C. A. Ayala-Grosso, K. Markham, Y. Huang, R. Chopra, J. McLaurin, K. Hynynen, and I. Aubert. Antibodies targeted to the brain with image-guided focused ultrasound reduces amyloid-beta plaque load in the TgCRND8 mouse model of alzheimer's disease. *PLoS One*, 5(5):e10549, 2010.

[143] J. F. Jordão, E. Thévenot, K. Markham-Coultes, T. Scarcelli, Y. Q. Weng, K. Xhima, M. O'Reilly, Y. Huang, J. McLaurin, K. Hynynen, and I. Aubert. Amyloid-beta plaque reduction, endogenous antibody delivery and glial activation by brain-targeted, transcranial focused ultrasound. *Exp Neurol*, 248:16–29, 2013.

[144] S. B. Raymond, L. H. Treat, J. D. Dewey, N. J. McDannold, K. Hynynen, and B. J. Bacskai. Ultrasound enhanced delivery of molecular imaging and therapeutic agents in alzheimer's disease mouse models. *PLoS One*, 3(5):e2175, 2008.

[145] T. Kobus, I. K. Zervantonakis, Y. Zhang, and N. J. McDannold. Growth inhibition in a brain metastasis model by antibody delivery using focused ultrasound-mediated blood-brain barrier disruption. *J Control Release*, 238:281–8, 2016.

[146] P. Y. Chen, H. Y. Hsieh, C. Y. Huang, C. Y. Lin, K. C. Wei, and H. L. Liu. Focused ultrasound-induced blood-brain barrier opening to enhance interleukin-12 delivery for brain tumor immunotherapy: a preclinical feasibility study. *J Transl Med*, 13:93, 2015.

[147] Q. Huang, J. Deng, Z. Xie, F. Wang, S. Chen, B. Lei, P. Liao, N. Huang, Z. Wang, Z. Wang, and Y. Cheng. Effective gene transfer into central nervous system following ultrasound-microbubbles-induced opening of the blood-brain barrier. *Ultrasound Med Biol*, 38(7):1234–43, 2012.

[148] E. Thévenot, J. F. Jordão, M. A. O'Reilly, K. Markham, Y. Q. Weng, K. D. Foust, B. K. Kaspar, K. Hynynen, and I. Aubert. Targeted delivery of self-complementary adeno-associated virus serotype 9 to the brain, using magnetic resonance imaging-guided focused ultrasound. *Hum Gene Ther*, 23(11):1144–55, 2012.

[149] S. Wang, O. O. Olumolade, T. Sun, G. Samiotaki, and E. E. Konofagou. Noninvasive, neuron-specific gene therapy can be facilitated by focused ultrasound and recombinant adeno-associated virus. *Gene Ther*, 22(1):104–10, 2015.

[150] A. Burgess, C. A. Ayala-Grosso, M. Ganguly, J. F. Jordao, I. Aubert, and K. Hynynen. Targeted delivery of neural stem cells to the brain using MRI-guided focused ultrasound to disrupt the blood-brain barrier. *PLoS One*, 6(11):e27877, 2011.

[151] R. Alkins, A. Burgess, M. Ganguly, G. Francia, R. Kerbel, W. S. Wels, and K. Hynynen. Focused ultrasound delivers targeted immune cells to metastatic brain tumors. *Cancer Res*, 73(6):1892–9, 2013.

[152] R. Alkins, A. Burgess, R. Kerbel, W. S. Wels, and K. Hynynen. Early treatment of HER2-amplified brain tumors with targeted NK-92 cells and focused ultrasound improves survival. *Neuro Oncol*, 18(7):974–81, 2016.

[153] A. Carpentier, M. Canney, A. Vignot, V. Reina, K. Beccaria, C. Horodyckid, C. Karachi, D. Leclercq, C. Lafon, J. Y. Chapelon, L. Capelle, P. Cornu, M. Sanson, K. Hoang-Xuan, J. Y. Delattre, and A. Idbaih. Clinical trial of blood-brain barrier disruption by pulsed ultrasound. *Sci Transl Med*, 8(343):343re2, 2016.

[154] Safety of BBB opening with the sonocloud. *ClinicalTrials.gov Identifier NCT02253212*.

[155] Blood-brain barrier disruption using transcranial MRI-guided focused ultrasound. *ClinicalTrials.gov Identifier NCT02343991*.

[156] C. Pinto Reis, R. J. Neufeld, A. J. Ribeiro, and F. Veiga. Nanoencapsulation i. methods for preparation of drug-loaded polymeric nanoparticles. *Nanomedicine*, 2(1):8–21, 2006.

[157] F. Chiellini, A. M. Piras, C. Errico, and E. Chiellini. Micro/nanostructured polymeric systems for biomedical and pharmaceutical applications. *Nanomedicine (Lond)*, 3(3):367–93, 2008.

[158] J. Nicolas and P. Couvreur. Synthesis of poly(alkyl cyanoacrylate)-based colloidal nanomedicines. *Wiley Interdiscip Rev Nanomed and Nanobiotechnol*, 1(1):111–127, 2009.

[159] C. Vauthier, D. Labarre, and G. Ponchel. Design aspects of poly(alkylcyanoacrylate) nanoparticles for drug delivery. *J Drug Target*, 15(10):641–63, 2007.

[160] K. Landfester. Synthesis of colloidal particles in miniemulsions. *Annu Rev Mater Res*, 36:231–79, 2006.

[161] A. Kumari, S. K. Yadav, and S. C. Yadav. Biodegradable polymeric nanoparticles based drug delivery systems. *Colloids Surf B Biointerfaces*, 75(1):1–18, 2010.

[162] E. Sulheim, H. Baghirov, E. von Haartman, A. Bøe, A. K. O. Åslund, Ý. Mørch, and C. de L. Davies. Cellular uptake and intracellular degradation of poly(alkyl cyanoacrylate) nanoparticles. *J Nanobiotechnology*, 14:1, 2016.

[163] R. H. Muller, C. Lherm, J. Herbort, T. Blunk, and P. Couvreur. Alkylcyanoacrylate drug carriers; 1. physicochemical characterization of nanoparticles with different alkyl chain-length. *Int J Pharm*, 84:1–11, 1992.

[164] E. Soma, P. Attali, and P. Merle. Chapter 11: A clinically relevant case study: the development of livatag for the treatment of advanced hepatocellular carcinoma. *Nanostructured Biomaterials for Overcoming Biological Barriers, The Royal Society of Chemistry*, pages 591–600, 2012.

[165] Efficacy and safety doxorubicin transdrug study in patients suffering from advanced hepatocellular carcinoma (relive). *ClinicalTrials.gov Identifier NCT01655693*.

[166] I. De Cock, G. Lajoinie, M. Versluis, S. C. De Smedt, and I. Lentacker. Sonoprinting and the importance of microbubble loading for the ultrasound mediated cellular delivery of nanoparticles. *Biomaterials*, 83:294–307, 2016.

[167] C. W. Burke, Y. H. Hsiang, E. th Alexander, A. L. Kilbanov, and R. J. Price. Covalently linking poly(lactic-co-glycolic acid) nanoparticles to microbubbles before intravenous injection improves their ultrasound-targeted delivery to skeletal muscle. *Small*, 7(9):1227–35, 2011.

[168] A. Kheirolomoom, P. A. Dayton, A. F. Lum, E. Little, E. E. Paoli, H. Zheng, and K. W. Ferrara. Acoustically-active microbubbles conjugated to liposomes: characterization of a proposed drug delivery vehicle. *J Control Release*, 118(3):275–84, 2007.

[169] A. F. H. Lum, M. A. Borden, P. A. Dayton, D. E Kruse, S. I. Simon, and K. W. Ferrara. Ultrasound radiation force enables targeted deposition of model drug carriers loaded on microbubbles. *J Control Release*, 111(1-2):128 – 134, 2006.

[170] B. Geers, I. Lentacker, N. N. Sanders, J. Demeester, S. Meairs, and S. C. De Smedt. Self-assembled liposome-loaded microbubbles: The missing link for safe and efficient ultrasound triggered drug-delivery. *J Control Release*, 152(2):249–256, 2011.

[171] S. Eggen, S. M. Fagerland, Ý. Mørch, R. Hansen, K. Søvik, S. Berg, H. Furu, A. D. Bohn, M. B. Lilledahl, A. Angelsen, B. Angelsen, and C. de L. Davies. Ultrasound-enhanced drug delivery in prostate cancer xenografts by nanoparticles stabilizing microbubbles. *J Control Release*, 187:39–49, 2014.

[172] A. K. O. Åslund, E. Sulheim, S. Snipstad, E. von Haartman, H. Baghirov, N. J. Starr, M. Kvåle Løvmo, S. Lelu, D. J. Scurr, C. de L. Davies, R. B. Schmid, and Ý. A. Mørch. Quantification and qualitative effects of different PEGylations on poly(butyl cyanoacrylate) nanoparticles. *Mol Pharm*, 2017.

[173] H. Baghirov, S. Melikishvili, Ý. Mørch, E. Sulheim, A. K. O. Åslund, T. Hianik, and C. de L. Davies. The effect of poly(ethylene glycol) coating and monomer type on poly(alkyl cyanoacrylate) nanoparticle interactions with lipid monolayers and cells. *Colloids Surf B Biointerfaces*, 150:373–383, 2017.

[174] S. Berg, M. Afadzi, E. Sulheim, Ý. Mørch, A. Hatletveit, A. Bjørkøy, C. de L. Davies, and R. Hansen. Acoustic characterization of nanoparticle-stabilized microbubbles for drug delivery. *Manuscript in preparation, to be submitted to Ultrasound Med Biol.*

[175] Gard Fostad Moe. Mechanical and acoustic characterization of perfluorocarbon microbubbles containing nanoparticles. *Master of Science in Physics and Mathematics, Master of Science in Physics and Mathematics, Norwegian University of Science and Technology*, 2015.

[176] Y. Zhao, F. Fay, S. Hak, J. Manuel Perez-Aguilar, B. L. Sanchez-Gaytan, B. Goode, R. Duivenvoorden, C. de Lange Davies, A. Bjørkøy, H. Weinstein, Z. A. Fayad, C. Perez-Medina, and W. J. Mulder. Augmenting drug-carrier compatibility improves tumour nanotherapy efficacy. *Nat Commun*, 7:11221, 2016.

[177] S. Hak, Z. Garaiova, L. T. Olsen, A. M. Nilsen, and C. de Lange Davies. The effects of oil-in-water nanoemulsion polyethylene glycol surface density on intracellular stability, pharmacokinetics, and biodistribution in tumor bearing mice. *Pharm Res*, 32(4):1475–85, 2015.

[178] P. A. Jarzyna, T. Skajaa, A. Gianella, D. P. Cormode, D. D. Samber, S. D. Dickson, W. Chen, A. W. Griffioen, Z. A. Fayad, and W. J. Mulder. Iron oxide core oil-in-water emulsions as a multifunctional nanoparticle platform for tumor targeting and imaging. *Biomaterials*, 30(36):6947–54, 2009.

[179] T. M. Allen and P. R. Cullis. Liposomal drug delivery systems: from concept to clinical applications. *Adv Drug Deliv Rev*, 65(1):36–48, 2013.

[180] S. Hak, J. Cebulla, E. M. Huuse, C. de L. Davies, W. J. Mulder, H. B. Larsson, and O. Haraldseth. Periodicity in tumor vasculature targeting kinetics of ligand-functionalized nanoparticles studied by dynamic contrast enhanced magnetic resonance imaging and intravital microscopy. *Angiogenesis*, 17(1):93–107, 2014.

[181] S. Hak, E. Helgesen, H. H. Hektoen, E. M. Huuse, P. A. Jarzyna, W. J. Mulder, O. Haraldseth, and C. de L. Davies. The effect of nanoparticle polyethylene glycol surface density on ligand-directed tumor targeting studied in vivo by dual modality imaging. *ACS Nano*, 6(6):5648–58, 2012.

[182] A. van Wamel, A. Healey, P. C. Sontum, S. Kvale, N. Bush, J. Bamber, and C. de L. Davies. Acoustic cluster therapy (ACT) - pre-clinical proof of principle

for local drug delivery and enhanced uptake. *J Control Release*, 224:158–64, 2016.

[183] A. J. Healey, P. C. Sontum, S. Kvale, M. Eriksen, R. Bendiksen, A. Tornes, and J. Ostensen. Acoustic cluster therapy: In vitro and ex vivo measurement of activated bubble size distribution and temporal dynamics. *Ultrasound Med Biol*, 42(5):1145–66, 2016.

[184] P. Sontum, S. Kvale, A. J. Healey, R. Skurtveit, R. Watanabe, M. Matsumura, and J. Ostensen. Acoustic cluster therapy (ACT)–a novel concept for ultrasound mediated, targeted drug delivery. *Int J Pharm*, 495(2):1019–27, 2015.

[185] O. Myhre, M. Bjorgan, D. Grant, S. O. Hustvedt, P. C. Sontum, and H. Dirven. Safety assessment in rats and dogs of acoustic cluster therapy, a novel concept for ultrasound mediated, targeted drug delivery. *Pharmacol Res Perspect*, 4(6):e00274, 2016.

[186] S. Kotopoulis, E. Stigen, M. Popa, M. M. Safont, A. Healey, S. Kvåle, P. Sontum, B. T. Gjertsen, O. H. Gilja, and E. McCormack. Sonoporation with acoustic cluster therapy (ACT) induces transient tumour volume reduction in a subcutaneous xenograft model of pancreatic ductal adenocarcinoma. *J Control Release*, 245:70–80, 2017.

[187] S. Bhattacharjee. DLS and zeta potential - what they are and what they are not? *J Control Release*, 235:337–51, 2016.

[188] R. Xu. Progress in nanoparticles characterization: Sizing and zeta potential measurement. *Particuology*, 6(2):112–115, 2008.

[189] M. Rieseberg, C. Kasper, K. F. Reardon, and T. Scheper. Flow cytometry in biotechnology. *Appl Microbiol Biotechnol*, 56(3-4):350–60, 2001.

[190] S. W. Paddock. Principles and practices of laser scanning confocal microscopy. *Mol Biotechnol*, 16(2):127–49, 2000.

[191] D. M. Shotton. Confocal scanning optical microscopy and its applications for biological specimens. *J Cell Sci*, 94:175–206, 1989.

[192] J. R. Albani. Principles and applications of fluorescence spectroscopy. *Blackwell Science*, pages 88–114, 2007.

[193] J. M. Hyvelin, I. Tardy, C. Arbogast, M. Costa, P. Emmel, A. Helbert, M. Theraulaz, A. D. Nunn, and F. Tranquart. Use of ultrasound contrast agent microbubbles in preclinical research recommendations for small animal imaging. *Invest Radiol*, 48(8):570–583, 2013.

[194] G. Choy, P. Choyke, and S. K. Libutti. Current advances in molecular imaging: noninvasive in vivo bioluminescent and fluorescent optical imaging in cancer research. *Mol Imaging*, 2(4):303–12, 2003.

[195] V. P. Torchilin. Recent approaches to intracellular delivery of drugs and DNA and organelle targeting. *Annu Rev Biomed Eng*, 8:343–75, 2006.

[196] K. C. Partlow, G. M. Lanza, and S. A. Wickline. Exploiting lipid raft transport with membrane targeted nanoparticles: A strategy for cytosolic drug delivery. *Biomaterials*, 29(23):3367–3375, 2008.

[197] G. M. Lanza, X. Yu, P. M. Winter, D. R. Abendschein, K. K. Karukstis, M. J. Scott, L. K. Chinen, R. W. Fuhrhop, D. E. Scherrer, and S. A. Wickline. Targeted antiproliferative drug delivery to vascular smooth muscle cells with a magnetic resonance imaging nanoparticle contrast agent: implications for rational therapy of restenosis. *Circulation*, 106(22):2842–7, 2002.

[198] P. M. Winter, A. M. Neubauer, S. D. Caruthers, T. D. Harris, J. D. Robertson, T. A. Williams, A. H. Schmieder, G. Hu, J. S. Allen, E. K. Lacy, H. Y. Zhang, S. A. Wickline, and G. M. Lanza. Endothelial alpha(v)beta(3) integrin-targeted fumagillin nanoparticles inhibit angiogenesis in atherosclerosis. *Arterioscler Thromb Vasc Biol*, 26(9):2103–2109, 2006.

[199] I. Tufto, R. Hansen, D. Byberg, K. H. Nygaard, J. Tufto, and C. de L. Davies. The effect of collagenase and hyaluronidase on transient perfusion in human osteosarcoma xenografts grown orthotopically and in dorsal skinfold chambers. *Anticancer Res*, 27(3B):1475–81, 2007.

[200] A. E. Hansen, A. L. Petersen, J. R. Henriksen, B. Boerresen, P. Rasmussen, D. R. Elema, P. M. Rosenschold, A. T. Kristensen, A. Kjaer, and T. L. Andresen. Positron emission tomography based elucidation of the enhanced permeability and retention effect in dogs with cancer using copper-64 liposomes. *ACS Nano*, 9(7):6985–95, 2015.

[201] C. Perez-Medina, D. Abdel-Atti, J. Tang, Y. Zhao, Z. A. Fayad, J. S. Lewis, W. J. Mulder, and T. Reiner. Nanoreporter PET predicts the efficacy of anti-cancer nanotherapy. *Nat Commun*, 7:11838, 2016.

[202] E. Sulheim, J. Kim, A. van Wamel, E. Kim, S. Snipstad, I. Vidic, I. H. Grimstad, M. Widerøe, D. J. Waxman, S. H. Torp, S. Lundgren, and C. de L. Davies. Multi-modal characterization of vasculature and nanoparticle accumulation in five tumor xenograft models. *Manuscript in preparation.*

[203] M. A. O'Reilly, Y. Huang, and K. Hynynen. The impact of standing wave effects on transcranial focused ultrasound disruption of the blood-brain barrier in a rat model. *Phys Med Biol*, 55(18):5251–67, 2010.

[204] A. Burgess and K. Hynynen. Microbubble-assisted ultrasound for drug delivery in the brain and central nervous system. *Adv Exp Med Biol*, 880:293–308, 2016.

[205] J. J. Choi, S. Wang, Y. S. Tung, B. Morrison, and E. E. Konofagou. Molecules of various pharmacologically-relevant sizes can cross the ultrasound-induced blood-brain barrier opening in vivo. *Ultrasound Med Biol*, 36(1):58–67, 2010.

[206] Habib Baghirov. Nanoparticle uptake by brain endothelial cells and focused ultrasound-mediated transport across the blood-brain barrier. *Thesis for the degree of Philosophiae Doctor, Department of Physics, The Norwegian University of Science and Technology*, 2016.

[207] B. Marty, B. Larrat, M. Van Landeghem, C. Robic, P. Robert, M. Port, D. Le Bihan, M. Pernot, M. Tanter, F. Lethimonnier, and S. Meriaux. Dynamic study of blood-brain barrier closure after its disruption using ultrasound: a quantitative analysis. *J Cereb Blood Flow Metab*, 32(10):1948–58, 2012.

[208] N. McDannold, N. Vykhodtseva, S. Raymond, F. A. Jolesz, and K. Hynynen. Mri-guided targeted blood-brain barrier disruption with focused ultrasound: histological findings in rabbits. *Ultrasound Med Biol*, 31(11):1527–37, 2005.

[209] A. N. Pouliopoulos, C. Li, M. Tinguely, V. Garbin, M. X. Tang, and J. J. Choi. Rapid short-pulse sequences enhance the spatiotemporal uniformity of acoustically driven microbubble activity during flow conditions. *J Acoust Soc Am*, 140(4):2469, 2016.

[210] S. Morse, A. N. Pouliopoulos, J. Lin, T. Chan, and J. J. Choi. Improved drug distribution using rapid short-pulse (RaSP) sequences in vivo to open the blood-brain barrier. *22nd European symposium on Ultrasound Contrast Imaging, Rotterdam*, 2017.

[211] S. B. Raymond, J. Skoch, K. Hynynen, and B. J. Bacskai. Multiphoton imaging of ultrasound/optison mediated cerebrovascular effects in vivo. *J Cereb Blood Flow Metab*, 27(2):393–403, 2007.

[212] E. E. Cho, J. Drazic, M. Ganguly, B. Stefanovic, and K. Hynynen. Two-photon fluorescence microscopy study of cerebrovascular dynamics in ultrasound-induced blood-brain barrier opening. *J Cereb Blood Flow Metab*, 31(9):1852–62, 2011.

[213] D. E. Goertz, M. Todorova, O. Mortazavi, V. Agache, B. Chen, R. Karshafian, and K. Hynynen. Antitumor effects of combining docetaxel (taxotere) with the antivascular action of ultrasound stimulated microbubbles. *PLoS One*, 7(12):e52307, 2012.

[214] A. Burgess, S. Dubey, S. Yeung, O. Hough, N. Eterman, I. Aubert, and K. Hynynen. Alzheimer disease in a mouse model: MR imaging-guided focused ultrasound targeted to the hippocampus opens the blood-brain barrier and improves pathologic abnormalities and behavior. *Radiology*, 273(3):736–45, 2014.

[215] M. A. O'Reilly and K. Hynynen. Blood-brain barrier: real-time feedback-controlled focused ultrasound disruption by using an acoustic emissions-based controller. *Radiology*, 263(1):96–106, 2012.

[216] C. P. Keravnou, I. De Cock, I. Lentacker, M. L. Izamis, and M. A. Averkiou. Microvascular injury and perfusion changes induced by ultrasound and microbubbles in a machine-perfused pig liver. *Ultrasound Med Biol*, 42(11):2676–2686, 2016.

[217] X. Hu, A. Kheirolomoom, L. M. Mahakian, J. R. Beegle, D. E. Kruse, K. S. Lam, and K. W. Ferrara. Insonation of targeted microbubbles produces regions of reduced blood flow within tumor vasculature. *Invest Radiol*, 47(7):398–405, 2012.

[218] J. T. Belcik, B. H. Mott, A. Xie, Y. Zhao, S. Kim, N. J. Lindner, A. Ammi, J. M. Linden, and J. R. Lindner. Augmentation of limb perfusion and reversal of tissue ischemia produced by ultrasound-mediated microbubble cavitation. *Circ Cardiovasc Imaging*, 8(4), 2015.

[219] Y. Song, X. Xie, Y. Gao, L. Jin, and P. Wang. Ultrasound-induced microbubble cavitation promotes angiogenesis in ischemic skeletal muscle of diabetic mice. *Int J Clin Exp Med*, 9(12):23345–23350, 2016.

[220] J. Qin, T.-Y. Wang, and J. K. Willmann. Sonoporation: Applications for cancer therapy. *Adv Exp Med Biol*, 880:263–91, 2016.

[221] H. L. Liu, C. H. Fan, C. Y. Ting, and C. K. Yeh. Combining microbubbles and ultrasound for drug delivery to brain tumors: current progress and overview. *Theranostics*, 4(4):432–44, 2014.

[222] J.-M. Escoffre, R. Deckers, C. Bos, and C. Moonen. Bubble-assisted ultrasound: Application in immunotherapy and vaccination. *Adv Exp Med Biol.*, 880:243–61, 2016.

[223] A. Burgess, Y. Huang, W. Querbes, D. W. Sah, and K. Hynynen. Focused ultrasound for targeted delivery of siRNA and efficient knockdown of Htt expression. *J Control Release*, 163(2):125–9, 2012.

[224] E. E. Konofagou. Neurorestoration of the nigrostriatal pathway through multiple treatments with FUS-facilitated brain drug delivery. *22nd European symposium on Ultrasound Contrast Imaging, Rotterdam*, 2017.

Paper I

Snipstad et al. Cancer Nanotechnology 2014, 5:8
http://www.cancer-nano.com/content/5/1/8

Cancer Nanotechnology
a SpringerOpen Journal

RESEARCH Open Access

Contact-mediated intracellular delivery of hydrophobic drugs from polymeric nanoparticles

Sofie Snipstad[1*], Sara Westrøm[1], Yrr Mørch[2], Mercy Afadzi[1], Andreas KO Åslund[1] and Catharina de Lange Davies[1]

* Correspondence:
sofie.snipstad@ntnu.no
[1]Department of Physics, The Norwegian University of Science and Technology, Høgskoleringen 5, 7491 Trondheim, Norway
Full list of author information is available at the end of the article

Abstract

Encapsulation of drugs in nanoparticles can enhance the accumulation of drugs in tumours, reduce toxicity toward healthy tissue, and improve pharmacokinetics compared to administration of free drug. To achieve efficient delivery and release of drugs at the target site, mechanisms of interaction between the nanoparticles and cells and the mechanism of delivery of the encapsulated drug are crucial to understand. Our aim was to determine the mechanisms for cellular uptake of a fluorescent hydrophobic model drug from poly(butylcyanoacrylate) nanoparticles. Prostate adenocarcinoma cells were incubated with Nile Red-loaded nanoparticles or free Nile Red. Uptake and intracellular distribution were evaluated by flow cytometry and confocal laser scanning microscopy. The nanoparticles mediated a higher intracellular level and more rapid uptake of encapsulated Nile Red compared to model drug administered alone. The main mechanism for delivery was not by endocytosis of nanoparticles but by nanoparticle-cell contact-mediated transfer directly to the cytosol and, to a smaller extent, release of payload from nanoparticles into the medium followed by diffusion into cells. The payload thus avoids entering the endocytic pathway, evading lysosomal degradation and instead gains direct access to intracellular targets. The nanoparticles are promising tools for efficient intracellular delivery of hydrophobic anticancer drugs; therefore, they are clinically relevant for improved cancer therapy.

Keywords: Contact-mediated; Drug delivery; Polymeric nanoparticles; Cellular uptake; Nile red

Background

Cancer treatment based on systemic chemotherapy is not cancer-specific, and toxic effects toward normal healthy tissue are challenging [1]. Nanoparticles carrying drugs may improve the tumour uptake of drugs and reduce their toxic effects through the enhanced permeability and retention (EPR) effect in tumour tissue [2]. EPR results in passive accumulation of nanoparticles in tumours due to the hyperpermeability of the vasculature and the lack of lymphatic drainage, whereas the nanoparticles are constrained to the blood vessels in normal tissue. To increase the fraction of nanoparticles reaching the tumour, a common strategy is to extend their time in systemic circulation [3]. This can be achieved by coating the nanoparticle surface with polyethylene glycol (PEG) [4,5] thereby preventing adsorption of opsonins via steric hindrance [6,7] and avoiding elimination through the mononuclear phagocyte system (MPS) [8,9]. Several different types of nanoparticles have been investigated as carriers for drug delivery [1,5,10],

including polymeric nanoparticles [5,11]. Of these, poly(alkylcyanoacrylate) (PACA) nanoparticles are promising due to their ease and reproducibility of preparation, satisfying drug-loading capacity, low toxicity, and feasibility for scale-up production [12]. Some PACA nanoparticles are already in clinical development for cancer therapy [13]. We have developed a novel, multimodal, multifunctional drug delivery system consisting of microbubbles stabilised by polymeric PACA nanoparticles [14]. The nanoparticles can contain contrast agents for optical and magnetic resonance imaging as well as drugs and targeting ligands for combined diagnosis and therapy. The integration of nanoparticles and microbubbles into one single microparticle further makes them a promising agent for ultrasound-mediated delivery of encapsulated drugs to the tumour [15]. When developing nanoparticles for drug delivery, it is of crucial importance to understand the mechanism of interaction between the nanoparticles and cells and the mechanism of delivery of the encapsulated drug to achieve efficient delivery and release of drugs to the target. Interactions between cells and nanoparticles and the mechanisms for intracellular drug delivery have been investigated for various nanoparticles [16-21]. In most cases, endocytosis of the nanoparticles is the main mechanism for internalization [22,23], and subsequently the drug has to be released from the nanoparticle. Polymeric nanoparticles can employ various release mechanisms such as diffusion of the load, matrix swelling, polymer erosion, partition of the load, or a burst release effect depending on properties of the polymer and of the payload [24]. To be effective, drugs internalized by endocytosis of the nanoparticles depend on endosomal escape to reach the cytosol, to avoid lysosomal degradation [25,26]. Various possibilities for delivering substances directly into cytosol have been discussed [22,23,25]. Such directed cytoplasmic delivery into a target cell could provide an avenue for delivering greater amounts of agent with more efficient and immediate access to intracellular targets [27]. An example is delivery of load from nanoparticles to cells by collisional interactions [28,29].

The aim of the present work was to study the mechanisms of cellular uptake of the hydrophobic model drug Nile Red from poly(butylcyanoacrylate) (PBCA) nanoparticles *in vitro* and to determine whether the uptake was based on endocytosis of nanoparticles, extracellular release of Nile Red followed by diffusion into cells, or a contact-based transfer from nanoparticles to cells [30]. One of the advantages of Nile Red is its unique spectral properties: it emits fluorescence at different wavelengths depending on the hydrophobicity of the molecule binding to it [31]. Prostate cancer cells were incubated with nanoparticles encapsulating Nile Red or with free Nile Red dissolved in growth medium. The cellular uptake and intracellular distribution of Nile Red were studied using flow cytometry (FCM) and confocal laser scanning microscopy (CLSM).

Methods

Cell cultures

Human prostate adenocarcinoma cells (PC3, American Type Culture Collection) were grown in Dulbecco's modified Eagle's medium (DMEM, Gibco Invitrogen) supplemented with 10% foetal bovine serum (FBS, Sigma-Aldrich), and maintained in exponential phase at 37°C and 5% CO_2.

Synthesis and characterisation of nanoparticles

Solid biodegradable and biocompatible PBCA nanoparticles in water were synthesised in a single step by the miniemulsion process [14]. Briefly, oil-in-water emulsions were

prepared by probe sonication (Branson Ultrasonifier, 3 min, 60% amplitude) of a monomer phase consisting of BCA (a kind gift from Henkel Loctite, 6 g) with co-stabiliser (hexadecane or Miglyol 810 N, 2% w/w) and the hydrophobic model drug Nile Red (Sigma-Aldrich, 0.03 or 0.15% w/w) in an acidic aqueous medium containing the surfactant sodium dodecyl sulfate (SDS, Merck, 12 mM, 24 ml, pH 1). Anionic polymerisation was carried out by adding a polyetheramine (Jeffamine M-1000, a kind gift from Huntsman Corporation, 0.05 M, 35 ml, pH 6), resulting in PEGylated nanoparticles. A dual-labelled nanoparticle containing 0.2% w/w Nile Red and 0.2% w/w p-HTAM (pentamer hydrogen thiophene acetic acid methyl ester, kindly provided by Linköping University) [32] was synthesized with Jeffamine M-2070 (kind gift from Huntsman Corporation, 0.05 M, 35 ml, pH 6) and the surfactant BrijL23 (Sigma-Aldrich, 19 mM, 30 ml). The two dyes are a good Förster resonance energy transfer (FRET) pair, and the particles were used to study uptake kinetics of different dyes. Excess PEG and surfactant were removed by dialysis against distilled water (6 shifts using a dialysis membrane with molecular weight cut-off of 12–14000). The size and the zeta potential of the nanoparticles (at pH 7) were measured by dynamic light scattering using a Zetasizer (Malvern Instruments). Successful PEGylation of the nanoparticle was verified by ^{1}H-NMR [14]. The excitation and emission spectra for Nile Red in the nanoparticles were determined using a spectrophotometer (Olis RSM 1000).

Incubation of cells with nanoparticles containing Nile Red or Nile Red in cell medium

Cells were incubated in growth medium supplemented with either nanoparticles containing Nile Red or free Nile Red in the same concentration range. The concentration of free Nile Red added to medium was estimated from the total amount of Nile Red added to the oil phase during particle synthesis. However, because SDS and PEG also associate with the oil droplets when nanoparticles are formed, the proportion of Nile Red in the final PEGylated particles will be smaller and is difficult to define exactly. The concentrations are estimated to be in the range of 4–6 ng/ml and 20–30 ng/ml for the particles with the lower and higher Nile Red content, respectively. A concentration of 20 μg/ml nanoparticles was used, corresponding to 10^4 nanoparticles per cell. This concentration was chosen to avoid cytotoxicity, as concentrations above 20 μg/ml were found to be cytotoxic in the Alamar Blue assay (Additional file 1). To determine the number of nanoparticles per ml, a PBCA density of 1.1481 g/cm^2 was used [33]. The nanoparticles with the lower Nile Red content were used in all experiments except for co-localisation studies between nanoparticles and early endosomes, in which particles with the higher Nile Red content were used to achieve similar fluorescence intensity as the labelled early endosomes.

For flow cytometric analysis, the appropriate number of cells was seeded in 6-well plates (Corning) to obtain 0.6×10^6 cells in each well on the day of the experiment. Then the medium was replaced with nanoparticles or approximately 4 ng/ml free Nile Red. Eight ng/ml was used in one set of experiments to study the effect of a higher Nile Red concentration on uptake. Nile Red was also diluted in phosphate-buffered saline (PBS, Sigma-Aldrich), to determine whether proteins in the growth medium would affect the cellular Nile Red uptake. Cells were incubated for 15 min, 30 min, or 1, 2, 3, or 4 h to study the kinetics of uptake. The medium was removed, and the cells were rinsed 3 times with PBS before being detached. The effect of more extensive washing was also studied by centrifuging (Heraeus Megafuge 1.0R) at 1000 rpm for 3 min and

resuspending the cells up to 3 times. In all experiments, the cells were placed on ice before flow cytometric analysis.

For microscopy, the appropriate number of cells were seeded in 8-well microscopy slides (Ibidi, Thistle Scientific) to obtain 30 000 cells in each well on the day of the experiment. The medium was replaced with medium containing either nanoparticles or free Nile Red, or the dual-labelled nanoparticles.

Inhibition of endocytosis

To determine whether the uptake of Nile Red was due to endocytosis, cells were incubated with 10 μg/ml chlorpromazine or 70 μg/ml genistein (both from Sigma Aldrich), to inhibit clathrin-dependent and caveolae-mediated endocytosis, respectively [34]. The cells were pre-incubated at 37°C for 30 min with growth medium containing endocytosis inhibitors, before the nanoparticles were added for 3 h and the cells were washed and analysed by FCM. Incubation with encapsulated or free Nile Red were performed at 37°C or 4°C to investigate whether the cellular uptake of Nile Red was energy dependent.

Labelling early endosomes and incubating with nanoparticles or Nile Red

Early endosomes were labelled using CellLight Early Endosomes-GFP (Invitrogen). 15 000 cells were seeded in 8-well microscopy slides and incubated for 24 h before replacing the medium with CellLight Early Endosomes-GFP at a concentration of 40 virus particles per cell. The cells were incubated for 24 h before replacing the medium with medium containing nanoparticles or 20 ng/ml free Nile Red. They were incubated for approximately 30 min before imaging with CLSM.

Cellular uptake measured with flow cytometry

Cellular uptake of Nile Red or nanoparticles was analysed by FCM (Gallios, Beckman Coulter). A total of 10 000 cells were counted per sample. A 561 nm laser was used to excite Nile Red, and emitted fluorescence was detected at 620 nm using a 30 nm band pass filter. Cellular fragments and debris were excluded from the analysis by using a side-scatter versus forward-scatter histogram to establish a collection gate.

Cellular uptake measured with confocal laser scanning microscopy

CLSM (Leica TCS SP5 or SP8) was used to study the intracellular distribution and uptake kinetics of Nile Red using a 63x/1.2 water objective. Live cell imaging up to 2,5 h was performed in 5% CO_2 and 34-37°C using a 63x/1.4 oil objective. To excite Nile Red, a 561 nm laser was used on the SP5 and an argon laser at 488 nm or a white light laser enabling a tuneable excitation wavelength was used on the SP8.

The excitation and emission spectra of Nile Red depend on the hydrophobicity of the molecules the dye is binding to; this was used to distinguish between Nile Red bound to lipids, Nile Red in nanoparticles, or Nile Red associated with less hydrophobic molecules. An emisson-scan was captured, in which the emission spectrum of Nile Red was recorded for one excitation wavelength, and an excitation-emission-scan was captured, in which the detection range varied from 480 to 690 nm while the excitation wavelength varied from 470 to 670 nm using the white light laser.

The fluorochrome CellLight Early Endosomes-GFP was excited at 488 nm, and emission was detected at 500–530 nm. The dye p-HTAM was excited at 405 nm, and emission

was detected at 470–530 nm. When studying FRET signal from the p-HTAM and Nile Red pair excitation of 405 nm was used, and emission was detected at 650–710 nm. The laser intensities and gains of the different detectors were adjusted with appropriate control samples to avoid cross-talk between the fluorochromes and to achieve a maximum signal with minimal saturation and background. The pinhole size was 1 airy unit. Fluorescence images, together with transmission microscopy images were captured.

Release of Nile Red from nanoparticles

Because Nile Red is quenched in water, its release from nanoparticles into an aqueous solution could not be measured directly using a spectrophotometer. Therefore, cell medium containing 20 μg/ml nanoparticles was incubated at 37°C for 3 h before the suspension was centrifuged (Beckman Coulter Avanti J-30I) for 2 h at 21 000 rpm (~50 000 g). The supernatant from the centrifuged nanoparticle medium was added to cells, which were imaged after 15–30 min to determine whether Nile Red was released into the cell medium from the nanoparticles and taken up into cells.

Furthermore, cell medium with 20 μg/ml nanoparticles was incubated at 37°C for 3 h, centrifuged and Nile Red was extracted from the supernatant with hexadecane. The solutions were rotated overnight before standing still for several minutes to allow phase separation of hexadecane and the aqueous cell medium phase. The hexadecane phase was collected and analysed with a fluorescence spectrophotometer (Gemini XPS Fluorescence Microplate Reader, Molecular Devices) to determine the amount of released Nile Red.

To determine the total amount of Nile Red associated with the particles, the nanoparticles were dissolved in tetrahydrofuran (THF). The solutions were stirred for 4 h to dissolve the particles, and the amount of Nile Red was measured detecting the fluorescence spectroscopically after 24 h. Nanoparticles without Nile Red were dissolved and used as a control.

Excitation and emission maxima of 493 nm and 540 nm, respectively, were determined for Nile Red in hexadecane; similarly, maxima of 527 nm and 604 nm, respectively, were determined for Nile Red in THF. These maxima were used for the subsequent analysis. Hexadecane and THF with 0.001 to 0.1 μg/ml Nile Red were used to obtain standard curves.

Data and regression analysis

FCM data were analysed with Kaluza Flow Cytometry Analysis software (Beckman Coulter) to determine the percentage of Nile Red-positive cells and the median fluorescence intensity (MFI), expressing the increase in fluorescence of the total population of cells relative to the autofluorescence.

Amira software (Visage Imaging) was used to construct 3-dimensional representations from z-stacks of images. The background fluorescence from the cytosol was removed by thresholding the CLSM co-localisation images and 3-dimensional representations.

Microsoft Excel was used for linear regression of standard curves. The kinetics of Nile Red uptake was analysed by non-linear regression using SigmaPlot. The exponential function $f(t)= a(1 - e^{-bt})$ was fitted to the averages of the FCM data, where the coefficients a and b represent the maximum value and the rate constant, respectively. The goodness

of each fit was determined by the square of the correlation coefficient (R^2) and p-values <0.05 were considered statistically significant.

Results

Characterisation of nanoparticles

All three batches of nanoparticles had a hydrodynamic diameter of approximately 150 nm and a polydispersity index (PDI) of approximately 0.1, as measured by dynamic light scattering using the Zetasizer. The zeta potentials were −19 mV and −15 mV for the particles with the lower and higher Nile Red content, respectively, and −4 mV for the dual-labelled nanoparticles.

Kinetics of the uptake of free or encapsulated Nile Red

The uptake kinetics of encapsulated Nile Red and Nile Red dissolved in cell medium or PBS were compared, and the cellular uptake of Nile Red was higher when Nile Red was associated with nanoparticles (Figure 1). Nearly 100% of the cells had taken up Nile Red from nanoparticles compared to 37% when Nile Red was dissolved in medium (Figure 1a). The amount of Nile Red fluorescence per cell was approximately 4 times higher in cells incubated with nanoparticles compared to cells incubated with medium or PBS containing free Nile Red (Figure 1b). There was no significant difference in the cellular uptake of Nile Red dissolved in PBS or cell medium. The uptake kinetics fit well to a first order reaction both when measuring the percentage of Nile Red-positive cells and the average fluorescence intensity. The initial rate constant for the percentage of positive cells was approximately 2 times higher when the cells were incubated with nanoparticles compared to cells incubated with Nile Red in the medium (Table 1). Within 1 h, approximately all cells incubated with nanoparticles were fluorescent, and the amount of Nile Red internalised into these cells increased further and reached a maximum after approximately 2 h. Cells were also incubated with 8 ng/ml Nile Red dissolved in medium; in this case, the uptake was not twice as high but rather showed a maximum increase in MFI of 30%, indicating no linear relationship between concentration and uptake of free dye (Additional file 2).

The difference in cellular uptake of free and encapsulated Nile Red was confirmed by CLSM. Cells were imaged every minute up to 1 h, and images from 0-, 5-, and 60-min incubations are shown (Figure 1c-h). The uptake of encapsulated Nile Red was rapid, and CLSM images show that all the cells were positive for Nile Red after only a few minutes of incubation (Figure 1g, i). Intracellular fluorescence was observed throughout the entire cytosol, and the intensity was higher in the cells incubated with nanoparticles than in the cells incubated with Nile Red in the medium.

To exclude the possibility that rapid uptake could be cell line-specific, HeLa cells were incubated with nanoparticles and analysed by FCM. The uptake of Nile Red in HeLa cells after 15 min and 3 h of incubation was very similar to that in PC3 cells, both with respect to the percentage of positive cells and MFI (Additional file 3).

Different uptake kinetics of Nile Red and p-HTAM

Dual-labelled nanoparticles were used to compare the uptake kinetics of different dyes encapsulated non-covalently in the same nanoparticle. Nile Red showed a rapid uptake and stained the entire cell after minutes of incubation. The uptake of p-HTAM was

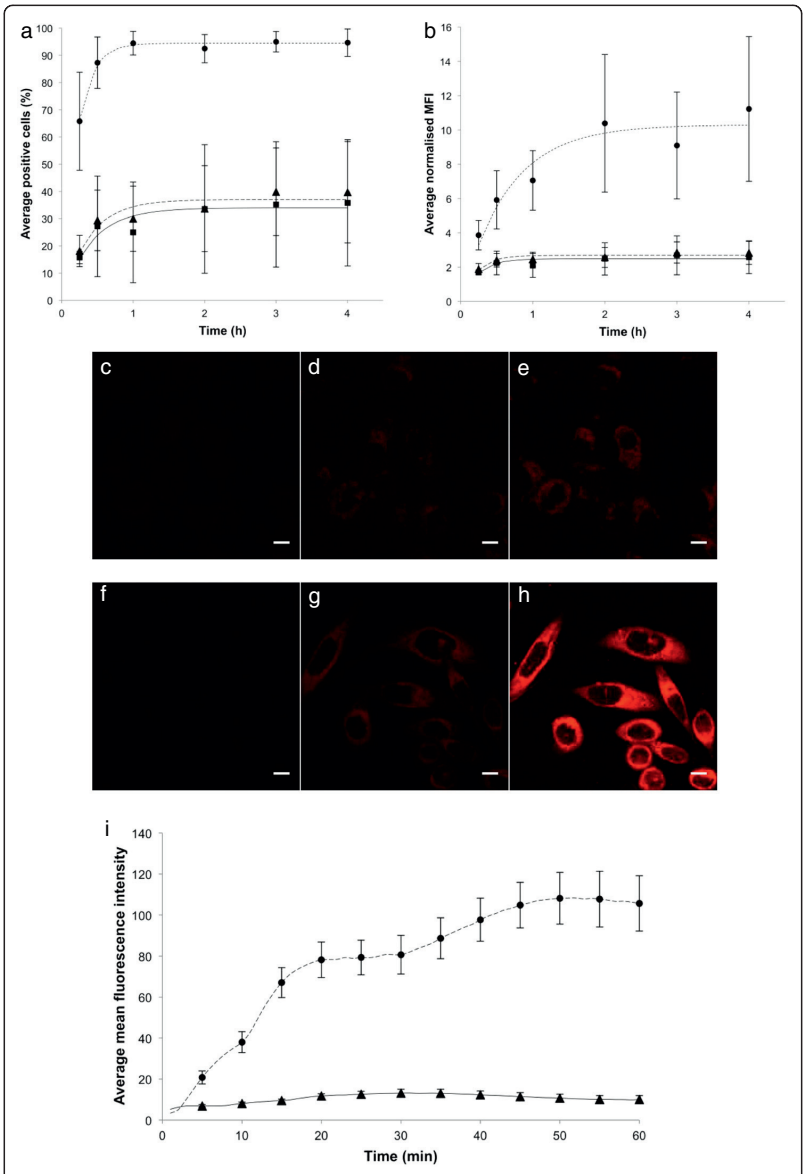

Figure 1 Kinetics of cellular uptake of Nile Red encapsulated in nanoparticles (●) or dissolved in medium (▲) or PBS (■). The cellular uptake was measured by FCM and is expressed as the percentage of Nile Red-positive cells **(a)** or median fluorescence intensity normalised to autofluorescence **(b)**. Each data point is the mean of 2–5 independent measurements. Bars indicate the standard deviation. The R^2 values of the regression curves ranged from 0.73 to 0.99, and p-values were less than 0.014. CLSM images of cells incubated with Nile Red in medium **(c, d, e)** or Nile Red in nanoparticles **(f, g, h)** after 0 min **(c, f)**, 5 min **(d, g)**, and 60 min **(e, h)** of incubation. Scale bars are 10 μm. Nile Red was excited at 488 nm, and fluorescence was detected at 520–700 nm. CLSM images were recorded every min for 1 h. The average mean Nile Red fluorescence intensities from cells (n= 5-11) at each time point with standard deviation at every 5^{th} min are shown **(i)**. The mean intensity of each cell was determined by drawing regions of interest around each cell.

Table 1 Rate constants (b) and maximum values (a) from regression curves $f(t)= a(1 - e^{-bt})$ fitted to data points from Nile Red uptake kinetics

Regression curve	Maximum value	Rate constant
Nanoparticles, normalised MFI	MFI 10.3	1.5 /h
Free Nile Red in medium, normalised MFI	MFI 2.7	-*
Free Nile Red in PBS, normalised MFI	MFI 2.5	-*
Nanoparticles, percentage positive cells	94%	4.9 /h
Free Nile Red in medium, percentage positive cells	37%	2.6 /h
Free Nile Red in PBS, positive cells	34%	2.4 /h

Curves were fitted to the percentage of positive cells and to MFI after incubation with free Nile Red in medium, free Nile Red in PBS, or nanoparticle-associated Nile Red.
*Regression curves fitted to average fluorescence intensity of cells incubated with Nile Red in cell medium or PBS had only two data points describing the initial increase and were therefore not reliable.

significantly slower, fluorescence was seen only from a few located spots in the cells after approximately half an hour and the number of spots increased with time (Figure 2). No FRET signal in the 650–710 nm channel was detected.

Inhibition of endocytosis

To study whether endocytosis was responsible for the cellular uptake of Nile Red from nanoparticles, endocytosis was inhibited either by inhibitors or by incubation of the cells at 4°C. The inhibitors chlorpromazine and genistein had no effect on the Nile Red uptake (Figure 3a), indicating that the cellular uptake of Nile Red was not due to endocytosis of the nanoparticles. This was further confirmed by incubation with nanoparticles at 4°C. The cellular uptake of Nile Red after incubation for 1 h at 4°C and 37°C was similar, both for cells incubated with Nile Red in the medium and Nile Red associated with nanoparticles (Figure 3b). This demonstrates that the uptake of Nile Red is not an energy-dependent process, but rather is likely due to diffusion.

Decreasing cellular Nile Red fluorescence by washing cells

To remove any nanoparticles or Nile Red binding to the cell surface, the adherent cells were rinsed 3 times with PBS. Furthermore, cells incubated with nanoparticles were washed by centrifugation and resuspended in medium containing serum up to 3 times. Nile Red fluorescence from cells incubated with nanoparticles for 3 h decreased with washing (Figure 4). After the third centrifugation, the median Nile Red fluorescence intensity was nearly reduced to the level of autofluorescence. The first centrifugation reduced the percentage of positive cells from 100% to 77%, the next to 27%, and the last to approximately 14%.

Intracellular distribution of Nile Red

Cells incubated with either Nile Red associated with nanoparticles or free Nile Red in medium showed similar intracellular distribution of Nile Red, although the fluorescence intensity was higher for cells incubated with nanoparticles. Nile Red was located in structures resembling vesicles, and it also showed diffuse cytosolic staining (Figure 5a, c). Spectral analysis of the fluorescence in vesicular structures and in the cytosol showed maximum emission at 584 nm and 616 nm, respectively (Figure 5b, d), demonstrating that the environment in the vesicular structure was more hydrophobic than the molecules Nile

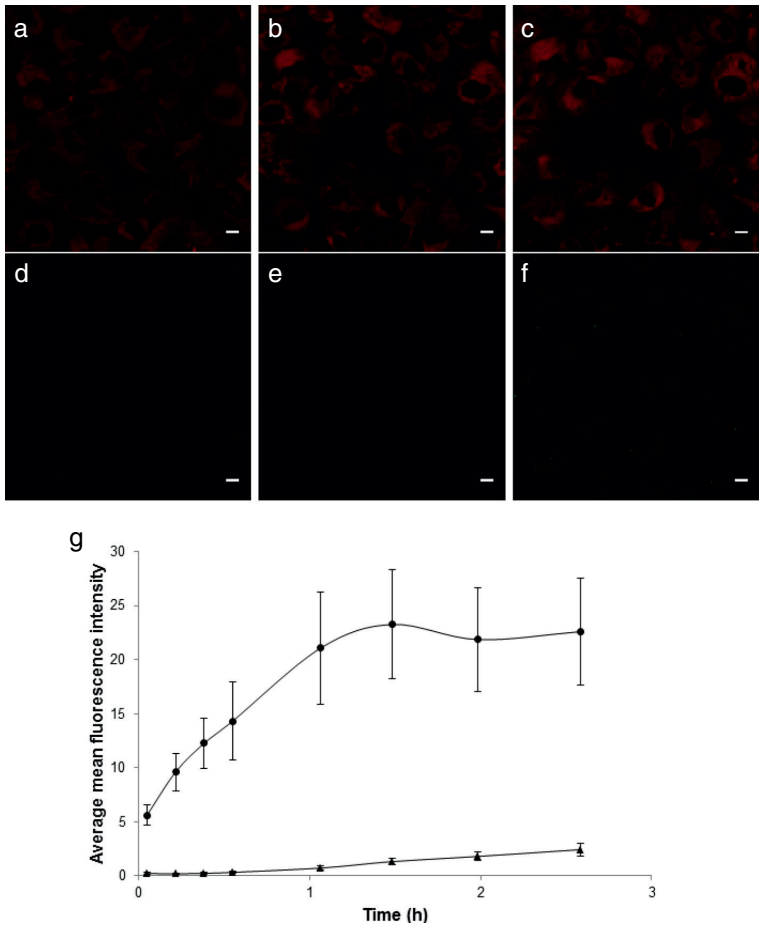

Figure 2 CLSM images of cells incubated with dual-labelled nanoparticles containing Nile Red (red) (a, b, c) and p-HTAM (green) (d, e, f) after 8 min (a, d), 64 min (b, e) and 155 min (c, f) of incubation. Scale bars are 10 um. Nile Red was excited at 540 and fluorescence detected at 650–710 nm, while p-HTAM was excited at 405 nm and detected at 470–530 nm. The average mean Nile Red (●) or p-HTAM (▲) fluorescence intensities with standard deviation from cells (n= 42-46) is shown from every 10 min for the first half hour, and from approximately every half hour after addition of particles **(g)**.

Red was binding to in the cytosol. The emission spectra were similar for cells incubated with nanoparticles and with free Nile Red. The emission spectrum from nanoparticles with encapsulated Nile Red measured by spectrophotometry has been included for comparison and showed a maximum emission at 597 nm. No spectra were found in intracellular vesicles that overlapped that of the nanoparticles.

To further exploit the spectral properties of Nile Red in the cytosol and vesicular structures, cells incubated with nanoparticles for 1 h were excited at 488 nm and 542 nm, and the fluorescence was detected at 550–590 nm and 650–720 nm, respectively (Figure 6a, b). From regions of interest representing a vesicular structure and cytosol, the excitation and emission intensity maps from the excitation-emission-scan along

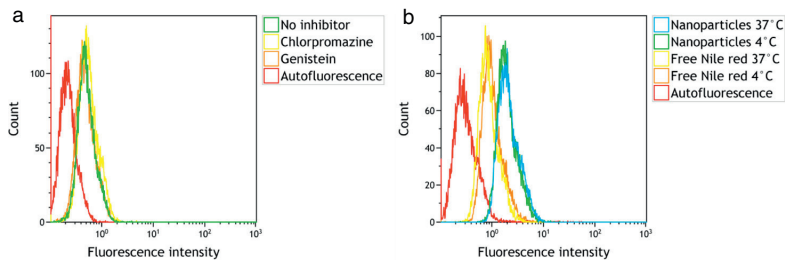

Figure 3 Flow cytometry histograms illustrating cellular uptake and inhibition of uptake of Nile Red. Cells incubated with nanoparticles for 3 h together with endocytosis inhibitors chlorpromazine or genistein **(a)** and cells incubated at 37°C or 4°C with either nanoparticles or free Nile Red for 1 h **(b)**.

with the excitation and emission spectra from the intensity maxima of the maps were determined. The excitation and emission maxima of Nile Red in the cytosol were found to be 560 nm and 627 nm, respectively (Figure 6c, d); these maxima were 527 nm and 585 nm, respectively, in vesicular structures (Figure 6e, f).

Cells with labelled early endosomes were incubated with Nile Red or nanoparticles to study co-localisation between Nile Red and early endosomes. From the CLSM images (Figure 7), we observed that there was very little or no co-localisation between Nile Red associated with vesicles (red) and early endosomes (green). The red and green spots were clearly separated from each other, and this was confirmed in the 3-dimensional z-stacks of the cells.

Release of Nile Red from nanoparticles

To determine whether Nile Red could be released from nanoparticles into the medium, a suspension of nanoparticles in cell medium was centrifuged, and the supernatant was added to cells before imaging with CLSM. It was found that Nile Red was released from the nanoparticles into the cell medium to some extent (Figure 8). From extraction experiments of Nile Red with hexadecane it was determined that approximately 50% of the total amount of Nile Red was released into the cell medium during 3 h (Table 2). The maximum release of Nile Red from nanoparticles was determined using THF which completely dissolves the particles. However, it cannot be determined to what

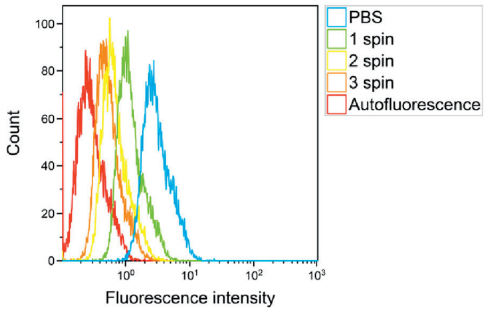

Figure 4 Flow cytometry histograms illustrating the effect of washing on cellular Nile Red fluorescence after incubation with nanoparticles. After incubation of 3 h at 37°C, the cells were rinsed 3 times with PBS and centrifuged and resuspended in medium 0 to 3 times.

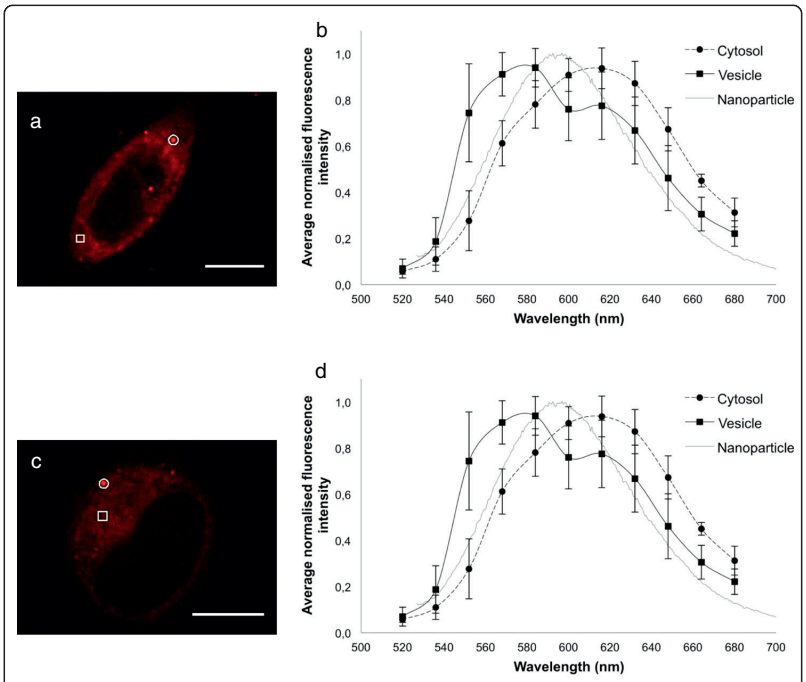

Figure 5 Representative CLSM fluorescence images and emission spectra of cells incubated with nanoparticles containing Nile Red (a, b) or free Nile Red (c, d) for 1 h. Scale bars are 10 μm. Nile Red was excited at 488 nm, and fluorescence was detected from 520 nm to 700 nm. Examples of regions of interest where emission spectra were captured from the cytosol (squares) and vesicular structures (circles) are shown. From an emission-scan with an excitation wavelength of 488 nm, the emission spectra from the cellular areas of interest are shown together with the emission spectrum from Nile Red in nanoparticles as measured by spectrophotometry **(b, d)**. In total, 8 cells incubated with nanoparticles were analysed with 12 regions of interest from the cytosol and 23 regions of interest from vesicles **(b)**. Three cells incubated with Nile Red were analysed with 6 regions of interest from the cytosol and 8 regions of interest from vesicles **(d)**.

extent the released Nile Red originated from surface-associated or encapsulated Nile Red. The values for total content of Nile Red in the nanoparticles were found to be in the expected range. Hence, the concentrations of 4 and 20 ng/ml that were chosen from the estimated Nile Red concentration range are in the same range as experimentally determined.

Discussion

The polymeric nanoparticles were found to increase both the intracellular level and uptake rate of the encapsulated model drug Nile Red compared to free Nile Red in growth medium or PBS. The delivery mechanism of encapsulated Nile Red was mainly by contact-mediated transfer directly into the cytosol and, to a smaller extent, release of Nile Red into the cell medium followed by diffusion into cells. Endocytosis of Nile Red encapsulated in nanoparticles was not observed.

There are several findings demonstrating that endocytosis was not responsible for the cellular uptake. Inhibition of clathrin-dependent and caveolae-mediated endocytosis did not result in decreased uptake of Nile Red. Furthermore, the energy-independent uptake at 4°C was similar to that at 37°C. Because all known endocytic pathways are energy-

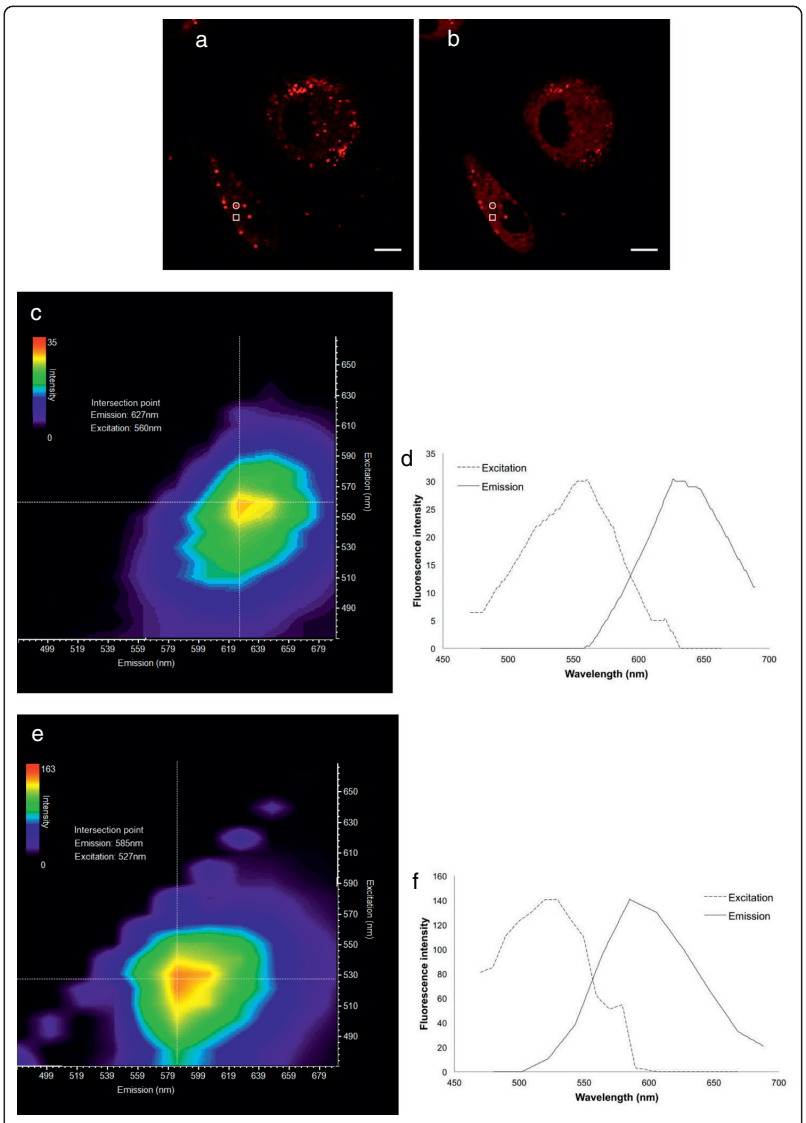

Figure 6 CLSM fluorescence imaging and excitation-emission-scans of cells incubated with nanoparticles for 1 h. Scale bars are 10 μm. Nile Red was excited at 488 nm and 542 nm with a white light laser, and fluorescence was detected at 550–590 nm **(a)** and at 650–720 nm **(b)**. An excitation-emission-scan was captured, and from the two regions of interest shown in the image, the excitation and emission intensity maps were obtained from the cytosol **(c)** and from a vesicular structure **(e)**. Corresponding excitation and emission spectra from the intensity maxima of the maps are shown in **(d)** and **(f)**, respectively.

dependent [21], cooling the cells to 4°C will inhibit endocytosis [35,36]. The high uptake of Nile Red after incubation at 4°C thus suggests that diffusion was responsible for the uptake. The very rapid uptake also supports our hypothesis that diffusion is responsible, as endocytosis-dependent uptake would not be expected to occur only minutes after

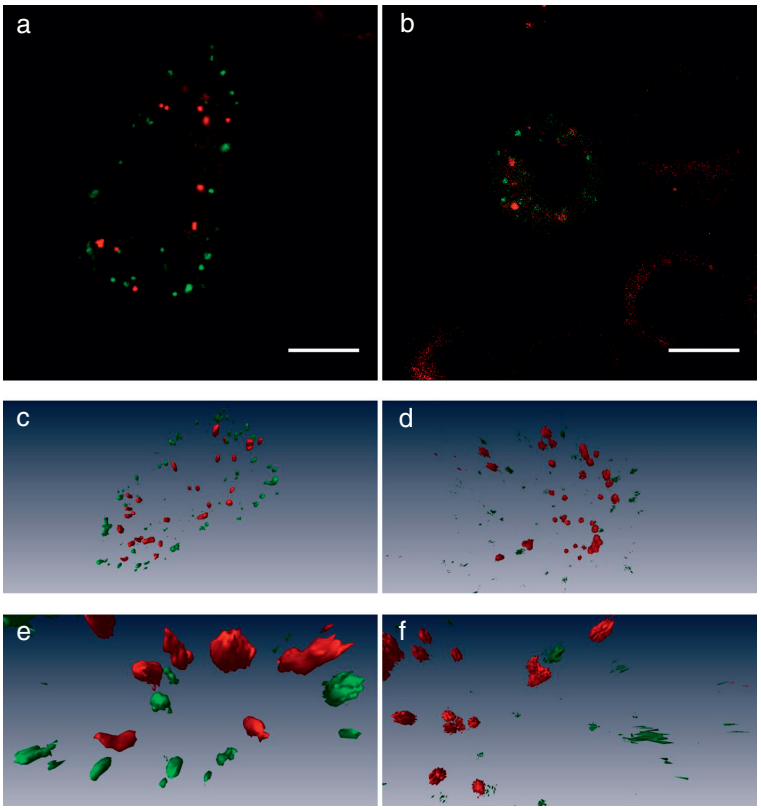

Figure 7 CLSM images of early endosomes labelled in cells incubated for 30 min with nanoparticles with encapsulated Nile Red (a) or with free Nile Red in medium (b). Below are 3-dimensional images generated from the CLSM z-stacks **(c and d)** together with zoomed in images of some vesicles **(e and f)**. Early endosomes are labelled with CellLight Early Endosomes-GFP, which is shown in green, Nile Red is shown in red. A 488 nm laser was used to excite CellLight GFP, and GFP fluorescence was detected at 500–530 nm, while Nile Red was excited at 540 nm with detection at 550–640 nm. Scale bars are 10 μm.

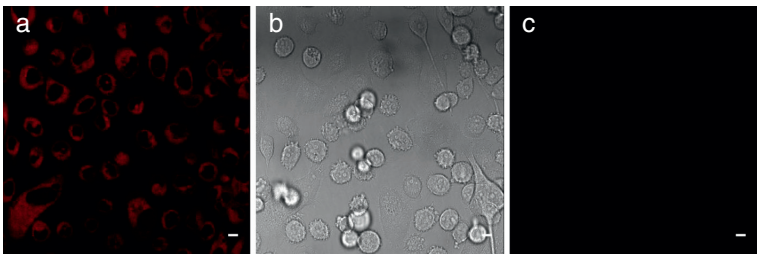

Figure 8 CLSM images of cells incubated with supernatant from a centrifuged nanoparticle suspension. Scale bars are 10 μm. Nile Red is shown in red. A fluorescence image obtained approximately 15 to 30 min after the addition of supernatant **(a)** and the corresponding transmission microscopy image **(b)** are shown together with a fluorescence image of untreated cells **(c)**. Nile Red was excited at 561 nm, and fluorescence was detected at 575–700 nm.

Table 2 The amount of Nile Red released into the cell medium as a percentage of experimentally determined total Nile Red content in the nanoparticles

Release medium	Total content	Percent released
2.9 ± 0.2 ng/ml	6.2 ng/ml	47%
12.7 ± 1.0 ng/ml	25.1 ng/ml	51%

"Release medium" is the measured amount of Nile Red released into the cell medium (n= 2) from the supernatant of centrifuged nanoparticle medium. The total amount of Nile Red in the particles was measured by dissolving the particles in THF.

addition of nanoparticles, as was observed in CLSM. That Nile Red is not taken up by endocytosis was further confirmed by synthesizing a dual-labelled nanoparticle. The dye p-HTAM was chosen since we know from experience that it leaks out of nanoparticles at a slower rate than Nile Red and that it is a FRET-pair with Nile Red. If nanoparticles were taken up by endocytosis this would be seen by FRET. However, the fluorescence from Nile Red appeared within minutes, whereas the fluorescence from p-HTAM appeared after half an hour, and during the experiment no FRET was detected. Also, the more diffuse staining of Nile Red compared with localized p-HTAM staining indicates different uptake mechanisms.

Futhermore, Nile Red was removed from cells by extensive washing, indicating that intracellular Nile Red fluorescence did not originate from Nile Red inside nanoparticles, but rather from Nile Red binding to hydrophobic molecules in the cytosol. The reduction in Nile Red fluorescence can be explained by efflux of Nile Red from cells into the surrounding medium with serum, as reported in the literature [16,31]. Low molecular weight compounds can, once the concentration gradient outside the cell is removed, efflux the cell rapidly [21]. CLSM images showed no surface-bound dye, hence this can be ruled out as source of the fluorescence reduction.

Diffuse intracellular fluorescence from Nile Red was observed throughout the cytosol and Nile Red was located in spots resembling vesicles. The diffuse staining confirms that endocytosis is not responsible for the uptake [37]. Spectral analysis revealed that Nile Red in the vesicular spots was binding to more lipophilic molecules than the diffuse Nile Red staining. These vesicles were not early endosomes, as no co-localisation between Nile Red-stained vesicles and early endosomes was observed. Nile Red is sensitive to the degree of lipid hydrophobicity [31,38]; thus, lipid droplets or membranes with a high percentage of non-polar lipids are easily identified as yellow spots, while membranes with polar lipids are stained in the red spectral range [39-41]. Red fluorescence could also occur from Nile Red binding to proteins [31]. The similarity in emission spectra from vesicles and cytosol in cells incubated with nanoparticles and cells incubated with free Nile Red suggest that intracellular Nile Red is not associated with nanoparticles and that Nile Red taken up into cells has already dissociated from the particles in the extracellular environment. Furthermore, the excitation-emission-scan suggested that the intracellular Nile Red is likely bound to something else than nanoparticles, as the excitation and emission maxima do not correspond to those of Nile Red in nanoparticles, which has excitation and emission maxima of 540 and 600 nm, respectively. Thus, the spectral analysis indicates that all Nile Red was released from the nanoparticles before reaching the cytosol. The spectral analysis is consistent with the work of Greenspan *et al.*, showing that Nile Red fluorescence above 528 nm corresponded to small discrete spots in smooth muscle cells or lipids in macrophages, whereas the diffuse Nile Red fluorescence above 590 nm probably represents intracellular membranes and organelles [31].

Nile Red being released from nanoparticles into the medium was likely due to the presence of serum proteins with hydrophobic domains in the solution, which has also been reported for poly(lactic-co-glycolic acid)(PLGA) nanoparticles and nanoemulsions [16,42]. The release of Nile Red from the polymeric nanoparticles could be due to three mechanisms: 1) Nile Red loosely associated with the particle surface may be released; 2) Nile Red may diffuse through the polymer matrix and into solution; or 3) surface erosion or degradation of the nanoparticles may result in release of Nile Red. The degradation of PBCA nanoparticles in a medium at pH 7.4 is limited during the first 3 hours [43]; thus, degradation of particles in not likely the main cause of Nile Red release. It is possible that in addition to encapsulated Nile Red, some Nile Red is also located on the surface of the nanoparticles, which is not completely removed by dialysis [44]. Thus, surface-bound Nile Red release is hard to differentiate from Nile Red diffusing from the polymer matrix.

As the cellular uptake of Nile Red dissolved in medium or PBS was found to be low and slow, it is not likely that much of the dye that is taken up in cells was first released from nanoparticles to medium. The low uptake and slow uptake kinetics of Nile Red dissolved in medium or PBS compared to Nile Red delivered by nanoparticles were most likely due to Nile Red aggregating and binding to proteins. The hydrophobic nature of the dye will cause it to spontaneously minimise contact with water. The concentration-independent uptake of Nile Red dissolved in the medium also suggests that dye-aggregates in the medium are not able to diffuse into the cells. The higher uptake rate of Nile Red from nanoparticles compared to free Nile Red thus indicates that contact-mediated transfer is the main mechanism responsible for intracellular delivery.

Collisions between nanoparticles and cells have been reported to cause contact-mediated transfer of Nile Red directly into the cytosol. Xu *et al.* showed that such a transfer can happen for Nile Red in PLGA nanoparticles [16], and others have also observed contact-based transfer of Nile Red from lipid nanoparticles [45] and nanoemulsions [30]. It has also been shown that poly(isobutylcyanoacrylate) (PIBCA) nanoparticles can increase the intracellular content of the hydrophilic drug doxorubicin compared to free drug, without being taken up by cells through endocytosis [46]. However, to the best of our knowledge, contact-mediated delivery of hydrophobic drugs between PBCA nanoparticles and cells has not been previously reported.

In accordance with other reports [44,47], this study demonstrates the importance of distinguishing between encapsulated dye and released dye when studying intracellular uptake of nanoparticles and not necessarily interpreting intracellular fluorescence as uptake of nanoparticles.

The study further illustrates that direct delivery of a hydrophobic drug into the cytosol mediated by collisions and contact between the nanoparticle and plasma membrane is an efficient way to deliver drugs normally unavailable for uptake. It has been shown *in vivo* that contact-facilitated drug delivery can be very effective, allowing a great reduction of the needed dose [48], which will also lead to less toxic effects of drugs. Thus, the polymeric PBCA nanoparticle can be used for efficient delivery of hydrophobic drugs without the drugs entering the endocytic pathway, thereby avoiding lysosomal degradation. Even though the PBCA nanoparticles must be optimised to avoid premature release of their payload into the circulation and ensure efficient delivery to the target cells, they hold great promise for delivering hydrophobic drugs to tumour cells.

Conclusion

Polymeric nanoparticles were found to mediate a higher intracellular level and a more rapid uptake of the encapsulated model drug compared to administration of the model drug alone; therefore, the nanoparticles could be used as a generic carrier of hydrophobic drugs for efficient drug delivery. The main mechanism of delivery was not via endocytosis of nanoparticles, but rather via nanoparticle-cell contact-mediated transfer directly to the cytosol and, likely to a smaller extent, release of payload from particles to the medium, followed by diffusion into cells. A contact-mediated mechanism of delivery into the cytosol could enable effective delivery of anticancer drugs directly to the intracellular molecular targets. The contact-based transfer mechanism and increased uptake of encapsulated drugs versus non-encapsulated drugs could also be exploited for the delivery of hydrophobic anticancer drugs to improve cancer therapy.

Additional files

Additional file 1: Cytotoxicity of nanoparticles after 3 h exposure measured by the Alamar Blue assay (n= 2). Cell viability is expressed as a percentage of control samples without nanoparticles, as a function of nanoparticle concentration.

Additional file 2: PC3 cells incubated with 4 or 8 ng/ml free Nile red for 1 h at 37°C. Cellular uptake measured by FCM.

Additional file 3: PC3 and HeLa cells incubated with nanoparticles for 3 h at 37°C. Cellular uptake measured by FCM.

Competing interests

The authors declare that they have no competing interests.

Authors' contributions

SS carried out cellular uptake studies and wrote the manuscript together with YM, AÅ and CD. MA carried out toxicity studies, SW participated in experiments on cellular uptake and toxicity, YM synthesized the nanoparticles, and AÅ did NMR measurements. All authors were involved in designing and planning experiments, and have read and approved the final manuscript.

Acknowledgements

The work was supported by The Central Norway Regional Health Authority and the Norwegian Research School in Medical Imaging. p-HTAM was generously provided by Marcus Bäck and K. Peter R. Nilsson, Linköping University, Sweden.

Author details

[1]Department of Physics, The Norwegian University of Science and Technology, Høgskoleringen 5, 7491 Trondheim, Norway. [2]SINTEF Materials and Chemistry, Trondheim, Norway.

Received: 1 October 2014 Accepted: 18 November 2014
Published online: 06 December 2014

References

1. Peer D, Karp JM, Hong S, Farokhzad OC, Margalit R, Langer R (2007) Nanocarriers as an emerging platform for cancer therapy. Nat Nanotechnol 2:751–760
2. Matsumura Y, Maeda H (1986) A new concept for macromolecular therapeutics in cancer chemotherapy: mechanism of tumoritropic accumulation of proteins and the antitumor agent smancs. Cancer Res 46:6387–6392
3. Bae YH, Park K (2011) Targeted drug delivery to tumors: myths, reality and possibility. J Control Release 153:198–205
4. Jokerst JV, Lobovkina T, Zare RN, Gambhir SS (2011) Nanoparticle PEGylation for imaging and therapy. Nanomedicine-UK 6:715–728
5. Kamaly N, Xiao ZY, Valencia PM, Radovic-Moreno AF, Farokhzad OC (2012) Targeted polymeric therapeutic nanoparticles: design, development and clinical translation. Chem Soc Rev 41:2971–3010
6. Drobek T, Spencer ND, Heuberger M (2005) Compressing PEG brushes. Macromolecules 38:5254–5259
7. Kenausis GL, Voros J, Elbert DL, Huang NP, Hofer R, Ruiz-Taylor L, Textor M, Hubbell JA, Spencer ND (2000) Poly(L-lysine)-g-poly(ethylene glycol) layers on metal oxide surfaces: attachment mechanism and effects of polymer architecture on resistance to protein adsorption. J Phys Chem B 104:3298–3309
8. Stolnik S, Illum L, Davis SS (1995) Long circulating microparticulate drug carriers. Adv Drug Deliv Rev 16:195–214
9. Storm G, Belliot SO, Daemen T, Lasic DD (1995) Surface modification of nanoparticles to oppose uptake by the mononuclear phagocyte system. Adv Drug Deliv Rev 17:31–48

10. Ma XW, Zhao YL, Liang XJ (2011) Theranostic nanoparticles engineered for clinic and pharmaceutics. Acc Chem Res 44:1114–1122
11. Pinto Reis C, Neufeld RJ, Ribeiro AJ, Veiga F (2006) Nanoencapsulation I. Methods for preparation of drug-loaded polymeric nanoparticles. Nanomedicine-UK 2:8–21
12. Nicolas J, Couvreur P (2009) Synthesis of poly(alkyl cyanoacrylate)-based colloidal nanomedicines. Wiley Interdiscip Rev Nanomed Nanobiotechnol 1:111–127
13. Vauthier C, Dubernet C, Fattal E, Pinto-Alphandary H, Couvreur P (2003) Poly(alkylcyanoacrylates) as biodegradable materials for biomedical applications. Adv Drug Deliv Rev 55:519–548
14. Mørch Ý, Hansen R, Berg S, Åslund AKO, Glomm WR, Eggen S, Schmid R, Johnsen H, Kubowicz S, Snipstad S, Sulheim E, Hak S, Singh G, McDonagh BH, Blom H, Davies C de L, Stenstad PM (2014) Nanoparticle-stabilized microbubbles for ultrasound-enhanced drug delivery and imaging. In review at Contrast Media Mol Imaging
15. Burke CW, Hsiang YH, Alexander E, Kilbanov AL, Price RJ (2011) Covalently linking poly(lactic-co-glycolic acid) nanoparticles to microbubbles before intravenous injection improves their ultrasound-targeted delivery to skeletal muscle. Small 7:1227–1235
16. Xu P, Gullotti E, Tong L, Highley CB, Errabelli DR, Hasan T, Cheng JX, Kohane DS, Yeo Y (2009) Intracellular drug delivery by poly(lactic-co-glycolic acid) nanoparticles, revisited. Mol Pharm 6:190–201
17. Panyam J, Labhasetwar V (2003) Biodegradable nanoparticles for drug and gene delivery to cells and tissue. Adv Drug Deliv Rev 55:329–347
18. Nam HY, Kwon SM, Chung H, Lee SY, Kwon SH, Jeon H, Kim Y, Park JH, Kim J, Her S, Oh YK, Kwon IC, Kim K, Jeong SY (2009) Cellular uptake mechanism and intracellular fate of hydrophobically modified glycol chitosan nanoparticles. J Control Release 135:259–267
19. Hillaireau H, Couvreur P (2009) Nanocarriers' entry into the cell: relevance to drug delivery. Cell Mol Life Sci 66:2873–2896
20. Taurin S, Nehoff H, Greish K (2012) Anticancer nanomedicine and tumor vascular permeability; where is the missing link? J Control Release 164:265–275
21. Panyam J, Labhasetwar V (2004) Targeting intracellular targets. Curr Drug Deliv 1:235–247
22. Iversen TG, Skotland T, Sandvig K (2011) Endocytosis and intracellular transport of nanoparticles: present knowledge and need for future studies. Nano Today 6:176–185
23. Lin Q, Chen J, Ng KK, Cao W, Zhang Z, Zheng G (2014) Imaging the cytosolic drug delivery mechanism of HDL-like nanoparticles. Pharm Res 31:1438–1449
24. Kumari A, Yadav SK, Yadav SC (2010) Biodegradable polymeric nanoparticles based drug delivery systems. Colloids Surf B Biointerfaces 75:1–18
25. Torchilin VP (2006) Recent approaches to intracellular delivery of drugs and DNA and organelle targeting. Annu Rev Biomed Eng 8:343–375
26. Panyam J, Zhou WZ, Prabha S, Sahoo SK, Labhasetwar V (2002) Rapid endo-lysosomal escape of poly(DL-lactide-co-glycolide) nanoparticles: implications for drug and gene delivery. FASEB J 16:1217–1226
27. Partlow KC, Lanza GM, Wickline SA (2008) Exploiting lipid raft transport with membrane targeted nanoparticles: a strategy for cytosolic drug delivery. Biomaterials 29:3367–3375
28. Hofmann D, Messerschmidt C, Bannwarth MB, Landfester K, Mailander V (2014) Drug delivery without nanoparticle uptake: delivery by a kiss-and-run mechanism on the cell membrane. Chem Commun 50:1369–1371
29. Lanza GM, Yu X, Winter PM, Abendschein DR, Karukstis KK, Scott MJ, Chinen LK, Fuhrhop RW, Scherrer DE, Wickline SA (2002) Targeted antiproliferative drug delivery to vascular smooth muscle cells with a magnetic resonance imaging nanoparticle contrast agent implications for rational therapy of restenosis. Circulation 106:2842–2847
30. Haynes LC, Cho MJ (1988) Mechanism of Nile Red transfer from O/W emulsions as carriers for passive-drug targeting to peritoneal-macrophages invitro. Int J Pharm 45:169–177
31. Greenspan P, Mayer EP, Fowler SD (1985) Nile Red: a selective fluorescent stain for intracellular lipid droplets. J Cell Biol 100:965–973
32. Åslund A, Sigurdson CJ, Klingstedt T, Grathwohl S, Bolmont T, Dickstein DL, Glimsdal E, Prokop S, Lindgren M, Konradsson P, Holtzman DM, Hof PR, Heppner FL, Gandy S, Jucker M, Aguzzi A, Hammarström P, Nilsson KPR (2009) Novel pentameric thiophene derivatives for in vitro and in vivo optical imaging of a plethora of protein aggregates in cerebral amyloidoses. ACS Chem Biol 4:673–684
33. Bootz A, Vogel V, Schubert D, Kreuter J (2004) Comparison of scanning electron microscopy, dynamic light scattering and analytical ultracentrifugation for the sizing of poly(butyl cyanoacrylate) nanoparticles. Eur J Pharm Biopharm 57:369–375
34. Garaiova Z, Strand SP, Reitan NK, Lelu S, Størset SØ, Berg K, Malmo J, Folasire O, Bjørkøy A, Davies C de L (2012) Cellular uptake of DNA-chitosan nanoparticles: the role of clathrin- and caveolae-mediated pathways. Int J Biol Macromol 51:1043–1051
35. Cartiera MS, Johnson KM, Rajendran V, Caplan MJ, Saltzman WM (2009) The uptake and intracellular fate of PLGA nanoparticles in epithelial cells. Biomaterials 30:2790–2798
36. Dausend J, Musyanovych A, Dass M, Walther P, Schrezenmeier H, Landfester K, Mailander V (2008) Uptake mechanism of oppositely charged fluorescent nanoparticles in HeLa cells. Macromol Biosci 8:1135–1143
37. Brambilla D, Nicolas J, Le Droumaguet B, Andrieux K, Marsaud V, Couraud PO, Couvreur P (2010) Design of fluorescently tagged poly(alkyl cyanoacrylate) nanoparticles for human brain endothelial cell imaging. Chem Commun 46:2602–2604
38. Diaz G, Melis M, Batetta B, Angius F, Falchi AM (2008) Hydrophobic characterization of intracellular lipids in situ by Nile Red red/yellow emission ratio. Micron 39:819–824
39. Brown WJ, Sullivan TR, Greenspan P (1992) Nile Red staining of lysosomal phospholipid inclusions. Histochemistry 97:349–354
40. Diaz G, Melis M, Musinu A, Piludu M, Piras M, Falchi AM (2007) Localization of MTT formazan in lipid droplets. An alternative hypothesis about the nature of formazan granules and aggregates. Eur J Histochem 51:213–218
41. Greenspan P, Fowler SD (1985) Spectrofluorometric studies of the lipid probe, Nile Red. J Lipid Res 26:781–789

42. Klymchenko AS, Roger E, Anton N, Anton H, Shulov I, Vermot J, Mely Y, Vandamme TF (2012) Highly lipophilic fluorescent dyes in nano-emulsions: towards bright non-leaking nano-droplets. Rsc Adv 2:11876–11886
43. Mørch ÝA, Eggen S, Åslund A, Sulheim E, Snipstad S, Borgos SEF, Glomm W, Singh G, Davies CDL, Stenstad PM, Schmid R (2014) Optimization and characterization of PACA nanoparticles for drug delivery and imaging. 41st Annual Meeting of the Controlled Release Society
44. Tenuta T, Monopoli MP, Kim J, Salvati A, Dawson KA, Sandin P, Lynch I (2011) Elution of labile fluorescent dye from nanoparticles during biological use. PLoS One 6:e25556
45. Petersen S, Fahr A, Bunjes H (2010) Flow cytometry as a new approach to investigate drug transfer between lipid particles. Mol Pharm 7:350–363
46. de Verdiere AC, Dubernet C, Nemati F, Poupon MF, Puisieux F, Couvreur P (1994) Uptake of doxorubicin from loaded nanoparticles in multidrug-resistant leukemic murine cells. Cancer Chemother Pharmacol 33:504–508
47. Salvati A, Aberg C, dos Santos T, Varela J, Pinto P, Lynch I, Dawson KA (2011) Experimental and theoretical comparison of intracellular import of polymeric nanoparticles and small molecules: toward models of uptake kinetics. Nanomedicine-UK 7:818–826
48. Winter PM, Neubauer AM, Caruthers SD, Harris TD, Robertson JD, Williams TA, Schmieder AH, Hu G, Allen JS, Lacy EK, Zhang HY, Wickline SA, Lanza GM (2006) Endothelial alpha(v)beta(3) integrin-targeted fumagillin nanoparticles inhibit angiogenesis in atherosclerosis. Arterioscler Thromb Vasc Biol 26:2103–2109

doi:10.1186/s12645-014-0008-4
Cite this article as: Snipstad *et al.*: Contact-mediated intracellular delivery of hydrophobic drugs from polymeric nanoparticles. *Cancer Nanotechnology* 2014 **5**:8.

Additional files

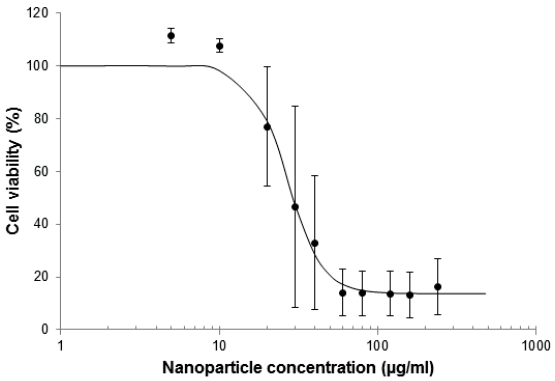

Additional file 1

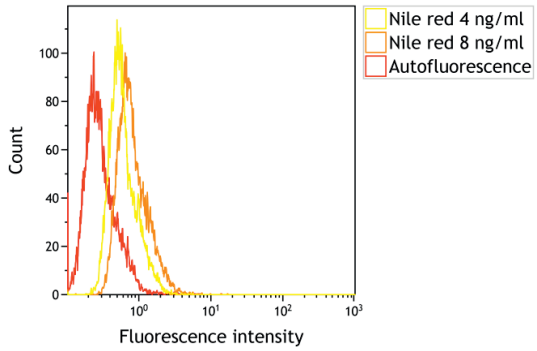

Additional file 2

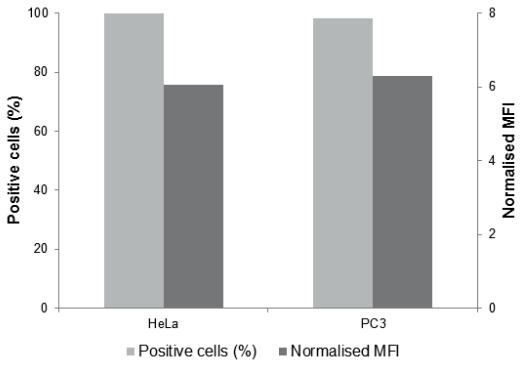

Additional file 3

Snipstad *et al. Cancer Nano (2015) 6:3*
DOI 10.1186/s12645-015-0011-4

Cancer Nanotechnology
a SpringerOpen Journal

ERRATUM Open Access

Erratum to: Contact-mediated intracellular delivery of hydrophobic drugs from polymeric nanoparticles

Sofie Snipstad[1*], Sara Westrøm[1], Yrr Mørch[2], Mercy Afadzi[1], Andreas K O Åslund[1] and Catharina de Lange Davies[1]

*Correspondence:
sofie.snipstad@ntnu.no
[1] Department of Physics, The Norwegian University of Science and Technology, Høgskoleringen 5, 7491 Trondheim, Norway
Full list of author information is available at the end of the article

Erratum to: Cancer Nanotechnology (2014) 5:8
DOI 10.1186/s12645-014-0008-4

After publication it was noted by the author that Figure 5 in the article 'Contact-mediated intracellular delivery of hydrophobic drugs from polymeric nanoparticles' (Snipstad et al. 2014) was published incorrectly. Panel b and panel d were identical. The corrected figure is shown below (Figure 5).

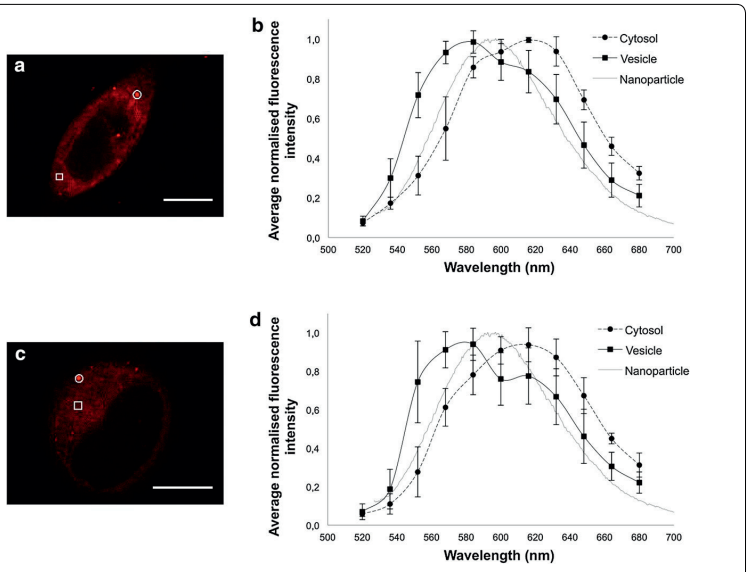

Figure 5 Representative CLSM fluorescence images and emission spectra of cells incubated with nanoparticles containing *Nile red* (**a**, **b**) or free *Nile red* (**c**, **d**) for 1 h. *Scale bars* are 10 μm. *Nile red* was excited at 488 nm, and fluorescence was detected from 520 to 700 nm. Examples of regions of interest where emission spectra were captured from the cytosol (*squares*) and vesicular structures (*circles*) are shown. From an emission-scan with an excitation wavelength of 488 nm, the emission spectra from the cellular areas of interest are shown together with the emission spectrum from *Nile Red* in nanoparticles as measured by spectrophotometry (**b**, **d**). In total, 8 cells incubated with nanoparticles were analysed with 12 regions of interest from the cytosol and 23 regions of interest from vesicles (**b**). Three cells incubated with *Nile Red* were analysed with 6 regions of interest from the cytosol and 8 regions of interest from vesicles (**d**).

Author details
[1] Department of Physics, The Norwegian University of Science and Technology, Høgskoleringen 5, 7491 Trondheim, Norway. [2] SINTEF Materials and Chemistry, Trondheim, Norway.

The online version of the original article can be found under doi:10.1186/s12645-014-0008-4.

Received: 25 June 2015 Accepted: 25 June 2015
Published online: 29 July 2015

Reference

Snipstad S, Westrøm S, Mørch Y, Afadzi M, Åslund AKO, de Lange Davies C (2014) Contact-mediated intracellular delivery of hydrophobic drugs from polymeric nanoparticles. Cancer Nanotechnol 5:8

Paper II

Cytometry
PART A
Journal of the International Society for Advancement of Cytometry

Labeling Nanoparticles: Dye Leakage and Altered Cellular Uptake

Sofie Snipstad,[1] Sjoerd Hak,[1,2] Habib Baghirov,[1] Einar Sulheim,[1,3] Ýrr Mørch,[3] Sylvie Lélu,[1] Eva von Haartman,[4,5] Marcus Bäck,[6] K. Peter R. Nilsson,[6] Andrey S. Klymchenko,[7] Catharina de Lange Davies,[1] Andreas K. O. Åslund[1]*

[1]Department of Physics, Norwegian University of Science and Technology, Trondheim, Norway

[2]Department of Circulation and Medical Imaging, Norwegian University of Science and Technology, Trondheim, Norway

[3]SINTEF Materials and Chemistry, Trondheim, Norway

[4]Pharmaceutical Sciences Laboratory, Åbo Akademi University, Turku, Finland

[5]Laboratory of Physical Chemistry, Åbo Akademi University, Turku, Finland

[6]Department of Physics, Chemistry and Biology, Linköping University, Linköping, Sweden

[7]Laboratoire de Biophotonique et Pharmacologie, UMR CNRS 7213, Université de Strasbourg, Strasbourg, France

Received 20 November 2015; Revised 2 February 2016; Accepted 17 March 2016

Grant sponsor: Central Norway Regional Health Authority; Grant sponsor: Research Council of Norway, Grant numbers: NANO2021 220005 and BIOTEK2021 226159.

Additional Supporting Information may be found in the online version of this article.

*Correspondence to: Andreas K. O. Åslund, Department of Physics, Norwegian University of Science and Technology, Høyskoleringen 5, 7491 Trondheim, Norway. E-mail: andreas.aslund@ntnu.no or andreas.aaslund@gmail.com

Conflict of interest: The authors declare no conflict of interest.

ISAC
International Society for Advancement of Cytometry

Abstract

In vitro and in vivo behavior of nanoparticles (NPs) is often studied by tracing the NPs with fluorescent dyes. This requires stable incorporation of dyes within the NPs, as dye leakage may give a wrong interpretation of NP biodistribution, cellular uptake, and intracellular distribution. Furthermore, NP labeling with trace amounts of dye should not alter NP properties such as interactions with cells or tissues. To allow for versatile NP studies with a variety of fluorescence-based assays, labeling of NPs with different dyes is desirable. Hence, when new dyes are introduced, simple and fast screening methods to assess labeling stability and NP–cell interactions are needed. For this purpose, we have used a previously described generic flow cytometry assay; incubation of cells with NPs at 4 and 37°C. Cell–NP interaction is confirmed by cellular fluorescence after 37°C incubation, and NP-dye retention is confirmed when no cellular fluorescence is detected at 4°C. Three different NP-platforms labeled with six different dyes were screened, and a great variability in dye retention was observed. Surprisingly, incorporation of trace amounts of certain dyes was found to reduce or even inhibit NP uptake. This work highlights the importance of thoroughly evaluating every dye–NP combination before pursuing NP-based applications.

Key terms

polymeric nanoparticles; nanoemulsions; liposomes; leakage; cellular uptake; flow cytometry

NANOTECHNOLOGY has enabled the development of multifunctional nanoparticles (NPs) for various medical applications. Improved diagnostics and therapy of various diseases have been achieved by incorporating contrast agents for imaging and drugs for therapy (1–5). To understand the behavior of NPs in vitro and in vivo, it is necessary to trace them. This is commonly done by encapsulation of fluorescent dyes in the NPs, which allows their detection with optical techniques (6–12). Encapsulating dyes and drugs in NPs might change the properties of both the NPs and the encapsulated molecules. This could modify surface properties (13) and change the NP charge (14) and interaction between the NPs and other molecules and cells. It is well known that changing the size, shape, or surface charge of NPs can alter the NP uptake in cells (15–17). Furthermore, the NP and the fluorescent probe do not always behave as a single unit; various examples of leakage of dyes from NPs have been reported (18–21). Fluorescence from released dyes can wrongly be interpreted as NP-fluorescence, causing the apparent cellular uptake, intracellular distribution, and biodistribution to not represent that of the NPs (18,22–24). This emphasizes the importance of choosing a fluorescent dye that is compatible with the NP-platform into which it is incorporated. Various procedures have been developed to evaluate NP-labeling stability (18,20,23,25–29). However, the majority of these assays do not include cells or serum, which could strongly affect dye release as these serve as

Published online 00 Month 2016 in Wiley Online Library (wileyonlinelibrary.com)
DOI: 10.1002/cyto.a.22853

acceptor compartments for released dye in vivo (18,24,29–33).

We have previously shown that Nile Red (NR) leaks out of poly(butyl cyanoacrylate) (PBCA)-NPs on cell contact (24), which is in line with various studies showing NR release from NPs (18,19,25,26). The hydrophobic analog NR668 was found to leak much less than NR from nanoemulsions (NEs; Ref. 18), and to be suitable for tracing the PBCA-NPs, as it was not released from the NPs until they were endocytosed and degraded (12). In search of alternative dyes for stable NP labeling and potential Förster resonance energy transfer (FRET) pairs, we performed the current study and applied a flow cytometric cell-based assay to screen a variety of dye–NP combinations. Cells were incubated with NPs at 4°C or 37°C, and cellular binding and uptake of dyes or NPs were quantified by flow cytometry (FCM). Energy depletion at 4°C (20,23) was used to determine whether cellular uptake was active or passive (22,34,35). Energy-dependent uptake (28,36) is likely the main mechanism for internalization of NPs. Thus, lack of fluorescence at 4°C indicates no leakage of the dye from the NP, whereas cellular fluorescence at 4°C might be due to dye leakage and subsequent energy-independent transfer of the dye to the cell or due to cell surface-associated NPs. No fluorescence at 37°C indicates lack of NP uptake, and the enhanced fluorescence from incubation at 4°C to 37°C results mainly from NPs being endocytosed (37) or associated with the plasma membrane (38). Thus, the assay provides information about both dye retention in NPs as well as how labeling NPs affects their association with and uptake by cells. Two different cell lines, with different propensities to take up PBCA-NPs (12), were used. The rat brain endothelial cell line RBE4 was chosen because of the reported ability of PBCA-NPs to cross the blood–brain barrier (39), and the human prostate cancer cell line PC3 was chosen because it is a widely used cancer cell line.

Six different hydrophobic fluorophores (Fig. 1) encapsulated in three commonly used NP-platforms, PBCA-NPs, NEs, and liposomes, were studied systematically. Hydrophobic dyes are often used as models for hydrophobic drugs, which because of their low solubility in water benefit from encapsulation in a nanocarrier. Three of these dyes, NR, DiI, and DiD (Fig. 1), are commercially available and commonly used for NP encapsulation. The other dyes were synthesized: NR668 designed to be more hydrophobic than NR, the oligothiophene p-HTAM has been used in a previous study of cellular uptake of NPs (12), and similarly to NR668, p-HTAH was designed to be more hydrophobic than p-HTAM. We demonstrate a large variability in NP-dye retention, and surprisingly found that encapsulation of different dyes significantly alters NP uptake in cells.

Materials and Methods

Cell Cultures

Human prostate adenocarcinoma cells (PC3; American Type Culture Collection, CRL-1435, Manassas, VA) were cultured in

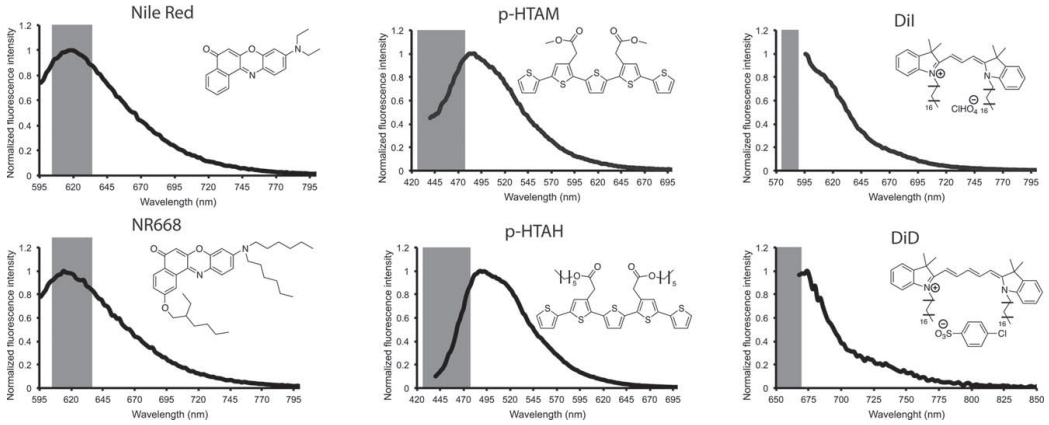

Figure 1. Chemical structures and emission spectra of the six dyes encapsulated in NPs at the excitation wavelengths used for FCM: 561 nm for NR and NR668; 405 nm for p-HTAM and p-HTAH; 561 nm for DiI and 633 nm for DiD. The detection bandpass filter used in FCM is shown in gray. The lack of overlap between the detection bandpass and spectrophotometer fluorescence spectra in some cases is due to limitations of the spectrophotometer (detection must start at least 35 nm above excitation). DiI, 1,1′-dioctadecyl-3,3,3′,3′-tetramethylindocarbocyanine perchlorate; DiD, 1,1′-dioctadecyl-3,3,3′,3′-tetramethylindodicarbocyanine 4-chlorobenzenesulfonate salt; NR668, 9-dihexylamino-2-(2-ethyl-hexyloxy)-benzo[*a*]phenoxazin-5-one; p-HTAH, (3‴-carboxymethyl-[2,2′;5′,2″;5″,2‴;5‴,2⁗]quinquethiophen-4′-yl)-acetic acid hexyl ester; p-HTAM, (3‴-carboxymethyl-[2,2′;5′,2″;5″,2‴;5‴,2⁗]quinquethiophen-4′-yl)-acetic acid methyl ester.

Dulbecco's modified Eagle's medium (DMEM; Gibco, Thermo Fischer Scientific, Waltham, MA) supplemented with 10% fetal bovine serum (Sigma-Aldrich, St. Louis, MO) at 37°C and 5% CO_2.

Rat brain endothelial cells (RBE4, a kind gift from Dr. Aschner, Vanderbilt University, Nashville, TN) were cultured at 37°C and 5% CO_2 in 1:1 mix of Ham's F-10 medium and MEM medium (both from Thermo Fischer Scientific) supplemented with 10% fetal bovine serum, 300 μg/ml G418, and 1 ng/ml basic fibroblast growth factor (Thermo Fischer Scientific).

Dyes Used to Label NPs

NR (catalog number 72485; Sigma-Aldrich), NR668 (18), p-HTAM (40), p-HTAH, DiI, and DiD (catalog numbers D-7757 and D-282, respectively; last two from Thermo Fischer Scientific) were encapsulated in NPs. The structures of the different dyes are shown in Figure 1, along with their emission spectra in NPs at the excitation wavelengths used for FCM.

Synthesis of p-HTAH

The synthesis of p-HTAH is given in Supporting Information and Supporting Scheme S1.

Synthesis of Polymeric- and Lipid-Based NPs

PBCA-NPs were synthesized by the miniemulsion process as described previously (41) and presented in the Supporting Information. Oil-in-water NEs were prepared as described previously (42) and presented in the Supporting information. Liposomes were prepared as the NEs, with the following differences: no soybean oil was added, and the sonication time was only 10 min.

Characterization of the NPs

The NPs were characterized for size and polydispersity index (PDI) using dynamic and electrophoretic light scattering (Zetasizer Nano ZS, Malvern Instruments, Westborough, MA) in 0.01 M phosphate buffer, pH 7. Surface charge (zeta-potential) was measured for the various PBCA-NPs.

To verify successful labeling of NPs, a spectrophotometer (Tecan Infinite 200Pro, Männedorf, Switzerland) was used to measure the fluorescence spectra from NPs in deionized water (20 μg/ml of PBCA for NPs, and 76 μg/ml amphiphilic lipid for liposomes and NEs) at the excitation wavelengths used in FCM.

Incubation with Cells

PC3 cells (125,000; passage 40–70) were seeded in 12-well plates (Corning, Corning, NY). After 48 h, the medium was changed, and at 72 h, the medium was replaced with medium containing 20 μg/ml PBCA-NPs or 76 μg/ml amphiphilic lipid for NEs and liposomes. The cells were incubated at 37°C or 4°C for 3 h. The cells at 4°C were preincubated at 4°C for 15 min before the addition of NPs. Before FCM, the cells were washed with PBS (4°C or 37°C) three times to remove surface-associated NPs, trypsinized, resuspended in 4°C medium, and placed on ice.

To study the association with RBE4 cells, 100,000 cells (passage 14–18) were seeded in 12-well plates (Corning). Forty-eight hours after seeding, the medium was changed to medium containing PBCA-NPs, NEs, or liposomes at concentrations given above, and the cells were prepared for FCM after 3 h incubation as described above, except that no incubation at 4°C was performed.

For coincubation of cells with NPs and free dyes, PC3 and RBE4 cells were coincubated with either DiI dye and PBCA-NPs containing p-HTAM, or with P-HTAH dye and PBCA-NPs containing NR668 for 3 h at 37°C, and the cells were prepared for FCM as described above. Cells were also incubated with the free dyes only. Concentrations of free dyes were similar to the amount of dye incorporated in NEs/liposomes.

Table 1. Physiochemical properties of the PBCA-NPs, NEs, and liposomes

	DIAMETER (NM)	PDI
PBCA-NPs	118–203	0.10–0.27
NEs	125–169	0.09–0.13
Liposomes	121–143	0.21–0.26

Quantification by FCM

Fluorescence from cells was measured using FCM (Beckman Coulter Gallios, Fullerton, CA). NR and NR668 were excited at 561 nm, and fluorescence was detected at 620 nm using a 30-nm bandpass filter. p-HTAM and p-HTAH were excited at 405 nm, and fluorescence was detected at 450 nm using a 50-nm bandpass filter. DiD was excited at 633 nm, and fluorescence was detected at 660 nm using a 20-nm bandpass filter, whereas DiI was excited at 561 nm and detected at 582 nm with a 15-nm bandpass filter.

A minimum of 10,000 cells were counted per sample, and cellular fragments and debris were excluded from the analysis by subjectively choosing a collection gate from the distribution in the side-scatter versus forward-scatter dot plot (an example is shown in Supporting Information Fig. S1). The data were analyzed using Kaluza Flow Cytometry Analysis software v1.2 (Beckman Coulter). Additional FCM details are presented in the Supporting information.

Results

The range of sizes and PDIs of the PBCA-NPs, NEs, and liposomes are presented in Table 1. All the NPs were successfully fluorescently labeled (Supporting Information Table S1). Zeta-potential of the various PBCA-NPs were −2 to −4 mV.

Dye Retention in NPs

FCM analysis of PC3 cells incubated with the various NPs at 4°C showed that dye retention varied greatly between the various dyes and NPs studied (Fig. 2A). In general, dyes were more stably incorporated into PBCA-NPs than in lipid-based NPs. The results are summarized in Table 2.

NR leaked out of all three NP platforms. The cellular fluorescence was almost the same at 4 and 37°C, indicating extensive NR release from the NPs, in accordance with our previously reported study of PBCA-NPs (24) and NEs (18).

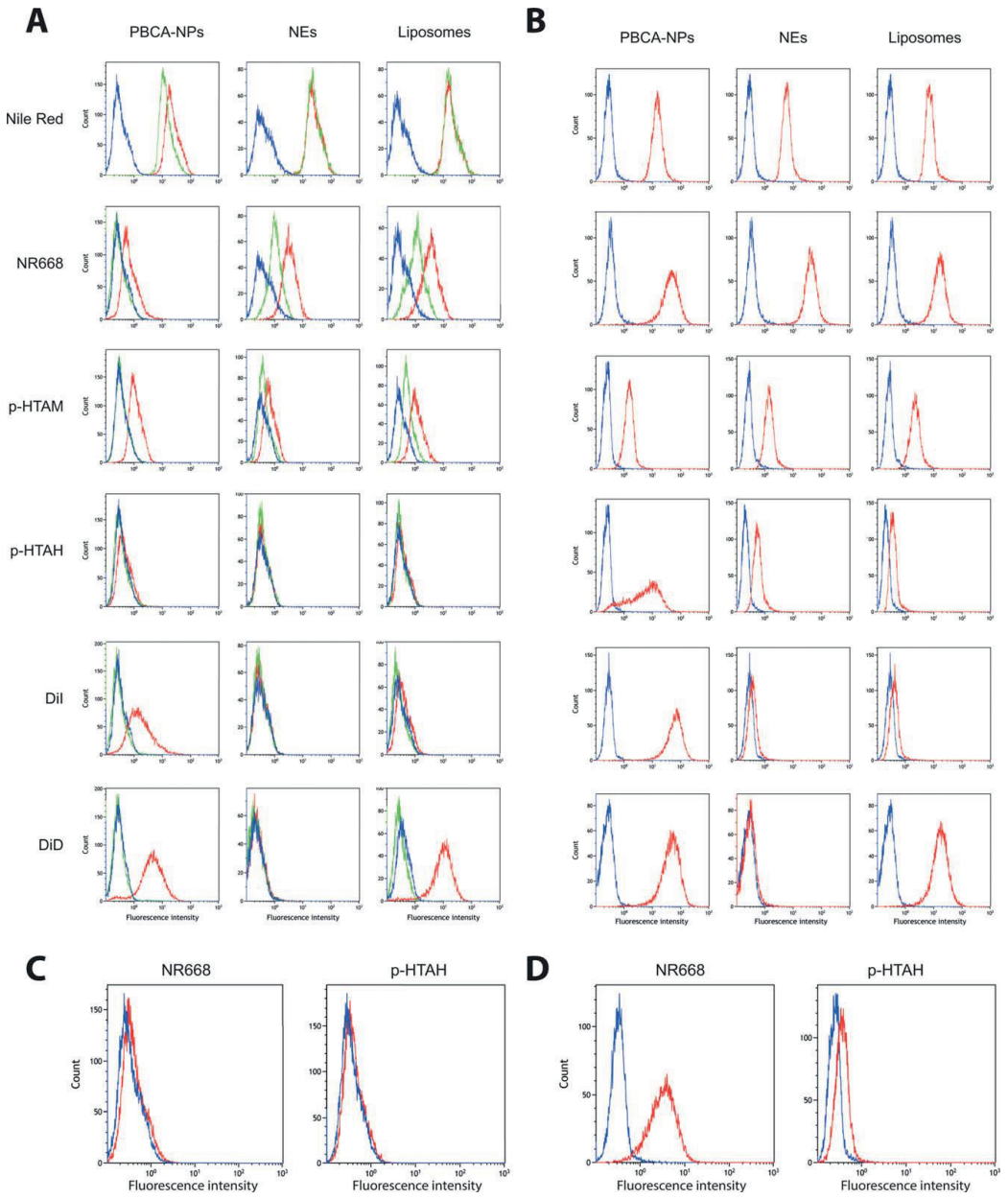

Figure 2. Flow cytometry histograms illustrating fluorescence from cells after incubation with NPs. The histograms show one representative experiment. Autofluorescence (blue), incubation at 4°C (green), and incubation at 37°C (red). Fluorescence from PC3 (**A**) or RBE4 (**B**) cells after incubation with NPs at 4 or 37°C. All experiments were repeated 2-3 times. NP association with PC3 (**C**) or RBE4 (**D**) cells, incubated with dual-labeled (p-HTAH and NR668) PBCA-NPs at 37°C. [Color figure can be viewed in the online issue, which is available at wileyonlinelibrary.com.]

Table 2. Summary of dye retention after incubation of PBCA-NPs, NEs, or liposomes with PC3 cells at 4°C

	NR	NR668	p-HTAM	p-HTAH	DiI	DiD
PBCA-NPs	+	−	−	−[a]	−	−
NEs	+	+	−	−[a]	−	−
Liposomes	+	+	+	−[a]	−	−

No fluorescence from cells denotes stable NP systems, and no dye leakage (−) and fluorescent cells indicate possible leakage (+).

[a]Retention uncertain, as free p-HTAH did not stain cells.

The hydrophobic analog of NR, NR668 (12,18), was retained within the PBCA-NPs; however, for the lipid-based NPs, some leakage was observed. The commonly used lipophilic carbocyanines, DiI and DiD, were retained within all three NP-platforms as no cellular fluorescence was detected at 4°C. p-HTAM was retained in PBCA-NPs and NEs; however, some leakage from liposomes was observed. Incubation using our newly synthesized oligothiophene, p-HTAH, which has hexane alkyl chains instead of methyl like p-HTAM, did not show any cellular fluorescence at 4°C, indicating that the dye is retained in the NPs. Surprisingly, no cellular fluorescence was detected at 37°C either, and free p-HTAH did not stain cells (data not shown).

Dye Encapsulation Can Prevent Cellular NP Uptake

The uptake of p-HTAH-NPs in PC3 cells was inhibited when compared with those with p-HTAM, even though p-HTAH-NPs showed higher or similar fluorescence intensity (Supporting Information Table S1). Similar to NPs with p-HTAH, NEs labeled with the two carbocyanines and liposomes labeled with DiI did not show cellular fluorescence at 37°C either (Fig. 2A). We have also found that PBCA-NPs encapsulating DiO were not taken up at 37°C (Supporting Information Fig. S2). NR668 and p-HTAM encapsulated in all three NPs as well as DiI and DiD in PBCA-NPs and DiD in liposomes showed higher cellular fluorescence at 37°C than 4°C, indicating endocytosis and/or surface binding of the NPs (Table 3 and Fig. 2A).

To further study the lack of cellular uptake of the various NPs at 37°C, RBE4 cells which internalizes PBCA-NP more efficiently than PC3 cells (12) were included. All PBCA-NPs, including those with encapsulated p-HTAH, showed RBE4 cell association (Table 3 and Fig. 2B). For liposomes and NEs, however, the association with RBE4 cells varied depending on the dye. NEs and liposomes labeled with NR668, p-HTAM, or p-HTAH all showed cellular fluorescence at 37°C. In accordance with the results from PC3 cells, RBE4 cells showed hardly any cellular fluorescence after incubation at 37°C with neither NEs nor liposomes labeled with DiI or NEs labeled with DiD.

To investigate whether the lack of fluorescence in PC3 cells incubated with p-HTAH encapsulated in PBCA-NPs was due to NPs not being endocytosed, PC3 and RBE4 cells were incubated at 37°C with PBCA-NPs labeled with both p-HTAH and NR668. No fluorescence from either dye was detected by FCM in PC3 cells, but both fluorophores were detected in RBE4 (Figs. 2C and 2D, respectively). This strengthened the indication that p-HTAH prevented NPs from being taken up in PC3 cells.

Furthermore, PC3 cells were coincubated at 37°C with one NP shown to be cell-associated and one NP that was not. The combinations used were NEs or liposomes with DiI (no cell association) together with PBCA-NPs containing p-HTAM (cell association), and NEs or liposomes with p-HTAH (no cell association) together with PBCA-NPs containing NR668 (cell association). Only the combination of DiI liposomes and PBCA-NPs with p-HTAM showed cellular fluorescence from PBCA-NPs. NEs with DiI and NEs/liposomes with p-HTAH thus prevented cellular association of both NR668 as well as p-HTAM-labeled PBCA-NPs (Supporting Information Fig. S3A). Interestingly, free DiI and p-HTAH did not affect cellular association of PBCA-NPs in coincubation experiments (Supporting Information Figs. 3B and 3C).

Discussion

In the current study, a rapid FCM-based screening method was used to evaluate the retention of six different dyes in three different NP-platforms. Various approaches are reported in the literature to determine the leakage of fluorescent dyes from NPs (12,18,20,23–29). Several studies are based on in vitro dye/drug release in aqueous solution by separation methods (25). Others have used lipid acceptor compartments to evaluate the dye's propensity to leak out of the NP (25–27). We chose to use a simple cell-based FCM assay which can be used with a wide variety of cell lines (20,22,24). The advantage of using FCM is that it is a rapid and quantitative method allowing screening of a large number of samples. A limitation is that the method does not separate fluorescence from internalized and surface-bound dyes or NPs (43). Thus, additional methods are needed to verify whether the NPs are internalized. Microscopy is another method used for studying uptake and distribution of NPs (18,22,37,43). However, microscopy should be used with care in the assessment of dye leakage, as free hydrophobic dyes will bind to intracellular hydrophobic molecules resulting in both diffuse and spotted staining pattern (12,24,30,33), thereby making the dye hard to separate from the fluorescence of intact NPs. In a previous study, we have shown that PBCA-NPs with NR668 are taken up in PC3 cells by endocytosis, verified by the use of time-consuming

Table 3. Summary of association (+) of PBCA-NPs, NEs, and liposomes with PC3/RBE4 cells at 37°C. No association is denoted by (−)[a]

	NR668	p-HTAM	p-HTAH	DiI	DiD
PBCA-NPs	+/+	+/+	−/+	+/+	+/+
NEs	+/+	+/+	−/+	−/−[b]	−/−
Liposomes	+/+	+/+	−/+	−/−[b]	+/+

[a]NPs with NR are not included in the table. NR was not retained in the NPs, whereas the majority of the other NPs resulted in increased fluorescence at 37°C when compared with 4°C, indicating NP–cell association.

[b]Hardly any association with RBE4.

intracellular spectral microscopy and fluorescence-lifetime imaging microscopy (12). This illustrates that although highly useful, microscopy is not suitable for rapid screening of a large number of samples. In several other studies, FRET has been used to study release from NPs (18,21,28). Although this represents an elegant approach and allows for real-time in vivo follow-up of dye release, it requires successful incorporation of two dyes, one donor and one acceptor, and extensive optimization and control experiments.

Dye Retention and Leakage from NPs

In the current study, some dyes were found to be retained in the NPs (NR668 for PBCA-NPs, p-HTAM for PBCA-NPs and NEs, and DiD and DiI in all NPs). In case of the other fluorophores (NR for all NPs, NR668 for NEs and liposomes, and p-HTAM for liposomes), dye leakage could not be ruled out. These results demonstrate that dye retention is highly dependent on both dye and NP-platform and that thorough evaluation of labeling stability is critical.

When no fluorescence was observed at 4°C, we concluded that the dyes are retained in the NPs. This is correct when the assumption that free dyes would enter the cells via energy-independent processes holds. The free dyes NR, NR668, and p-HTAM have indeed been confirmed to stain cells in our previous work using microscopy (12,24). In addition, DiD and DiI are known to diffuse across the plasma membrane (28,44,45). Thus, DiI and DiD in NEs and liposomes are most likely retained, as any leakage of the dyes from NPs would presumably stain the cells. However, free p-HTAH was not found to label cells, and it is possible that not even a DMSO formulation is enough to solubilize the very hydrophobic p-HTAH in aqueous solutions, thus retention of this fluorophore by the NPs is uncertain.

The problem of fluorophore leakage has also been recognized by others, and their observations are largely in agreement with our results (18,19,21,22,25,26,28,46–48). NR has repeatedly been shown to leak out of various NPs (18,19,25,26), and we concluded in a previous study that NR was taken up by cells through contact-mediated transfer within minutes after addition of PBCA-NPs (24). The retention of a dye in a NP is largely governed by hydrophobic and electrostatic interactions between the dye and NP. Its compatibility with the hydrophobic phase in the NPs (polymer core in the case of PBCA-NPs, oil core and phospholipid monolayer in the case of NE, and phospholipid bilayer in the case of liposomes) plays an important role in dye release. For dyes which do not leak from the NPs, the dye is likely to have a strong preference for the hydrophobic phase and to be confined within the hydrophobic compartment. Thus, it is not released from the NP until the NP degrades. A dye that is not retained efficiently is presumably more present at the NP-surface when compared with nonleaky dyes (18). Accordingly, these dyes are present in the shell of the NP, and a continuous release not associated with NP degradation may occur.

Dye Encapsulation Can Prevent Cellular NP Uptake

The study of cellular uptake of NPs is commonly done by labeling the NPs with fluorescent dyes. In accordance with this practice, we studied the uptake of PBCA-NP in PC3 and RBE4 cells, and to our surprise found that when encapsulating some dyes, no cellular uptake was detected. Thus, we performed the systematic study presented here. Both the carbocyanines DiI and DiD and the oligothiophene p-HTAH inhibited cellular uptake of NPs. To further study this inhibition, we encapsulated both NR668 (that is taken up by PC3-cells) and p-HTAH (that is not taken up) in PBCA-NP. As a result, the NP was not taken up in PC3 cells; however, a clear uptake in RBE4 was still detected, in accordance with the uptake behavior of the individually encapsulated dyes. Next, PC3 cells were coincubated with an NP that was taken up and one that was not. In three of the four combinations, uptake of the NPs was inhibited by the NP-dye that inhibits uptake. The mechanisms underlying the observed effect are not clear. The reduced cellular uptake was not due to the size or zeta-potential of the NPs; the encapsulation of the dyes did not change the size of the NPs significantly, and for all the PBCA-NPs, the zeta-potential was -2 to -4 mV.

The chemical composition and structure of the encapsulated dye might affect the cellular uptake. The common denominators for NP-encapsulated dyes that inhibit cellular uptake are long alkyl chains (hexyl or longer) and quartenary amines. However, NR668 has both these functionalities but did not inhibit cellular uptake of NPs. The carbocyanines on the other hand, having quartenary amines, inhibited cellular uptake of lipid-based NPs. This inhibition also depended on the interaction with the NPs, as cellular uptake of liposomes with DiD was not inhibited. To fully elucidate how the NP interaction with the cell changes on a change of dyes would require a more thorough study of both the NP chemistry and the processes involved in endocytosis.

Conclusions

A systematic study of different hydrophobic dyes encapsulated in three different NP-platforms has been performed. Dye retention was found to vary greatly between the various dyes and NPs studied. Moreover, we have shown that the choice of dye may also impact the uptake behavior of the NP. The implications of our observations are significant for anyone that is studying the properties of NPs with fluorescence-based methods or when trace amounts of a fluorophore are replaced with high payloads of drugs for drug delivery purposes. Our findings highlight the importance of evaluating every combination of encapsulated agent and NP-platform before making conclusions about interactions with cells and tissue or payload release.

Acknowledgments

The authors thank Anne Rein Hatletveit, Lars Erik Parnas, Sidsel Sundseth, and Kristin Grendstad Sæterbø for technical support. The authors also thank Henkel Loctite, Cremer, and Huntsman for kindly providing cyanoacrylate, Miglyol, and Jeffamine, respectively.

Literature Cited

1. Murthy SK. Nanoparticles in modern medicine: State of the art and future challenges. Int J Nanomed 2007;2:129–141.
2. Naahidi S, Jafari M, Edalat F, Raymond K, Khademhosseini A, Chen P. Biocompatibility of engineered nanoparticles for drug delivery. J Control Release 2013;166: 182–194.
3. Salata O. Applications of nanoparticles in biology and medicine. J Nanobiotechnol 2004;2:3.
4. Etheridge ML, Campbell SA, Erdman AG, Haynes CL, Wolf SM, McCullough J. The big picture on nanomedicine: The state of investigational and approved nanomedicine products. Nanomedicine 2013;9:1–14.
5. Skotland T, Iversen TG, Sandvig K. Development of nanoparticles for clinical use. Nanomedicine 2014;9:1295–1299.
6. Licha K, Olbrich C. Optical imaging in drug discovery and diagnostic applications. Adv Drug Deliv Rev 2005;57:1087–1088.
7. Sokolova V, Epple M. Synthetic pathways to make nanoparticles fluorescent. Nanoscale 2011;3:1957–1962.
8. Elsabahy M, Wooley KL. Design of polymeric nanoparticles for biomedical delivery applications. Chem Soc Rev 2012;41:2545–2561.
9. Liong M, Lu J, Kovochich M, Xia T, Ruehm SG, Nel AE, Tamanoi F, Zink JI. Multifunctional inorganic nanoparticles for imaging, targeting, and drug delivery. ACS Nano 2008;2:889–896.
10. Torchilin VP. Fluorescence microscopy to follow the targeting of liposomes and micelles to cells and their intracellular fate. Adv Drug Deliv Rev 2005;57:95–109.
11. Hak S, Helgesen E, Hektoen HH, Huuse EM, Jarzyna PA, Mulder WJ, Haraldseth O, Davies Cde L. The effect of nanoparticle polyethylene glycol surface density on ligand-directed tumor targeting studied in vivo by dual modality imaging. ACS Nano 2012;6:5648–5658.
12. Sulheim E, Baghirov H, von Haartman E, Bøe A, Åslund AK, Mørch Y, Davies CL. Cellular uptake and intracellular degradation of poly(alkyl cyanoacrylate) nanoparticles. J Nanobiotechnol 2016;14:1.
13. Panyam J, Labhasetwar V. Biodegradable nanoparticles for drug and gene delivery to cells and tissue. Adv Drug Deliv Rev 2003;55:329–347.
14. Sahoo SK, Panyam J, Prabha S, Labhasetwar V. Residual polyvinyl alcohol associated with poly(d,l-lactide-*co*-glycolide) nanoparticles affects their physical properties and cellular uptake. J Control Release 2002;82:105–114.
15. He C, Hu Y, Yin L, Tang C, Yin C. Effects of particle size and surface charge on cellular uptake and biodistribution of polymeric nanoparticles. Biomaterials 2010;31: 3657–3666.
16. Champion JA, Katare YK, Mitragotri S. Particle shape: A new design parameter for micro- and nanoscale drug delivery carriers. J Control Release 2007;121:3–9.
17. Ma N, Ma C, Li C, Wang T, Tang Y, Wang H, Moul X, Chen Z, Hel N. Influence of nanoparticle shape, size, and surface functionalization on cellular uptake. J Nanosci Nanotechnol 2013;13:6485–6498.
18. Klymchenko AS, Roger E, Anton N, Anton H, Shulov I, Vermot J, Mely Y, Vandamme TF. Highly lipophilic fluorescent dyes in nano-emulsions: Towards bright non-leaking nano-droplets. RSC Adv 2012;2:11876–11886.
19. Xu P, Gullotti E, Tong L, Highley CB, Errabelli DR, Hasan T, Cheng JX, Kohane DS, Yeo Y. Intracellular drug delivery by poly(lactic-*co*-glycolic acid) nanoparticles, revisited. Mol Pharm 2009;6:190–201.
20. Andreozzi P, Martinelli C, Carney RP, Carney TM, Stellacci F. Erythrocyte incubation as a method for free-dye presence determination in fluorescently labeled nanoparticles. Mol Pharm 2013;10:875–882.
21. Simonsson C, Bastiat G, Pitorre M, Klymchenko AS, Bejaud J, Mely Y, Benoit JP. Inter-nanocarrier and nanocarrier-to-cell transfer assays demonstrate the risk of an immediate unloading of dye from labeled lipid nanocapsules. Eur J Pharm Biopharm 2016;98:47–56.
22. Salvati A, Aberg C, dos Santos T, Varela J, Pinto P, Lynch I, Dawson KA. Experimental and theoretical comparison of intracellular import of polymeric nanoparticles and small molecules: Toward models of uptake kinetics. Nanomedicine 2011;7: 818–826.
23. Tenuta T, Monopoli MP, Kim J, Salvati A, Dawson KA, Sandin P, Lynch I. Elution of labile fluorescent dye from nanoparticles during biological use. PLoS One 2011;6: e25556.
24. Snipstad S, Westrøm S, Mørch Y, Afadzi M, Åslund AK, Davies CL. Contact-mediated intracellular delivery of hydrophobic drugs from polymeric nanoparticles. Cancer Nanotechnol 2014;5:8.
25. Petersen S, Fahr A, Bunjes H. Flow cytometry as a new approach to investigate drug transfer between lipid particles. Mol Pharm 2010;7:350–363.
26. Bastiat G, Pritz CO, Roider C, Fouchet F, Lignieres E, Jesacher A, Glueckert R, Ritsch-Marte M, Schrott-Fischer A, Saulnier P, et al. A new tool to ensure the fluorescent dye labeling stability of nanocarriers: A real challenge for fluorescence imaging. J Control Release 2013;170:334–342.
27. Shabbits JA, Chiu GN, Mayer LD. Development of an in vitro drug release assay that accurately predicts in vivo drug retention for liposome-based delivery systems. J Control Release 2002;84:161–170.
28. Chen HT, Kim SW, Li L, Wang SY, Park K, Cheng JX. Release of hydrophobic molecules from polymer micelles into cell membranes revealed by Forster resonance energy transfer imaging. P Natl Acad Sci USA 2008;105:6596–6601.
29. Zhao Y, van Rooy I, Hak S, Fay F, Tang J, Davies Cde L, Skobe M, Fisher EA, Radu A, Fayad ZA, et al. Near-infrared fluorescence energy transfer imaging of nanoparticle accumulation and dissociation kinetics in tumor-bearing mice. ACS Nano 2013;7: 10362–10370.
30. Greenspan P, Mayer EP, Fowler SD. Nile red: A selective fluorescent stain for intracellular lipid droplets. J Cell Biol 1985;100:965–973.
31. Greenspan P, Fowler SD. Spectrofluorometric studies of the lipid probe, Nile Red. J Lipid Res 1985;26:781–789.
32. Skajaa T, Zhao Y, van den Heuvel DJ, Gerritsen HC, Cormode DP, Koole R, van Schooneveld MM, Post JA, Fisher EA, Fayad ZA, et al. Quantum dot and Cy5.5 labeled nanoparticles to investigate lipoprotein biointeractions via Forster resonance energy transfer. Nano Lett 2010;10:5131–5138.
33. Brown WJ, Sullivan TR, Greenspan P. Nile Red staining of lysosomal phospholipid inclusions. Histochemistry 1992;97:349–354.
34. Verma A, Uzun O, Hu Y, Hu Y, Han HS, Watson N, Chen S, Irvine DJ, Stellacci F. Surface-structure-regulated cell-membrane penetration by monolayer-protected nanoparticles. Nat Mater 2008;7:588–595.
35. Mahmoudi M, Abdelmonem AM, Behzadi S, Clement JH, Dutz S, Ejtehadi MR, Hartmann R, Kantner K, Linne U, Maffre P, et al. Temperature: The "ignored" factor at the NanoBio interface. ACS Nano 2013;7:6555–6562.
36. Dausend J, Musyanovych A, Dass M, Walther P, Schrezenmeier H, Landfester K, Mailander V. Uptake mechanism of oppositely charged fluorescent nanoparticles in HeLa cells. Macromol Biosci 2008;8:1135–1143.
37. Brambilla D, Nicolas J, Le Droumaguet B, Andrieux K, Marsaud V, Couraud PO, Couvreur P. Design of fluorescently tagged poly(alkyl cyanoacrylate) nanoparticles for human brain endothelial cell imaging. Chem Commun (Camb) 2010;46: 2602–2604.
38. Lesniak A, Salvati A, Santos-Martinez MJ, Radomski MW, Dawson KA, Aberg C. Nanoparticle adhesion to the cell membrane and its effect on nanoparticle uptake efficiency. J Am Chem Soc 2013;135:1438–1444.
39. Weiss CK, Kohnle MV, Landfester K, Hauk T, Fischer D, Schmitz-Wienke J, Mailander V. The first step into the brain: Uptake of NIO-PBCA nanoparticles by endothelial cells in vitro and in vivo, and direct evidence for their blood–brain barrier permeation. ChemMedChem 2008;3:1395–1403.
40. Åslund A, Sigurdson CJ, Klingstedt T, Grathwohl S, Bolmont T, Dickstein DL, Glimsdal E, Prokop S, Lindgren M, Konradsson P, et al. Novel pentameric thiophene derivatives for in vitro and in vivo optical imaging of a plethora of protein aggregates in cerebral amyloidoses. ACS Chem Biol 2009;4:673–684.
41. Mørch Y, Hansen R, Berg S, Hansen Y, Åslund A, Schmid R, Kubowicz S, Johnsen H, Eggen S, Blom H, et al. Nanoparticle-stabilized microbubbles for multimodal imaging and drug delivery. Contrast Media Mol Imaging 2015;10:356–366.
42. Jarzyna PA, Skajaa T, Gianella A, Cormode DP, Samber DD, Dickson SD, Chen W, Griffioen AW, Fayad ZA, Mulder WJ. Iron oxide core oil-in-water emulsions as a multifunctional nanoparticle platform for tumor targeting and imaging. Biomaterials 2009;30:6947–6954.
43. Gottstein C, Wu GH, Wong BJ, Zasadzinski JA. Precise quantification of nanoparticle internalization. ACS Nano 2013;7:4933–4945.
44. Cheng C, Trzcinski O, Doering LC. Fluorescent labeling of dendritic spines in cell cultures with the carbocyanine dye "DiI". Front Neuroanat 2014;8:30.
45. Bananis E, Nath S, Gordon K, Satir P, Stockert RJ, Murray JW, Wolkoff AW. Microtubule-dependent movement of late endocytic vesicles in vitro: Requirements for Dynein and Kinesin. Mol Biol Cell 2004;15:3688–3697.
46. Sun X, Li F, Wang Y, Liang W. Cellular uptake and elimination of lipophilic drug delivered by nanocarriers. Pharmazie 2010;65:737–742.
47. Hofmann D, Messerschmidt C, Bannwarth MB, Landfester K, Mailander V. Drug delivery without nanoparticle uptake: Delivery by a kiss-and-run mechanism on the cell membrane. Chem Commun 2014;50:1369–1371.
48. Chan M, Schopf E, Sankaranarayanan J, Almutairi A. Iron oxide nanoparticle-based magnetic resonance method to monitor release kinetics from polymeric particles with high resolution. Anal Chem 2012;84:7779–7784.

Supplementary:

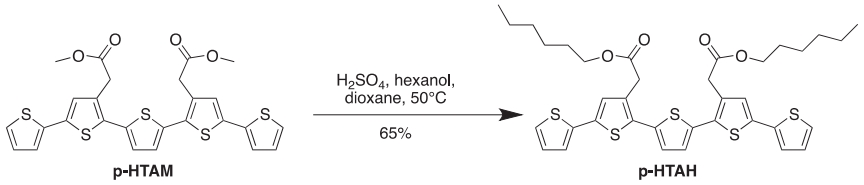

Scheme 1: Synthesis of p-HTAH.

Synthesis of p-HTAH

All chemicals were purchased from Sigma-Aldrich. p-HTAM (0.085 g, 0.153 mmol) was dissolved in dry dioxane (4 mL). Conc. H_2SO_4 (0.045 mL, 0.844 mmol) was added and the solution was heated at 50 °C overnight. The reaction was quenched with saturated $NaHCO_3$ (aq) and extracted with dichloromethane. The organic phase was dried, filtered and concentrated. Purification by high pressure liquid chromatography gave p-HTAH (0.069 g, 65%) as an orange glue. ^{1}H NMR (300 MHz, $CDCl_3$) δ 0.85 (t, J = 7.0 Hz, 6H), 1.18-1.40 (m, 12H), 1.54-1.70 (m, 4H), 3.76 (s, 4H), 4.14 (t, J = 6.7 Hz, 4H), 7.01 (dd, J = 5.1, 3.6 Hz, 2H), 7.13 (s, 2H), 7.17 (dd, J = 3.6, 1.1 Hz, 2H), 7.19 (s, 2H), 7.22 (dd, J = 5.1, 1.1 Hz, 2H); ^{13}C NMR (75 MHz, $CDCl_3$) δ 14.1, 22.7, 25.7, 28.7, 31.5, 35.9, 65.5, 124.1, 124.9, 126.9, 127.4, 128.0, 131.3, 131.6, 135.6, 136.3, 136.8, 170.8. ESI-MS m/z 697.2 [$(M+H)^+$ calcd for $C_{36}H_{41}O_4S_5^+$ 697.2].

Synthesis of PBCA-NPs

PBCA-NPs were synthesized by the miniemulsion process as described previously (41). Briefly, an oil-in-water emulsion was prepared by mixing a monomer oil phase with a water phase containing a PEG stabilizer (Brij®L23, Sigma-Aldrich). The monomer phase contained butyl cyanoacrylate (BCA, a kind gift from Henkel Loctite, Dublin, Ireland), a neutral oil as co-stabilizer (Miglyol® 810N, kind gift from Cremer, Hamburg, Germany), a radical initiator (V65, Azobisdimetyl valeronitril, Wako, Osaka, Japan) and 0.5 wt% of the fluorescent dye(s). After emulsifying using sonication (Branson Ultrasonifier, Danbury, USA), Jeffamine®M-2070 (a polyetheramine with a 19-unit PEG chain, Huntsman Corporation, Salt Lake City, USA), was added to initiate the polymerization at the droplet surface. Polymerization was carried out at room temperature overnight. Potential unreacted monomer in the particle core was polymerized by increasing the temperature to 50°C for 8 h, activating free radical polymerization by V65. The particles were rinsed by extensive dialysis and stored in the dark at 4°C.

Synthesis of NEs

Oil-in-water NEs were prepared through a method based on swift evaporation of organic solvents as previously described (42). The amphiphilic lipids 1,2-disteraoyl-sn-glycero-3-phosphocholine (DSPC), cholesterol, and 1,2-disteraoyl-sn-glycerol-3-phosphoethanolamine-N-[methoxy(polyethylene glycol)-2000] (PEG–DSPE) (all from Avanti Polar Lipids, Alabaster, USA) were used at a molar ratio of 62:33:5. 0.5 mol% fluorophore and 2.6 mg of soybean oil per µmole of the amphiphilic lipid mixture were included. All components (typically 5 µmole of amphiphilic lipids) were combined in chloroform and dripped into 4.5 ml deionized H_2O at 72°C under vigorous magnetic stirring (1300 rpm). The chloroform evaporated instantly and the obtained crude emulsions were tip-sonicated for 20 min (Heat System Ultrasonics, W-225R, duty cycle 35%, 30 W and 20 kHz) in a water bath in order to maintain room temperature. The NEs were stored in the dark at 4°C until use.

Additional information about FCM experiments

The instrument was manufactured 2009 and installed the same year. The optical filters used are original. The instrument has been serviced at a yearly basis. Before each experiment a quality control protocol was performed with to verify laser stability with Flow-check Pro Fluorospheres (A63493 - Beckmann Coulter).

The following lasers were used:
488nm default, 405nm, 561nm, 633nm
Photo multiplier tubes (PMT) were used as analyte detectors (FL2 582 nm, BP 15 nm; FL3 620 nm, BP 30 nm; FL6 660 nm, BP 20 nm; FL9 450 nm, BP 50 nm).

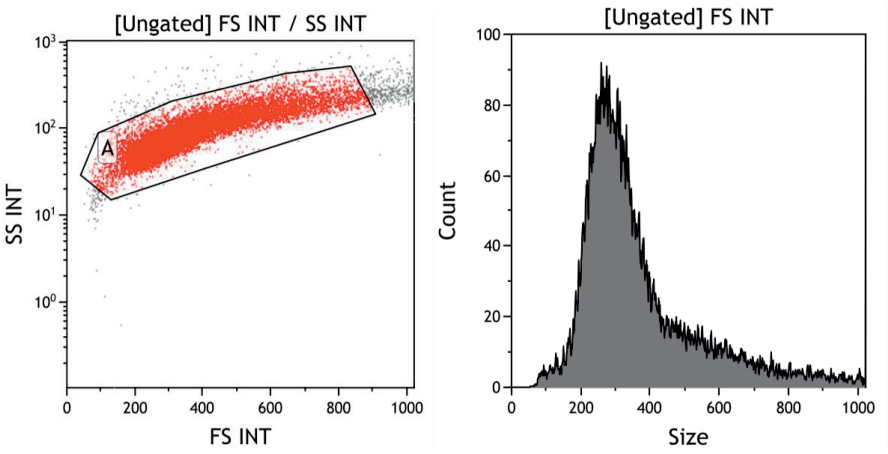

Figure 1: Example of a collection gate in the side-scatter versus forward-scatter dot plot and the corresponding histogram.

Table 1: Fluorescence intensity from PBCA-NPs, liposomes and NEs measured by spectrophotometer. Excitation/emission wavelengths were as follows: 561/620 nm for NR and NR668, 405/450 nm for p-HTAH and p-HTAH, 633/668 nm for DiD and 561/596 nm for DiI. Average and standard deviation are shown, n = 2-4.

	NR	NR668	p-HTAM	p-HTAH	DiI	DiD
PBCA-NPs	44473±431	34178±745	9130±104	43422±341	44796±110	46272±400
NEs	46352±168	61432±2	8965±43	11026±158	44101±227	46005±32[a]
Liposomes	12995±413	3014±39	5600±3	5367±34	53110±162	21132±193
Water	315±11	315±11	4726±181	4726±181	174±6	719±41

[a]Measured at lower gain compared to the other DiD-NPs

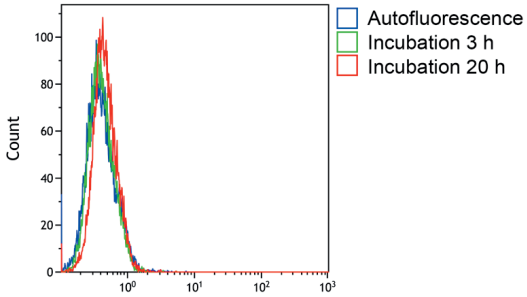

Figure 2: Flow cytometric histograms illustrating fluorescence from PC3 cells incubated with DiO-PBCA-NPs for 3 h and 20 h.

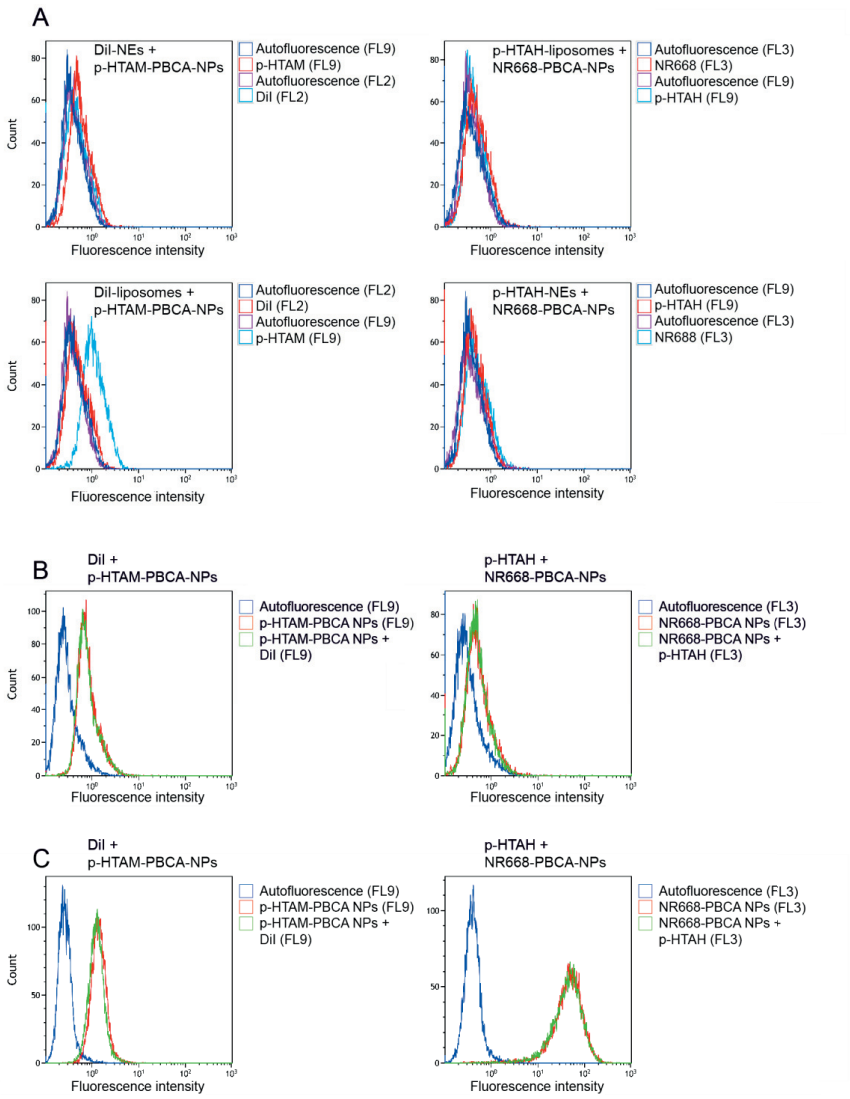

Figure 3: Flow cytometric histograms from co-incubation of NEs/liposomes with DiI/p-HTAH and PBCA-NPs with p-HTAM/NR668 in PC3 cells (A), and co-incubation of free dyes (DiI/p-HTAH) with PBCA-NPs with p-HTAM/NR668 in PC3 (B) and RBE4 cells (C).

Paper III

Ultrasound improves the delivery and therapeutic effect of nanoparticle-stabilized microbubbles in breast cancer xenografts

Sofie Snipstad[a,*], Sigrid Berg[b,c], Ýrr Mørch[d], Astrid Bjørkøy[a], Einar Sulheim[a,d], Rune Hansen[b,c], Ingeborg Grimstad[a], Annemieke van Wamel[a], Astri F. Maaland[a], Sverre H. Torp[e,f], Catharina de Lange Davies[1]

[a]*Department of Physics, Norwegian University of Science and Technology (NTNU), Høgskoleringen 5, 7491 Trondheim, Norway;*
[b]*SINTEF Technology and Society, P.O. Box 4760 Sluppen, 7465 Trondheim, Norway;*
[c]*Department of Circulation and Medical Imaging, P.O. Box 8905, 7491 NTNU, Trondheim, Norway;*
[d]*SINTEF Materials and Chemistry, P.O. Box 4760 Sluppen, 7465 Trondheim, Norway;*
[e]*Department of Laboratory Medicine, Children's and Women's Health, NTNU, P.O. Box 8905, N-7491 Trondheim, Norway;*
[f]*Department of Pathology, St. Olavs University Hospital, Postboks 3250 Sluppen,7006 Trondheim, Norway*

[*]*Corresponding author: sofie.snipstad@ntnu.no, phone 0047 93223938*

Abstract
Encapsulation of drugs in nanoparticles can improve efficacy and reduce toxicity compared to conventional chemotherapy. However, delivery of nanoparticles is often insufficient and heterogeneous, due to various biological barriers and uneven tumor perfusion. A unique multifunctional drug delivery system was investigated, consisting of microbubbles stabilized by polymeric nanoparticles (NPMBs), enabling ultrasound-mediated drug delivery. The aim was to examine mechanisms of ultrasound-mediated delivery, and to determine if increased tumor uptake had a therapeutic benefit. Cellular uptake and toxicity, circulation and biodistribution were characterized. After intravenous injection of NPMBs in mice, tumors were treated with ultrasound of various pressures and pulse lengths, and distribution of nanoparticles was imaged on tumor sections. No effects of low pressures were observed, whereas complete bubble destruction at higher pressures improved tumor uptake 2.3 times, without tissue damage. An enhanced therapeutic effect was demonstrated in a promising proof-of-concept study, where all tumors showed regression into complete remission.

Keywords: drug delivery, focused ultrasound, microbubbles, nanomedicine, poly(alkyl cyanoacrylate), cabazitaxel, triple negative breast cancer

Introduction

Normally in chemotherapy, only a small fraction of the injected dose, 0.01 to 0.001% (Gerber, et al. 2009, Kurdziel, et al. 2011), reaches the tumor in patients. Most of the dose accumulates in healthy tissue causing severe side-effects or is rapidly excreted. Nanoparticles (NPs) have attracted great attention in drug delivery and diagnostics (Lammers, et al. 2010), especially in cancer. Leaky tumor vasculature (Hanahan and Weinberg 2011) and nonfunctional lymphatics result in the enhanced permeability and retention (EPR) effect, which allows NPs to selectively extravasate and accumulate in tumors, while the healthy tissue is less exposed (Maeda, et al. 2000). Incorporating drugs in NPs can therefore potentially improve pharmacokinetics, increase efficacy and reduce toxicity of the drug compared to conventional chemotherapy, resulting in reduced dose-limiting side effects. Furthermore, potent drugs with poor solubility or high toxicity, which are a hurdle for the pharmaceutical industry (Desai 2012) can benefit from encapsulation.

Promising preclinical therapeutic studies have resulted in the development of several nanomedicine-formulations that are being tested in clinical trials (Etheridge, et al. 2013, He, et al. 2015, Taurin, et al. 2012). Many nanomedicines have shown reduced side-effects (He, et al. 2015) but limited efficacy in clinical trials (Wilhelm, et al. 2016), and the progression of anti-cancer nanomedicines into the clinic has been slow. To date, only a few are used clinically. For successful delivery, the NPs have to circulate in blood for a sufficient amount of time, extravasate from the vasculature, penetrate the extracellular matrix (ECM), and deliver their payload to the intracellular targets. However, numerous barriers that limit therapeutic response exist (Anchordoquy, et al. 2017, Desai 2012), such as heterogeneous EPR-effect between and within tumors (Hansen, et al. 2015, He, et al. 2015, Maeda 2015, Prabhakar, et al. 2013), poor vascularization, high interstitial fluid pressure, high tumor cell density (Padera, et al. 2004), and dense ECM (Chauhan, et al. 2011, Desai 2012). A recently published meta-analysis including 117 reports, found that a median of only 0.7% of injected dose reached the tumor (Wilhelm, et al. 2016). This emphasizes the need for new strategies that can increase the controlled delivery to the target.

Focused ultrasound (FUS), in particular when combined with microbubbles (MBs), has emerged as a promising method to non-invasively improve the delivery of drugs or NPs to tumor tissue (Burke, et al. 2014, Frenkel 2008, Heath, et al. 2012, Lammertink, et al. 2015, Pitt, et al. 2004, van Wamel, et al. 2016), and has recently been shown to increase survival in mice (Burke, et al. 2014, Kotopoulis, et al. 2014, van Wamel, et al. 2016) and humans with inoperable pancreatic cancer (Georg Dimcevski, et al. 2016). FUS treatment is non-invasive, and can be applied locally for various forms of tumors. Another important application for low-intensity FUS in conjunction with intravenously administered MBs is to transiently and selectively open the blood-brain barrier, as demonstrated in small animals (Burgess, et al. 2011, Hynynen, et al. 2001) and non-human primates (Downs, et al. 2015, Marquet, et al. 2011). This opens the possibility to treat aggressive glioblastoma and other diseases in the central nervous system. Currently, there are two ongoing clinical trials in glioblastoma patients (ClinicalTrials.gov Identifier NCT02343991 and NCT02253212) (Carpentier, et al. 2016).

FUS for therapeutic purposes can be employed to create thermal and mechanical effects such as cavitation and radiation force (Frenkel 2008, Pitt, et al. 2004). Cavitation is

the creation and oscillation of gas bubbles upon exposure to the acoustic wave. At relatively low pressures, the acoustic pressure waves will cause stable cavitation of the MBs. Stable cavitation is characterized by sustained bubble radius oscillation about its equilibrium. This generates microstreaming, fluid flow around the MBs (Elder 1959). Resulting shear stresses on the blood vessel wall when the MBs are close to or in contact with the endothelium, can cause formation of small pores and increase the vascular permeability, and enhance endocytosis (Afadzi, et al. 2013, Lentacker, et al. 2014, Meijering, et al. 2009). At higher pressures, the oscillations will increase in amplitude, become more transient and result in a violent collapse of the bubbles. This is termed inertial cavitation, and can lead to the formation of shock waves and jet streams in the vasculature, which can create both temporary and permanent pores in the capillary wall and in cell membranes (Lentacker, et al. 2014). The probability of inertial cavitation in a medium is determined by the mechanical index (MI), which is given by the peak negative pressure of the US wave divided by the square root of its center frequency. It is reasonable to assume that the probability for the occurrence of permanent tissue damage increases above the threshold for inertial cavitation. Altogether, FUS can thus locally increase the extravasation across the capillary wall and potentially improve penetration through the ECM, thereby improving the accumulation and distribution of NPs and drugs in tumors (Burke, et al. 2014, Frenkel 2008, Georg Dimcevski, et al. 2016, Kotopoulis, et al. 2014, Lin, et al. 2010, Lin, et al. 2012, van Wamel, et al. 2016, Wang, et al. 2015).

A unique multifunctional drug delivery system consisting of MBs stabilized by polymeric NPs (NPMBs) to be used in image-guided and FUS-mediated drug delivery as illustrated in Figure 1, has been developed (Mørch, et al. 2015). Biodegradable poly(alkyl cyanoacrylate) (PACA) NPs (Nicolas and Couvreur 2009, Vauthier, et al. 2003, Vauthier, et al. 2007) are prepared in a one-step synthesis, can encapsulate a range of drugs or contrast agents with high loading capacity and can be functionalized with polyethylene glycol (PEG) (Mørch, et al. 2015). One type of PACA NPs have already reached phase III clinical trials for treatment of liver cancer (Livatag, Onxeo, ClinicalTrials.gov Identifier NCT01655693) (Soma, et al. 2012). The MBs are formed by self-assembly of NPs into a shell. We have previously shown that this platform in combination with FUS can be employed to improve delivery of NPs to xenograft tumors in mice (Eggen, et al. 2014) and delivery across the blood-brain barrier in healthy rats (Åslund, et al. 2015). In our previous work, poly(butyl cyanoacrylate) (PBCA) NPs were used, whereas poly(2-ethyl-butyl cyanoacrylate) (PEBCA) NPs were applied in the present study. Due to a longer and branched alkyl monomer chain, they probably have a slower degradation rate (Muller, et al. 1992, Sulheim, et al. 2016), which might be therapeutically favorable.

In the present work, the PEBCA NPs were characterized with respect to *in vitro* cellular uptake and efficacy in a triple negative breast cancer cell line. *In vivo* circulation half-life and biodistribution of NPs was determined, and circulation of the MBs was evaluated. The main aim of the present study was to systematically study the effect of various ultrasound (US) parameters, and investigate the mechanisms of US-mediated delivery, to determine the importance of cavitation and bubble destruction for improved extravasation and enhanced NP delivery to tumor tissue. Furthermore, we aimed to determine safe acoustic pressures which enhance the delivery of the nanomedicine to tumor tissue, and to determine

if the increased delivery had a therapeutic benefit. Subcutaneous human breast cancer xenografts were grown in athymic mice, and NPMBs were injected intravenously, while the tumors were treated with FUS of various pressures and burst lengths. The delivery of NPs to tumors was evaluated by confocal microscopy on frozen tumor sections. To evaluate whether the increased delivery had a therapeutic benefit, the first proof-of-concept preclinical treatment study was performed with NPMBs encapsulating the anti-cancer drug cabazitaxel.

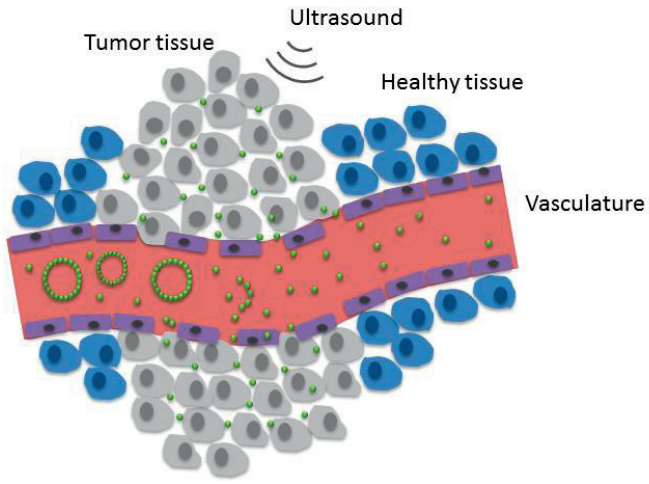

Figure 1: A schematic illustration of enhanced drug delivery to tumor tissue by use of FUS and NPMBs (in green).

Materials and methods

Synthesis and characterization of nanoparticles and microbubbles

PEGylated PEBCA NPs were synthesized by miniemulsion polymerization as described previously (Mørch, et al. 2015). Briefly, an oil phase consisting of 2-ethyl-butyl cyanoacrylate (monomer, Henkel Loctite, Düsseldorf, Germany) containing 0.1 wt% methane sulfonic acid (Sigma-Aldrich, St. Louis, MO, USA), 2 wt% Miglyol 812 (co-stabilizer, Cremer, Cincinnati, OH, USA) and 0.8 wt% azo bis-dimethyl valeronitril (V65, oil-soluble radical initiator, Waco, Osaka, Japan) was prepared. Fluorescent particles for optical imaging were prepared by adding either NR668 (modified NileRed (Klymchenko, et al. 2012), custom synthesis, 0.5 wt%) or IR-780 Lipid (near-infrared dye, custom synthesis, CEA, Grenoble, France, 0.5 wt%) to the oil phase. Particles containing cytostatic drug for treatment were prepared by adding cabazitaxel (10 wt%, Biochempartner, Wuhan, Hubei, China) to the oil phase.

An aqueous phase consisting of 0.1 M HCl containing Brij L23 (10mM, 23 PEG units, MW 1225, Sigma-Aldrich) and Kolliphor HS15 (10mM,15 PEG units, MW 960, Sigma-Aldrich) was added to the oil phase and immediately sonicated for 3 min on ice (6x30 sec intervals, 60% amplitude, Branson Ultrasonics digital sonifier 450, Danbury, CT, USA). The solution was kept on magnetic stirring for 1 h at room temperature before adjusting the pH to 5 using 0.1M NaOH. The polymerization was continued for 2 h at room temperature before increasing the temperature to 50°C for 8 h while the solution was rotated (15 rpm). The dispersion was dialyzed (Spectra/Por dialysis membrane MWCO 100,000 Da, Spectrum Labs, Rancho Dominguez, CA, USA) against 1mM HCl to remove unreacted PEG. The dialysate was replaced 3 times. Details regarding PEGylation of NP-platform have been published previously (Baghirov, et al. 2017, Mørch, et al. 2015, Åslund, et al. 2017). The size, polydispersity index (PDI) and the zeta potential of the NPs were measured by dynamic light scattering using a Zetasizer Nano ZS (Malvern Instruments, Malvern, UK). To calculate the amount of encapsulated drug, drug content was extracted from the particles and the extracted amount was quantified by liquid chromatography coupled to mass spectrometry (LC-MS/MS, Agilent 6490 triple quadrupole coupled with Agilent 1290 HPLC, Agilent Technologies, Santa Clara, CA, USA).

NPMBs were prepared by self-assembly of the NPs (1 wt%, 10 mg/ml) at the gas-water interface by the addition of 0.5% casein in phosphate-buffered saline and vigorous stirring using an ultra-turrax (T-25, IKAWerke, Staufen, Germany) as described (Mørch, et al. 2015). Perfluoropropane (F2 Chemicals, Preston, Lancashire, UK) was used instead of air for increased circulation time. The average MB diameter, size distribution and concentration were determined using light microscopy and image analysis (ImageJ 1.48v, National Institute of Health, Bethesda, MA, USA). The NPMB solution is a combination of free NPs and NPMBs, where only a small percentage of the NPs are located on MBs. The MBs where characterized with respect to acoustic destruction as described below.

Cell culture

The triple-negative human breast adenocarcinoma cells MDA-MB-231 (kind gift from Department of Circulation and Medical Imaging, NTNU, Trondheim, Norway (HTB-26,

American Type Culture Collection, Manassas, VA, USA)) were cultured in Roswell Park Memorial Institute (RPMI) 1640 Medium (21875-034, Gibco, Thermo Fisher Scientific, Waltham, MA, USA) supplemented with 10% fetal bovine serum (Sigma-Aldrich). The cells were kept at 37°C and 5% CO_2 and maintained in exponential growth. 0.1% gentamicin solution (Sigma-Aldrich) was added to the medium for cells that were to be implanted *in vivo* and for *in vitro* toxicity studies.

Animals and tumors

All experimental procedures were approved by the *Norwegian Animal Research Authorities*. Female Balb/c nude mice (Envigo, Cambridgeshire, United Kingdom) were purchased at 7-8 weeks of age, 16-21 g. They were housed in specific pathogen free conditions, in groups of 4-5 in individually ventilated cages (Model 1284 L, Tecniplast, Lyon, France) at temperatures of 22-23°C, 50–60% relative humidity, 70 air changes per h, with *ad libidum* access to food and sterile water.

Subcutaneous xenograft tumors were grown from breast cancer MDA-MB-231 cells. Animals were anesthetized by inhalation of 2-3% isoflurane in O_2 and NO_2 (Baxter, Deerfield, IL, USA), before 50 µl medium containing 3×10^6 cells was slowly injected subcutaneously on the lateral aspect of the left hind leg, between the knee and the hip. During the following weeks, the animals were weighed and tumors measured using calipers 2-3 times a week. Tumor volume was calculated by $\pi lw^2/6$, where l and w are the length and width of the tumor, respectively. Tumor growth did not affect the weight of the animals.

During experiments, the animals were anesthetized by a subcutaneous injection of fentanyl (0.05 mg/kg, Actavis Group HF, Hafnarfirdi, Iceland), medetomidine (0.5 mg/kg, Orion Pharma, Oslo, Norway), midazolam (5 mg/kg, Accord Healthcare Limited, North Harrow, United Kingdom), water (2:1:2:5) at a dose of 0.1 ml per 10 g. When necessary, a subcutaneous injection of atipemazol (2.5 mg/kg, Orion Pharma, Oslo, Norway), flumazenil (0.5 mg/kg, Fresenius Kabi, Bad Homburg vor der Höhe, Germany), water (1:1:8) at a dose of 0.1 ml per 10 g was used as antidote to terminate the anesthesia. During all experiments, the body temperature of the animals was maintained by external heating and eyes were kept moist with Viscotears Liquid gel (Alcon, Fort Worth, TX, USA). At the end of the experiment, anesthetized animals were euthanized by cervical dislocation.

In vivo circulation half-life of nanoparticles

The mice were anesthetized as described above, and NPs containing NR668 were diluted to 7 mg/ml in phosphate buffer and injected intraveneously as a bolus of 200 µl through the lateral tail vein in 5 mice (70 mg/kg). Blood samples of 10-15 µl were drawn from the saphenous vein pre-injection and 10 min, 30 min, 1, 2, 4, 6 and 24 h post injection. In between the 4, 6, and 24 h samples, the animals were placed in a recovery rack (Blue Line, Scanbur, Copenhagen, Denmark) where the temperature was kept at 28°C to avoid hypothermia. Blood samples were diluted in 40 µl 10 IU/ml heparin (Leo Pharma A/S, Ballerup, Denmark) and vortexed (444-1372, VWR, Radnor, PA, USA), before they were centrifuged at 3000 rpm for 7 min (Micromax, International Equipment Company (IEC), Needham, MA, USA) Fluorescence in the supernatant was measured with a spectrophotometer (Infinite 200Pro, Tecan, Männedorf, Switzerland) by excitation at 535 nm

(bandwidth 9 nm) and detection at 620 nm (bandwidth 20 nm). A 384-well plate (Corning, Corning, NY, USA) with 10 µl from each blood sample was analyzed. Fluorescence intensity per volume of blood diluted in heparin, plotted as a function of time, was fitted by a monoexponential decay curve (f(t)=ae^-bt) using SigmaPlot (12.0, Systat Software, San Jose, CA, USA), resulting in a circulation half-life ($t_{1/2}$=ln(2)/b).

In vivo circulation of microbubbles

Inflow and circulation of fluorescently labelled NPMBs in tumors was imaged by contrast enhanced US using a Vevo 2100 and the MS250 probe (FujiFilm VisualSonics, Toronto, ON, Canada). The tail veins of anesthetized mice were cannulated (BD Neoflon 24G, Becton Dickinson & Company, Franklin Lakes, NJ, USA) and 200 µl of NPMBs (10mg/ml NPs) were injected intravenously. Perfusion of the tumor was imaged using nonlinear contrast enhanced imaging mode, with a transmit frequency of 18MHz, a power of 10% and a frame rate of 10 fps. Data were exported using the VisualSonics software (1.6.0, FujiFilm VisualSonics, Toronto, ON, Canada) and displayed using Matlab (R2014b, MAthWorks, Natick, MA, USA). NPMBs loaded with cabazitaxel were also imaged *in vivo* to ensure that the drug did not affect the circulation, and the inflow and circulation in a kidney were imaged using the same settings, and a frame rate of 20 fps.

Biodistribution of nanoparticles

Mice were anesthetized and the lateral tail veins were cannulated as described, before a bolus of 200 µl NPMBs (10mg/ml NPs, resulting in 100 mg/kg) containing the infrared dye IR-780 lipid were injected. Antidote was administered and the animals were kept in a recovery rack. Six h post injection, animals euthanized and spleen, liver, kidney, heart, lungs, brain and tumor, were excised. The organs were imaged using a near infrared Pearl Impulse small animal imaging system (LI-COR Biosciences Ltd., Lincoln, NE, USA). Excitation/emission settings were 785/820 nm. Images were processed using ImageJ to quantify the accumulation of NPs. Regions of interest (ROI) were drawn around each organ, and the sum of the intensity values of the pixels in the selection was calculated. Nine known concentrations of NPs in phosphate buffer ranging from 0-2 mg/ml were imaged to obtain a standard curve (Supplementary Figure S1). From this, the accumulated dose of NPs, as a percentage of the total injected dose, and as weight of NPs per weight of tissue was determined.

Cellular uptake of nanoparticles

In vitro cellular uptake was determined using flow cytometry (FCM) and CLSM. For quantification with FCM, 300 000 cells in 3 ml medium were seeded in 6-wells plates (Corning Costar, Sigma-Aldrich), and 30 000 cells in 300 µl medium were seeded in 8-well slides (Ibidi, Martinsried, Germany) for CLSM. 48 h later, the medium was changed, and at 72 h the medium was replaced by medium containing 20 µg/ml NPs with NR668. After 3 h incubation, the cells were rinsed 2-3 times with PBS. The cells for FCM were trypsinized (Sigma-Aldrich) and placed on ice until FCM analysis. Incubation was done at 37°C, but also at 4°C to assure that no leakage of the dye was observed (Snipstad, et al. 2016, Snipstad, et

al. 2014, Sulheim, et al. 2016). At this temperature, NP uptake by endocytosis is not expected, and staining of the cells would likely be due to leakage of the dye.

In FCM (Gallios, Beckman Coulter, Indianapolis, IN, USA), a 561 nm laser was used to excite NR668 and fluorescence was detected at 620 nm using a 30 nm bandpass filter. Cellular fragments, debris and aggregates were excluded from the analysis by gating the side-scatter versus forward-scatter dot plot. Approximately 10 000 events were counted from each sample. The percentage of cells taking up NPs and their median fluorescence intensity was determined using Kaluza Flow Cytometry Analysis software v1.3 (Beckman Coulter).

CLSM imaging (TCS SP8, Leica, Wetzlar, Germany) was performed using a 63x1.2 water objective, and a pin hole of 1 airy unit. A white light laser at 540 nm was used to excite NR668, and fluorescence was detected at 569–699 nm. The fluorescence signal was superimposed with a bright field image from the same laser. Images were captured using a frame size of 1024x1024 pixels (184x184 μm).

In vitro toxicity

Cellular toxicity was studied using the colorimetric alamarBlue assay (Thermo Fischer Scientific). Cells were seeded in black 96 well plates (Corning, Corning, NY, USA), 2500 cells per 200 μl medium. At 72 h, medium with NPs containing cabazitaxel was added. Concentrations of NPs ranging from 0 to 10 000 ng/ml were used, corresponding to cabazitaxel concentrations of 0 to 1000 ng/ml (10%). Free drug (in polysorbate 80 (Sigma-Aldrich) and ethanol) at the same concentrations, as well as the NPs without the drug, were used for comparison. The cells were incubated at 37°C with 5% CO2 for 24 h, before being rinsed 3 times with medium. AlamarBlue was diluted 1:10 with medium, and 110 μl was added to each well. Medium with alamarBlue without cells was used as blank. The cells were incubated for 2 h at 37°C, protected from light. Fluorescence was measured using a microplate reader (SpectraMax i3x, Molecular Devices, Sunnyvale, CA, USA), with an excitation wavelength of 550±9 nm and emission detected at 590±20 nm. Metabolically active cells reduced resazurin to the fluorescent resorufin, from which the percentage of viable cells was estimated. Dose response curves $f(x)= y_{min}+((y_{max}-y_{min})/(1+(x/IC50)^{k}))$ were fitted to the experimental datapoints using SigmaPlot (4 parameter logistic curve). y_{min} and y_{max} are the minimum and maximum survival values, IC50 is the concentration that gives a response half way between baseline and maximum, and k is the slope of the curve. y_{min} and y_{max} were constrained to be between 0 and 100%.

Ultrasound setup

A custom made, single element focused transducer with a center frequency of 1 MHz (Imasonic, Besancon, France) was used. The signal was generated by a waveform generator (33500B, Agilent Technologies, Santa Clara, CA, USA), and amplified by a 50 dB power amplifier (2100L, E&I, Rochester, NY, USA). The transducer was mounted at the bottom of a water chamber (Figure 2A), and a lid with an absorber was placed at the water surface. The animals were placed on the lid, and the tumor-bearing leg lowered into the water through a 10 mm opening. The tumor was placed in the far field of the FUS beam at a distance of 190 mm. The water in the tank was heated to 34°C to avoid hypothermia and altered blood flow in the mouse leg (Hyvelin, et al. 2013). The transducer had a diameter of 50 mm and a distance to

the focal area of 125 mm. It was characterized in a water tank using a hydrophone (HGL-0200, Onda, Sunnyvale, CA, USA), and the beam profile can be found in supplementary materials (Supplementary Figure S2). The 3dB and 6 dB beam widths at 190 mm had diameters of 6 mm and 10 mm, respectively.

Characterization of microbubble destruction

Destruction of the NPMBs was evaluated by imaging NPMBs in an in-vitro flow phantom (model 524, ATS Laboratories, Bridgeport, CT, USA) were the flow was driven by a peristaltic pump. The NPMBs were sonicated (1000 cycles, PRF=10ms) at MIs of 0.1, 0.2 and 0.5 using the 1 MHz transducer (Imasonic) while flowing through the tube of the phantom. Simultaneously, a section of the tube downstream from the sonicated region was imaged using pulse inversion at an MI of 0.07 by a clinical US scanner in contrast mode (Vivid E9 scanner and 9L transducer, GE Healthcare, Chicago, IL, USA). Destruction of MBs was determined by visual inspection (Berg, et al.).

Ultrasound exposure optimization

To investigate how various acoustical settings in combination with our MBs affected NP accumulation in tumor tissue, subcutaneous tumors in 18 mice were allowed to grow for 4-8 weeks until they had reached a diameter of approximately 7-8 mm in the longest direction and a volume of approximately 120-250 mm^3. The animals were anesthetized and the lateral tail veins were cannulated, and NPMBs containing NR668 were injected intravenously, at a dose of 200 µl with 10 mg/ml NPs (100 mg/kg). The US treatment was initialized when the injection started. The mice were randomly distributed in different groups, and tumors were treated with one of six different FUS treatments (Figure 2). Acoustic pressures ranged from 0.1 to 1 MPa (MIs ranging from 0.1 to 1). All tumors (except group 4) received bursts of 10 000 cycles (10 ms) every 100 ms (local PRF 10 Hz) for 0.5 s treatment, followed by 1.5 s break (global PRF 0.5 Hz, and total duty cycle 2.5%). For the highest pressure, a short flash of 3 cycles was also investigated. The total treatment time was 2 min;

1. Control group, no US treatment (n=3 animals).
2. MI 0.1 (Figure 2B). Limited destruction of MBs visible in phantom (n=3 animals).
3. MI 0.1, with 3 additional cycles flash of MI 1 to destroy the MBs after each 10 000 cycles (Figure 2C), (n=3 animals).
4. Only the 3 cycles flash of MI 1 (Figure 2D) (n=3 animals).
5. MI 0.25. Significant destruction of MBs observed in phantom (n=2 animals).
6. MI 0.5 (Figure 2E) (n=3 animals). Complete destruction of MBs observed in phantom.
7. MI of 1. Because tissue damage was observed with this treatment, only 1 animal was treated.

In the groups where MB destruction is expected, reperfusion of MBs in the sonicated area is important to allow new MBs to reach the tumor, and thus a PRF of 0.5 Hz was used. Blood vessels were stained by intravenously injecting 100 µl fluorescein-labeled *Lycopersicon esculentum* (tomato) lectin (FITC-lectin, Sigma-Aldrich) diluted in 0.9% NaCl to 1 mg/ml (5 mg/kg) 2 h post treatment, and allowing it to circulate for 5 min before

euthanasia. The tumors were excised and sectioned for imaging by CLSM or for histological evaluation as described below.

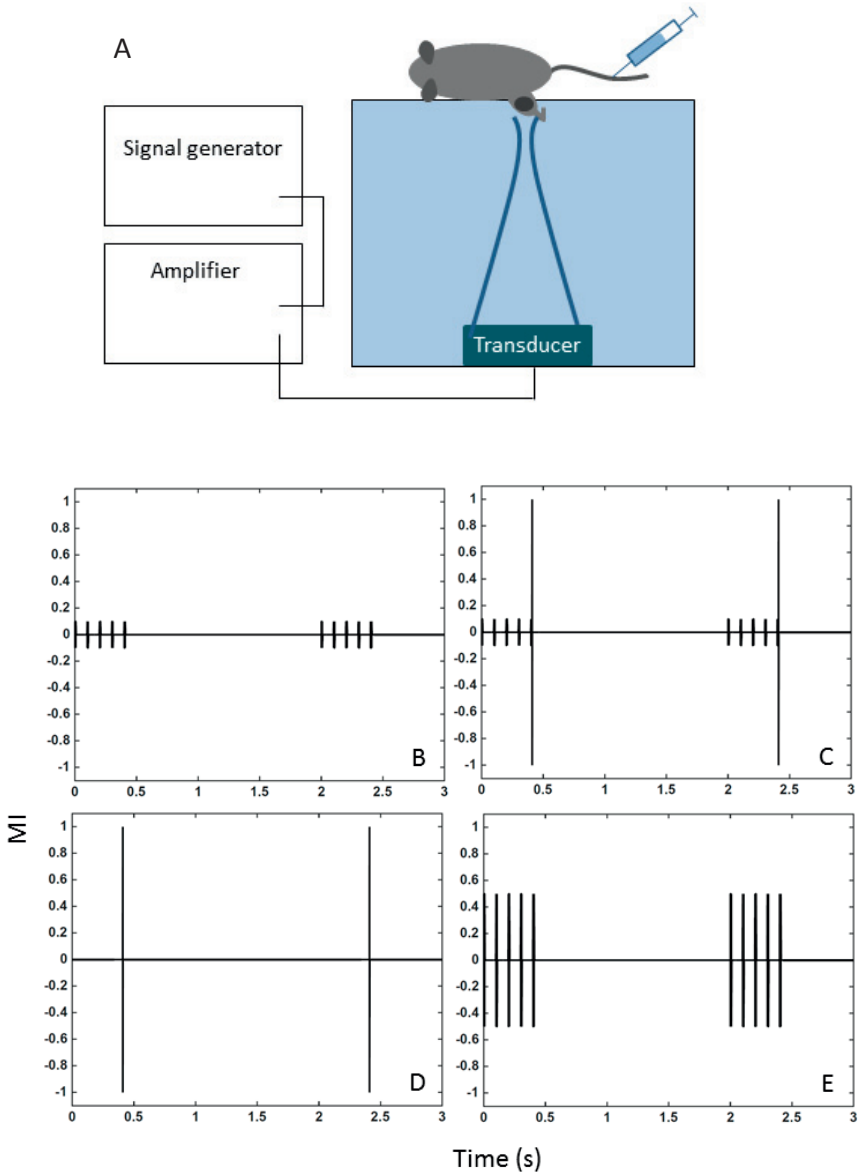

Figure 2: A schematic of the US setup (A) is shown together with schematic illustrations of selected US treatments; group 2 (B), 3 (C), 4 (D) and 6 (E), showing MI as a function of time for the first 3 sec of each treatment. Each vertical line illustrates a burst.

Confocal imaging of tumor sections and quantification of nanoparticle delivery

The excised tumors were embedded in OCT Tissue Tek (Sakura, Alphen aan den Rijn, The Netherlands) and frozen in liquid N_2. The first 1000 µm were removed, before 3 frozen sections of 25 µm and 1 section of 4 µm were prepared from 5 depth levels in the tumor, with 300 µm between each level. The sections were mounted on objective glass slides and the microdistribution of NPs was imaged by CLSM (TCS SP5, Leica). In sequential scans, a DPSS 561 laser was used to excite NR668-labeled NPs, and fluorescence was detected at 590-650 nm. An argon laser at 488 nm was used to excite FITC-labeled vasculature, and fluorescence was detected at 500-550 nm. A HCX PL APO CS 20x0.7 dry objective was used, and tile scans of the entire tumor sections were captured using a frame size of 512x512 pixels (775x775 µm), 400 Hz scan speed. An optical section of 5 µm was used (airy unit 2.8, pinhole 170 µm), and images through the section were captured every 2.5 µm to make z-stacks. The laser intensity and detector gain were kept the same for all sections, and were set to minimize noise and utilize the gray scale. When acquiring tile scans, the sections were imaged dry because mounting media disturbed the distribution of the fluorescence during long acquisition times. For more detailed example images of NP distribution, a zoom factor of 3 was used, resulting in images of 258.33 µm. These sections were mounted with Vectashield (Vector Laboratories, Burlingame, CA, USA) to image FITC, and selected areas were imaged within minutes after mouting.

The tile scans were processed using ImageJ to quantify the tumor uptake of NPs. A maximum intensity projection of each z-stack was made. An ROI was drawn around each section. The image was thresholded using the inbuilt ImageJ Yen algorithm (determined to give the most suitable thresholding by visual inspection), and "analyze particles" was used to quantify the number of above-threshold pixels and their intensity. The results were displayed as number of pixels divided by the area of the respective tumor section.

Histology

Tumors for histological evaluation were fixed for minimum two days in 4% neutral buffered formaldehyde. The samples were then embedded in paraffin, before 4 µm sections (Leica Tissue processor) were made from the middle of the tumor. They were stained with hematoxylin erythrosine saffron (HES), and imaged to evaluate tissue damage after the US treatment. The sections were analyzed by an experienced senior pathologist, blinded to which tumor received which treatment.

Treatment of triple negative breast cancer MDA-MB-231 xenografts with nanoparticle-microbubble encapsulated cabazitaxel

The tumors were allowed to grow for 3 weeks until they had reached approximately 4 mm in the longest direction. The number of animals and control groups was, in compliance with the "3Rs" (replacement, reduction, refinement)(Fenwick, et al. 2009), kept low in this pilot study. 12 animals were randomly distributed into 3 groups;

1. Animals injected with saline, control group
2. Animals injected with NPMB containing cabazitaxel

3. Animals injected with NPMB containing cabazitaxel and tumors exposed to the previsouly described US treatment (MI=0.5).

The mice were treated two weeks in a row (day 21 and 29 after implantation of cells). At the day of treatment, animals were anesthetized and the tail vein cannulated. An intravenous bolus of 200 µl saline or NPMB was given. The concentration of NP in the bubble solution was 10 mg/ml, resulting in a total dose of 2 mg NPs per animal, and thus 10mg/kg cabazitaxel. This dose was chosen based on literature (Semiond, et al. 2013, Vrignaud, et al. 2014, Vrignaud, et al. 2013). The optimal US treatment from the optimization of various MIs was used (group 6 with an MI of 0.5 as described above) for the first treatment. Unfortunately, the transducer broke after the first treatment. In order to continue the experiment, the second treatment was done with another transducer (RK-100 system, aperture 52 mm and distance to the focal area of 60 mm, FUS Instruments, Toronto, ON, Canada). It had a frequency of 1.1 MHz, and due to a smaller focal diameter, the transducer was scanned to cover the tumor area. 16 spots (4x4) were scanned during 3.5 sec. In each spot, a burst of 10 000 cycles was transmitted. The total treatment time was increased from 2 min, to 3.5 min to achieve 60 sonications, to make the treatment as similar as possible to that of the first treatment with the Imasonic transducer.

After the treatment, the antidote was administered to terminate anesthesia, and the animals were placed in a recovery rack until the next morning to avoid hypothermia in the recovery period. The rack kept a temperature of 28°C. The days following a treatment, the animals were given Diet gel boost (ClearH2O, Westbrook, ME, USA) as a supplement to the dry food. The tumor growth was measured using calipers and the animals were weighed 2 times per week for 14 weeks after end of treatment. The criteria for humane endpoints where animals were euthanized were tumor size of 15 mm diameter or weight loss of 15%.

A third treatment was planned a week after the second treatment, but the two first animals who received the third treatment died shortly after the injection. Therefore, the remaining animals were not treated a third time. One animal in the control group was euthanized because the tail became partly necrotic.

Statistical analysis

A two-tailed unpaired t-test was used to evaluate if the difference in NP uptake between group 1 and 6 was statistically significant (Excel 2010, Microsoft, Redmond, WA, USA). A p-value less than 0.05 was considered statistically significant.

Results

Characterization of nanoparticles and microbubbles

The NPs had diameters in the range of 140-195 nm (z-average), a PDI below 0.2 and zeta-potential in the range of -1 to -2.5 mV. The determined loading efficiency of cabazitaxel was close to 100% with a drug payload of 10 wt%.

The self-assembled MBs had an average mean diameter of 2.6±1.3 µm. The concentration of MBs was approximately 5e8 MBs/ml. From characterization in the *in vitro* flow phantom, the MBs showed no destruction at MI 0.1, partial destruction at MI 0.2 and complete destruction at MI 0.5 (Berg, et al.).

In vivo circulation half-life of nanoparticles

In vivo circulation half-life of the PEGylated PEBCA NPs was found to be 136 min. An exponential decay $f(t)=206160.9e^{-0.0051t}$ fitted the experimental data of fluorescence intensity in blood (R^2=0.67 and p-values ≤0.0001) (Figure 3).

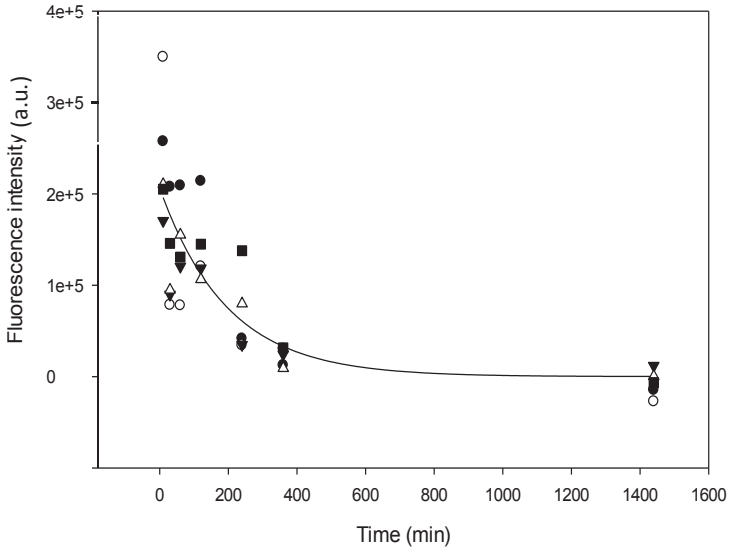

Figure 3: Circulation time of nanoparticles: fluorescence intensity in blood as a function of time, and a monoexponential decay $f(t)=206160.9e^{-0.0051t}$ fitted the data with R^2=0.67 and p-values ≤0.0001, resulting in a circulation half-life $t_{1/2}$=136 min (n=5 animals). The various symbols represent different animals.

In vivo circulation of microbubbles

The MBs stabilized by the self-assembled NPs were found to be suitable for *in vivo* contrast enhanced US imaging and image guided drug delivery. The contrast enhancement in a tumor imaged by US is shown in Figure 4B. From an ROI surrounding the tumor, the contrast was quantified (Figure 4C). NPMBs could be detected for approximately 4-5 min. NPMBs containing cabazitaxel were imaged in the kidney of a mouse, and inflow through the

venous circulation could be seen before the MBs reached the arterial circulation and filled the kidney (Supplementary Figure S3).

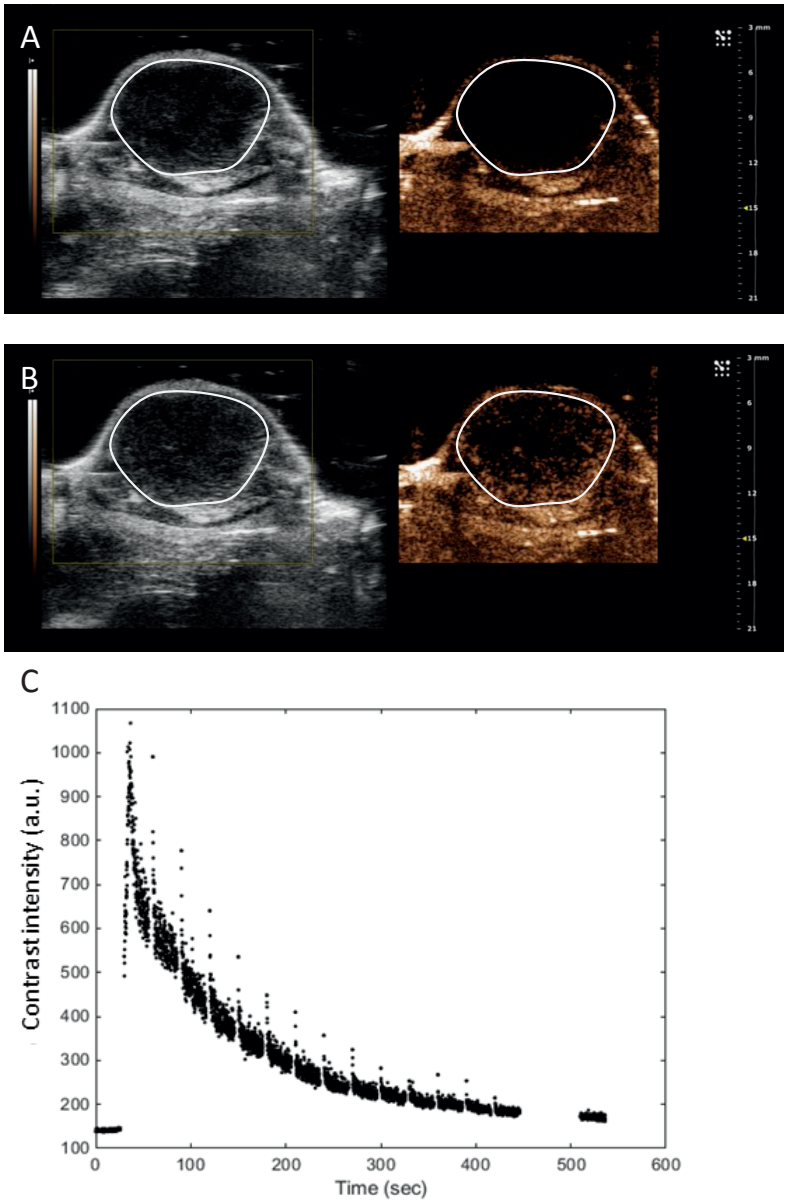

Figure 4: Circulation of microbubbles: representative B-mode US (left) and non-linear contrast images (right) of a tumor pre (A) and post (B) injection of NPMBs. The contrast intensity was quantified (white ROI), shown as a function of time to illustrate the timescale at which MBs are present in circulation (C).

Biodistribution

The biodistribution of NPs was determined 6 h post injection of NPMBs containing IR-780 lipid, when the NPs are nearly cleared from the circulation. Representative fluorescence intensities from organs and tumor from one animal is shown in Figure 5, along with percentage of accumulated dose in the various tissues. A standard curve (Supplementary Figure S1) was used to determine amount of NPs in the various tissues based on measured fluorescence intensities. The average weight of the respective organs, tumor and brain can be seen in Supplementary Table S1. A total dose of 2 mg NPs (10 mg/ml*0.2ml) was injected in each animal, and about 1% of the dose was located in the tumor. The majority of the dose was located in the liver and spleen. Altogether, approximately 87% of the injected dose was found in spleen, liver, kidney, heart, lungs, tumor and brain. The rest is likely distributed in urine, stool, skin, muscle, bone, lymph nodes and other tissues.

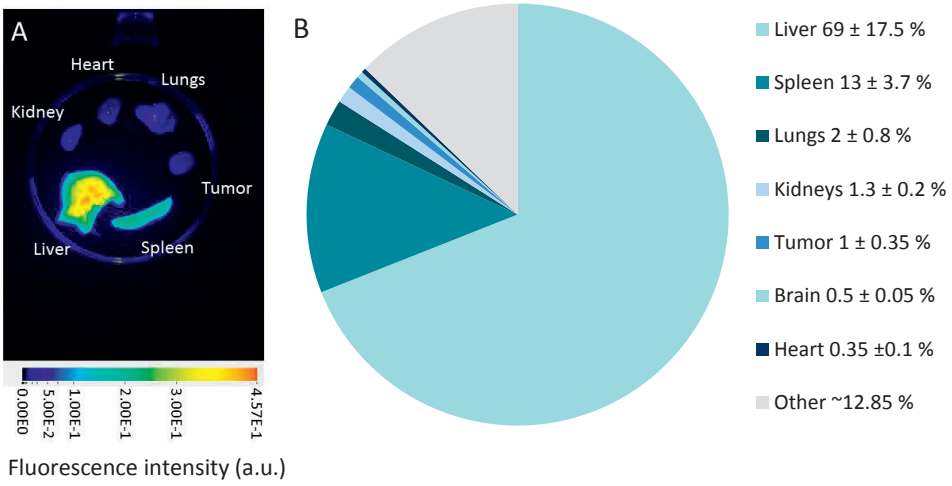

Figure 5: Biodistribution of NPs in the various organs, tumor and brain. Representative fluorescence intensities from the various tissues (A) and the quantified percentage of NPs in the various tissues (B) is shown as mean and standard deviation from n=4-7 animals.

Cellular uptake of nanoparticles

Cellular uptake of NPs in the breast cancer cell line was confirmed by CLSM (Figure 6A). The NPs were imaged by detecting the encapsulated fluorescent dye NR668. FCM quantified the cellular uptake, 90% of the cells had taken up NPs by endocytosis after 3 h incubation (Figure 6B), and the median fluorescence intensity was 18 times higher than autofluorescence. No uptake was seen after incubation at 4°C, confirming that NR668 did not leak from the NPs, as previously reported (Snipstad, et al. 2016, Sulheim, et al. 2016).

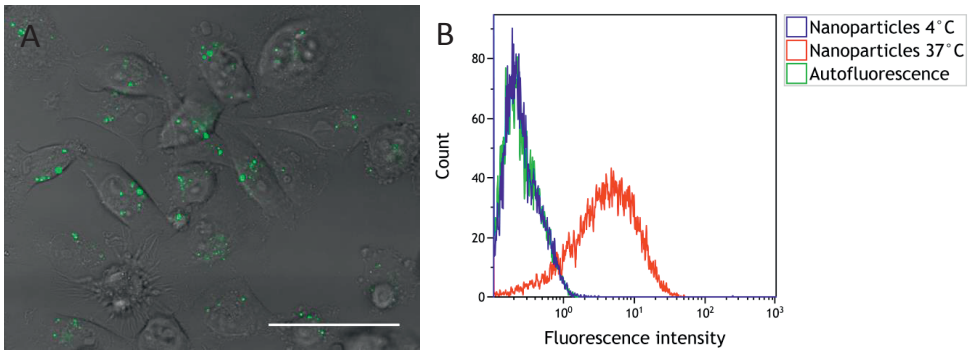

Figure 6: Cellular uptake: a CLSM and bright field image of the breast cancer MDA-MB-231 cells which have taken up NPs (A). The encapsulated dye NR668 is shown in green. Scale bar is 50 µm. A representative histogram from FCM quantifying the uptake of NPs after 3 h incubation at 4°C or 37°C (B).

In vitro toxicity

The *in vitro* toxicity of NPs with cabazitaxel for the breast cancer cell line MDA-MB-231 was determined by the alamarBlue assay. Figure 7 indicates that the drug is effective against the cell line. The free drug is more effective than the encapsulated drug. After 24 h incubation, IC_{50} values were 5.7 and 1.1 for the encapsulated and free drug, respectively, while the y_{min} values were 37 and 32%. The ratio between the IC_{50} values was similar even at 72 h, however the y_{min} values decreased with time (not shown). The empty NPs were by themselves not toxic, except for the highest concentration of 1000 ng/ml (not shown).

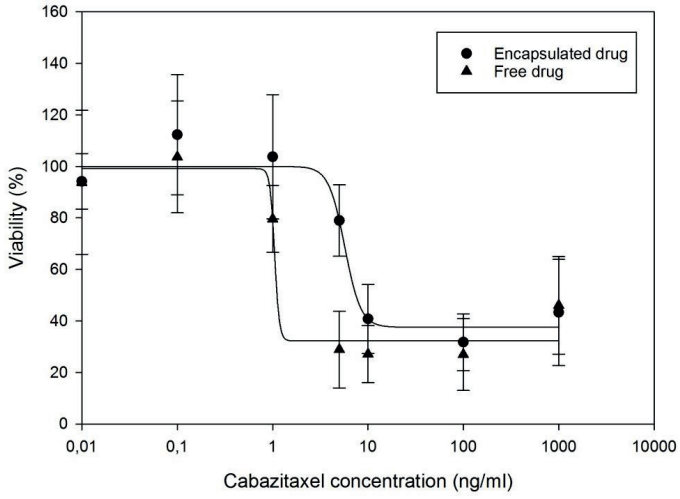

Figure 7: Cytotoxicity of encapsulated and free cabazitaxel for the breast cancer cell line MDA-MB-231 after 24 h exposure, measured by the alamarBlue assay. The data are averages from n=6 samples, shown with standard deviation. The percentage of viable cells is expressed as a function of concentration of the drug. The fitted dose response curves are shown.

Microdistribution of nanoparticles

The microdistribution of NPs in the tumors 2 h post US treatment was imaged using CLSM. Representative images from the control group that did not receive US treatment and a tumor treated with FUS at MI of 0.5 are shown in Figure 8. An increased delivery of NPs is observed in the treated tumor compared to the control tumor. Much more NPs were seen in the FUS treated tumor, and the NPs were displaced from the blood vessel into the ECM.

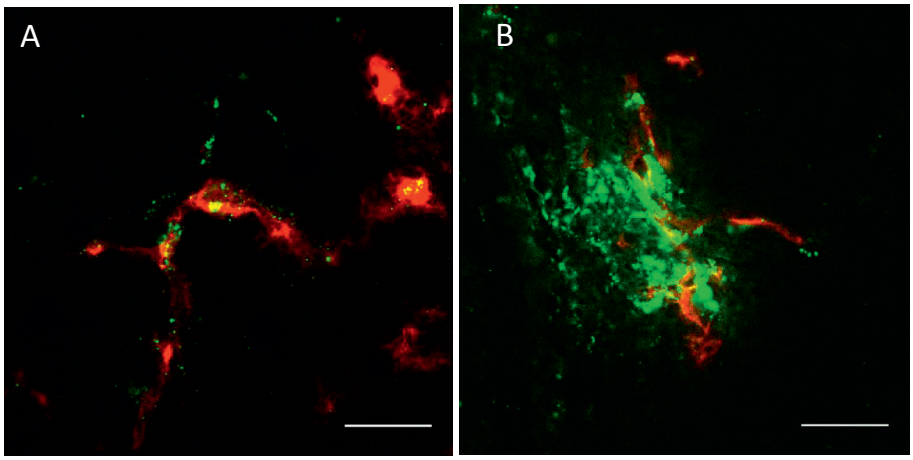

Figure 8: Distribution of nanoparticles: representative CLSM images from a tumor that did not receive any US treatment (A) and a tumor treated with an MI of 0.5 (B). Blood vessels (FITC) are shown in red and nanoparticles (NR668) in green. Scale bars are 50 μm.

Quantification of nanoparticle tumor accumulation

To obtain a semi-quantitative measurement of the tumor uptake, CLSM tile-scans of entire tumor sections from each animal were acquired and analyzed. One section from level 3 in each tumor was used (approximately 1.84 mm inside the tumor). A representative tile scan (Figure 9A) shows the variation in distribution of NPs across the tumor section (from group 6). The number of above-threshold pixels and their intensities were measured for each section. The results were displayed as the number of pixels divided by the area of the respective tumor section, for each animal in the different treatment groups (Figure 9B). When presented as number of pixels multiplied by their respective intensities, divided by area of the tumor section, the results were similar (not shown). Accumulation of NPs was not affected by low pressures (group 2 and 3), whereas the complete bubble destruction (group 6) and violent collapse of MBs at higher MIs (group 7) increased the delivery of NPs to tumors. The short flash at high MI (group 3 and 4) did not increase tumor uptake of NPs. To obtain more data points and information about the variation within tumors, sections from level 5 (approximately 2.6 mm inside the tumor) were also analyzed for group 1 and 6 (Figure 9C). In general, level 5 sections showed lower NP uptake than level 3 sections. The overall mean relative fluorescence intensity in mice exposed to MI 0.5 was approximately 2.3 times higher than the mean of the control group that did not receive any US treatment, and the difference was statistically significant ($p=0.0314$).

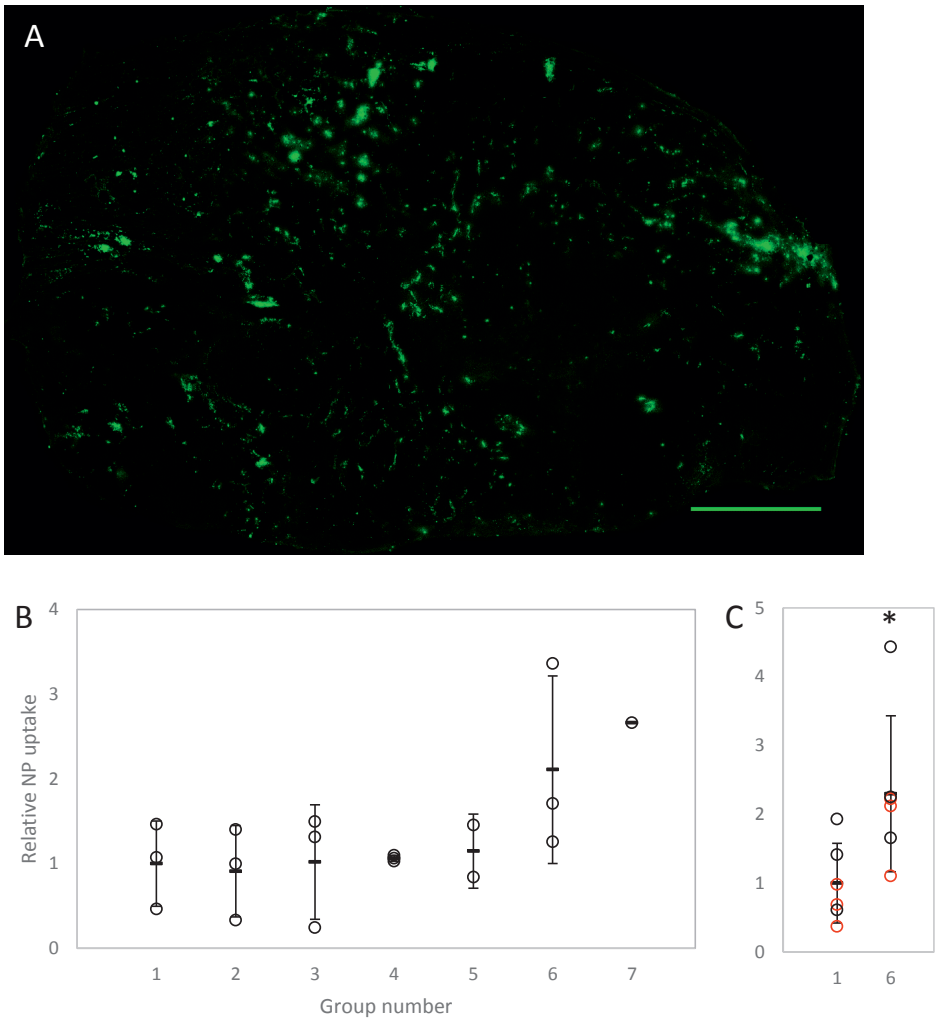

Figure 9: Tumor uptake of nanoparticles: an example of a CLSM tile scan from an entire tumor section from group 6 showing NPs (NR668) in green, scale bar is 1000 µm (A). Quantification of number of pixels with NPs (NR668), divided by the area of the respective tumor section (B). Data points represent one level 3 section from each animal in the different treatment groups. Each individual animal is shown (○), together with the group mean (**-**) ± standard deviation. All data points are normalized to the mean of group 1. Groups: 1: control, no US (n=3 animals), 2: MI 0.1, limited MB destruction (n=3 animals), 3: MI 0.1 + flash MI 1 (n=3 animals), 4: flash MI 1 (n=3 animals), 5: significant MB destruction with intermediate MI 0.25 (n=2 animals), 6: complete MB destruction with MI 0.5 (n=3 animals), 7: violent collapse MI 1 (n=1 animal). Sections from both level 3 (black) and level 5 (red) are shown for group 1 and 6 (C), altogether n=6 sections per group. The average in group 6 is 2.3 times higher than group 1, the difference between the two groups was statistically significant (* p=0.0314).

Histology

Except for the highest MI (group 7), which caused substantial visual hemorrhage, evaluation of HES stained tumor sections showed that all other FUS treatments could be considered safe. An example of an overview image of a non-treated tumor section and representative images of non-treated and treated tissue are shown in Figure 10. All sections, including the untreated, had some areas with a few microbleedings, but there were no significant differences between the different groups. The microbleedings could be from fragile neoangiogenic vessels, but there were no structural or histological, morphological or pathological differences between the different treatment groups. The tumor was for the most circumscribed, with a necrotic core, and infiltrative growth in adjacent connective and muscular tissue was seen (Figure 10A). Histologically, the tumor was highly cellular with varying degree of atypia and a lot of mitotic cells. Thus, all characteristics of an aggressive, highly malignant and tumor were present. Observations of vasculature with malignant cells confirm a metastatic model.

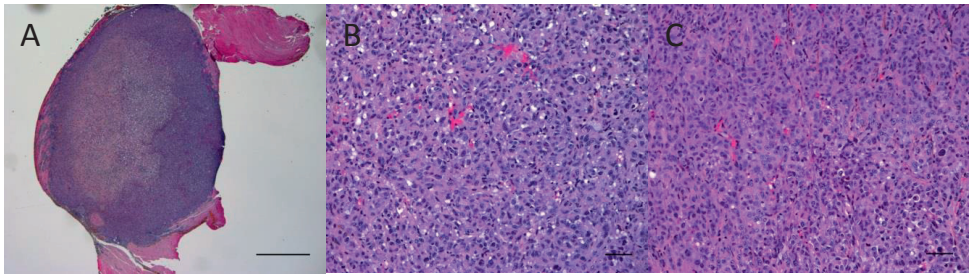

Figure 10: Histology: representative overview image of a HES stained section from an untreated breast cancer MDA-MB-231 tumor (A), and images of non-treated (B) and treated tissue (C). Scale bars are 1000 µm (A) and 50 µm (B, C).

Treatment of tumors with nanoparticle-microbubbles containing cabazitaxel

As a proof-of-principle, to evaluate whether the increased delivery of NPs to the tumor tissue would be sufficient to improve treatment with encapsulated cytostatic drugs, a small treatment study was performed. The average tumor growth for the 3 treatment groups is shown in Figure 11. Untreated animals (saline) showed a continuous tumor growth and were sacrificed at day 62, 69 and 72 after implantation when the tumors reached 15 mm. The group treated with NPMB encapsulating cabazitaxel showed reduced tumor growth compared to the non-treated animals, and all animals responded to treatment, but with large variations in tumor volume between the animals. The tumors started regrowing approximately 80 days after implantation (50 days after treatment end). One animal was sacrificed at day 120 when the tumor reached 15 mm, and the two other were still alive at the end of the study, with tumors of 13 and 4,5 mm in length. The group treated with FUS in addition to NPMB with cabazitaxel showed a larger reduction in tumor growth, and from day 48, all animals were in complete remission. At the end of the study, approximately 100 days after end of treatment, all animals were still alive and in complete remission. Data points for all the individual

animals are shown in Figure 11C-E, and shows the variation in treatment response for the NPMB treated tumors.

The animals did not lose any weight due to the treatment, neither the control animals nor the animals treated with encapsulated cabazitaxel and FUS (Figure 12).

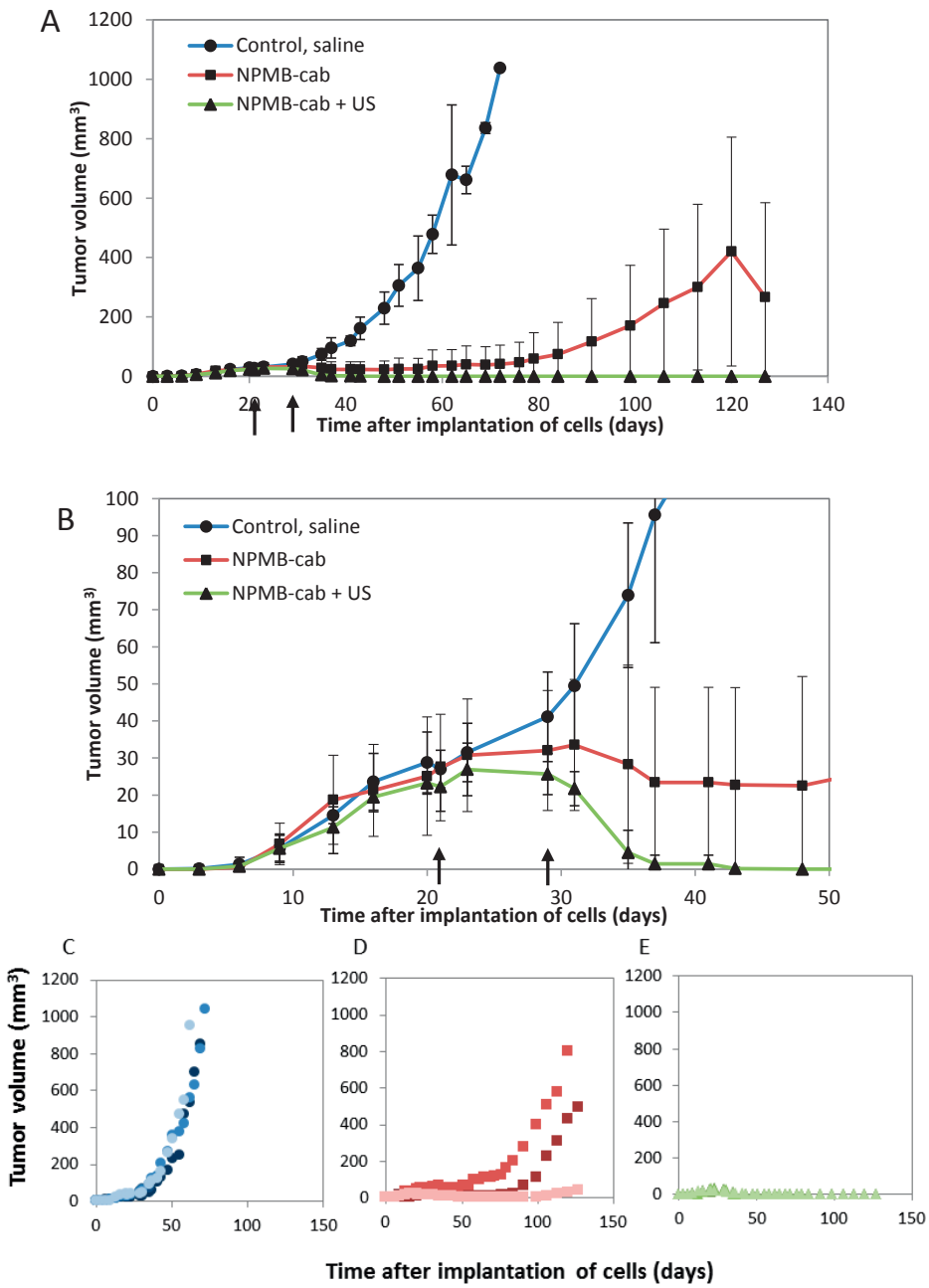

Figure 11: Tumor volume as a function of time after implantation of cells (day 0). Mice were treated with saline, NPMB with cabazitaxel, or NPMB with cabazitaxel and FUS (A). Treatments were performed at day 21 and 29 (arrows). Data are shown as mean and standard deviation from n=4 animals in each group until day 35, and n=3 animals per group from day 37. A zoomed in figure is shown for the first 50 days (B). Data points for all the individual animals treated with saline (C), NPMB with cabazitaxel (D), or NPMB with cabazitaxel and US (E) are shown, with different colors representing different animals.

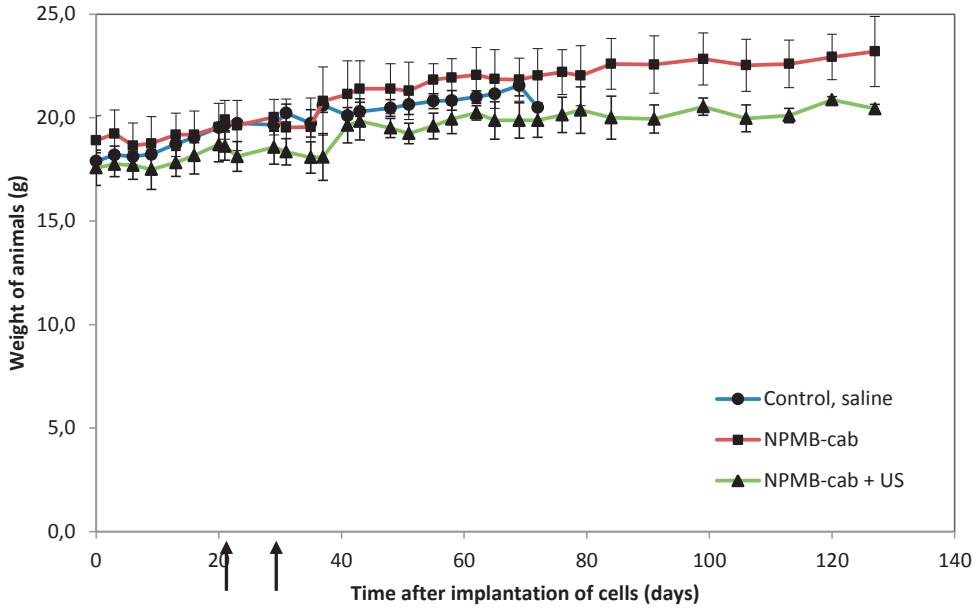

Figure 12: Weight of the treated animals after implantation of cells (day 0) and treatments with saline, NPMB with cabazitaxel, or NPMB with cabazitaxel and FUS. Treatments were performed at day 21 and 29 (arrows). Data are shown as mean and standard deviation from n=4 animals in each group until day 35, n=3 from day 37.

Discussion

In vivo circulation and biodistribution

In vivo circulation of NPs depends on particle material, shape, size, surface chemistry and charge, and varies significantly between different NP formulations (Alexis, et al. 2008, Longmire, et al. 2008). For efficient delivery, the NPs must circulate for a sufficient amount of time to accumulate in the target tissue, and avoid premature degradation and release of payload in blood. Ideally, NPs that are not delivered to the target should be cleared before the particles release the drug. A common strategy to increase circulation is PEGylation, which prevents aggregation and creates a water corona around the NP. Generally, the water corona reduces protein adsorption and opsonization, and thus prevents recognition by the reticuloendothelial system in liver and spleen (Harris and Chess 2003, Jokerst, et al. 2011). The majority of opsonized particles are cleared within a few minutes due to the high concentration of phagocytic cells in the liver and spleen, or they are excreted (Alexis, et al. 2008). However, it has recently also been reported that PEG can affect the composition of the protein corona that forms around nanocarriers, and that the presence of distinct proteins is necessary to prevent non-specific cellular uptake (Schottler, et al. 2016). The NPs used in the present work had a half-life of 136 min, which is more than three times that of their PBCA counterparts with similar PEGylation, as determined in our previous work (Åslund, et al. 2017). The increased circulation is likely due to increased PEGylation, a decreased degradation rate (Muller, et al. 1992, Sulheim, et al. 2016) and presumably a slower dissociation/release of PEG from the particle surface. The more hydrophobic polymer (PEBCA vs PBCA) could also give a stronger anchoring of the PEG, which is attached by hydrophobic interactions. Similar half-lives in the order of a few hours have been reported also by others, for PBCA NPs loaded with doxorubicin (Reddy and Murthy 2004) and for hexadecyl cyanoacrylate (PHDCA) NPs (Fang, et al. 2006).

The amount of NPs accumulating in the tumor was measured when the NPs were nearly cleared from the circulation (6 h post injection), and 1% of the injected NP dose was found to be located in the tumor. This corresponds well with the reported median of 0.7%, from a survey of 117 reports during the past 10 years (Wilhelm, et al. 2016) and with reported liposome uptake in human tumors (Harrington, et al. 2001). This is a clear improvement compared to what has been reported for chemotherapeutic drugs, where only 0.01 to 0.001% of the injected drug reaches the tumor (Gerber, et al. 2009, Kurdziel, et al. 2011). The majority of the NPs was found in the liver and spleen, which corresponds well with the literature (Douglas, et al. 1986, Harrington, et al. 2001, Owens and Peppas 2006, Tang, et al. 2014, Wilhelm, et al. 2016), and would also be expected since these organs are responsible for clearing particles with sizes larger than 100 nm (Alexis, et al. 2008, Desai 2012). As expected, less NPs were localized in the kidneys, likely because the NPs don't degrade much during this time period (Sulheim, et al. 2016).

The MBs were injected intravenously, and could be imaged both in venous and arterial circulation using a pre-clinical US scanner. In the tumor tissue, NPMBs could be detected for approximately 4-5 min, which is comparable to other commercial MBs (Hyvelin, et al. 2013). The wash-out of MBs is due to MB collapse and clearance from the vasculature

by reticuloendothelial system capture (Hyvelin, et al. 2013). We cannot exclude that, in addition to circulating MBs, some MBs might be adhering to the microvasculature.

In vitro cellular uptake and toxicity

The uptake of PACA NPs has been observed to vary greatly between different cell lines and for NPs of different polymers (Sulheim, et al. 2016). The efficient *in vitro* uptake of the PEBCA NPs observed for the MDA-MB-231 breast cancer cell line, indicates that once the NPs have reached the tumor interstitium, they can effectively be taken up by the breast cancer cells. Once the NPs have been internalized, they should eventually degrade in order to release the cytostatic cargo. Based on the *in vitro* toxicity, this cell line responds well to the drug, and the encapsulated drug is also efficient. If the NPs were not internalized, alternative mechanisms would be that the NPs degrade and release the drug extracellularly, followed by cellular uptake of the free drug, or that the drug is delivered by direct contact-mediated transfer into cells which has been observed for other hydrophobic model drugs (Snipstad, et al. 2014).

Ultrasound-enhanced delivery of nanoparticles

To determine the optimal treatment for this NPMB and achieve enhanced delivery of NPs to the tumor tissue, various US treatments were investigated. Understanding the cavitation processes is crucial to maximize efficiency and safety in US-mediated drug delivery. The response of a MB to US depends highly on the frequency, pressure level and pulse duration (Lammertink, et al. 2015, Lentacker, et al. 2014), as well as properties of the MB such as size, shell thickness and stiffness (Lentacker, et al. 2014). The effect of US-mediated delivery of NPs also depends on tumor characteristics as the barriers for delivery of nanomedicine can vary greatly between tumor types.

In the breast cancer model used here, lower acoustic pressures (MI of 0.1 or 0.25) did not enhance tumor uptake of NPs. Acoustic characterization (data not shown) and *in vitro* US contrast imaging of NPMBs have shown that the NPMBs are acoustically active and oscillate at these pressure levels, and that there is partial destruction at an MI of 0.25 (Berg, et al.). Still, these low pressures did not affect the vascular permeability enough to allow extravasation of NPs *in vivo*. It has been suggested that US intensities may be adapted to create pore sizes which correlate with drug size (Lentacker, et al. 2014), and that delivery of larger agents such as NPs may require higher US pressures compared to delivery of low molecular weight drugs (Wang, et al. 2015).

At higher acoustic pressure (MI of 0.5 and 1), the delivery of NPs to tumors was improved, indicating that complete destruction of the NPMB is necessary for enhanced permeability. At an MI of 0.5, there was a significantly improved tumor accumulation; the amount of NPs delivered was in average 2.3 times higher than the non-treated group. If the MB is located close enough to the capillary wall, the oscillating and collapsing MB will induce forces on the endothelial cells through shear stresses, fluid streaming, shock waves and jet streams. The increased extravasation and distribution of NPs are thus likely due to one or a combination of the following; increased vascular permeability through increased number of fenestrations, increased endocytosis/exocytosis of NPs in endothelial cells, or increased fluid convection in the vasculature and interstitium (Burke, et al. 2014, Frenkel 2008,

Lentacker, et al. 2014). The variation in NP accumulation within treatment groups is likely due to different amount of vasculature between different animals, as well as variations in leakiness of the vasculature, and different size of the necrotic core. The short flash of MI 1 did not improve the uptake of NPs, demonstrating that a longer pulse is needed. The longer pulse might push the MB towards the vessel wall, possibly resulting in a closer proximity to the endothelial cells at the time of the burst of the MB. During the long pulse, the NPMB will burst, and the released gas can form new and possibly smaller MBs, which again will oscillate and potentially coalesce. Altogether, long pulses facilitate sustained bioeffects from the oscillating bubbles.

Except for the highest MI (1.0), which caused substantial visual hemorrhage, evaluation of HES stained tumor sections showed that all other FUS treatments can be considered safe. When bleeding is induced due to inertial cavitation, a high amount of extravasated NPs would also be expected. The fact that tissue damage was observed at MI 1, but not at 0.5, suggests that the threshold for inertial cavitation is above 0.5 for our NPMBs. This indicates a window where enhanced accumulation can be achieved without damaging the tissue, at an MI of 0.5.

FUS mediated delivery of NPs to tumor tissue has been reported by others using even higher MIs than used here. High pressure (1 MHz, 1.2 MPa) was used by Lin *et al.* (Lin, et al. 2010) to deliver lipid-coated quantum dots by pulsed FUS and SonoVue, where they concluded that they effectively enhanced the vascular permeability in the sonicated tumors. They reported no cellular damage in the sonicated tumors. They did however use a slightly lower duty cycle of 1%. The same treatment was used to increased delivery of PEGylated liposomal doxorubicin (Lin, et al. 2012). Wang *et al.* (Wang, et al. 2015) hypothesized that delivery of nanocarriers, of a size similar to those used in our work, required inertial cavitation. They used a subcutaneous, well vascularized xenograft of human colon cancer in mice, and found that the amount of NPs delivered increased with increasing acoustic pressures. They reported that US induced only minimal tissue damage, but slightly increased hemorrhage was observed with higher acoustic pressures (1.8 MHz, 0-6.9 MPa). They used 1000 bursts of 5 cycles delivered at a PRF of 100 Hz.

The direct association between the NPs and MB will probably result in a higher local concentration of NPs when the MBs are destroyed, compared to co-injection of NPs and MBs. Burke *et al.*(Burke, et al. 2014) used poly(lactic-co-glycolic acid) (PLGA) NPs linked to MBs, and showed that ultrasonic activation of the MBs increased delivery to the tumor, and that the loaded drug 5-fluorouracil could reduce tumor growth and prolong survival in mice with subcutaneous, well-vascularized C6 gliomas. Their NPs were of similar size to those used here, and they showed that coupling the NP to MBs resulted in more efficient delivery compared to a co-injection of NPs and MBs.

Treatment of tumors with nanoparticle-microbubbles loaded with cabazitaxel

The efficient reduction in tumor growth using our NPMBs in combination with FUS, is highly promising for enhanced, localized delivery of encapsulated chemotherapeutic drugs. The tumors treated with NPMB with cabazitaxel and FUS went into complete remission. This is probably due to the enhanced accumulation and improved distribution of NPs, observed after FUS exposure of MI 0.5, and the effective cellular uptake.

All tumors treated with NPMB encapsulating cabazitaxel, but no FUS, responded to treatment, and showed a reduced growth compared to control animals. They were in stable remission until approximately 80 days after implantation (50 days after treatment end), before starting to regrow with large variation between the animals. The improved therapeutic response combining FUS with NPMBs, compared to NPMB administrated alone, indicates that the EPR-effect for the NPs was not sufficient on its own. This could be due to low vascular density and permeability, as well as necrotic regions. Cabazitaxel, like the other taxanes, binds to tubulin molecules, and thus inhibit microtubule depolymerization, thereby blocking mitosis and causing cell death (McGrogan, et al. 2008, Vrignaud, et al. 2014, Vrignaud, et al. 2013). Cabazitaxel has been shown effective against tumors with resistance to other taxanes, and predominantly affects tissue with a high cell turnover. It is thus possible that some quiescent cells respond less, causing the observed variations between tumors. For the treatment to be curative, every single cell must be eradicated. However, cancer cells with therapeutic resistance, such as hypoxic cells or cancer stem cells, may reside in perinecrotic and/or hypoxic regions and niches displaying low accumulation of nanocarriers (Hansen, et al. 2015).

Regarding safety and toxicity of the treatment, weight loss, which is a common side effect of treatment with cytostatic drugs, was not observed for any of the treatments, nor was FUS-induced bleeding observed using an MI at 0.5.

FUS treatment with MBs and nanomedicine could possibly be used as a curative treatment, as neoadjuvant chemotherapy for solid tumors followed by surgical resection, or in combination with/after surgery or radiation to remove residual cells. The first clinical phase I trial combining FUS and MBs with chemotherapy has already been reported, where 10 patients with inoperable, locally advanced pancreatic cancer received an infusion of gemcitabine, followed by SonoVue injected intravenously during US treatment (Georg Dimcevski, et al. 2016). Altogether, these results illustrate the potential of combining FUS with MBs for increased efficacy of therapeutic drugs, and indicates that our NPMB is a promising novel platform for such applications.

Conclusion

US sonication and destruction of NPMBs was found to substantially improve the accumulation and distribution of NPs in tumors, at a safe pressure level. US in combination with the NPMBs encapsulating cabazitaxel resulted in complete, stable remission in all treated animals, clearly showing that this unique NPMB platform is very useful for controlled drug delivery.

Acknowledgements

Dr. Andrey Klymchenko is acknowledged for kindly providing NR668, and Kristin Sæterbø, Andreas Åslund, Anne Rein Hatletveit, Maria Gellein, Sven Even Borgos and Kai Vernstad for technical support. Housing and care of animals was provided by the Comparative Medicine Core Facility (CoMed) and tissue sections were prepared by the Cellular and Molecular Imaging Core Facility (CMIC), both at NTNU. The project was funded by The Central Norway Regional Health Authorities and The Research Council of Norway (240410/F20 Multibubble and 254832/O70 BubbleCAN).

Competing interests

The authors declare no conflict of interest.

References

Afadzi M, Strand SP, Nilssen EA, Måsøy SE, Johansen TF, Hansen R, Angelsen BA, Davies CdL. Mechanisms of the ultrasound-mediated intracellular delivery of liposomes and dextrans. IEEE Trans Ultrason Ferroelectr Freq Control 2013; 60:21-33.

Alexis F, Pridgen E, Molnar LK, Farokhzad OC. Factors affecting the clearance and biodistribution of polymeric nanoparticles. Mol Pharm 2008; 5:505-15.

Anchordoquy TJ, Barenholz Y, Boraschi D, Chorny M, Decuzzi P, Dobrovolskaia MA, Farhangrazi ZS, Farrell D, Gabizon A, Ghandehari H, Godin B, La-Beck NM, Ljubimova J, Moghimi SM, Pagliaro L, Park JH, Peer D, Ruoslahti E, Serkova NJ, Simberg D. Mechanisms and Barriers in Cancer Nanomedicine: Addressing Challenges, Looking for Solutions. ACS nano 2017.

Åslund AKO, Berg S, Hak S, Mørch Ý, Torp SH, Sandvig A, Widerøe M, Hansen R, Davies CdL. Nanoparticle delivery to the brain--By focused ultrasound and self-assembled nanoparticle-stabilized microbubbles. J Control Release 2015; 220:287-94.

Åslund AKO, Sulheim E, Snipstad S, von Haartman E, Baghirov H, Starr NJ, Kvåle Løvmo M, Lelu S, Scurr DJ, Davies CdL, Schmid RB, Mørch ÝA. Quantification and qualitative effects of different PEGylations on PBCA nanoparticles. Mol Pharm 2017.

Baghirov H, Melikishvili S, Mørch Y, Sulheim E, Åslund AKO, Hianik T, Davies CdL. The effect of poly(ethylene glycol) coating and monomer type on poly(alkyl cyanoacrylate) nanoparticle interactions with lipid monolayers and cells. Colloids Surf B Biointerfaces 2017; 150:373-83.

Berg S, Afadzi M, Sulheim E, Mørch Y, Hatletveit A, Bjørkøy A, Davies CdL, Hansen R. Acoustic characterization of nanoparticle-stabilized microbubbles for drug delivery. Manuscript in preparation, to be submitted to Ultrasound Med Biol.

Burgess A, Ayala-Grosso CA, Ganguly M, Jordao JF, Aubert I, Hynynen K. Targeted delivery of neural stem cells to the brain using MRI-guided focused ultrasound to disrupt the blood-brain barrier. PloS one 2011; 6:e27877.

Burke CW, Alexander Et, Timbie K, Kilbanov AL, Price RJ. Ultrasound-activated agents comprised of 5FU-bearing nanoparticles bonded to microbubbles inhibit solid tumor growth and improve survival. Mol Ther 2014; 22:321-8.

Carpentier A, Canney M, Vignot A, Reina V, Beccaria K, Horodyckid C, Karachi C, Leclercq D, Lafon C, Chapelon JY, Capelle L, Cornu P, Sanson M, Hoang-Xuan K, Delattre JY, Idbaih A. Clinical trial of blood-brain barrier disruption by pulsed ultrasound. Sci Transl Med 2016; 8.

Chauhan VP, Stylianopoulos T, Boucher Y, Jain RK. Delivery of molecular and nanoscale medicine to tumors: transport barriers and strategies. Annu Rev Chem Biomol Eng 2011; 2:281-98.

Desai N. Challenges in development of nanoparticle-based therapeutics. AAPS J 2012; 14:282-95.

Douglas SJ, Davis SS, Illum L. Biodistribution of Poly(Butyl 2-Cyanoacrylate) Nanoparticles in Rabbits. Int J Pharm 1986; 34:145-52.

Downs ME, Buch A, Karakatsani ME, Konofagou EE, Ferrera VP. Blood-Brain Barrier Opening in Behaving Non-Human Primates via Focused Ultrasound with Systemically Administered Microbubbles. Sci Rep-Uk 2015; 5.

Eggen S, Fagerland SM, Mørch Ý, Hansen R, Søvik K, Berg S, Furu H, Bohn AD, Lilledahl MB, Angelsen A, Angelsen B, Davies CdL. Ultrasound-enhanced drug delivery in prostate cancer xenografts by nanoparticles stabilizing microbubbles. J Control Release 2014; 187:39-49.

Elder SA. Cavitation Microstreaming. J. Acoust. Soc. Am. 1959; 31:54-64.

Etheridge ML, Campbell SA, Erdman AG, Haynes CL, Wolf SM, McCullough J. The big picture on nanomedicine: the state of investigational and approved nanomedicine products. Nanomedicine-Uk 2013; 9:1-14.

Fang C, Shi B, Pei YY, Hong MH, Wu J, Chen HZ. In vivo tumor targeting of tumor necrosis factor-alpha-loaded stealth nanoparticles: effect of MePEG molecular weight and particle size. Eur J Pharm Sci 2006; 27:27-36.

Fenwick N, Griffin G, Gauthier C. The welfare of animals used in science: how the "Three Rs" ethic guides improvements. Can Vet J 2009; 50:523-30.

Frenkel V. Ultrasound mediated delivery of drugs and genes to solid tumors. Adv Drug Deliv Rev 2008; 60:1193-208.

Georg Dimcevski, Spiros Kotopoulis, Tormod Bjånes, Dag Hoem, Jan Schjøt, Bjørn Tore Gjertsen, Martin Biermann, Anders Molven, Halfdan Sorbye, Emmet McCormack, Michiel Postema, Gilja OH. A human clinical trial using ultrasound and microbubbles to enhance gemcitabine treatment of inoperable pancreatic cancer. J Control Release 2016; doi: 10.1016/j.jconrel.2016.10.007.

Gerber HP, Senter PD, Grewal IS. Antibody drug-conjugates targeting the tumor vasculature Current and future developments. Mabs 2009; 1:247-53.

Hanahan D, Weinberg RA. Hallmarks of cancer: the next generation. Cell 2011; 144:646-74.

Hansen AE, Petersen AL, Henriksen JR, Boerresen B, Rasmussen P, Elema DR, Rosenschold PM, Kristensen AT, Kjaer A, Andresen TL. Positron Emission Tomography Based Elucidation of the Enhanced Permeability and Retention Effect in Dogs with Cancer Using Copper-64 Liposomes. ACS nano 2015; 9:6985-95.

Harrington KJ, Mohammadtaghi S, Uster PS, Glass D, Peters AM, Vile RG, Stewart JS. Effective targeting of solid tumors in patients with locally advanced cancers by radiolabeled pegylated liposomes. Clin Cancer Res 2001; 7:243-54.

Harris JM, Chess RB. Effect of pegylation on pharmaceuticals. Nat Rev Drug Discov 2003; 2:214-21.

He C, Chan C, Weichselbaum RR, Fleming GF, Yamada SD, Lin W. Nanomedicine for Combination Therapy of Cancer. EBioMedicine 2015; 2:366-7.

Heath CH, Sorace A, Knowles J, Rosenthal E, Hoyt K. Microbubble Therapy Enhances Anti-tumor Properties of Cisplatin and Cetuximab In Vitro and In Vivo. Otolaryng Head Neck 2012; 146:938-45.

Hynynen K, McDannold N, Vykhodtseva N, Jolesz FA. Noninvasive MR imaging-guided focal opening of the blood-brain barrier in rabbits. Radiology 2001; 220:640-6.

Hyvelin JM, Tardy I, Arbogast C, Costa M, Emmel P, Helbert A, Theraulaz M, Nunn AD, Tranquart F. Use of Ultrasound Contrast Agent Microbubbles in Preclinical Research Recommendations for Small Animal Imaging. Invest Radiol 2013; 48:570-83.

Jokerst JV, Lobovkina T, Zare RN, Gambhir SS. Nanoparticle PEGylation for imaging and therapy. Nanomedicine-Uk 2011; 6:715-28.

Klymchenko AS, Roger E, Anton N, Anton H, Shulov I, Vermot J, Mely Y, Vandamme TF. Highly lipophilic fluorescent dyes in nano-emulsions: towards bright non-leaking nano-droplets. Rsc Adv 2012; 2:11876-86.

Kotopoulis S, Delalande A, Popa M, Mamaeva V, Dimcevski G, Gilja OH, Postema M, Gjertsen BT, McCormack E. Sonoporation-enhanced chemotherapy significantly reduces primary tumour burden in an orthotopic pancreatic cancer xenograft. Mol Imaging Biol 2014; 16:53-62.

Kurdziel KA, Kalen JD, Hirsch JI, Wilson JD, Bear HD, Logan J, McCumisky J, Moorman-Sykes K, Adler S, Choyke PL. Human Dosimetry and Preliminary Tumor Distribution of F-18-Fluoropaclitaxel in Healthy Volunteers and Newly Diagnosed Breast Cancer Patients Using PET/CT. J Nucl Med 2011; 52:1339-45.

Lammers T, Kiessling F, Hennink WE, Storm G. Nanotheranostics and image-guided drug delivery: current concepts and future directions. Mol Pharm 2010; 7:1899-912.

Lammertink BH, Bos C, Deckers R, Storm G, Moonen CT, Escoffre JM. Sonochemotherapy: from bench to bedside. Front Pharmacol 2015; 6:138.

Lentacker I, De Cock I, Deckers R, De Smedt SC, Moonen CT. Understanding ultrasound induced sonoporation: definitions and underlying mechanisms. Adv Drug Deliv Rev 2014; 72:49-64.

Lin CY, Huang YL, Li JR, Chang FH, Lin WL. Effects of focused ultrasound and microbubbles on the vascular permeability of nanoparticles delivered into mouse tumors. Ultrasound Med Biol 2010; 36:1460-9.

Lin CY, Li JR, Tseng HC, Wu MF, Lin WL. Enhancement of focused ultrasound with microbubbles on the treatments of anticancer nanodrug in mouse tumors. Nanomedicine-Uk 2012; 8:900-7.

Longmire M, Choyke PL, Kobayashi H. Clearance properties of nano-sized particles and molecules as imaging agents: considerations and caveats. Nanomedicine (Lond) 2008; 3:703-17.

Maeda H. Toward a full understanding of the EPR effect in primary and metastatic tumors as well as issues related to its heterogeneity. Adv Drug Deliv Rev 2015; 91:3-6.

Maeda H, Wu J, Sawa T, Matsumura Y, Hori K. Tumor vascular permeability and the EPR effect in macromolecular therapeutics: a review. J Control Release 2000; 65:271-84.

Marquet F, Tung YS, Teichert T, Ferrera VP, Konofagou EE. Noninvasive, transient and selective blood-brain barrier opening in non-human primates in vivo. PloS one 2011; 6:e22598.

McGrogan BT, Gilmartin B, Camey DN, McCann A. Taxanes, microtubules and chemoresistant breast cancer. Bba-Rev Cancer 2008; 1785:96-132.

Meijering BD, Juffermans LJ, van Wamel A, Henning RH, Zuhorn IS, Emmer M, Versteilen AM, Paulus WJ, van Gilst WH, Kooiman K, de Jong N, Musters RJ, Deelman LE, Kamp O. Ultrasound and microbubble-targeted delivery of macromolecules is regulated by induction of endocytosis and pore formation. Circ Res 2009; 104:679-87.

Muller RH, Lherm C, Herbort J, Blunk T, Couvreur P. Alkylcyanoacrylate Drug Carriers .1. Physicochemical Characterization of Nanoparticles with Different Alkyl Chain-Length. Int J Pharm 1992; 84:1-11.

Mørch Ý, Hansen R, Berg S, Åslund AKO, Glomm WR, Eggen S, Schmid R, Johnsen H, Kubowicz S, Snipstad S, Sulheim E, Hak S, Singh G, McDonagh BH, Blom H, Davies CdL, Stenstad PM. Nanoparticle-Stabilized Microbubbles for Multimodal Imaging and Drug Delivery. Contrast Media Mol Imaging 2015; 10:356-66.

Nicolas J, Couvreur P. Synthesis of poly(alkyl cyanoacrylate)-based colloidal nanomedicines. Wiley Interdiscip Rev Nanomed and Nanobiotechnol 2009; 1:111-27.

Owens DE, Peppas NA. Opsonization, biodistribution, and pharmacokinetics of polymeric nanoparticles. Int J Pharm 2006; 307:93-102.

Padera TP, Stoll BR, Tooredman JB, Capen D, di Tomaso E, Jain RK. Pathology: cancer cells compress intratumour vessels. Nature 2004; 427:695.

Pitt WG, Husseini GA, Staples BJ. Ultrasonic drug delivery--a general review. Expert Opin Drug Deliv 2004; 1:37-56.

Prabhakar U, Maeda H, Jain RK, Sevick-Muraca EM, Zamboni W, Farokhzad OC, Barry ST, Gabizon A, Grodzinski P, Blakey DC. Challenges and key considerations of the enhanced permeability and retention effect for nanomedicine drug delivery in oncology. Cancer Res 2013; 73:2412-7.

Reddy LH, Murthy RS. Pharmacokinetics and biodistribution studies of Doxorubicin loaded poly(butyl cyanoacrylate) nanoparticles synthesized by two different techniques. Biomed Pap Med Fac Univ Palacky Olomouc Czech Repub 2004; 148:161-6.

Schottler S, Becker G, Winzen S, Steinbach T, Mohr K, Landfester K, Mailander V, Wurm FR. Protein adsorption is required for stealth effect of poly(ethylene glycol)- and poly(phosphoester)-coated nanocarriers. Nat Nanotechnol 2016; 11:372-77.

Semiond D, Sidhu SS, Bissery MC, Vrignaud P. Can taxanes provide benefit in patients with CNS tumors and in pediatric patients with tumors? An update on the preclinical development of cabazitaxel. Cancer Chemother Pharmacol 2013; 72:515-28.

Snipstad S, Hak S, Baghirov H, Sulheim E, Mørch Ý, Lélu S, von Haartman E, Bäck M, Nilsson KPR, Klymchenko AS, Davies CdL, Åslund AKO. Labeling nanoparticles: Dye leakage and altered cellular uptake. Cytometry 2016; doi: 10.1002/cyto.a.22853.

Snipstad S, Westrøm S, Mørch Ý, Afadzi M, Åslund AKO, Davies CdL. Contact-mediated intracellular delivery of hydrophobic drugs from polymeric nanoparticles. Cancer Nanotechnol 2014; 5.

Soma E, Attali P, Merle P. CHAPTER 11: A Clinically Relevant Case Study: the Development of Livatag for the Treatment of Advanced Hepatocellular Carcinoma. Nanostructured Biomaterials for Overcoming Biological Barriers. 2012; The Royal Society of Chemistry:591-600.

Sulheim E, Baghirov H, von Haartman E, Bøe A, Åslund AKO, Mørch Ý, Davies CdL. Cellular uptake and intracellular degradation of poly(alkyl cyanoacrylate) nanoparticles. J Nanobiotechnology 2016; 8.

Tang L, Yang XJ, Yin Q, Cai KM, Wang H, Chaudhury I, Yao C, Zhou Q, Kwon M, Hartman JA, Dobrucki IT, Dobrucki LW, Borst LB, Lezmig S, Helferich WG, Ferguson AL, Fan TM, Cheng JJ. Investigating the optimal size of anticancer nanomedicine. P Natl Acad Sci USA 2014; 111:15344-49.

Taurin S, Nehoff H, Greish K. Anticancer nanomedicine and tumor vascular permeability; Where is the missing link? J Control Release 2012; 164:265-75.

van Wamel A, Sontum PC, Healey A, Kvåle S, Bush N, Bamber J, Davies CdL. Acoustic Cluster Therapy (ACT) enhances the therapeutic efficacy of paclitaxel and Abraxane® for treatment of human prostate adenocarcinoma in mice. J Control Release 2016; 236:15-21.

Vauthier C, Dubernet C, Fattal E, Pinto-Alphandary H, Couvreur P. Poly(alkylcyanoacrylates) as biodegradable materials for biomedical applications. Adv Drug Deliv Rev 2003; 55:519-48.

Vauthier C, Labarre D, Ponchel G. Design aspects of poly(alkylcyanoacrylate) nanoparticles for drug delivery. J Drug Target 2007; 15:641-63.

Vrignaud P, Semiond D, Benning V, Beys E, Bouchard H, Gupta S. Preclinical profile of cabazitaxel. Drug Des Dev Ther 2014; 8:1851-67.

Vrignaud P, Semiond D, Lejeune P, Bouchard H, Calvet L, Combeau C, Riou JF, Commercon A, Lavelle F, Bissery MC. Preclinical Antitumor Activity of Cabazitaxel, a Semisynthetic Taxane Active in Taxane-Resistant Tumors. Clin Cancer Res 2013; 19:2973-83.

Wang TY, Choe JW, Pu KY, Devulapally R, Bachawal S, Machtaler S, Chowdhury SM, Luong R, Tian L, Khuri-Yakub B, Rao JH, Paulmurugan R, Willmann JK. Ultrasound-guided delivery of microRNA loaded nanoparticles into cancer. J Control Release 2015; 203:99-108.

Wilhelm S, Tavares AJ, Dai Q, Seiichi O, Audet J, Dvorak HF, Chan WCW. Analysis of nanoparticle delivery to tumours. Nat Rev Mater 2016; 1:1-12.

Supplementary information

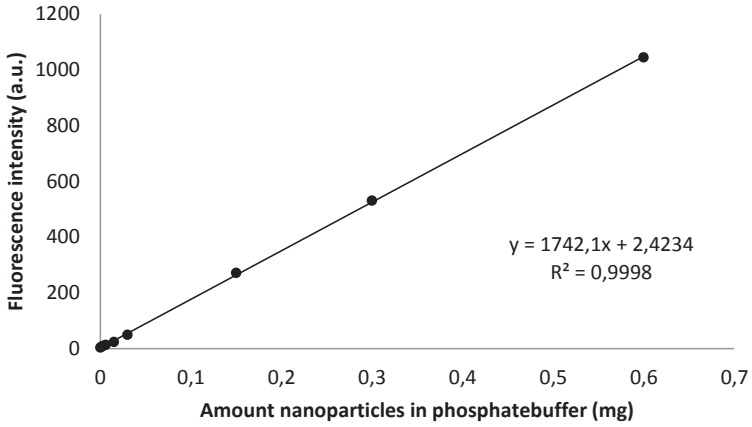

Figure S1: Dilution series of NPMBs with IR-780 lipid imaged in whole animal scanner, various concentrations in a known volume, and fluorescence determined from ROIs in imageJ. The curve was used as a standard curve in biodistribution studies to quantify amount of NPs accumulated in different tissues.

Table S1: Biodistribution of NPs in the different organs, tumor and brain (n=4-7 animals). The accumulated dose per organ is shown (ug NPs/mg tissue), together with the weight of each organ. The total dose of µg NPs in each organ, and the percentage of the total dose in the respective organs are given. All numbers are given as mean and standard deviation.

	Spleen	Liver	Kidney	Heart	Lungs	Tumor	Brain
µg NPs/ mg tissue	1.86±0.39	1.52±0.35	0.11±0.01	0.07±0.02	0.33±0.12	0.16±0.05	0.03±0.00
Weight (mg tissue)	140±27	908±93	119±13	105±6	123±14	125±22	335±24
Total dose (µg NPs)	260±74	1380±350	26±4*	7±2	41±16	20±7	10±1
Percentage of dose	13±3.7	69±17.5	1.3±0.2*	0.35±0.1	2 ±0.8	1±0.35	0.5±0.05

*The dose measured in one kidney was multiplied with 2 to determine the total dose in the kidneys.

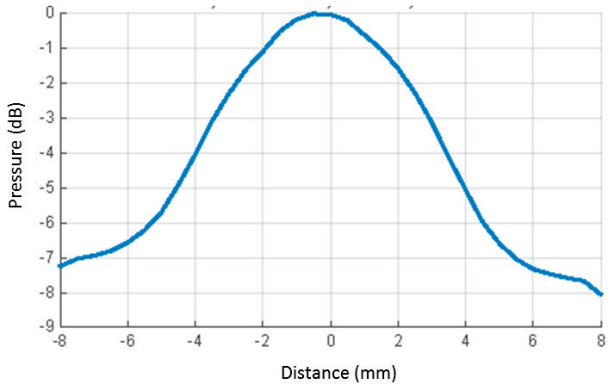

Figure S2: US characterization beam profile, shows a line scan of intensity at a distance of 190 mm from the Imasonic transducer.

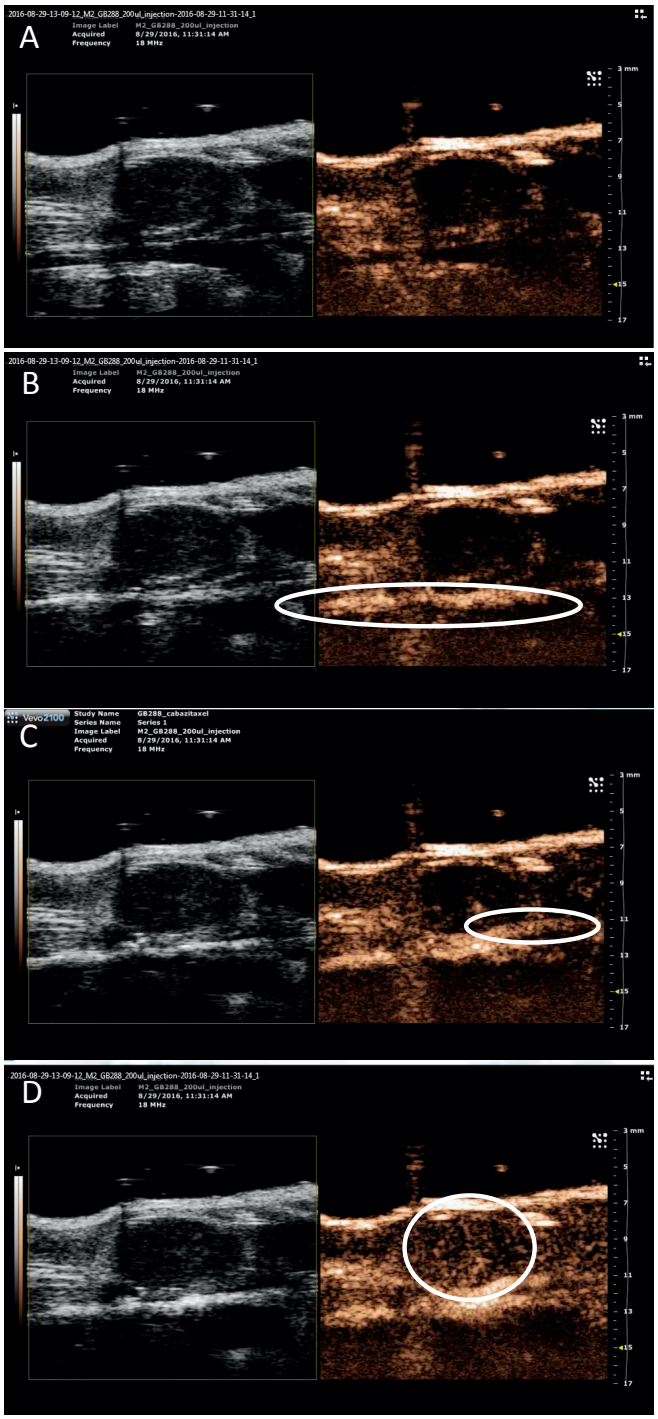

Figure S3: The kidney of a mouse imaged using US pre and post injection of NPMB loaded with cabazitaxel. The pre image (A) is followed by an image showing venous inflow (B), arterial flow (C) and filling of the kidney (D). Areas of interest are highlighted using white circles.

Paper IV

Ultrasound-mediated delivery and distribution of polymeric nanoparticles in the normal brain parenchyma and melanoma metastases

Habib Baghirov[a], Sofie Snipstad[a], Einar Sulheim[a,b], Sigrid Berg[c,d], Rune Hansen[c,d], Frits Thorsen[e], Yrr Mørch[b], Catharina de Lange Davies[a], Andreas K.O. Åslund[a]*

[a] Department of Physics, The Norwegian University of Science and Technology (NTNU), 7491 Trondheim, Norway
[b] SINTEF Materials and Chemistry, 7465 Trondheim, Norway
[c] SINTEF Medical Technology, 7465 Trondheim, Norway
[d] Department of Circulation and Medical Imaging, The Norwegian University of Science and Technology (NTNU), 7491 Trondheim, Norway
[e]Molecular Imaging Center and Kristian Gerhard Jebsen Brain Tumour Research Centre, Department of Biomedicine, University of Bergen, 5020 Bergen, Norway

*Corresponding author. Tel.: +4773593688. Email: catharina.davies@ntnu.no

Abstract

Brain cancer treatment is hindered by the blood-brain barrier (BBB) preventing most chemotherapeutics from entering the brain. Focused ultrasound (FUS) with microbubbles can open the BBB safely and reversibly. Systemic drug injection might induce toxicity, but encapsulation into nanoparticles reduces accumulation in normal tissue. Here we used a novel platform based on poly(2-ethyl-butyl cyanoacrylate) nanoparticle-stabilized microbubbles to permeabilize the BBB in a melanoma brain metastasis model. With a dual-frequency ultrasound transducer generating FUS at 1.1 MHz and 7.8 MHz, we opened the BBB using nanoparticle-microbubbles and low-frequency FUS, and applied high-frequency FUS to generate acoustic radiation force and push nanoparticles through the extracellular matrix. Using confocal microscopy and image analysis, we quantified nanoparticle extravasation and distribution in the brain parenchyma. We also evaluated haemorrhage, as well as the expression of P-glycoprotein, a key BBB component. FUS and microbubbles distributed nanoparticles in the brain parenchyma, and the distribution depended on the extent of BBB opening. The results from acoustic radiation force were not conclusive, but in a few animals some effect could be detected. P-glycoprotein was not altered immediately after sonication. In summary, FUS with our nanoparticle-stabilized microbubbles can achieve accumulation and displacement of nanoparticles in the brain parenchyma.

Keywords: acoustic radiation force, blood-brain barrier, focused ultrasound, P-glycoprotein, poly(alkyl cyanoacrylate) nanoparticles

Introduction

Chemotherapeutic treatment of primary brain malignancies as well as metastatic brain tumours has so far shown only minimal effects on tumour growth and patient survival[1]. One of the obstacles hindering successful treatment is the blood-brain barrier (BBB) - a dynamic interface that protects the brain's internal milieu and filters out 98% of small molecular drugs (about 400-500 Da) and all large molecular drugs[2-4]. The passage of drugs across the BBB is blocked both paracellularly, due to tight junctions connecting endothelial cells, and transcellularly, in large part due to the action of multidrug resistance transporters such as P-glycoprotein (P-gp) located in the plasma membrane. One of the challenges in drug delivery across the BBB is accumulation of drugs in therapeutically relevant doses in the brain. This has precluded the advancement of several promising drug candidates to the clinic because, after systemic administration, the doses required to achieve a therapeutic effect were also prohibitively toxic[1].

Drug-loaded nanoparticles (NPs) have emerged as a powerful tool to reduce drug toxicity after systemic administration[5] and provide controlled and sustained release, targeting and functionalization[6]. In the case of solid tumours, NP-based drug delivery also benefits from the enhanced permeability and retention (EPR) effect whereby NPs are retained in the tumour mass due to its leaky neovasculature and reduced lymphatic drainage[7,8]. Poly(alkyl cyanoacrylate) (PACA) NPs have been shown to be promising drug carriers due to ease of synthesis and functionalization, as well as biodegradability[9,10]. These properties have recently allowed them to reach a Phase III clinical trial in advanced hepatocellular carcinoma (ReLive study, ClinicalTrials.gov Identifier: NCT01655693)[11]. In the case of brain malignancies, however, NP transport across the BBB is complicated even more than it is with small molecular drugs. Paracellular transport across an intact BBB is virtually impossible[12], and NP size is far above the passive transcellular transport threshold. Biofunctionalization of NPs with moieties conferring BBB transport properties, as well as the use of EPR in solid brain tumours do offer benefits, but the efficiency of the former approach is highly dependent on the carrier and the transport moiety, and the use of EPR has so far produced only a modest increase in drug accumulation[13].

Focused ultrasound (FUS) in combination with microbubbles (MBs) that are normally used in diagnostic ultrasonography has been shown to open the BBB safely and reversibly[14-16]. It has been employed to transport NPs across the BBB in several studies[17-20]. The use of MBs in combination with FUS to open the BBB was first demonstrated by Hynynen et al. in 2001[21] and is based on the volumetric oscillation of MBs in the proximity of blood vessels in the ultrasound (US) focus, causing a mechanical stress on the vessel wall and leading to enhanced extravasation. The use of MBs considerably reduced the acoustic power required for cavitation-dependent opening of the BBB by FUS alone, thereby enabling safe application of transcranial US. Our group has recently demonstrated FUS-mediated BBB opening using a platform consisting of PACA NP-stabilized gas-filled MBs[22]. Evaluation of efficiency as a platform for brain drug delivery requires thorough assessment of NP transport across the BBB.

Another matter that merits attention is the fate of extravasated NPs. Penetrating the extracellular matrix (ECM) to reach target cells is no trivial task for NPs due to their size[23].

Without efficient penetration of the ECM, drug delivery will have to rely on NP degradation or release of drugs in the ECM with subsequent drug diffusion. This renders a number of potential NP benefits inapplicable, such as targeting to or controlled release within target cells. While FUS-induced cavitation of MBs in the proximity of brain endothelium can disrupt the BBB and facilitate NP transport into the brain, it can also potentially push NPs further through the ECM. Acoustic radiation force (ARF) produced by high frequency, high intensity and highly focused US, causes a transfer of momentum from the US wave to the propagation medium and can potentially increase the displacement of NPs in the ECM. ARF has primarily been used to improve targeting of MBs[24,25] or for improved drug delivery using drug-loaded or drug-decorated MBs[26,27]. Compared to NPs, MBs are large and highly compressible, and they therefore experience a much larger effect caused by ARF. In a limited number of studies, ARF was used for drug delivery with liquid NPs[28,29].

Since P-gp is the key component of the BBB, restricting the passage of many small and lipophilic molecules, including drugs, by pumping them back into the bloodstream[2], it is also important to assess how FUS treatment affects P-gp in the brain. Recent studies have found that FUS induces down-regulation of P-gp *in vivo* after 24 hours[30] and after 1 hour[31]. At this time point, FUS-mediated P-gp down-regulation may involve delayed onset mechanisms, and it may also be informative to study the immediate effect of FUS on P-gp expression.

In this study, we used a novel US system that can generate FUS at two frequencies, with magnetic resonance imaging (MRI) guided selection of the exposure area. 1.1 MHz was used in combination with a poly(2-ethyl-butyl cyanoacrylate) (PEBCA)-based NP-MB platform to open the BBB and deliver the NPs into the brain parenchyma and to melanoma brain metastases. In addition, 7.8 MHz was employed to generate ARF and investigate whether it could push NPs through the ECM away from blood vessels. We also evaluated how FUS at 1.1 MHz affected the expression of P-gp in the brain tissue immediately post-sonication. We verified BBB opening and quantified NP extravasation and distribution in the brain parenchyma in relation to the extent of BBB opening. Our results show the potential of our novel PACA NP-MB platform for FUS-mediated drug delivery across the BBB and through the brain tissue.

Results

Characterization of the PEBCA NP-MB platform

The synthesized PEBCA NPs were analysed using dynamic light scattering (DLS) and had a Z-average of 274 nm and polydispersity index of 0.25 while the ζ-potential was 0 mV. The MBs had a mean size of 1.6±0.85 μm (Supplementary Figure 2) and a mean concentration of 4.5E8±1.0E8 MBs/ml.

Development of melanoma brain metastases

Melanoma brain metastases were detected using T1-RARE MRI at 28±2 days after intracardiac injection of tumour cells. Due to the metal scavenging properties of melanin[32] that is highly abundant in the tumours, the metastases were visible in MRI images without any contrast

enhancement (Figure 1a). Metastatic tumours were also visible in the histological examination of formalin-fixed paraffin-embedded sections, in line with the results reported in[33] (Figure 1b), as well as in confocal laser scanning microscopy (CLSM) images of cryosections (Figure 1c). In the CLSM images and haematoxylin and eosin (H&E)-stained sections, the metastases appeared at higher cell density and with larger nuclei than normal brain cells. We did not evaluate leakiness of the metastases; however, an earlier study has shown that the percentage of leaky tumours at week 4 was about 1%[33].

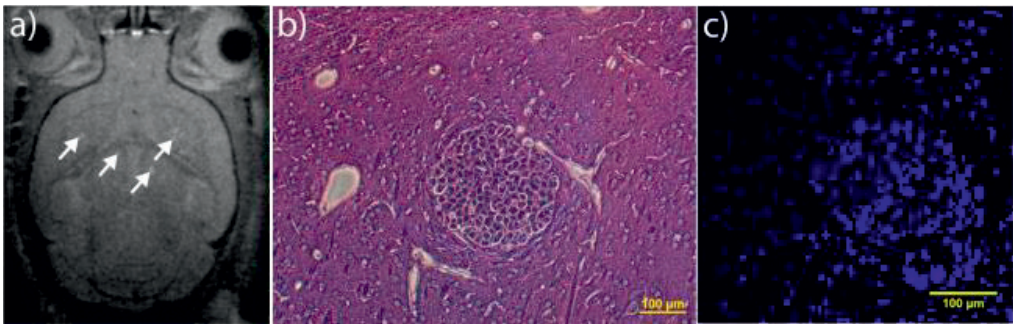

Fig. 1. Melanoma brain metastases 4 weeks after tumour cell inoculation. Metastatic tumours are visible in a) T1 RARE MR images without contrast enhancement (some tumours are indicated by arrows), b) H&E-stained sections, as a spherical group of cells, c) CSLM with nuclei counterstaining, as a cluster of tightly packed nuclei.

FUS-mediated BBB opening

FUS-mediated BBB opening was observed in all animals in all groups, but its extent, assessed using signal intensity in T1 FLASH images, varied between the animals (Figure 2 a-c).

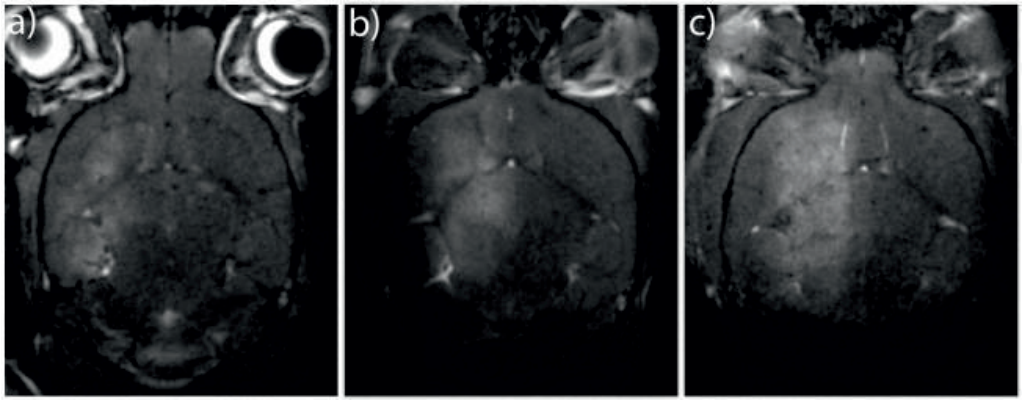

Fig 2 FUS-mediated BBB opening with PEBCA NP-MBs. Different extents of BBB opening are shown in panels a-c). The three brains show increasing amount of gadolinium-based contrast in the treated region, from hardly any contrast a), to large areas of high intensity contrast c) compared to the non-treated contralateral hemisphere. MRI images were normalized so that areas not exposed to FUS in different images have a comparable intensity.

T1 FLASH images from MRI demonstrated some extent of red blood cell (RBC) extravasation. This was also evident from tile scans of histological brain sections (Figure 3). The extent of RBC extravasation varied from relatively small and localized to covering large areas of the treated hemisphere, depending on the extent of the BBB opening.

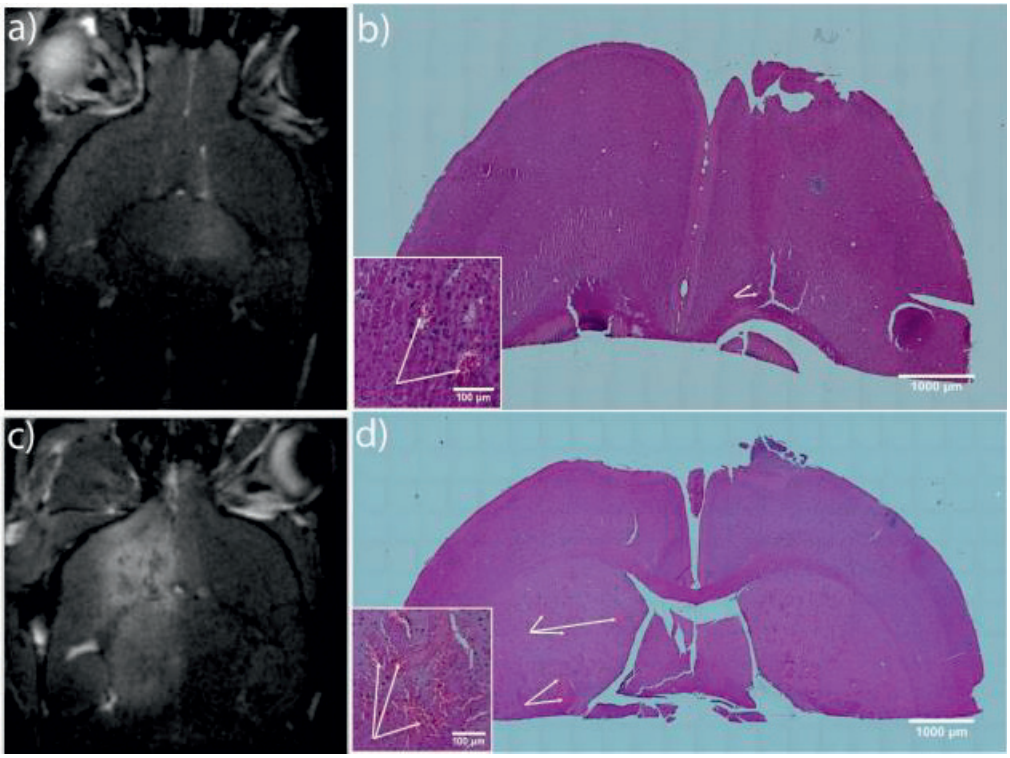

Fig. 3. RBC extravasation in H&E-stained brain sections. a-b) MR image of a brain with a corresponding H&E-stained section with limited RBC extravasation. c-d) MR image of another brain with corresponding H&E-stained section with considerable extravasation of RBC. In b) and d), arrows show RBC extravasation and insets show zoomed areas with RBC extravasation. MRI images were normalized so that areas not exposed to FUS in different images have a comparable intensity.

NP transport across the BBB and distribution in the brain parenchyma and metastases

BBB opening-dependent transport of NPs following FUS exposure was demonstrated (Figure 4 a-d). The amount of NPs entering into the brain parenchyma and the extent of NP displacement from the nearest blood vessel wall correlated with increasing MRI contrast agent intensity (Figure 4 e-f). Up to 7.7 times more NPs (average 2.8 times) were found in the treated hemisphere compared to the untreated. The average displacement of NPs from the nearest blood vessel was up to 2.3 times higher in the treated hemisphere compared to the untreated one. Changes in the transport and distribution of NPs were minor up to a certain BBB opening extent (ratio of MRI intensities approx. 1.5-2.0), and then increased rapidly. NPs were also visible in

melanoma brain metastases (Figure 4 g-h) both inside and outside of blood vessels (shown in enlargement as an inset in Figure 4g). Figure 4 is from mice in group 2 and the sections analysed are from the part of the brain only exposed to 1.1 MHz. The transport of NPs across the BBB in animals in group 1 also increased proportionally to the extent of BBB opening (not shown).

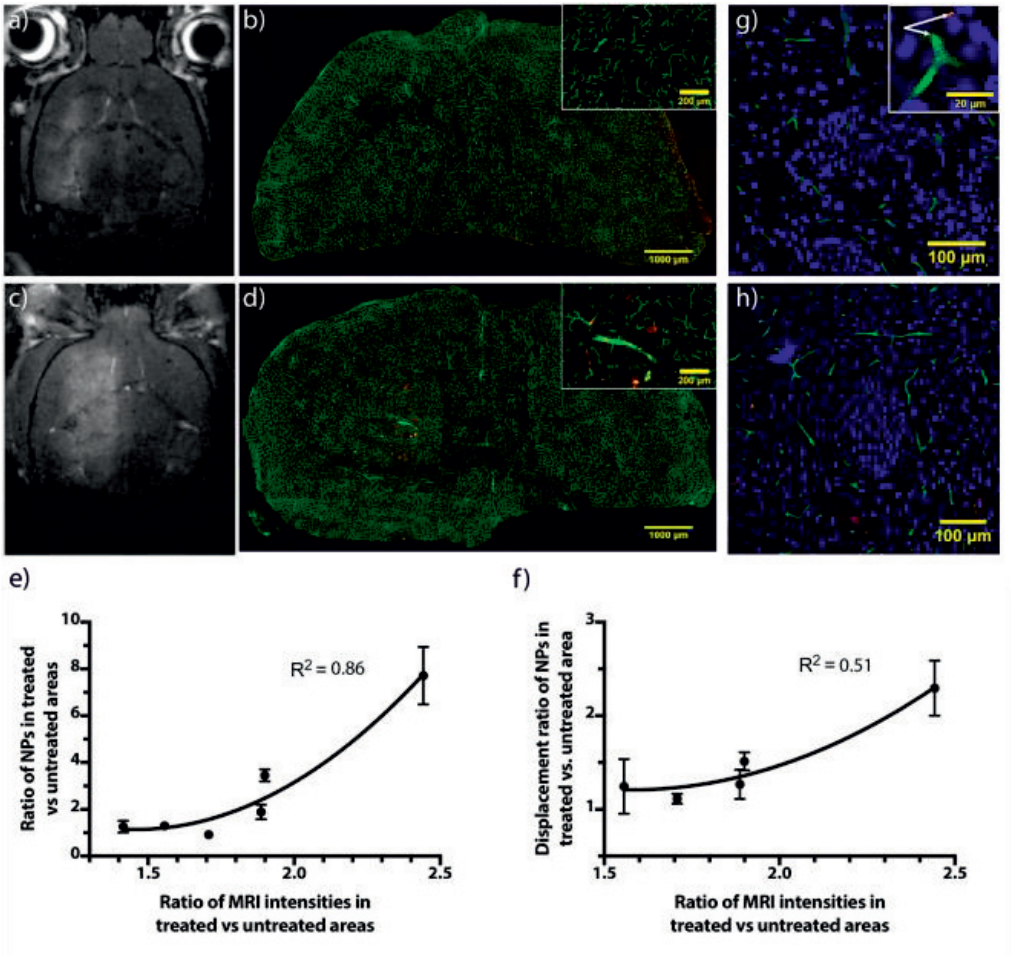

Fig. 4. FUS-mediated NP transport across the BBB and distribution in the brain parenchyma. a) MR image of a brain with a corresponding CLSM tile scan b) showing little difference between NP amount in the treated and untreated hemispheres. c) MR image of another brain with a corresponding CLSM tile scan d) showing substantially greater differences between NP amount in the treated and untreated hemispheres. Insets in Fig. 4b and Fig. 4d show an enlarged image of the treated area. e) Uptake of NPs across the BBB. n= 3-5 sections per mouse. f) Displacement of NPs away from blood vessels. n=3-5 sections per mouse. Values represent the mean of each animal, and error bars give standard error of the mean. g-h) CLSM images with tumour metastases visible as a cluster of tightly packed nuclei. Inset g) shows an enlarged area of the tumour, with NPs visible both inside and outside of a blood vessel (indicated by arrows). Colours in CLSM images are: Red – NPs, blue – nuclei, green – blood vessels. MRI images were normalized so that areas not exposed to FUS in different images have a comparable intensity.

ARF effect on the displacement of NPs

To study whether ARF could increase the displacement of NP from blood vessels even further, smaller regions of brains were also treated with higher frequency and highly focused US to generate ARF. An example of a tile scan image of the entire brain is shown in Figure 5a, and the inset shows one individual image of the tile scan. A Dunn's multiple comparison showed that some sections in animal 1 (Figure 5b) and 4 (Figure 5e) indicated enhanced displacement compared to the control, however, in animal 1 one section was significantly lower than the control. Animal 2 (Figure 5c) and 3 (Figure 5d) did not indicate any enhanced displacement. It should be noted that the tile scan in Figure 5a is shown for illustration purposes, and the actual image analysis was performed on individual images shown in the inset and the white box in the tile scan.

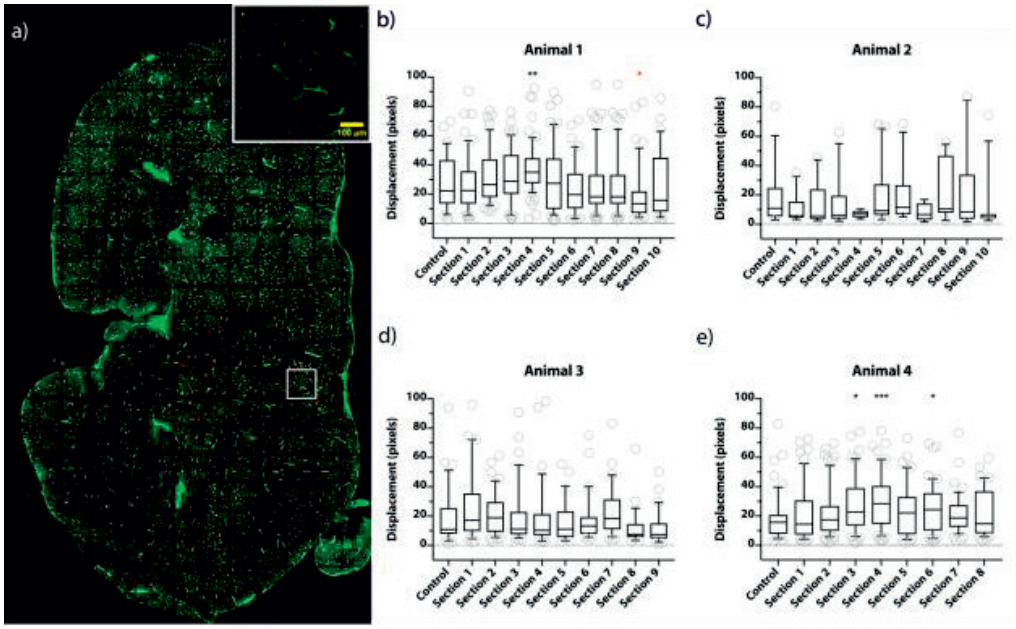

Fig. 5. The effect of the ARF on NP displacement in the brain parenchyma. a) A tile scan of an entire brain section taken with a 20x objective. NPs are shown in red and blood vessels in green. Inset shows an individual image of the tile scan; scale bar in the inset – 100 μm. b-e) Image analysis of ARF effect from four animals. Control denotes a section from the brain area that only received 1.1 MHz FUS treatment, while numbered columns refer to sections located within and slightly extending beyond the estimate area of the ARF effect. Each column refers to one section and each circle in b-e) represents the median displacement from blood vessels of all NPs in a specific image from a section (marked with a white box in a)). Data is represented as a box-and-whisker plot where the whiskers correspond to the 10-90 percentile. 1 pixel corresponds to 0.45 μm. * $p \leq 0.05$, ** $p \leq 0.01$,*** $p \leq 0.001$, (significantly lower than control).

P-gp effect

P-gp staining in the brains removed immediately after sonication is shown in Figure 6 a-b. FUS-mediated BBB opening does not seem to induce any apparent alteration in P-gp staining in the brain immediately after sonication. No difference in the antibody staining of P-gp can be seen between the treated and non-treated hemisphere, indicating that FUS did not induce any direct damage of the P-gp.

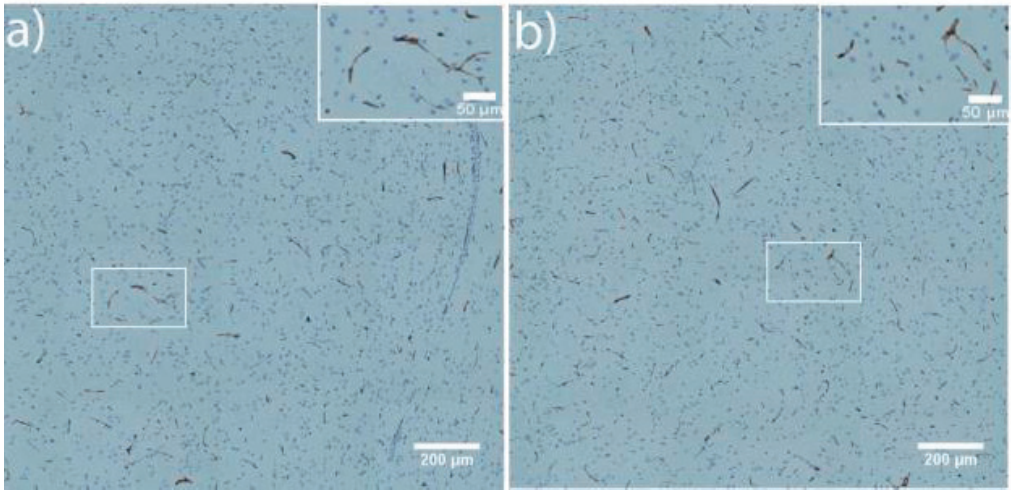

Fig. 6. The effect of FUS-mediated BBB opening on P-gp levels immediately after sonication. Fragment of a brain section tile scan showing P-gp staining in a) treated hemisphere, b) untreated hemisphere. Enlarged area with P-gp staining are shown in insets. P-gp is shown in brown, and cell nuclei in blue.

Discussion

While it is difficult to deny the potentially enormous advantages that materials science can confer to nanomedicine in preference to traditional drug formulations, the initial enthusiasm surrounding nanomedicine's application in the treatment of solid tumours has been called into question in light of the limited number of translational successes. A survey of the literature from the past 10 years has shown that solid tumours retain only 0.7% (median) of the administered NP dose[13]. In brain tumours, this situation is even more complicated due to the BBB. The delivery of therapeutic NPs to the brain can be aided by BBB opening techniques such as FUS-mediated BBB disruption. However, even with FUS, the question is whether NP delivery to the brain parenchyma is sufficient to achieve a therapeutic effect.

In this work, the BBB was opened using FUS in combination with a novel PEBCA NP-MB platform[34]. The platform consists of PEBCA NPs sized approx. 270 nm stabilizing MBs sized 1.6 µm. Our group has recently used this platform for FUS-mediated BBB opening in rats, demonstrating reversible BBB opening and the delivery of poly(butyl cyanoacrylate) (PBCA)

NPs into brain parenchyma[22]. In that study, several MIs were used; BBB opening could be occasionally achieved with an MI of 0.15 and consistently with an MI of 0.25 and higher. The application of MI 0.25 did not produce any pathology or RBC extravasation in histological sections. In this study, we used the EBCA monomer. PEBCA polymers degrade more slowly, which can be of therapeutic benefit. Degradation of PACA NPs is dependent on the length and bulkiness of the alkyl chain[10,35], and PEBCA is bulkier than PBCA due to branching alkyl chains. In the present work, we opened the BBB by applying FUS at an estimated *in situ* pressure of 0.31-0.34 MPa in order to obtain sufficient NP extravasation for quantitative measurement of NP distribution. Although BBB opening with 1.1. MHz FUS was done using the same US parameters in all animals, the extent of opening, as judged by contrast enhancement in MRI, varied. This variability could be attributed to angle and height differences in skull positioning during the FUS treatment, batch-to-batch variability in NP-stabilized MBs or a combination of these factors. The NP transport across the BBB correlated with the extent of BBB opening. In addition, the extent of BBB opening also correlated with RBC extravasation as observed in histological sections. However, a certain amount of RBC in the tissue might be clinically acceptable when treating terminal diseases such as brain cancer.

While some NPs were shown to be delivered to melanoma brain metastases, the delivery was restricted as compared to the surrounding brain tissue. This is consistent with the properties of this melanoma metastasis model at week 4 post-inoculation. As observed in Thorsen et al.[33], at this time point the mean vascular area fraction in the tumours is lower than in the normal brain. This is also evident in our CLSM images. It is therefore likely that reduced vascularization would diminish NP delivery into the tumour tissue in our study.

Assuming mainly paracellular transport across the BBB, NP size can be a critical factor. Size dependence of FUS-mediated NP transport has been investigated in several works. For instance, Choi et al. used fluorescently labelled dextrans of 3, 70 and 2000 kDa and reported that the molecular weight of dextrans that could be delivered to the brain parenchyma using FUS in combination with SonoVue MBs (0.57 MPa corresponding to MI of 0.46) was between 70 kDa and 2000 kDa, and that 2000 kDa dextrans (54.4 nm) could not be delivered[36]. However, in a subsequent study from the same group, 2000 kDa dextrans co-administered with MBs (Definity) 6 seconds after the start of sonication were delivered into brain parenchyma at 0.84 MPa[37]. In a study using FUS exposure parameters that were similar to the ones used by Choi et al.[36] and NPs injected after sonication, the maximum gap between endothelial cells caused by FUS exposure was found to be close to 65 nm[38]. The authors suggested the transport of large objects >100 nm to be difficult, assuming purely paracellular mode of transport. However, there are several studies demonstrating that NPs with diameters in the range of 60-120 nm have been delivered into the brain parenchyma using FUS-mediated BBB opening. For instance, biodegradable polymeric NPs sized 60 nm and 75-nm could be delivered across the BBB after FUS exposure when albumin MBs, similar to Optison, were co-injected with the NPs immediately before FUS exposure[17]. The extent of NP transport across the BBB was shown to depend on the acoustic pressure. Mead et al.[20], have found that DNA-bearing NPs sized 100 nm and co-injected with the

same MBs as used in Nance et al.[17] were delivered into the brain parenchyma after FUS exposure with 0.6 MPa and a duration of 2 minutes. Diaz et al.[18] reported brain delivery of 50 nm and 120 nm gold NPs after FUS-mediated BBB opening with approximately 0.23 MPa when NPs were injected 8 minutes prior to sonication. An overview of these studies indicates that the extent of brain delivery is dependent on numerous variables (properties of NPs, concentration and circulation time of MBs, FUS exposure parameters etc.), of which the most important ones appear to be the size of the NPs, the mechanical index and the presence of NPs in blood during sonication. In our study, the NPs, being part of the NP-MB platform, were present in the bloodstream during FUS-mediated BBB opening and were delivered more effectively compared to the control, despite being significantly larger than the NPs discussed above. NPs lining the shell of the MBs, moreover, were in the immediate proximity to the MBs during FUS-induced cavitation of the latter, which has been shown to improve NP delivery to tumours[39] and may facilitate their transport across the BBB.

The FUS exposure performed in the presence of circulating NP-MBs, which induce cavitation, will probably produce biomechanical effects on the blood vessel wall. We demonstrated that in addition to the increased transport of NPs across the BBB, FUS at 1.1 MHz increases NP distribution in the brain parenchyma, i.e. displacement from blood vessels, although the exact mechanism is unclear. From *in vitro* measurements, we know that the majority of the PEBCA NP-MBs will collapse at the *in situ* acoustic pressure used in the current experiment. During sonication, the MBs will be pushed towards the endothelial cell lining, and it is well known that under asymmetric boundary conditions the bubble collapse will also be asymmetrical[40], resulting in a liquid jet impinging on, and potentially penetrating, the solid boundary (i.e. the endothelial lining). In addition to BBB opening, this process may also facilitate NP distribution in the brain tissue, which is a considerable advantage given that passive diffusion of NPs in the ECM can be very restricted, especially in the case of large NPs[17].

The effect of the ARF could potentially further increase NP displacement from blood vessels, improving their distribution in the brain. Due to lower acoustic absorption, the intensities required to directly affect liquid and solid NPs using ARF are higher compared to gas-filled particles. However, high intensity ARF can also act on the bulk fluid, which can induce acoustic streaming that can indirectly affect the NPs and increase NP displacement in the brain parenchyma[29]. The effect of ARF NPs was limited in this study, and should be considered an incentive for further studies. The reason could be that the method used to assess the effect of ARF had some inherent limitations. As this method was based on image analysis, any NP displaced from a given blood vessel beyond the distance half way to the neighbour vessel would be registered as originating from that vessel. This makes it challenging to isolate the effect of the ARF if it is combined with the effect of another exposure (at 1.1 MHz) that already causes displacement of NPs. Moreover, the variation in the effect of ARF might be due to analysing not only tissue in the small focal region of the high frequency transducer.

Down-regulation of P-gp by US has been observed in glioma cells[41] and, in very recent studies, FUS caused localized P-gp down-regulation at the BBB 24 h[30] and 1 h[31] post sonication.

In our study, no obvious effects of FUS on P-gp levels were observed immediately after sonication, indicating that FUS-mediated changes in P-gp activity are not due to direct damage or alteration of the P-gp, but rather caused by signalling alterations that require a certain period of time post-sonication to exert their effect.

In conclusion, we have shown that our PACA NP-stabilized MB platform designed for the application of FUS in drug delivery can transport NPs across the BBB and achieve their distribution in the brain tissue, and that the NP transport depends on the extent of FUS-mediated BBB opening. The ARF study needs to be followed up in order to make solid conclusions regarding its effect on NP displacement. Overall, our results show that while FUS-mediated BBB opening, like any generic BBB opening technique, may impose size restrictions on NP extravasation, combining NPs and MBs into a single unit such as the one used in our study can achieve a substantial increase in the transport and distribution of NPs up to 270 nm in the brain parenchyma.

Methods

Nanoparticles and microbubbles

PEBCA NPs were synthesized by the miniemulsion polymerization method as described and used previously to make PBCA NPs[34]. In the oil phase, the monomer (EBCA, Henkel Loctite) was mixed with a co-stabilizer (Miglyol 810N, Cremer), the fluorescent dye NR668 (modified Nile red[42]), V-65 (2,2'-Azobis(2,4-dimethylvaleronitrile, 1wt%, Wako) and methanesulphonic acid (MSA, 0.1wt%, Sigma-Aldrich). The water phase contained the PEG-stabilizers Kolliphor HS15 (Sigma-Aldrich) and Brij L23 (Sigma-Aldrich), and 0.1M HCl. The phases were mixed and sonified on ice for 4 minutes using an ultrasonic homogenizer (Branson). The resulting emulsion was left to polymerize for 1 h at ambient temperature before adjusting the pH to 5. The polymerization was continued for another 2 h at ambient temperatures followed by 8 h at 50°C. Finally, the NPs were dialyzed extensively against 1 mM HCl (MWCO 100,000) and centrifuged at 3000 rpm for 15 minutes to remove unwanted aggregates. Size and ζ-potential were measured in phosphate buffer (pH 7) using DLS (Zetasizer Nano ZS, Malvern).

MBs were made following the procedure described previously[22,34]. In brief, NPs were diluted to a concentration of 10 mg/ml in 5 mg/ml casein (Sigma-Aldrich) and 1x phosphate-buffered saline (PBS). The solution was then saturated with perfluoropropane gas (Fluorochem) and mixed violently for 2 minutes before using an Ultra Turrax (ICA Werke) to create NP-stabilized MBs with a gas core. Size and concentration of MBs was analysed using a cell counting chamber slide (Countess, Thermo Fisher). Eight positions on the slide were imaged using bright field microscopy at 20x magnification, and the size distribution and concentration was calculated using ImageJ 1.48j[43] and Excel 2010.

Cells and animals

The H1_DL2 cell line used in this study is based on the H1 cell line isolated from a patient biopsy of human melanoma brain metastases as described previously[44]. The H1_DL2 cell line

was developed by transducing H1 cells with two lentiviral vectors encoding Luciferase and a GFP variant of Dendra[32]. The cells were cultured in Dulbecco's modified Eagle's medium supplemented with 10% fetal bovine serum (Gibco), 2% L-glutamine (ThermoFisher Scientific), and MEM Non-Essential Amino Acids Solution (100X) (ThermoFisher Scientific) diluted 1:25. The growth medium was exchanged twice a week.

Female NOD/SCID mice (eight weeks of age, 18-22 g of weight) were purchased from Harlan. The mice were housed in individually ventilated cages (Techniplast). In accordance with the recommendations set forth by the Federation of European Laboratory Animal Science Associations, animal housing conditions were free of specific pathogens. The mice were provided with sterile water and food ad libitum. All animal procedures were approved by the Norwegian National Animal Research Authorities.

Intracardiac injection of tumour cells

Before and during tumour cell inoculation, the animals were anesthetized with 3% isoflurane in oxygen (flow 2 l/min). 5×10^5 of H1_DL2 cells in 0.1 ml PBS were injected into the left cardiac ventricle of the mice using a 30G insulin syringe (Omnican50, B. Braun Melsungen AG). The injection was guided by ultrasonography using a Vevo® 2100 System with an MS200 transducer (FujiFilm Ultrasonics). The procedure of intracardiac injection of tumour cells is shown in Supplementary Video 1. After the intracardiac injection, the mice received a subcutaneous injection of temgesic (Reckitt Benckiser) (0.05 mg/kg) for prolonged analgesia. The metastases were allowed to develop for 28±2 days.

Magnetic resonance imaging

MRI was performed using a 7.05 T horizontal bore magnet (Biospec 70/20 Avance III, Bruker Biospin). The mouse was anesthetized using a subcutaneous injection of a 2:1:2:5 mixture of fentanyl (Actavis Group hf), medetomidine (Orion Pharma), midazolam (Accord Healthcare Limited) and water at a dose of 100 µl per 10 g of body weight, and cannulated in the tail vein with a 24G catheter (BD Neoflon, Becton Dickinson Infusion Therapy). Temperature and respiration rate were monitored using rectal temperature and pressure-sensitive probes (SA Instruments), respectively. The temperature of the animal was maintained at 37 °C. Once the mouse was placed in the MR scanner, the coils were tuned and matched, followed by acquisition of a localizer scan. The following MR sequences were used for pre- and post-treatment images: T1-RARE for detecting melanoma brain metastases as described previously[33], and T1 Fast Low Angle Shot (FLASH) for detecting BBB disruption based on the extravasation of a gadolinium-based contrast agent Omniscan (GE Healthcare AS, 0.5 mmol/kg, 1 ml/kg) and for detection of haemorrhages. All MR sequences had the same geometry with FOV of 40 × 27 mm, matrix size (MTX) of 200 × 135, and 12 slices at 1 mm. MRI parameters were set using Bruker Paravision v6.

Characterization of US attenuation through the skull

The RK-100 system for MRI guided FUS treatments (FUS Instruments) including a custom made dual frequency transducer was used in the experiments. The transducer had an inner circular part (7.8 MHz) and an outer ring (1.1 MHz), with apertures of 39 mm and 52 mm, respectively. Both were focused at 60 mm. The acoustic attenuation through the skull bone was measured at both frequencies on harvested mouse skulls from animals of similar size as the ones used for BBB disruption experiments. The measurements were conducted as described by Åslund et al.[22] and were performed with pulse lengths of 20 μs (22 cycles at 1.1 MHz and 155 cycles at 7.8 MHz). At 1.1 MHz the acoustic pressure was attenuated between 10 and 17 %, and at 7.8 MHz the attenuation was between 70 and 75 %, depending on the angular position of the skull with respect to the incoming wave.

FUS treatments

The mice were divided into four groups. All groups were treated with BBB-opening FUS (1.1 MHz, 5 min, pulse repetition frequency (PRF) 0.33 Hz, estimated *in situ* pressure 0.31-0.34 MPa, 10 ms burst length). Additionally, group 2 was treated with ARF (7.8 MHz, 60 min, PRF 1 Hz, estimated in situ pressure of 0.75 – 0.9 MPa, 5 ms burst length). The frequency (7.8 MHz) was chosen to significantly enhance tissue attenuation (compared to 1.1 MHz). The rationale behind the duty cycle (pulsing scheme) was a trade-off between enhancing the impulse delivered by the radiation force and limiting the local temperature increase.

- Group 1 (n=3): BBB-opening treatment, euthanized 2 h after treatment start. Used for the assessment of FUS-mediated NP transport across the BBB and NP distribution in the brain parenchyma.
- Group 2 (n=6): BBB-opening and ARF treatment, euthanized 2 h after treatment start. Used for investigating the effect of the ARF (see Supplementary Figure 1).
- Group 3 (n=2) BBB-opening treatment, euthanized 2 h after treatment start. Used for haematoxylin and eosin staining.
- Group 4 (n=3): BBB-opening treatment, euthanized immediately post treatment. Used to investigate the immediate effect of FUS-mediated BBB disruption on P-gp in the brain.

Before FUS treatment, the animals were anesthetized as described above in 2.4. After the heads were shaved, a depilatory cream was applied to remove the remaining hair. The mice were placed in the MR bed, and the bed was placed in the scanner. Two different MRI scans were acquired, T1-RARE without Omniscan and T1-FLASH with Omniscan. The T1-FLASH sequence was used for treatment planning according to Supplementary Figure 1a. A grid of 6x2 circular treatment locations (beam width: 1.6 mm per location) was used to open the BBB in the left hemisphere in all animals, except for one animal in Group 2 that was treated in the right hemisphere since no metastases were visible in the left hemisphere. The contralateral hemisphere was used as non-treated control. The animal was placed above the transducer, and Omniscan (1

mL/kg) and NP-MBs (5 mL/kg) were injected sequentially. The FUS treatment (1.1 MHz) was initiated upon injection of the NP-MBs using a RK-100 system for MRI-guided FUS-mediated BBB disruption. After the treatment, the animal was scanned with MRI (T1-FLASH) for verification of BBB opening as well as indications of haemorrhage. The post-treatment T1-FLASH was used for ARF treatment planning and a grid of 2x2 treatment locations (beam width: 0.5 mm per location) was defined in the area where BBB opening had been successful (Supplementary Figure 1b). ARF treatment was initiated 30 min after BBB opening treatment start. 2 h post anesthetization a new anaesthetic dose was injected subcutaneously at half the initial dose to maintain deep anaesthesia. 2 h post BBB opening, animals in Group 1 and Group 2 were injected with DyLight 649-labeled Lycopersicon esculentum (tomato) lectin (Vector Laboratories Inc) (5 mg/kg) to label the vasculature. Five minutes later, the mice were euthanized by cervical dislocation. The brains were removed, divided according to Supplementary Figure 1d, embedded in Tissue-Tek™ CRYO-OCT Compound (Sakura), and frozen in a mixture of 2-methylbutane and dry ice. Animals in Group 3 were euthanized by i.v. injection of pentobarbital (100 mg/kg) followed by intracardiac perfusion with PBS and 4% paraformaldehyde. The brains were removed and submerged in 10 % formalin for at least 24 h before paraffin embedding and sectioning into 4 μm sections for H&E staining. Animals in Group 4 were euthanized by cervical dislocation immediately after the FUS treatment. The brains were removed without prior injection of Lycopersicon esculentum (tomato) lectin and frozen as described above. Brains in Group 2 were sectioned as described in Supplementary Figure 1d, and brains in Group 1 were sectioned axially; in both groups, the brains were cut into 4 and 20 μm cryosections. Frozen sections in Group 4 were stained using an anti-P glycoprotein antibody (EPR10364-57, Abcam, 1:200 dilution) followed by incubation with HRP (horseradish peroxidase) Rabbit EnVision – Polymer and DAB+ (3,3'-Diaminobenzidine) Chromogen (both from DAKO).

Confocal laser scanning microscopy

For quantification of NR668-containing PEBCA NPs in the brain tissue and assessment of the ARF effect, cryosections were thawed for approx. 10 min and tile scans of entire brain sections were obtained using a Leica TCS SP8 CLSM (Leica Microsystems) without mounting. Tile scans were acquired using 10x/0.45 and 20x/0.75 air objectives. For images taken with the 10x/0.45 objective, the following parameters were used: image size: 1024x1024 pixels, zoom factor: 1.5, pixel size: 758 nm. For images taken with the 20x/0.75 objective, the following parameters were used: image size: 1280x1280 pixels, zoom factor: 1.5, pixel size: 454 nm. A white light laser was used to excite NR668 (excitation wavelength 535 nm, emission wavelength range 560-630 nm) and DyLight 649 (excitation - 649 nm, emission wavelength range 660-710 nm). In order to visualize melanoma brain metastases with tightly packed nuclei, some sections were mounted with Vectashield mounting medium (Vectorlabs) containing 4',6-diamidino-2-phenylindole (DAPI) as a nuclei counterstain. DAPI was excited using a 405 nm laser with a

detection of 416–468 nm. H&E-stained sections were imaged using an LSM 800 (Zeiss) CLSM with 20x air objective.

Image analysis

MR images were processed using Sante DICOM Viewer v. 5.04 and ImageJ 1.49k. Processing and analysis of CLSM images were performed, depending on the required task, by ImageJ 1.49k, Icy v.1.8.6.0[45] or CellProfiler 2.1.1[46]. ImageJ and CellProfiler were collectively used for image conversion, image stitching, calculation of intensity ratios in MR images, background removal, filtering, thresholding, quantification of NP count and quantification of NP displacement, Icy - for k-means thresholding and distance transform used in algorithm validation and comparison of different thresholding strategies. A more detailed description of image analysis is provided in Supplementary Document 1.

For the quantification of the ARF effect, NP displacement from blood vessels was analysed in those parts of brain sections that corresponded to the hemisphere exposed to FUS at 1.1 MHz and 7.8 MHz. The area of ARF exposure was estimated using T1 Flash MR images as shown in Supplementary Fig. 1c, and the corresponding brain sections were selected appropriately to cover and slightly extend beyond this area. Control sections for ARF corresponded to areas only exposed to FUS at 1.1 MHz located approximately 3 mm from the estimated ARF exposure area, in order to minimize the effect of local inhomogeneity in BBB opening. The extent of BBB opening in T1 FLASH MR images was assessed by determining the ratio of intensities in the treated and untreated brain hemispheres.

Data analysis

Data were analysed using MS Excel 2010 and SPSS v17. In addition to the filters built in the image analysis algorithm, filters were applied in data analysis software to eliminate situations with unacceptable image or staining quality. Those are described in Supplementary Document 1. Analysis of ARF data was performed with Prism 7 (GraphPad Software Inc.) using a nonparametric ANOVA Kruskal-Wallis test followed by an uncorrected Dunn’s test against the control.

References

1 Laquintana, V. *et al.* New strategies to deliver anticancer drugs to brain tumors. *Expert Opin. Drug Deliv*. **6**, 1017-32 (2009).

2. Pardridge, W.M. The blood-brain barrier: bottleneck in brain drug development. *NeuroRx*. **2,** 3-14 (2005).

3. Pardridge, W.M. Drug transport across the blood-brain barrier. *J Cereb Blood Flow Metab*. **32,** 1959-72 (2012).

4. Hawkins, B.T. and Davis, T.P. The blood-brain barrier/neurovascular unit in health and disease. *Pharmacol. Rev*. **57,** 173-85 (2005).

5. Yildirimer, L., Thanh, N.T, Loizidou, M. and Seifalian, A.M. Toxicology and clinical potential of nanoparticles. *Nano Today*. **6**, 585-607 (2011).

6. Sun, T. *et al.* Engineered nanoparticles for drug delivery in cancer therapy. *Angew. Chem.* **53**, 12320-64 (2014).

7. Maeda, H., Tsukigawa, K. and Fang, J. A Retrospective 30 Years After Discovery of the Enhanced Permeability and Retention Effect of Solid Tumors: Next-Generation Chemotherapeutics and Photodynamic Therapy-Problems, Solutions, and Prospects. *Microcirculation*. **23,** 173-82 (2016).

8. Matsumura, Y. and Maeda, H. A new concept for macromolecular therapeutics in cancer chemotherapy: mechanism of tumoritropic accumulation of proteins and the antitumor agent smancs. *Cancer Res*. **46,** 6387-92 (1986).

9. Kumari, A., Yadav, S.K. and Yadav, S.C. Biodegradable polymeric nanoparticles based drug delivery systems. *Colloids Surf., B*. **75**, 1-18 (2010).

10. Sulheim, E. *et al.* Cellular uptake and intracellular degradation of poly(alkyl cyanoacrylate) nanoparticles. *J Nanobiotechnology*. **14,** 1 (2016).

11. Soma, E., Attali, P. and Merle, P. Chapter 11 A Clinically Relevant Case Study: the Development of Livatag® for the Treatment of Advanced Hepatocellular Carcinoma, in *Nanostructured Biomaterials for Overcoming Biological Barriers* (eds. Alonso M.J and Csaba N.S.) 591-600 (RCS Publishing, 2012).

12. Cecchelli, R. *et al.* Modelling of the blood-brain barrier in drug discovery and development. *Nat. Rev. Drug Discov*. **6,** 650-61 (2007).

13. Wilhelm, S. *et al.* Analysis of nanoparticle delivery to tumours. *Nat. Rev. Mater.* **1**, 16014 (2016).

14. Hynynen, K. Focused ultrasound for blood-brain disruption and delivery of therapeutic molecules into the brain. *Expert Opin. Drug Deliv*. **4**, 27-35 (2007).

15. Hynynen, K. Ultrasound for drug and gene delivery to the brain. *Adv. Drug Deliv. Rev*. **60**, 1209-17 (2008).

16. Etame, A.B. *et al.* Focused ultrasound disruption of the blood-brain barrier: a new frontier for therapeutic delivery in molecular neurooncology. *Neurosurg Focus*. **32**, E3 (2012).

17. Nance, E. *et al.* Non-invasive delivery of stealth, brain-penetrating nanoparticles across the blood-brain barrier using MRI-guided focused ultrasound. *J. Control. Release*. **189**, 123-32 (2014).
18. Diaz, R.J. *et al.* Focused ultrasound delivery of Raman nanoparticles across the blood-brain barrier: potential for targeting experimental brain tumors. *Nanomed Nanotech Biol Med*. **10,** 1075-87 (2014).
19. Lammers, T. *et al.* Theranostic USPIO-Loaded Microbubbles for Mediating and Monitoring Blood-Brain Barrier Permeation. *Adv. Funct. Mater*. **25**, 36-43 (2015).
20. Mead, B.P. *et al.* Targeted gene transfer to the brain via the delivery of brain-penetrating DNA nanoparticles with focused ultrasound. *J. Control. Release*. **223**, 109-17 (2016).
21. Hynynen, K., McDannold N., Vykhodtseva N. and Jolesz F.A. Noninvasive MR imaging-guided focal opening of the blood-brain barrier in rabbits. *Radiology*. **220**, 640-6 (2001).
22. Åslund, A.K.O. *et al.* Nanoparticle delivery to the brain--By focused ultrasound and self-assembled nanoparticle-stabilized microbubbles. *J. Control. Release*. **220,** 287-94 (2015).
23. Nance, E.A. *et al.* A dense poly(ethylene glycol) coating improves penetration of large polymeric nanoparticles within brain tissue. *Sci. Transl. Med*. **4**, 149ra19 (2012).
24. Dayton, P., Klibanov, A., Brandenburger, G. and Ferrara, K. Acoustic radiation force in vivo: a mechanism to assist targeting of microbubbles. *Ultrasound Med. Biol*. **25**, 1195-201 (1999).
25. Rychak, J.J., Klibanov, A.L. and Hossack, J.A. Acoustic radiation force enhances targeted delivery of ultrasound contrast microbubbles: in vitro verification. *IEEE Trans. Ultrason., Ferroelect., Freq. Control*. **52**, 421-33 (2005).
26. Shortencarier, M.J. *et al.* A method for radiation-force localized drug delivery using gas-filled lipospheres. *IEEE Trans. Ultrason., Ferroelect., Freq. Control*. **51**, 822-31 (2004).
27. Lum, A.F. *et al.* Ultrasound radiation force enables targeted deposition of model drug carriers loaded on microbubbles. *J. Control. Release*. **111**, 128-34 (2006).
28. Crowder, K.C. *et al.* Sonic activation of molecularly-targeted nanoparticles accelerates transmembrane lipid delivery to cancer cells through contact-mediated mechanisms: implications for enhanced local drug delivery. *Ultrasound Med. Biol*. **31**, 1693-700 (2005).
29. Dayton, P.A. *et al.* Application of ultrasound to selectively localize nanodroplets for targeted imaging and therapy. *Mol. Imaging*. **5**, 160-74 (2005).
30. Cho, H. *et al.* Localized Down-regulation of P-glycoprotein by Focused Ultrasound and Microbubbles induced Blood-Brain Barrier Disruption in Rat Brain. *Sci. Rep*. **6**, 31201 (2016).
31. Aryal, M. *et al.* Effects on P-Glycoprotein Expression after Blood-Brain Barrier Disruption Using Focused Ultrasound and Microbubbles. *PLoS One* **12(1),** e0166061, (2017)

32. Enochs, W. S., Petherick, P., Bogdanova, A., Mohr, U., Weissleder, R. Paramagnetic metal scavenging by melanin: MR imaging. *Radiology* **204 (2),** 417-23 (1997)
33. Thorsen, F. *et al.* Multimodal imaging enables early detection and characterization of changes in tumor permeability of brain metastases. *J. Control. Release*. **172**, 812-22, (2013).
34. Mørch, Y. *et al.* Nanoparticle-stabilized microbubbles for multimodal imaging and drug delivery. *Contrast Media Mol Imaging*. **10**, 356-66 (2015).
35. Kante, B. *et al.* Toxicity of polyalkylcyanoacrylate nanoparticles I: Free nanoparticles. *J. Pharm. Sci*. **71,** 786-90 (1982).
36. Choi, J.J., Wang, S., Tung, Y.S., Morrison, I.B. and Konofagou, E.E. Molecules of Various Pharmacologically-Relevant Sizes Can Cross the Ultrasound-Induced Blood-Brain Barrier Opening in vivo. *Ultrasound Med. Biol*. **36,** 58-67 (2010).
37. Chen, H. and Konofagou, E.E. The size of blood-brain barrier opening induced by focused ultrasound is dictated by the acoustic pressure. *J Cereb Blood Flow Metab*. **34**, 1197-204 (2014).
38. Marty, B. *et al.* Dynamic study of blood-brain barrier closure after its disruption using ultrasound: a quantitative analysis. *J Cereb Blood Flow Metab*. **32**, 1948-58 (2012).
39. Burke, C.W., Alexander, E 4th., Timbie, K., Kilbanov, A.L. and Price, R.J. Ultrasound-activated agents comprised of 5FU-bearing nanoparticles bonded to microbubbles inhibit solid tumor growth and improve survival. *Mol Ther.* **22**, 321-8 (2014).
40. Leighton T. *The acoustic bubble* 531-536 (Elsevier Inc., 1994)
41. Zhang, Z. *et al.* Low intensity ultrasound promotes the sensitivity of rat brain glioma to Doxorubicin by down-regulating the expressions of p-glucoprotein and multidrug resistance protein 1 in vitro and in vivo. *PloS One*. **8**, e70685, (2013).
42. Klymchenko, A.S. *et al.* Highly lipophilic fluorescent dyes in nano-emulsions: towards bright non-leaking nano-droplets. *RSC Advances*. **2**, 11876-86 (2012).
43. Schneider, C.A., Rasband, W.S. and Eliceiri, K.W. NIH Image to ImageJ: 25 years of image analysis. *Nat. Methods*. **9**, 671-5 (2012).
44. Wang, J. *et al.* A novel brain metastases model developed in immunodeficient rats closely mimics the growth of metastatic brain tumours in patients. *Neuropathol Appl Neurobiol*. **37**, 189-205 (2011).
45. de Chaumont, F *et al.* Icy: an open bioimage informatics platform for extended reproducible research. *Nat. Methods*. **9**, 690-6 (2012).
46. Kamentsky, L. *et al.* Improved structure, function and compatibility for CellProfiler: modular high-throughput image analysis software. *Bioinformatics*. **27**, 1179-80 (2011)

Acknowledgements
Anne Rein Hatletveit and Maria Gellein are thanked for technical assistance with NP and MB synthesis. Annemieke van Wamel and Tina Bugge are thanked for technical assistance with tail-vein cannulation. Astrid Bjørkøy and the imaging facility at Centre for Molecular Imaging of the

Faculty of Natural Sciences and Technology, NTNU, are thanked for technical assistance with CLSM. Marius Widerøe is thanked for technical assistance with MRI. Brain sectioning and staining of brain sections was performed at the Cellular and Molecular Imaging Core Facility, NTNU. MRI imaging was performed at the MR Core Facility, NTNU. Animals used in this study were housed at the Comparative Medicine Core Facility, NTNU. Confocal microscopy was performed at the Centre for Molecular Imaging at NV, NTNU.

This study was funded by The Research Council of Norway (NANO2021 project number 220005, FRIMEDBIO project number 240316 and BIOTEK2021 project number 226159), and The Central Norway Regional Health Authority.

Author contributions

HB, CD and AÅ designed the study with the assistance of RH, YM and FT. AÅ, HB, SS, SB and ES performed *in vivo* experiments. HB, AÅ and SB analysed data and HB performed *ex vivo* imaging and image analysis. HB wrote the manuscript. All authors contributed in writing the manuscript and approved the manuscript.

Additional information

The authors declare no competing financial interest.

Supplementary information

Supplementary Figure 1 shows FUS treatment planning, both for FUS exposure at 1.1 MHz and for FUS exposure at 7.8 MHz, as well as a schematic of brain sectioning after brain removal and estimation of the ARF exposure area using an MR image. A grid of 6x2 circular regions each with a diameter of 1.6 mm were treated with FUS at 1.1 MHz **(panel a)** for BBB opening. An area of 2x2 regions each with a diameter of 0.5 mm was treated with FUS at 7.8 MHz for ARF **(panel b)**. The distance between this area and the top of the brain was measured in MR images as shown in **panel c**. Blue squares in panels **a-b** indicate the grid areas where FUS treatment started.

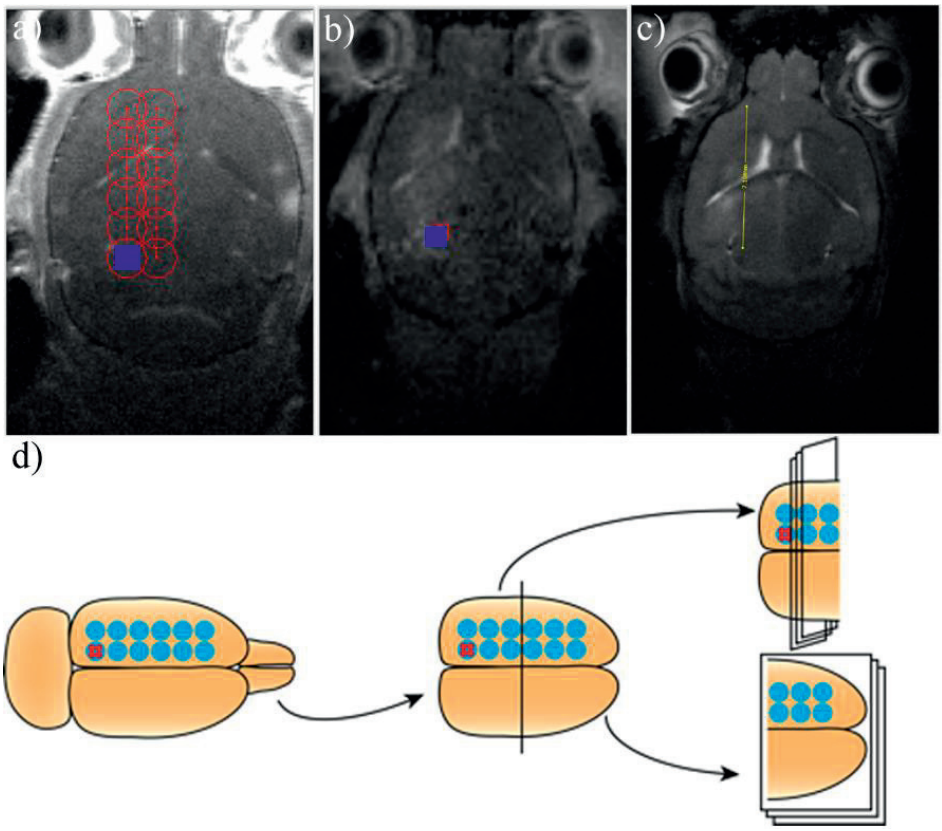

Supplementary Figure 1. Illustration of FUS treatment planning and post-treatment brain sectioning in the study. a) Treatment plan for FUS exposure at 1.1 MHz, b) treatment plan for FUS exposure at 7.8 MHz, c) estimation of the ARF exposure area, d) brain sectioning schematics, coronal sections were used for ARF quantification in group 3 and horizontal sections were used for NP quantification in group 1, for histology in group 2 and P-gp evaluation in group 4.

Supplementary Figure 2 shows a histogram with the size distribution of MBs used in this study.

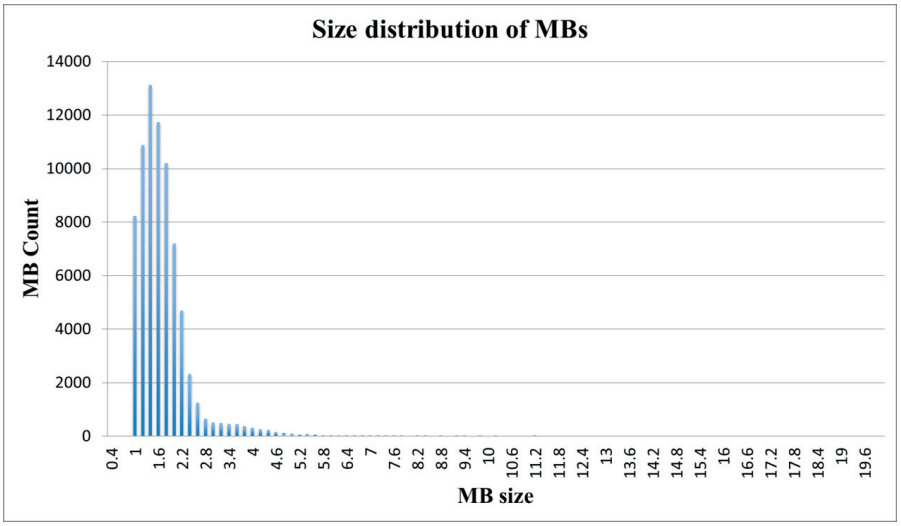

Supplementary Figure 2. Size distribution of MBs used in our study.

Legend Supplementary video 1
Intracardiac injection of human melanoma cells in a NOD/SCID mouse.

Supplementary document 1 describes image analysis used for the determination of NP displacement away from blood vessels.

For NP quantification and assessment of their displacement away from blood vessels, images were thresholded and segmented using a three-level Otsu thresholding algorithm. Blood vessel segmentation uses a median filter and has built-in filters to remove obvious debris. NP segmentation was performed without any median filtering and relied on the quality of the raw images, although it also has built-in filters to remove artefacts (extremely large clumps). The reason is that additional filtering even with a small filtering radius could eliminate a significant number of NP. For determining NP displacement from blood vessels, NPs with a certain axis length, deemed to be inside blood vessels even where the corresponding blood vessel staining either failed or produced a signal that was too weak, were eliminated. Afterwards, NPs located outside of blood vessels were isolated by applying a sequence of image masks. Finally, the distance between NPs and the nearest blood vessels was found by object expansion until the neighboring pixels touched. Image analysis of simulated images and confocal image scenarios is shown below.

Analysis of simulated images

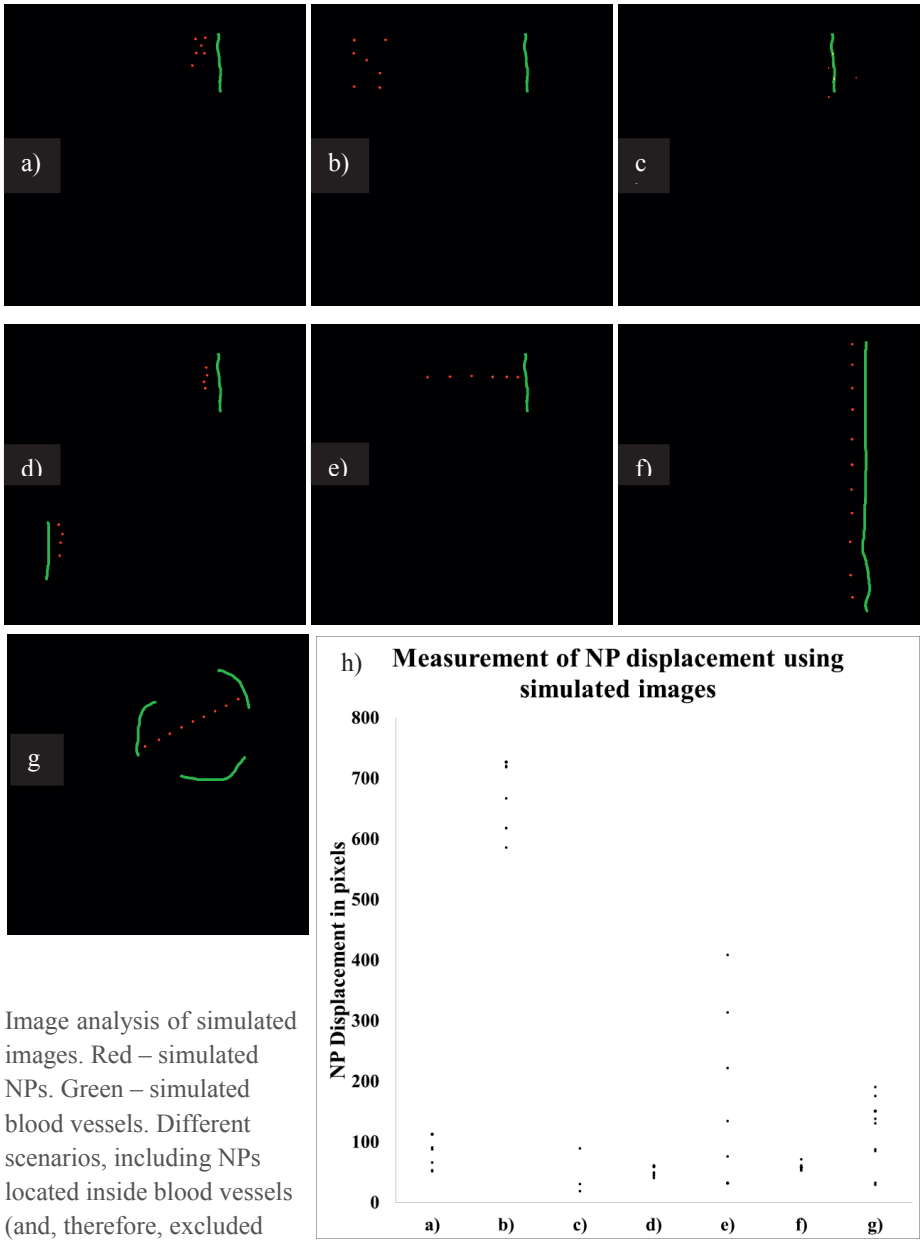

Image analysis of simulated images. Red – simulated NPs. Green – simulated blood vessels. Different scenarios, including NPs located inside blood vessels (and, therefore, excluded from displacement quantification – panel c) are shown in Panels a-g. Quantification results are shown in Panel h.

Shown below are several of the actual CLSM image scenarios used in algorithm training and optimization. For illustration purposes, scenarios are divided into four images. The first two images in a row are raw unprocessed images showing blood vessels and NPs, respectively. The 3rd image shows segmented NPs overlaid on segmented blood vessels. In this image, NPs that are inside blood vessels are shown in blue (based the application of masks), and NPs outside of blood vessels are shown in red. No other filtering steps are applied in this image. The 4th image is similar to the 3rd except that NPs seemingly located outside of blood vessels have been additionally filtered to exclude those that are deemed to be inside blood vessels, even though staining of the corresponding blood vessel either failed or was too dim to be accurately segmented in a uniform segmentation applied to all images in the dataset. Additional filters applied on the image level are: **1)** blood vessel count over 50, **2)** blood vessel area between 2 and 12% of the image, **3)** number of NPs outside blood vessels over 3, and **4)** the ratio of the number of NPs located within 100 to 1000 pixels from the nearest blood vessel to the number of NPs located within 100 pixels from the nearest blood vessel less than 0.5 (this threshold substantially exceeds the average ratio of ≤ 0.1 and is set to adjust for all reasonable scenarios). These are referred to as **exclusion criteria** and were set on the basis of visual inspection of images in order to exclude images with poor staining or automatic segmentation quality.

Scenario 1: Regular Scenario

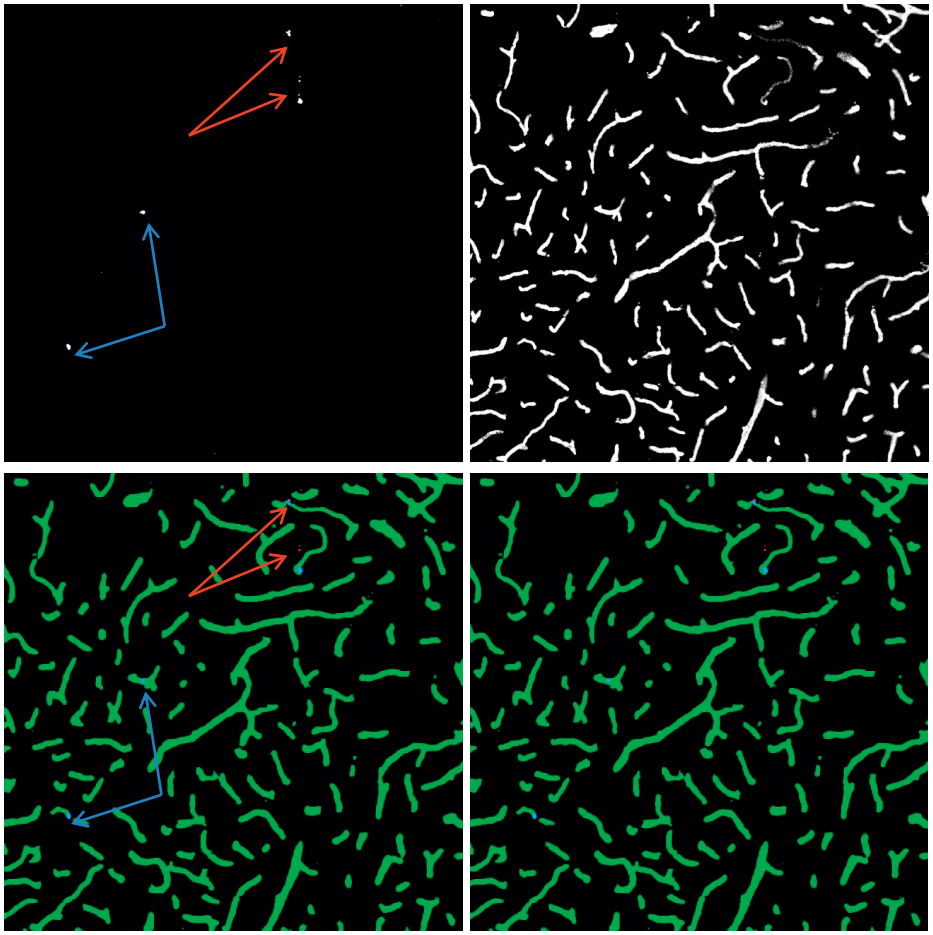

This is a good scenario showing NPs both inside and outside of blood vessels (indicated by red and blue arrows, respectively). No particular image analysis challenges are observed.

Scenario 2: All NPs inside blood vessels

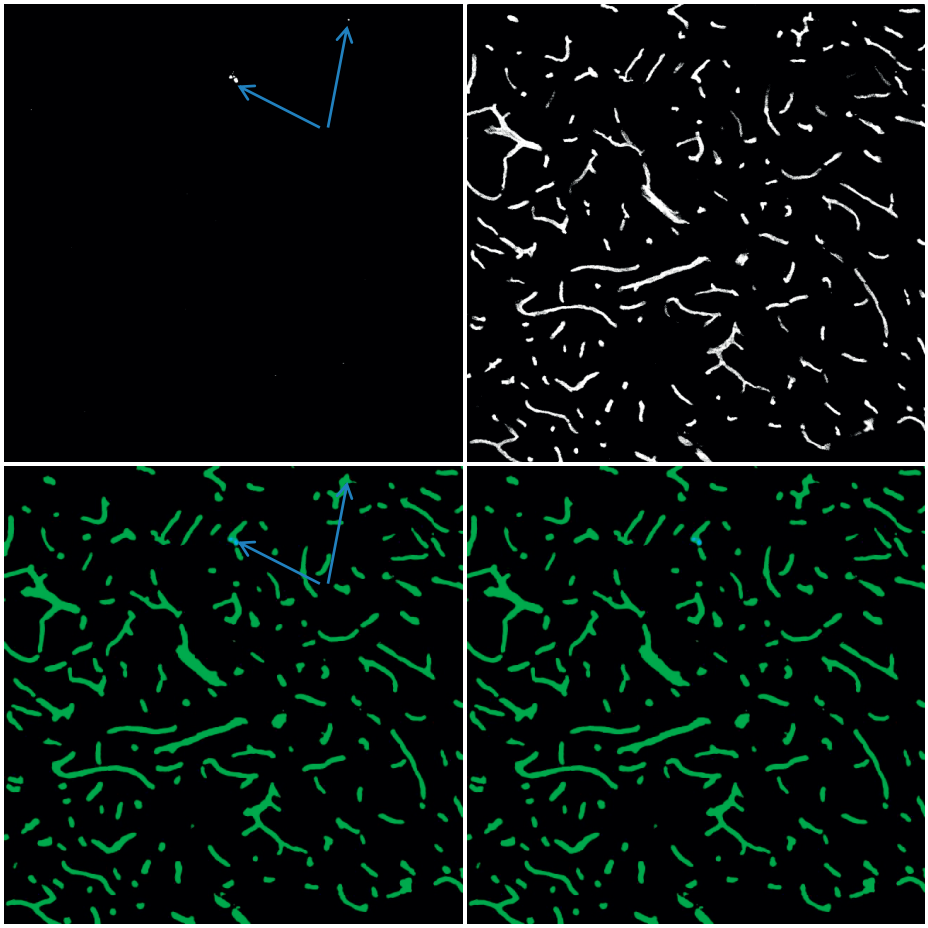

Again, a relatively easy scenario similar to Scenarios 1-2. Isolated spots are can still be detected inside of blood vessels (indicated by blue arrows), but the image fails the NP count exclusion criterion **(Exclusion Criterion 3).**

Scenario 3: Unrealistic Blood Vessels

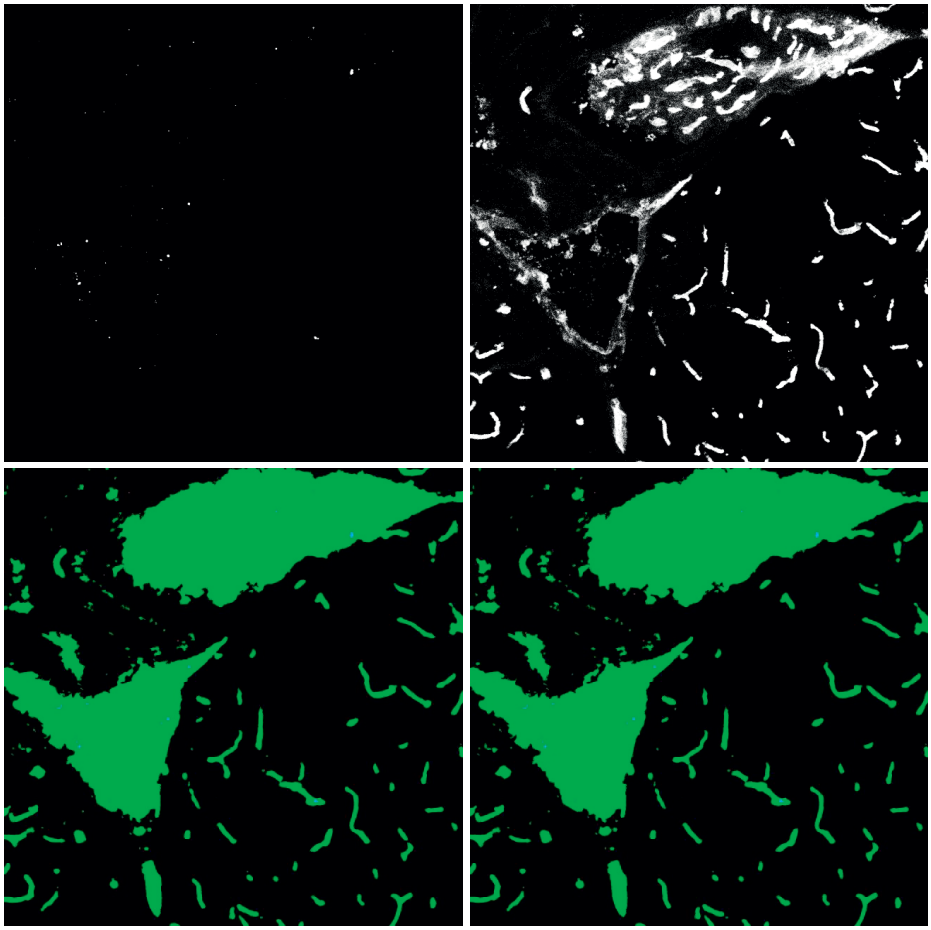

This scenario clearly shows an abnormal segmentation result. Filters could easily be applied to remove the two large 'blood vessel' clumps, but we preferred to filter out the entire image instead, based on the unreasonably large blood vessel area (25.5% of the image), i.e. this image failed **Exclusion Criterion 2**.

Scenario 4: Dispersed NPs without blood vessels

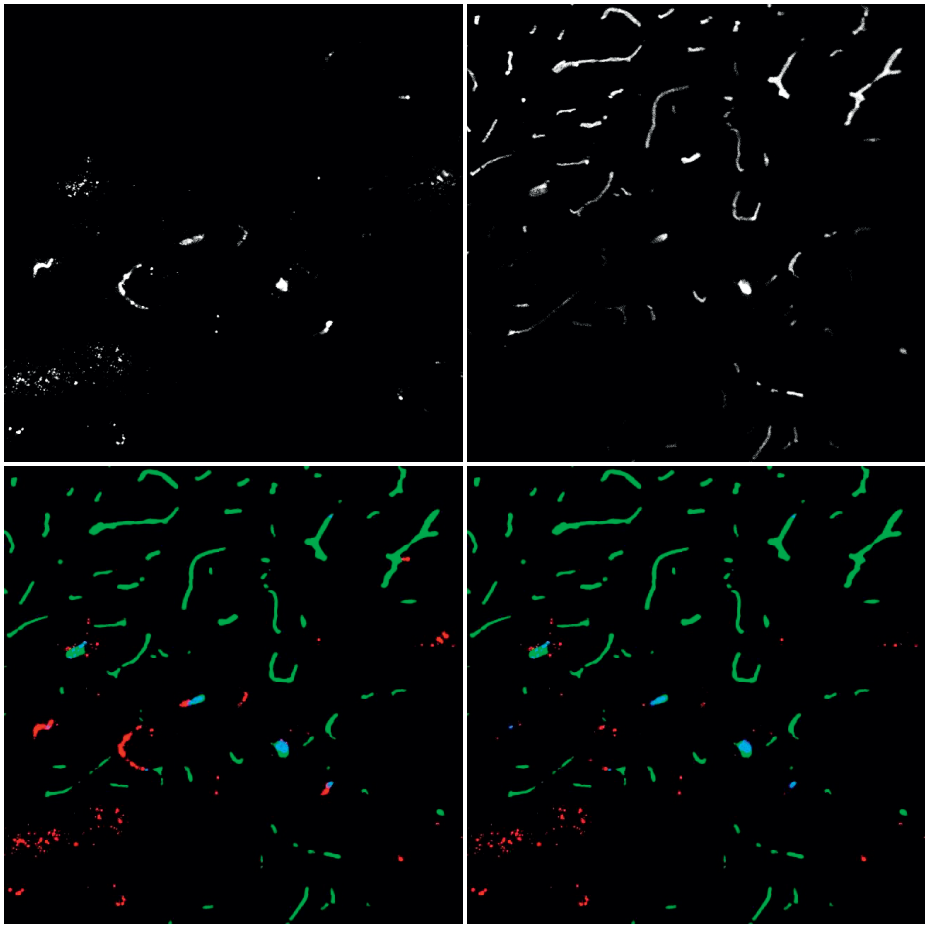

This is a relatively difficult scenario. Clumps of NPs that are clearly inside blood vessels, even though the corresponding blood vessel staining failed, can be filtered out easily (see below). However, we decided not to remove a cluster of NPs in the lower left corner even though they may or may not originate from a blood vessel that is not visible due to failed staining. This is both because of the lack of obvious exclusion criteria (no clear line connecting the NPs, unless one believes they have originated from a very thick blood vessel where the staining happens to have failed and the possibility that these NPs may have actually been displaced from the nearest visible blood vessel. In addition, the use of very sophisticated parameters (number of neighbors detected within a certain distance etc.) would considerably increase processing time and could affect segmentation in other images in a manner that can be difficult to predict, assuming uniform application of the algorithm throughout the entire dataset. However, this particular

image is filtered out altogether, based on **Exclusion Criterion 4**. In this image, the ratio is 0.98, well above the average value. In addition, while this image does not fail **Exclusion Criterion 2**, it is very close to the criterion's lower limit.

Scenario 5: Clumped NPs

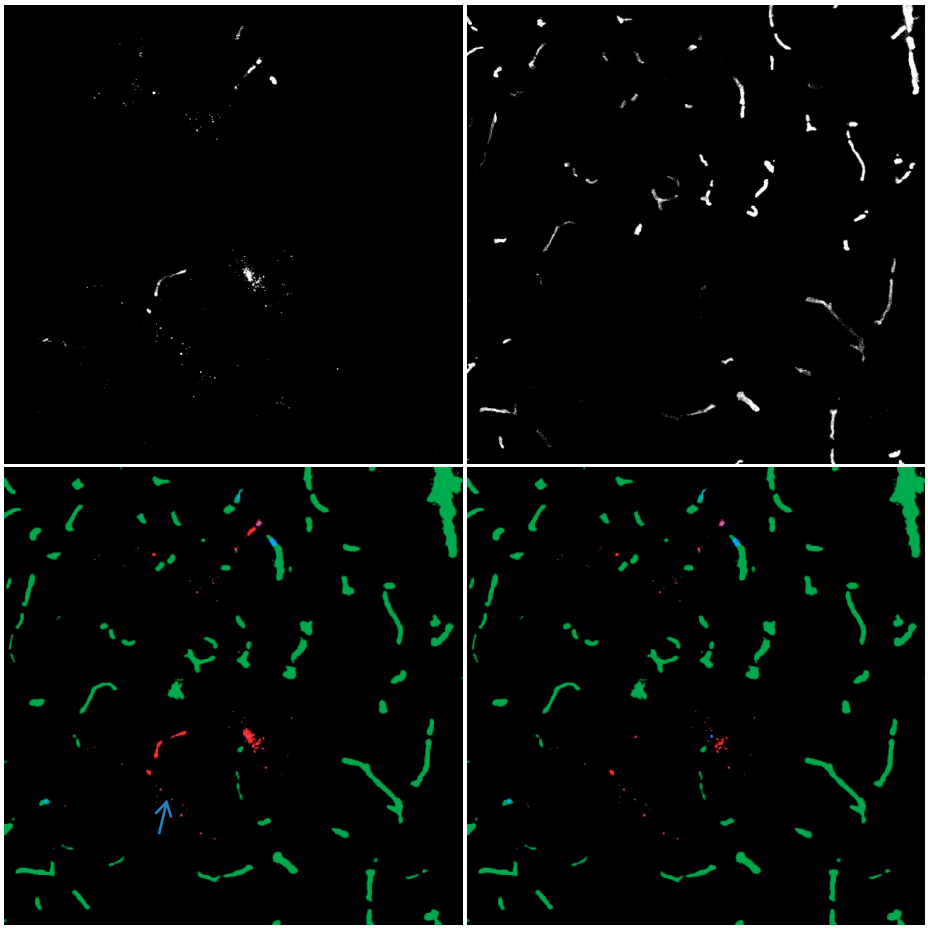

This is a fairly common case observed when there is a substantial number of NPs in an image. Some of the NPs in clumps are clearly in the blood vessels and are filtered by using axis length as a criterion. Setting the limit to exclude these and other similar clumps is a subjective call based on visual inspection of images, but the same criterion is applied to all images in the dataset. One can argue that the isolated group of the NPs located along a line (indicated by an arrow) should also be filtered. This is, however, not a trivial task to be performed consistently in automated image analysis.

Scenario 6: Few NPs, mostly inside blood vessels

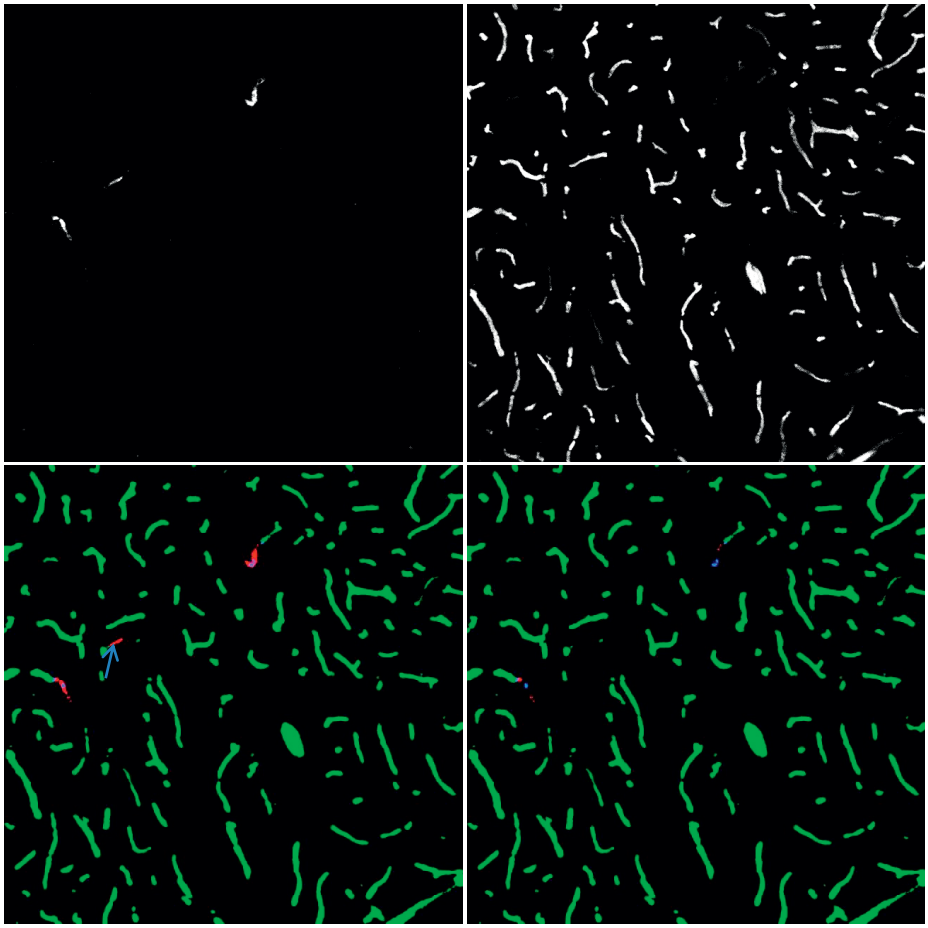

A relatively easy scenario, mostly shown to illustrate filtering or NPs that are deemed to be inside their adjacent blood vessels (indicated by an arrow).

Scenario 7: Clustered and elongated NPs

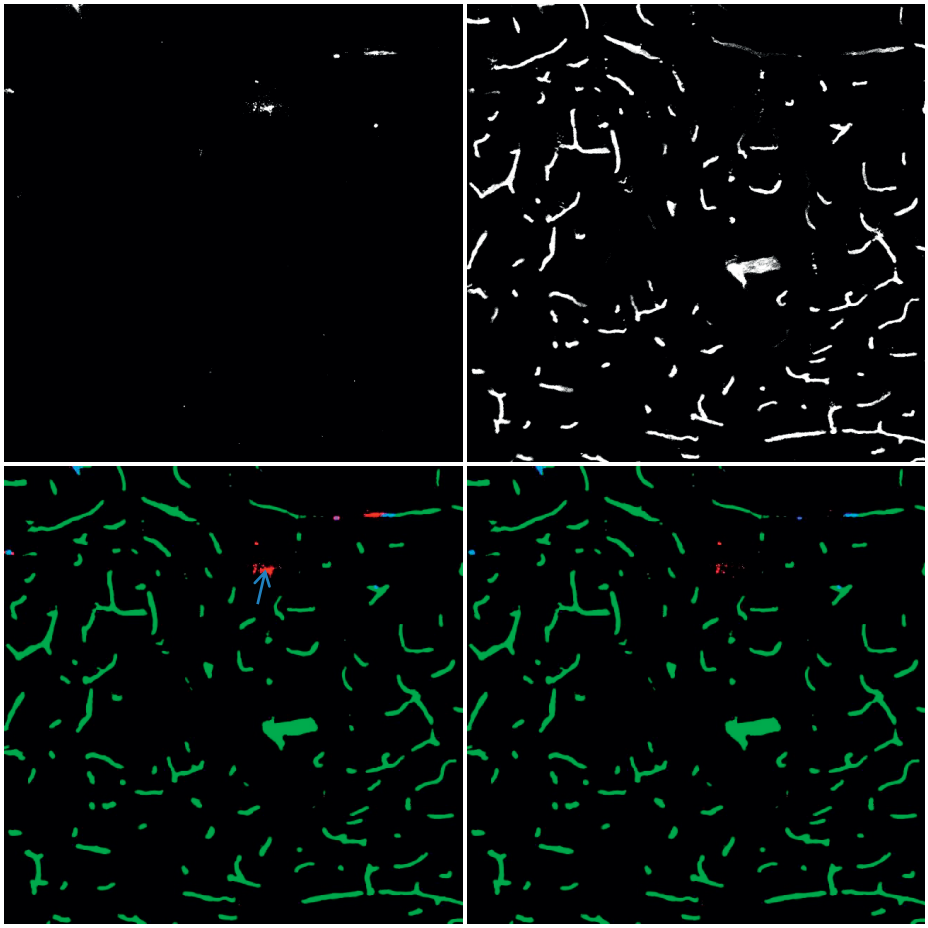

This scenario shows both clustered and elongated NPs. The group of NPs indicated by an arrow most likely originates from a blood vessel, and the central part is filtered out, although the dispersed cloud is retained. This is similar to Scenario 5.

Scenario 8: Very few blood vessels with poor staining, large spread of NPs

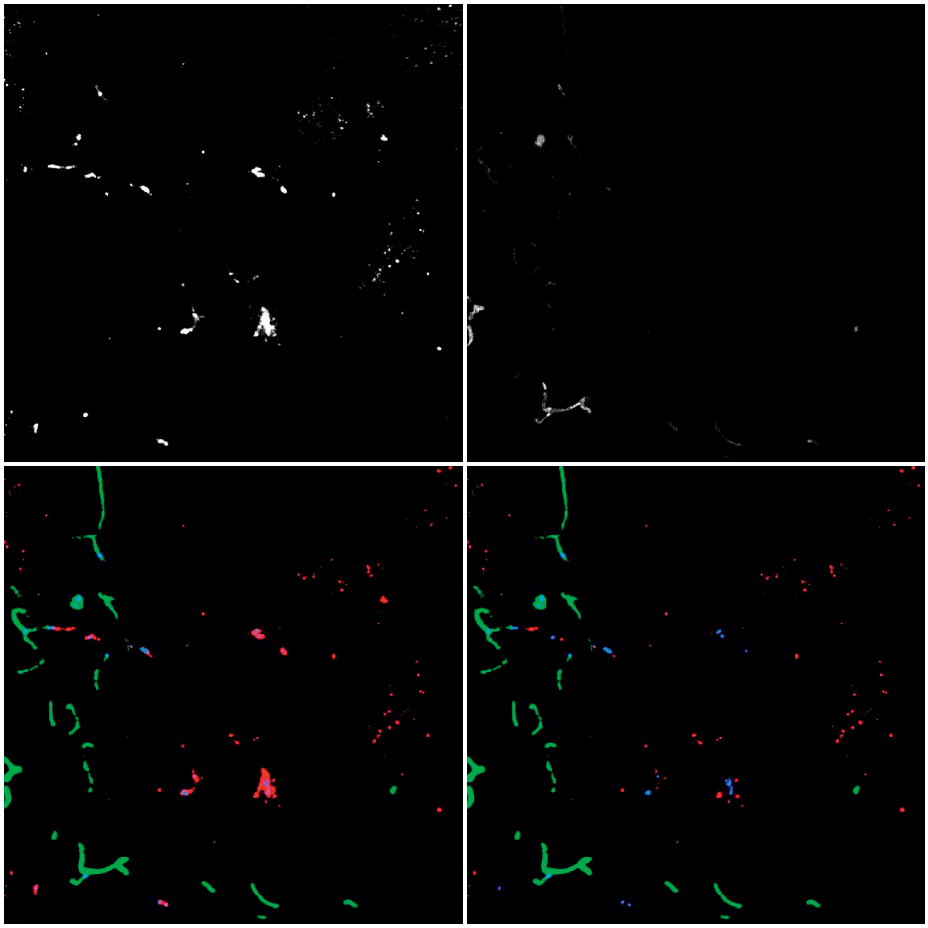

This is a relatively easy scenario. While the algorithm segments blood vessels rather well, given poor staining quality, this image fails several exclusion criteria at once (total area of blood vessels in the image being too low, number of segmented blood vessels being too low, and the ratio of NPs located within 100 to 1000 pixels from the nearest blood vessel to NPs located within 100 pixels from the nearest blood vessel being too high.

Paper V

IVYSPRING INTERNATIONAL PUBLISHER

Theranostics

2017; 7(1): 23-30. doi: 10.7150/thno.16577

Research Paper

Efficient Enhancement of Blood–Brain Barrier Permeability Using Acoustic Cluster Therapy (ACT)

Andreas K.O. Åslund[1]✉, Sofie Snipstad[1], Andrew Healey[2], Svein Kvåle[2], Sverre H. Torp[3,4], Per C. Sontum[2], Catharina de Lange Davies[1], Annemieke van Wamel[1]

1. Department of Physics, Norwegian University of Science and Technology (NTNU), Trondheim, Norway;
2. Phoenix Solutions AS, Oslo, Norway;
3. Department of Pathology and Medical Genetics, St. Olavs University Hospital, Trondheim, Norway;
4. Department of Laboratory Medicine, Children's and Women's Health, NTNU, Trondheim, Norway.

✉ Corresponding author: andreas.aslund@ntnu.no, andreas.aaslund@gmail.com.

Received: 2016.06.23; Accepted: 2016.08.23; Published: 2017.01.01

Abstract

The blood-brain barrier (BBB) is a major obstacle in drug delivery for diseases of the brain, and today there is no standardized route to surpass it. One technique to locally and transiently disrupt the BBB, is focused ultrasound in combination with gas-filled microbubbles. However, the microbubbles used are typically developed for ultrasound imaging, not BBB disruption. Here we describe efficient opening of the BBB using the promising novel Acoustic Cluster Therapy (ACT), that recently has been used in combination with Abraxane® to successfully treat subcutaneous tumors of human prostate adenocarcinoma in mice. ACT is based on the conjugation of microbubbles to liquid oil microdroplets through electrostatic interactions. Upon activation in an ultrasound field, the microdroplet phase transfers to form a larger bubble that transiently lodges in the microvasculature. Further insonation induces volume oscillations of the activated bubble, which in turn induce biomechanical effects that increase the permeability of the BBB. ACT was able to safely and temporarily permeabilize the BBB, using an acoustic power 5-10 times lower than applied for conventional microbubbles, and successfully deliver small and large molecules into the brain.

Key words: Blood-brain barrier opening, focused ultrasound, acoustic cluster therapy (ACT), enhanced drug delivery

Introduction

The blood-brain barrier (BBB) maintains the homeostasis of the brain and protects it from unwanted or harmful substances. Unfortunately, the BBB also blocks >98% of small drugs (<600 Da) and all larger therapeutic molecules from entering the brain, unless active transport of the substances is possible [1]. Thus, the presence of an intact BBB limits the distribution of a large number of therapeutic agents, including anti-cancer and anti-viral drugs, as well as novel therapeutic approaches that do not translate to clinical practice because of this biological barrier. For this reason, diseases like brain cancer, Alzheimer's disease, amyotrophic lateral sclerosis (ALS) and more, remain untreatable. New ways to pass the BBB have to be explored for every single drug lead, resulting in a severe restriction on the development of medicinal therapies for brain diseases. Since its introduction in 2001 [2], focused ultrasound (FUS) in combination with microbubbles has been explored to increase the permeability of the BBB in various pre-clinical settings [3]. In brief, insonation of the vascular compartment containing microbubbles leads to a variety of biomechanical effects that increase the permeability of the endothelial barrier both paracellularly or transcellularly [4]. The increased permeability leads to enhanced extravasation, distribution and uptake of drug molecules in the target tissue [5-7]. This approach is currently being evaluated in two separate

clinical trials (ClinicalTrials.gov identifier NCT02343991 [8] and NCT02253212) [9, 10]. Most studies using FUS for BBB disruption (BBBD) are employing commercial ultrasound contrast agent microbubbles, such as Definity®, Sonovue® and Optison® [2, 11-16]. To improve treatment strategies, incorporation of drugs into custom-made microbubbles has also been investigated [17-19]. Whereas the concept clearly holds merit, it also has limitations. The microbubbles need to be close to the endothelial wall to maximize biomechanical effects [20, 21]. However, regular contrast microbubbles are small (1-3 µm), and their average distance to the vessel wall is often too large to induce a significant biomechanical effect. Furthermore, the circulation lifetime of most microbubbles is typically in the order of 2-3 min, thus limiting the exposure time. Although conventional microbubbles have shown promise for opening the BBB and for drug delivery to the brain, these microbubbles were developed for diagnostic imaging, not for therapy. Microbubble formulations designed for therapy are likely to be needed to enable optimal treatment regimens.

A recently proposed concept for ultrasound mediated, targeted drug delivery; Acoustic Cluster Therapy (ACT), makes use of similar mechanisms as regular microbubbles, but addresses important shortcomings of the latter. Details of the ACT formulation concept are described previously [22-24]. In brief, the ACT formulation is produced by electrostatic complexation between negatively charged microbubbles and positively charged oil microdroplets. The active moiety comprises microbubble/microdroplet clusters engineered to be stable *in vivo*. After *intravenous* injection of the clusters, ultrasound is applied to the diseased area and the microbubbles transfer acoustic energy to the attached droplets, which undergo a liquid-to-gas phase shift (the "Activation" Step). The resulting ACT-bubbles undergo a rapid expansion to approximately 25 µm and are temporarily deposited in the local capillary network, transiently blocking blood flow for up to 10 min. Further application of ultrasound (the "Enhancement" step) induces volume oscillation of the ACT-bubbles, which result in non-thermal mechanisms such as cavitation and shear forces that increase the local permeability of the vasculature, increasing transport of co-administered drugs across the capillary wall and through the extracellular matrix [23, 24]. Being approx. three orders of magnitude larger in volume than regular contrast microbubbles, ACT bubbles will deliver a significantly larger biomechanical effect. In addition, the ACT bubble is in close contact with the endothelial wall over a significant segment, ensuring optimal coupling between the vessel wall and the oscillating bubble. Finally, the ACT bubble stays for typically 10 minutes, prolonging the treatment time window compared to regular contrast microbubbles. We have recently shown that this concept can be utilized to induce a strong enhancement of the therapeutic efficacy of paclitaxel and nab-paclitaxel (Abraxane®) for treatment of solid tumors such as human prostate adenocarcinoma growing subcutaneously in athymic mice [25]. When combining the ACT treatment with a clinically relevant dose of Abraxane®, all of the treated mice were alive at the end of the study (120 days after treatment start, 99 days after treatment end) and 67% were in complete remission. Conversely, the group treated with Abraxane, without ACT treatment, had a median survival time 72 days' post treatment start (0% survival at the end of the study). Furthermore, during treatment, this group showed little tumor regression and more importantly, tumor growth continued immediately after the treatment was stopped. The median survival of the control group time was 28 days'.

In the current paper, we have investigated the ACT concept for opening the BBB for model drugs in rats. With the new ACT approach, it is possible to generate bubbles, *in-situ*, that more effectively deliver small and large model drugs into the brain, compared to regular contrast microbubbles. In addition, the applied ultrasound pressure in this study is 5 to 10 times lower than typical levels used with regular microbubbles, potentially making the treatment safer.

Materials and Methods

ACT and Sonazoid™

The ACT formulation consisted of a dispersion of microbubble/microdroplet clusters made from reconstituting the ultrasound contrast agent Sonazoid™ with 2 ml of perfluoromethylcyclopentane (PFMCP) microdroplets (3 µl/ml) stabilized with a distearoyl-phosphatidylcholine (DSPC) phospholipid membrane with 3% (mol/mol) stearylamine (SA), dispersed in 5 mM Tris(hydroxymethyl)aminomethane (TRIS) buffer. ACT was diluted 1/8 in (TRIS)-HCl buffer (pH 7.4) before injection [23].

Sonazoid™ (GE Healthcare AS, Norway) is an ultrasound contrast agent comprising perfluorobutane (PFB) microbubbles, stabilized with a hydrogenated egg phosphatidylserine-sodium (HEPS-Na) phospholipid membrane, embedded in a lyophilized sucrose matrix [26]. Sonazoid™ was diluted 1/8 in TRIS-HCl buffer (pH 7.4) before injection. Further details on the ACT formulation and the microbubble/microdroplet ratio are provided by

Sontum et al [23]. ACT and Sonazoid™ were kindly provided by Phoenix Solution AS, Oslo, Norway.

Animals

Healthy female Sprague Dawley rats (NTac:SD; Taconic), 8-12 weeks old with a weight of 240-280 grams, were used. All experimental procedures were conducted in compliance with protocols approved by the Norwegian Animal Research Authorities. Animals were housed in a specific pathogen free environment at a 12h night/day cycle with controlled temperature and humidity. Food and water were provided *ad libitum*.

Ultrasound Setup and Treatment Regimen

A 1 MHz FUS transducer (Imasonic SAS) with a diameter of 50 mm and a focal length of 125 mm (f-number 2.5) was used. The transducer was positioned in a water bath and a specially designed magnetic resonance imaging (MRI) bed [19], with the animal in a supine position, placed on top of the water tank. The skull of the animal was positioned approximately 120 mm from the transducer.

The animal was sedated by gas anesthesia (isoflurane ~ 4% and 2% induction and maintenance, respectively, in 78% medical air/20% O_2). The head of the animal was shaved using a trimmer, and depilatory cream was applied to the shaved area for 1 min to remove remaining hair. The tail vein was cannulated (BD Neoflon 24G, Becton Dickinson & Co), and the animal placed on the MRI bed. Omniscan (1 ml/kg, 0.5 mmol gadododiamide/kg) was injected and MR images were recorded. Sonazoid™ (1 ml/kg) or ACT (1 ml/kg) was injected and the cannula was flushed with 0.1 ml of 1 U/ml heparin. Immediately after injection, the ultrasound treatment was initiated. The treatment was divided into an activation step followed by an enhancement step using the same transducer and the same sonication sequence with two different mechanical indexes (MIs). The MI was calculated from the estimated *in situ* pressure, assuming 40% attenuation of the ultrasound power through the skull of the animal [19]. For the activation step, the parameters were: MI 0.28, 4 µs pulse length, pulse repetition frequency (PRF) 1 kHz, sonication time 30 s. For the enhancement step, MI was 0.09, 4 µs pulse length, PRF 1 kHz, sonication time 10 min. Each animal was treated two times in two different positions, posterior and anterior of the cerebrum, and the two treatments were sometimes from different treatment groups. The contralateral side of the treated position was used as an internal negative control. After treatment, MR images were recorded. The animals were intravenously injected with pentobarbital and perfused with phosphate saline buffer 1x (PBS) and 4% paraformaldehyde (PFA) in PBS and the brain was submerged in formalin (10%) for at least 24 h, before being sectioned for histology. The experimental timeline is shown in Fig. 1.

Five treatment groups were investigated.

1. ACT + Activation ultrasound + Enhancement ultrasound (ACT+A+E) (8 animals for BBBD, 4 animals for BBB recovery, 2 animals for bioluminescence of IRDye 800CW-PEG).

2. ACT + Activation ultrasound (ACT+A). (4 animals for BBBD, 2 animals for bioluminescence of IRDye 800CW-PEG).

3. ACT + Enhancement (ACT+E) (5 animals).

4. Sonazoid™ + Activation ultrasound + Enhancement ultrasound (Sonazoid™+A+E) (3 animals).

5. Saline + Activation ultrasound + Enhancement ultrasound (Saline+A+E) (3 animals).

MRI

MR images were acquired using a 7.05 T horizontal bore magnet (Biospec 70/20 Avance III, Bruker Biospin) with an 86 mm volume resonator for RF transmission and a phased array rat brain surface coil for reception. A pressure sensitive- and a temperature probe recorded respiration and temperature, respectively, of the rat (SA Instruments). Gas anesthesia (isoflurane ~2% in 78% medical air/20% O_2) was adjusted appropriately and the body temperature was maintained at 37 °C by water circulation in the MRI bed. The animala was placed in the scanner, coils were tuned and matched and a tri-pilot with navigator scan (30 s) was acquired. MRI was acquired pre- and post-treatment. To verify BBBD and to detect hemorrhage *in vivo*, a Fast-Low Angle Shot (FLASH) sequence was used (Flip angle of 60°, TE/TR 5/350 ms, zero fill acceleration of 1.3, 10 averages, lasting 6 min and 8 s). The geometry of the MR sequence had a field of view of 40x27 mm, matrix size of 200x135 and 12 slices á 1 mm.

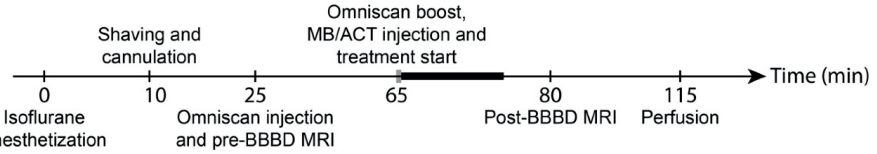

Figure 1. Treatment timeline. Grey bar indicates activation step period and black bold bar indicates enhancement step period.

Analysis of BBBD

To evaluate the effect of BBBD, the intensity of the contrast agent in the MR images from each treatment region was estimated. When BBBD was visibly detectable, an ROI was drawn around the opened area and the same ROI was used on the non-treated contralateral side of the brain. The ratio of the average intensities of the ROIs was calculated using ImageJ [27]. Positioning of the ultrasound was manual, thus the exact coordinates for the BBBD was not available. To quantify the BBBD, it was therefore required to be able to observe the contrast agent in the image. Hence, quantitative data is only available for 3 of the 5 groups in Fig. 2.

Bioluminescence optical imaging

Successful delivery of a near infrared pegylated macromolecule (IRDye 800CW-PEG, LI-COR Biosciences Ltd) was verified using bioluminescence imaging (Pearl Impulse Imager, LI-COR Biosciences Ltd.). The excitation and emission settings were 785 and 820 nm, respectively. Animals were treated according to treatment group 1 and 2 with IRDye 800CW-PEG (10 nmol/kg) injected immediately after gadodiamide. The pegylated dye of approximately 45 kDa was used for assessing macromolecule vascular permeability [28]. 1 h after FUS treatment, the animals were injected with pentobarbital and perfused with PBS, before the brain was removed and imaged.

BBB recovery

To evaluate recovery of the BBB, treated animals were taken off anesthesia and decannulated. The animals were imaged again approximately 24 h and 72 h post treatment. For each MRI session, the animals were sedated and cannulated as described and Omniscan (1 ml/kg) was injected to evaluate the BBB recovery.

Histology

Paraformaldehyde fixated brains were cast into paraffin and cut into 4 µm thick sections. The sections were stained by haematoxylin-eosin-saffron (HES). Sections were imaged on an EVOS FL Auto (objective, 20x/ 0.25, air, Invitrogen/ThermoFisher). Images were stitched using the built-in software.

Statistical analysis

All statistical analysis was performed using Prism 6 (GraphPad Software, Inc.). Mean, standard deviation (with N-1 degree's freedom), analysis of variance (ANOVA) and Bonferroni's multiple comparison test were calculated for the BBBD groups (Fig. 2). Mean, standard deviation and monoexponential decay ($f(t)=a*e^{(-K*t)}+b$) were calculated for the BBB recovery group (Fig. 4).

Results and discussion

Gadodiamide extravasation to the brain

ACT in combination with the activation and enhancement step clearly opened the BBB allowing MRI contrast agent to enter into the brain tissue (Fig. 2). Fig. 2 shows strong gadodiamide signal in the brain treated with ACT and activation and enhancement FUS, whereas only giving ACT and the activation FUS exposure showed hardly any signal. ACT was also much more efficient than the commercial Sonazoid in opening the BBB in combination with ultrasound. To obtain more quantitative data, the ratio of gadodiamide signal in the treated part vs. the non-treated contralateral part of the brain was calculated. In average, the ratio increased 50% for ACT+A+E treatment, compared to 18% for the Sonazoid™+A+E treatment (Fig. 2d). The extravasation of gadodiamide into the brain caused by ACT+A+E was significantly higher ($p<0.01$, Figure 2d) than with Sonazoid™+A+E (groups 1 and 4, respectively). ACT+A (group 2) caused similar gadodimamide extravasation as for Sonazoid™+A+E. ACT+E only (group 3) and Saline+A+E (group 5) did not induce BBBD and are thus not included in Fig. 2.

With the ultrasound activation and enhancement regimes applied, the ACT treatment clearly induced a significantly higher extravasation of gadodiamide to the brain than regular, small contrast microbubbles. Several important distinctions may contribute to this difference in effect level. The ACT-bubbles are in close contact with the endothelium over a significant segment of the vessel wall, ensuring a large interfacing area between the oscillating bubble and the endothelial cells. Sonazoid™, on the other hand, is free flowing and the average distance between the microbubble surface and the endothelial cells may limit the biomechanical effect level. ACT-bubbles are approximately 1000 times larger (by volume) than Sonazoid™ microbubbles and the biomechanical effects these large bubbles induce, even at low ultrasound pressures, should be orders of magnitude larger than with regular contrast microbubbles. Moreover, the lodged ACT-bubble will cause an increased microvascular pressure on the arterial side of the bubble and the induced transcapillary pressure gradient will enhance extravasation.

Comparing ACT+A with ACT+A+E, the 10 min, low MI enhancement step in the later treatment scheme is clearly increasing extravasation. Whether this is due to generation of larger openings with prolonged treatment, greater influx from longer

treatment time, or a combination, cannot be determined from these experiments. Moreover, the enhancement step alone fails to produce BBBD with ACT, indicating that the phase shift event is a prerequisite for an effective BBBD.

In this study, Sonazoid™ has been used to represent commercial microbubbles, as it is a constituent of ACT. The commercial microbubbles have different properties with respect to size, size-distribution and shell properties. Nonetheless, the acoustic parameters used for effective BBBD are often similar for these MBs. This has been investigated in the case of Optison vs. Definity by McDannold et al [16] and for microbubbles of different sizes by Samiotaki et al. [14]. Another phase shift microbubble, based on acoustically active oil nanodroplets, has previously been used to open the BBB [29]. The nanodroplets had a size of 100-200 nm and ultrasound activation of the volatile oil created a microbubble of similar size to those in conventional ultrasound contrast agents. The study found that the nanodroplets were less effective in opening the BBB than commercial contrast agents at similar ultrasound settings. The main advantages of phase shift nanodroplets are that their size makes it possible for the nanodroplet to enter into the interstitium and cells, enabling abluminal activation, and their long circulation time, hours compared to minutes for conventional microbubbles, enabling prolonged treatment time. Except for the phase shift, nanodroplets and ACT are not easily compared; for instance, the nanodroplet is similar in size and blood circulation half-life to standard contrast microbubbles after activation, while the size and circulation half-life of ACT are more similar before activation.

IRDye 800CW-PEG extravasation into the brain

To explore if ACT facilitate extravasation of larger molecules, IRDye 800CW-PEG was injected before the treatment. IRDye 800CW-PEG extravasated into brain tissue both after ACT+A+E and ACT+A treatment (Fig. 3), the former clearly at a much higher level. IRDye 800CW-PEG is a macromolecule with a molecular weight of approximately 45 kDa, which is a relevant size for many applications within medicinal therapy where macromolecules are used. In a number of therapeutic approaches, including immunotherapy, larger molecules such as proteins or other nanosized agents are applied, hence, enabling delivery of such

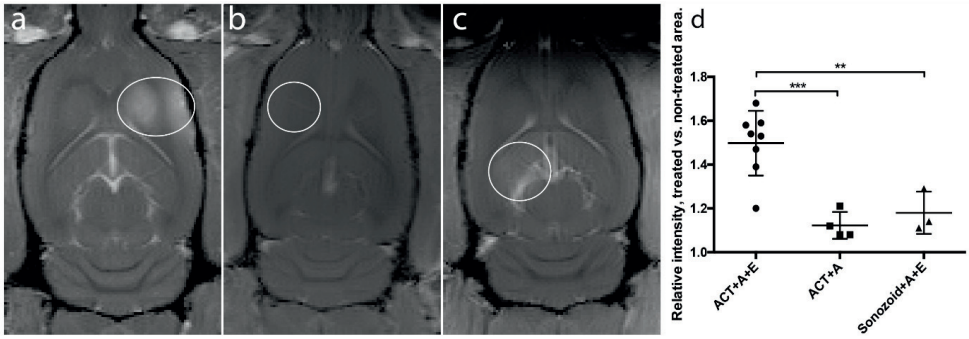

Figure 2: Comparison of gadodiamide signal intensities from MR-images. White rings indicate BBBD, (a) ACT+A+E, (b) ACT+A, (c) Sonazoid™ +A+E. (d) Scatter plot with mean and standard deviation. ** ($p<0.01$), *** ($p<0.001$).

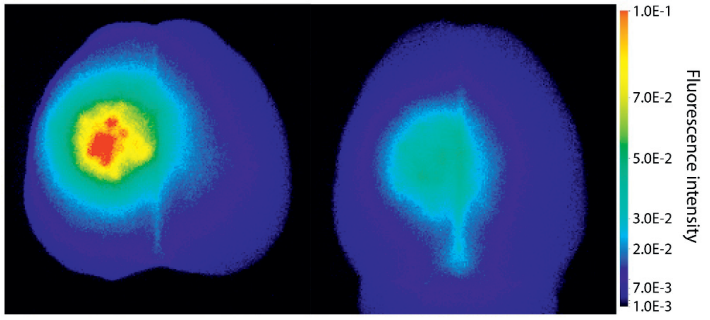

Figure 3: Extravasation of the fluorescent macromolecule IRDye 800CW-PEG to the brain after treatment with (left) ACT+A+E and (right) ACT+A.

large molecules to the brain is an imperative for the success of these therapeutic agents. Even though the literature states that the BBB can be open for several days post treatment, this is only true for smaller molecules, such as gadodiamide [19, 30, 31]. Larger openings generated, allowing larger molecules to enter the brain, are only present for a short time [32]. According to Marty et al. [32], any molecule larger than 15-20 nm would in principle only benefit from FUS mediated BBBD for the duration of the FUS treatment. Hence, the large and deposited ACT bubbles, which are present for a longer time than regular microbubbles and in closer contact with the endothelial wall, are likely to be more effective for delivery of large therapeutic molecules. Furthermore, the efficient delivery observed shows that larger molecules can be delivered to a specific volume of the brain.

Recovery of BBBD

The recovery after the BBBD following ACT+A+E procedure was not complete 1 day after treatment (Fig. 4a-c). At this point, the extravasation of gadodiamide revealed a spot like pattern, rather than a diffuse extravasation pattern, which was observed immediately after ultrasound exposure. This pattern was seen in all recovery animals, and can also be seen in animals injected with IRDye 800CW-PEG (Fig. 3). The spots might be a result of the *in situ* ultrasound beam profile being heterogenous in the sonication focus. Although the beam profile measured in a water thank is homogenous [19], penetrating the skull might generate a more heterogeneous beam profile. This resulted in some areas where the opening was more substantial and consequently prolonged the recovery time. At 3 days' post treatment, a little gadodiamide extravasation into the brain was detectable for some animals, indicating that the BBB was close to or fully recovered. A monoexponential fit ($f(t)=0.73 \cdot e^{-0.85t}+0.96$, $R^2=0.89$) gave a half-life of BBBD recovery of 0.82 days. Previous studies have shown that the BBB closes after 1 to several days [19, 30, 31]. The present recovery kinetics of BBBD are thus similar to those for regular FUS microbubble treatment.

Histology

The *in situ* MI applied in this study was well below the threshold for what has previously been published as risk for damage to the brain/vasculature [33]. This is corroborated by the T1-FLASH and HES-staining, which revealed no signs of hemorrhage. Brains from group 1, 2 and 4 were stained with HES and analyzed for any signs of damage from the different treatments. Group 2 (ACT+A) and 4 (Sonazoid™+A+E), that showed the weakest BBBD, had no signs of adverse effects. Group 1 (ACT+A+E) showed only a few occurrences of focal microhemorrhages (exemplified in Fig. 4a-c), but the damage scored mild and was of no clinical relevance. No signs of eosinophilic degeneration of neurons, gliosis, inflammation or microglial/macrophage reaction were detected.

Conclusions

The present study demonstrates that ACT can be utilized to open the BBB in a safe manner, using a lower pressure FUS regimen than regular contrast microbubbles. ACT is clearly more efficient than regular microbubbles in opening the BBB in combination with ultrasound. The ACT treatment induces a significantly enhanced extravasation of gadodiamide as well as delivery of macromolecules.

This study demonstrates a new application for ACT which previously has shown great promise in enhancing the delivery of co-injected drugs to solid tumors growing in mice [24] and in treating tumors growing in mice [25].

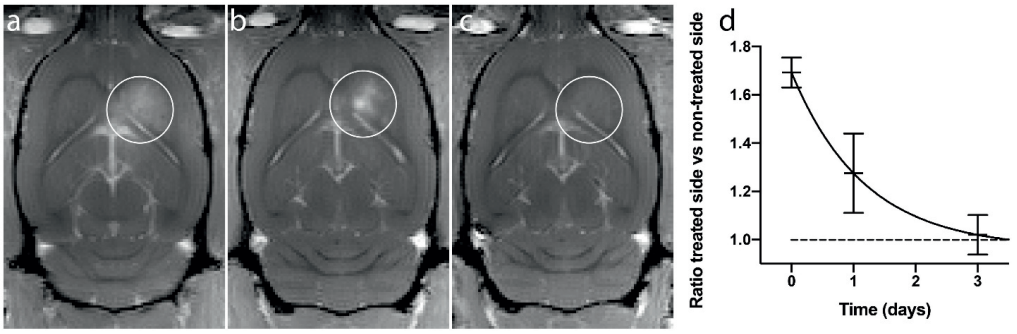

Figure 4: BBBD from a representative animal. (a) Immediately after treatment, (b) 1 day after treatment and (c) 3 days after treatment. (d) Ratio of treated vs non-treated side of the brain, mean and standard deviation from 4 animals.

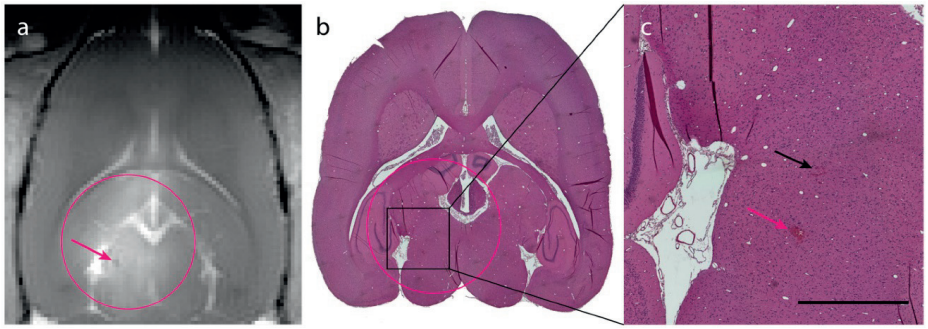

Figure 5: Histological analysis of ACT+A+E treatment. (a) T1-FLASH image showing BBB opening after treatment (magenta circle indicates treated area; magenta arrow indicates microhemorrhage). (b) HES stained image of the brain (magenta circle indicates treated area). (c) Magnified area of b showing two sites of extravasated erythrocytes (magenta arrow corresponds to the microhemorrhage in panel a, black arrow indicates small amount of extravasated erythrocytes; scale bar: 1 mm).

Acknowledgments

Histological samples were prepared by the Cellular and Molecular Imaging Core Facility (CMIC), MRI was performed at the MR core facility, and housing and care of animals was provided by the Comparative Medicine Core Facility (CoMed), all at the Norwegian University of Science and Technology (NTNU) and funded by the Faculty of Medicine and Central Norway Regional Health Authority.

The project is supported by The Research Council of Norway, NANO2021 grant number 220005 and grant number 228604, Central Norway Regional Health Authority and Center for Innovative Ultrasound Solutions (CIUS).

Competing Interests

The authors have declared that no competing interest exists.

References

1. Pardridge WM. Drug transport across the blood-brain barrier. J Cereb Blood Flow Metab. 2012; 32: 1959-72.
2. Hynynen K, McDannold N, Vykhodtseva N, Jolesz FA. Noninvasive MR imaging-guided focal opening of the blood-brain barrier in rabbits. Radiology. 2001; 220: 640-6.
3. Etame AB, Diaz RJ, Smith CA, Mainprize TG, Hynynen K, Rutka JT. Focused ultrasound disruption of the blood-brain barrier: a new frontier for therapeutic delivery in molecular neurooncology. Neurosurg Focus. 2012; 32: E3.
4. Sheikov N, McDannold N, Vykhodtseva N, Jolesz F, Hynynen K. Cellular mechanisms of the blood-brain barrier opening induced by ultrasound in presence of microbubbles. Ultrasound Med Biol. 2004; 30: 979-89.
5. Khokhlova TD, Haider Y, Hwang JH. Therapeutic potential of ultrasound microbubbles in gastrointestinal oncology: recent advances and future prospects. Therap Adv Gastroenterol. 2015; 8: 384-94.
6. Martin KH, Dayton PA. Current status and prospects for microbubbles in ultrasound theranostics. Wiley Interdiscip Rev Nanomed Nanobiotechnol. 2013; 5: 329-45.
7. Unga J, Hashida M. Ultrasound induced cancer immunotherapy. Adv Drug Deliv Rev. 2014; 72: 144-53.
8. Blood-Brain Barrier Disruption Using Transcranial MRI-Guided Focused Ultrasound. U.S. National Institute of Health; 2016.
9. Safety of BBB Opening With the SonoCloud. U.S. National Institute of Health; 2016.
10. Carpentier A, Canney M, Vignot A, Reina V, Beccaria K, Horodyckid C, et al. Clinical trial of blood-brain barrier disruption by pulsed ultrasound. Science translational medicine. 2016; 8.
11. McDannold N, Vykhodtseva N, Raymond S, Jolesz FA, Hynynen K. MRI-guided targeted blood-brain barrier disruption with focused ultrasound: histological findings in rabbits. Ultrasound Med Biol. 2005; 31: 1527-37.
12. Chopra R, Vykhodtseva N, Hynynen K. Influence of exposure time and pressure amplitude on blood-brain-barrier opening using transcranial ultrasound exposures. ACS Chem Neurosci. 2010; 1: 391-8.
13. Liu HL, Hua MY, Chen PY, Chu PC, Pan CH, Yang HW, et al. Blood-Brain Barrier Disruption with Focused Ultrasound Enhances Delivery of Chemotherapeutic Drugs for Glioblastoma Treatment. Radiology. 2010; 255: 415-25.
14. Samiotaki G, Vlachos F, Tung YS, Konofagou EE. A quantitative pressure and microbubble-size dependence study of focused ultrasound-induced blood-brain barrier opening reversibility in vivo using MRI. Magn Reson Med. 2012; 67: 769-77.
15. Fan CH, Liu HL, Ting CY, Lee YH, Huang CY, Ma YJ, et al. Submicron-Bubble-Enhanced Focused Ultrasound for Blood-Brain Barrier Disruption and Improved CNS Drug Delivery. PloS one. 2014; 9: e96327.
16. McDannold N, Vykhodtseva N, Hynynen K. Use of ultrasound pulses combined with Definity for targeted blood-brain barrier disruption: a feasibility study. Ultrasound in medicine & biology. 2007; 33: 584-90.
17. Fan CH, Ting CY, Lin HJ, Wang CH, Liu HL, Yen TC, et al. SPIO-conjugated, doxorubicin-loaded microbubbles for concurrent MRI and focused-ultrasound enhanced brain-tumor drug delivery. Biomaterials. 2013; 34: 3706-15.
18. Lammers T, Koczera P, Fokong S, Gremse F, Vogt M, Storm G, et al. Theranostic USPIO-loaded Microbubbles for MR-controlled Blood-Brain Barrier Permeation. Adv Funct Mater. 2015; 7: 36-43.
19. Åslund AKO, Berg S, Hak S, Morch Y, Torp SH, Sandvig A, et al. Nanoparticle delivery to the brain - By focused ultrasound and self-assembled nanoparticle-stabilized microbubbles. J Control Release. 2015; 220: 287-94.
20. Liu HL, Fan CH, Ting CY, Yeh CK. Combining microbubbles and ultrasound for drug delivery to brain tumors: current progress and overview. Theranostics. 2014; 4: 432-44.
21. Kooiman K, Vos HJ, Versluis M, de Jong N. Acoustic behavior of microbubbles and implications for drug delivery. Adv Drug Deliv Rev. 2014; 72: 28-48.
22. Healey AJ, Sontum PC, Kvåle S, Eriksen M, Bendiksen R, Tornes A, et al. Acoustic Cluster Therapy: In Vitro and Ex Vivo Measurement of Activated Bubble Size Distribution and Temporal Dynamics. Ultrasound Med Biol. 2016; 42: 1145-66.
23. Sontum P, Kvåle S, Healey AJ, Skurtveit R, Watanabe R, Matsumura M, et al. Acoustic Cluster Therapy (ACT)--A novel concept for ultrasound mediated, targeted drug delivery. Int J Pharm. 2015; 495: 1019-27.
24. van Wamel A, Healey A, Sontum PC, Kvåle S, Bush N, Bamber J, et al. Acoustic Cluster Therapy (ACT) - pre-clinical proof of principle for local drug delivery and enhanced uptake. J Control Release. 2016; 224: 158-64.
25. van Wamel A, Sontum PC, Healey A, Kvåle S, Bush N, Bamber J, et al. Acoustic Cluster Therapy (ACT) enhances the therapeutic efficacy of paclitaxel and Abraxane(R) for treatment of human prostate adenocarcinoma in mice. J Control Release. 2016; DOI: 10.1016/j.jconrel.2016.06.018.
26. Sontum PC. Physicochemical characteristics of Sonazoid, a new contrast agent for ultrasound imaging. Ultrasound Med Biol. 2008; 34: 824-33.
27. Schneider CA, Rasband WS, Eliceiri KW. NIH Image to ImageJ: 25 years of image analysis. Nat Methods. 2012; 9: 671-5.
28. Billaud M, Ross JA, Greyson MA, Bruce AC, Seaman SA, Heberlein KR, et al. A new method for in vivo visualization of vessel remodeling using a near-infrared dye. Microcirculation. 2011; 18: 163-71.
29. Chen CC, Sheeran PS, Wu SY, Olumolade OO, Dayton PA, Konofagou EE. Targeted drug delivery with focused ultrasound-induced blood-brain barrier opening using acoustically-activated nanodroplets. Journal of controlled release : official journal of the Controlled Release Society. 2013; 172: 795-804.

30. Wang S, Samiotaki G, Olumolade O, Feshitan JA, Konofagou EE. Microbubble type and distribution dependence of focused ultrasound-induced blood-brain barrier opening. Ultrasound Med Biol. 2014; 40: 130-7.
31. Samiotaki G, Konofagou EE. Dependence of the reversibility of focused-ultrasound-induced blood-brain barrier opening on pressure and pulse length in vivo. IEEE transactions on ultrasonics, ferroelectrics, and frequency control. 2013; 60: 2257-65.
32. Marty B, Larrat B, Van Landeghem M, Robic C, Robert P, Port M, et al. Dynamic study of blood-brain barrier closure after its disruption using ultrasound: a quantitative analysis. J Cereb Blood Flow Metab. 2012; 32: 1948-58.
33. McDannold N, Vykhodtseva N, Hynynen K. Blood-brain barrier disruption induced by focused ultrasound and circulating preformed microbubbles appears to be characterized by the mechanical index. Ultrasound Med Biol. 2008; 34: 834-40.